

# **Design and Prototyping of the Image Derotator for the ELT Infrared Instrument MICADO**

A thesis accepted by the Faculty of Aerospace Engineering and Geodesy of the  
University of Stuttgart in partial fulfillment of the requirements for the degree of  
Doctor of Engineering Sciences (Dr.-Ing.)

by

**M.Sc. Santiago Barboza**

Born in: Mérida, Venezuela

Main referee: Prof. Dr. Jörg Wagner  
Co-referee: Prof. Dr. Klaus Meisenheimer  
Date of defense: November 23, 2018

Chair of Adaptive Structures in Aerospace Engineering  
University of Stuttgart

2018





*Este trabajo está dedicado a mi papa y a mi hija...*



*The research of this dissertation has been conducted at the Max Planck Institute for Astronomy (MPIA), Heidelberg, in collaboration with the Chair of Adaptive Structures in Aerospace Engineering (PAS), University of Stuttgart.*

*The daily activities were supervised by Dr. Jörg-Uwe Pott, Ralf-Rainer Rohloff, Prof. Dr. Klaus Meisenheimer (all from MPIA) and Prof. Dr. Jörg Wagner (PAS, University of Stuttgart).*

*The work related to this thesis was undertaken between October 2014 and March 2018. Financially supported by a scholarship from the German Academic Exchange Service (DAAD) during the first two and a half years and by the MPIA during the last year.*



# Acknowledgments

Before I begin, I would really like to remark, that I only managed to get through this challenge and successfully finish my PhD, with the help and support of many great people along the way. Whilst I cannot name them all here I could not have been more fortunate of having them around me. Therefore, I want to thank all those who in one way or another contributed to this accomplishment.

My family deserves the first mention; I want to thank my Mother, brother and sister for their absolute support in my decision of moving to Germany and their help during these last years. I really appreciate your commitment to Eva and to me. I also want to thank Mónica, without her for following me to Germany my PhD would not have happened.

I began my interaction with astronomical instrumentation when I still was at University (ULA), where I started with the design of a Heliostat for the Centro de Investigaciones de Astronomía (CIDA). I would like to thank my supervisors at ULA, Sebastian Provenzano and Rubén Chacón for guiding me in the beginning of my carrier.

I worked at CIDA until I moved to Germany, leaving there great colleagues and friends. I want to thank my former colleagues for their support. Especially Franco Della Prugna, Gerardo Sánchez, Gustavo Sánchez, Gustavo Barroeta, José Segnini, Gladis Magris, Johnny Cova, Carlos Abad, Ceser Briceño, Kathy Vivas, Cecilia Mateu, Juan Downes and Gustavo Bruzual. I learned a lot from all of you, both professionally and personally and without any doubt my experience at CIDA made all this possible. I will never forget that.

The experience in the Instituto de Astronomía de la UNAM, played a key role in my professional development. I want to thank Alejandro Farah for his unlimited support during my stay in Mexico and his motivation to start a PhD. It worked out Dr.

My history in Germany started in 2008, when I visited Heidelberg for the first time to attend a summer school on astronomical instrumentation. The trip was a huge motivation professionally. I was really impressed by the Max Planck Institute for Astronomy (MPIA) and captivated by the German culture. Back then I never imagined that I would end up working at MPIA. I would like to thank Cesar Briceño and Franco Della Prugna for promoting and supporting that trip.

## Acknowledgments

---

I could not believe how lucky I was, when I was accepted for an internship at MPIA. I truly want to thank Ralf-Rainer Rohloff for the opportunity he gave me back in 2010 and his trust until today. The idea of this PhD was born during that internship.

Jörg-Uwe Pott has been a key person since the beginning of this “endeavor”. He taught me (among many other things) the importance of showing your motivation and determination to do what you want to accomplish. I feel proud to specially thank him here, for his countless support during the last eight years.

A single email back in 2010 made this collaboration with Prof. Wagner (University of Stuttgart) possible, and Cecilia Scorza is responsible for that. It is my pleasure to thank her for the great support and help professionally, but also on a personal level. Your advice, Cecilia, has always been very important.

Prof. Wagner, I am honored to have had you as my supervisor. Thank you very much for accepting to be my “Doktorvater”, for guiding me and for the fantastic recommendations and advice during the past years. It was not easy to be accepted as a PhD student, but it would have been simply impossible without your support.

Related to the admission process, I did not miss the deadline thanks to Graciano Molina and Rubén Chacón. Thank you for “accelerating” the process to get the required signatures of my documents at ULA. The effort was not in vain and this is the best way to express my gratitude for that.

I would like to thank my officemates Harald Baumeister, Armin Huber, Norbert Münch and Monica Ebert for their welcoming reception and company. You not only helped me through the hard process of learning German (still ongoing), but also taught me “the art of German engineering” (still ongoing as well). Working at MPIA would not have been possible without the support of its directors Hans-Walter Rix and Thomas Henning. Thanks a lot for this opportunity and all the considerations taken to deal with my case. I also want to thank Ingrid Apfel for always making things easier. Heide Seifert owns a special acknowledgment, she just made possible to deal with the visa applications and the house-hunting in Heidelberg (don’t know which one is more difficult). Thank you very much Heide for your unconditional support all these years.

The contributions of the MICADO team at MPIA were of great importance and these results would not have been possible without them. Especially, I would like to thank Friedrich Müller, Ralph Hofferbert, Lars Mohr, José Ramos and Vianak Naranjo. I also want to express my gratitude to Martin Glück and Benjamin Greiner for their great support with MATLAB and ANSYS during my PhD.

I want to thank also Klaus Meisenheimer for his support as co-referee of this thesis and, Hans Kärcher and Wolfram Schlossmacher for their great technical support as external advisors.

I will probably not find a way to reattribute what my friends Vianak, Gabriele, Rob, Kalyan, Faustine, Conchi, Jörg-Uwe, Mariana, Miguel, Torsten, Leticia, Mario, Petra, Ana and Shannon did for me. I was able to go through the mess of 2017 because of you guys. Thanks a lot.

## Acknowledgments

---

Despite the distance, your friendship has been a great support. Thanks for being always there: Luis, Chocho, Clau, Andrea, Gabriel (2x), Giulli, Gordo, Javi, Jeni, Rodo, Luigi, Caro y Rebe. My brothers of the MRC also deserve my Acknowledgments. Our experiences together have constantly helped me to move forward.

I want to thank Myriam for her support during the last stage of the PhD. You gave me the energy to finish up writing the thesis.

Is also my pleasure to thank Natalia for helping me preparing the defense. I am pretty sure the outcome wouldn't have been the same without all the tips you gave me. Thank you also for the opportunity of sharing this moment with you.

Finally, I must thank my daughter Eva, without her knowing, she has been the reason to keep going, even when I thought I could not continue.



Heidelberg, December 12, 2018.

## Acknowledgments

---



# Contents

<b>Abstract</b> .....	<b>v</b>
<b>Zusammenfassung</b> .....	<b>vii</b>
<b>List of figures</b> .....	<b>ix</b>
<b>List of tables</b> .....	<b>xix</b>
<b>List of abbreviations</b> .....	<b>xxi</b>
<b>List of symbols</b> .....	<b>xxiii</b>
<b>1 Introduction</b> .....	<b>1</b>
1.1 The European Extremely Large Telescope .....	2
1.1.1 Location .....	4
1.1.2 Optical Design.....	5
1.1.3 Mechanical Design.....	6
1.1.4 Instruments.....	8
1.2 The MICADO Instrument.....	10
1.2.1 Key Capabilities of the Instrument .....	12
1.2.2 The MICADO Concept.....	12
1.3 The Image Derotator .....	16
1.4 Motivation and Thesis Objectives.....	17
1.5 Thesis Outline .....	19
<b>2 Alt-Azimuth Telescopes Field Rotation</b> .....	<b>21</b>
2.1 Deriving the Parallactic Angle .....	23
2.2 Field Rotation at Cassegrain Focus.....	25

2.3	Field Rotation at Nasmyth Focus .....	27
2.3.1	Field rotation at ELT Nasmyth platform A .....	28
2.4	Pupil Rotation at Nasmyth Focus .....	30
2.5	Variables Affecting the Field Rotation Trajectory .....	32
<b>3</b>	<b>Field De-Rotation for MICADO .....</b>	<b>35</b>
3.1	Derotator Requirements .....	38
3.2	Bearing Technology Trade-off .....	40
3.2.1	Slewing Bearings .....	40
3.2.2	Hydrostatic Oil Bearings .....	41
3.2.3	Hydrostatic Air Bearings .....	42
3.2.4	Magnetic Bearings .....	43
3.2.5	Bearing Technology Trade-off Comparative Summary .....	44
3.3	Existing Technical Solutions .....	45
3.3.1	LINC-NIRVANA Ground-Layer Wavefront Sensor .....	45
3.3.2	The Ground-Layer Adaptive Optics Assisted by Laser .....	46
3.3.3	The ALMA Antenna Azimuth Mechanism .....	47
3.3.4	LBT Gregorian Focus Rotator .....	49
3.3.5	Daniel K. Inouye Solar Telescope Coudé Rotator .....	49
3.3.6	TMT Infrared Imaging Spectrograph (IRIS) Rotator .....	51
<b>4</b>	<b>The MICADO Derotator .....</b>	<b>53</b>
4.1	The Custom Designed Slewing Bearing .....	54
4.1.1	Bearing Mechanical Interfaces .....	57
4.2	Bearing Support Structure Optimization .....	59
4.2.1	Results of the Optimization Function $I_A$ .....	65
4.2.2	Results of the Optimization Function $I_R$ .....	67
4.2.3	Discussion of the Optimization Process Results .....	68
4.3	Derotator design proposal .....	69
4.3.1	Bearing Support Structure .....	70
4.3.2	Bearing Thermal Compensation Rings .....	77
4.3.3	Drive System .....	80
4.3.4	Positioning Measurement System .....	83
4.3.5	Controller Architecture .....	84
4.3.6	Derotator Mass Budget .....	85
4.4	Derotator Static Structural Analysis .....	86

---

4.4.1	Modeling a Four-Point Contact Ball Bearing .....	86
4.4.2	Summary of the Bearing FEM Comparative Analysis .....	95
4.4.3	Validation of the Bearing FEA .....	96
4.5	Results of the Derotator FEA .....	100
4.6	MICADO Instrument Eigenfrequency .....	109
4.7	Optimization of the Warping Moment Effect .....	111
<b>5</b>	<b>The end-to-end simulation.....</b>	<b>117</b>
5.1	Basics of structural dynamics .....	118
5.1.1	Body under Free Oscillations with Damping.....	120
5.1.2	Body under Forced Oscillations with Damping.....	121
5.1.3	State-Space Representation.....	122
5.1.4	Structural Transfer Function .....	123
5.2	Specific challenges of modelling the derotator.....	124
5.3	Modeling the bearing friction .....	130
5.4	Implementation of the end-to-end model.....	132
<b>6</b>	<b>The experiment: Derotator test stand .....</b>	<b>135</b>
6.1	Design of the experiment .....	136
6.1.1	Support structure and dummy mass .....	138
6.1.2	Alignment system .....	139
6.1.3	Test Stand Drive System.....	141
6.1.4	Test Stand Positioning measurement system .....	142
6.1.5	Test Stand Friction Simulator .....	142
6.2	Assembly, integration and verification (AIV) .....	143
6.3	Test campaign .....	149
6.3.1	Parameter Identification of the Friction Model.....	150
6.3.2	Parameters Identification of the Mechanical system .....	152
6.3.3	Relative Angular Positioning Accuracy.....	154
6.4	Experimental results vs End-to-End Simulation .....	157
<b>7</b>	<b>Summary and Conclusions.....</b>	<b>161</b>
	<b>Appendix A .....</b>	<b>165</b>
	<b>Drive Unit Calculations .....</b>	<b>165</b>
A.1	Motor Torque Estimation.....	165

## Contents

---

A.2 Harmonic Drive Gear Selection .....	167
<b>Appendix B.....</b>	<b>169</b>
<b>Friction Simulator Calculations.....</b>	<b>169</b>
<b>Appendix C .....</b>	<b>171</b>
<b>Steady State Friction Torque Measurement.....</b>	<b>171</b>
<b>Bibliography .....</b>	<b>175</b>
<b>Curriculum Vitae .....</b>	<b>183</b>

# Abstract

The **M**ulti-Adaptive Optics Imaging **C**AMERA for **D**eep **O**bservations (MICADO), one of the first light instruments for the 39 m Extremely Large Telescope (ELT), is being designed and optimized to work with the **M**ulti-conjugate Adaptive Optics **R**elaY (MAORY). The MICADO-MAORY configuration will provide diffraction limited imaging over a large field of view, which defines the precision requirements of the instrument's derotator. Meeting these requirements with an adequate design is the central task of this thesis. The MICADO consortium started the preliminary design phase on October 7, 2015.

The current concept of the MICADO instrument consists of a cryostat carrying the main optics and the cold detector array. The cryostat is mounted via its central annular flange directly onto the image derotator. The whole assembly is suspended several meters above the ELT's Nasmyth platform by an octopod-type support structure. The instrument electronics cabinets, the cable-wrap and the cooling system are placed on a separated co-rotating platform below the cryostat.

This thesis engages in the design of the MICADO image derotator, a key mechanism that allows rotating the cryostat assembly around its optical axis with an angular positioning accuracy better than 2 arcsec (rms), in order to compensating for the optical field rotation due to the alt-azimuth mount of the ELT. This device consists of a high precision bearing, gears, motors, encoders and stiff mechanical interfaces towards the cryostat and the instrument support structure. A trade-off analysis considering different bearing technologies was performed to select the most suitable one for this application. As a result, the MICADO derotator is being developed using a custom-made four-point contact ball bearing. Special attention is given to estimate and simulate the performance of the derotator during the design phase and both static and dynamic behaviors are being considered in parallel. The static flexure analysis is performed using a detailed finite element model while the dynamic simulation is performed with the mathematical model of the MICADO instrument mechanical system. Finally, both aspects are combined through a realistic end-to-end model of the instrument, verifying that the concept matches the requirements.

The design and construction of a representative prototype, the so-called derotator test stand, has been included into the frame work of the thesis. The main goal of the experiment is to obtain performance data in the early stage of the project and to

minimize the risk of design flaws in the current concept of the derotator. The test stand will also contribute to the parameter identification of the end-to-end simulation and optimization of the control architecture.

The main challenges to be handled in this thesis are: (i) the design of the mechanical interfaces to minimize mass and deformation of the bearing, (ii) the development of a reliable bearing FEM, (iii) the analysis of the friction in the bearing at low tracking velocities and, (iv) the set up and verification of the derotator end-to-end model.

# Zusammenfassung

Die **Multi-Adaptive Optics Imaging CAmera für Deep Observations (MICADO)**, eines der „First Light“ Instrumente für das 39m European Extremely Large Telescope (ELT), wird derzeit entwickelt und optimiert, um mit dem **Multi-conjugate Adaptive Optics RelaY (MAORY)** zu arbeiten. Die MICADO-MAORY-Konfiguration bietet eine beugungsbegrenzte Bildgebung über ein großes Gesichtsfeld, was die Genauigkeitsanforderungen des MICADO-Derotators definiert. Diesen Anforderungen gerecht zu werden, ist die zentrale Aufgabe der vorliegenden Arbeit. Das MICADO-Konsortium begann mit der Vorentwurfsphase am 7. Oktober 2015.

Das derzeitige Konzept des MICADO-Instruments besteht aus einem Kryostaten, der die Hauptoptik und das kalte Detektor-Array trägt. Der Kryostat wird über seinen zentralen Ringflansch direkt auf den MICADO-Derotator montiert. Die gesamte Baugruppe ist mehrere Meter über der ELT Nasmyth-Plattform mittels einer Stützstruktur vom Oktopod-Typ aufgehängt. Die Elektronik-Schränke, die Kabelkette und das Kühlsystem sind auf einer separaten, sich drehenden Plattform unter dem Kryostaten angeordnet.

Diese Arbeit beschäftigt sich mit dem konstruktiven Entwurf des MICADO-Derotators, einem Schlüsselmechanismus, der es erlauben soll, die Kryostatanordnung um ihre optische Achse mit einer Winkelpositionierungsgenauigkeit von weniger als 2 Bogensekunden (rms) zu drehen, um die optische Feldrotation zu kompensieren, welche durch die Alt-Azimet-Aufhängung des ELT bedingt ist. Dieses Gerät besteht aus einem hochpräzisen Lager, Getrieben, Motoren, Encodern und steifen mechanischen Schnittstellen zum Kryostaten und der Instrumententrägerstruktur. Eine Abwägungsanalyse unter Berücksichtigung verschiedener Lagertechnologien wurde durchgeführt, um die für diese Anwendung am besten geeignete auszuwählen. Infolgedessen wird der MICADO-Derotator mit einem maßgeschneiderten Vierpunkt-Kugellager entwickelt. Besonderes Augenmerk wird darauf gelegt, die Leistungsfähigkeit des Derotators während der Entwurfsphase abzuschätzen und zu simulieren, um sowohl das statische als auch das dynamische Verhalten parallel zu betrachten. Die statische Deformationsanalyse wird unter Verwendung eines detaillierten Finite-Elemente-Modells durchgeführt, während die Dynamiksimulation

mit dem mathematischen Modell eines Mehrkörpersystem des MICADO-Instruments durchgeführt wird. Schließlich werden beide Aspekte durch ein realistisches End-to-End-Modell des Instruments kombiniert, um sicherzustellen, dass das Konzept den Anforderungen entspricht.

Der Entwurf und der Bau eines repräsentativen Prototyps, des sogenannten Derotator-Teststandes, wurde in diese Arbeit ebenfalls aufgenommen. Das Hauptziel des Experiments besteht darin, Leistungsdaten in der frühen Phase des Projekts zu erhalten und das Risiko von Konstruktionsfehlern im gegenwärtigen Konzept des Derotators zu minimieren. Der Prüfstand konnte massgeblich zur Parameteridentifikation der End-to-End-Simulation und zur Optimierung der Regler-Architektur beitragen.

Die wichtigsten Herausforderungen, die in dieser Arbeit behandelt wurden, sind: (i) der Entwurf der mechanischen Schnittstellen, um Masse und Deformation im Lager zu minimieren, (ii) die Entwicklung eines zuverlässigen Lager FEM, (iii) die Analyse der Reibung im Lager bei niedrigen Nachführungsgeschwindigkeiten und (iv) die Generierung und Überprüfung des MICADO-Derotators End-to-End Modells.



# List of figures

Figure 1: Cerro Armazones, ELT location in the Atacama Desert, Chile (Image source: downloaded from <a href="http://www.eso.org">www.eso.org</a> on December 2016).....	4
Figure 2: ELT five mirrors optical design (Image source: downloaded from <a href="http://www.eso.org">www.eso.org</a> on December 2016).....	5
Figure 3: 42m ELT conceptual design in 2007 (Image source: downloaded from <a href="http://www.eso.org">www.eso.org</a> on December 2016).....	7
Figure 4: ELT azimuth structure (top left), altitude structure (bottom left) and complete main structure with pre-focal stations (right) (Image source: downloaded from <a href="http://www.eso.org">www.eso.org</a> December 2016). ....	8
Figure 5: ELT rendering and the location of the MICADO instrument on top of the Nasmyth platform A (left side) for both SCAO and MCAO configurations (Image source: downloaded from <a href="http://www.eso.org">www.eso.org</a> on December 2016). ....	10
Figure 6: MICADO Cryostat CAD model (Image source: MICADO consortium). .	13
Figure 7: The MCAO configuration MICADO-MAORY (Image source: MICADO consortium). ....	15
Figure 8: The SCAO configuration MICADO “stand alone” (Image source: MICADO consortium). ....	16
Figure 9: Equatorial coordinate system (left) and equatorial mounts (right) (image source downloaded from <a href="https://quantumredpill.wordpress.com">https://quantumredpill.wordpress.com</a> and <a href="http://bibliotecadigital.ilce.edu.mx">http://bibliotecadigital.ilce.edu.mx</a> on July 2017). ....	22

## List of figures

---

- Figure 10: Horizontal coordinate system (left) and alt-azimuth mount (right) (Image source: downloaded from <https://en.wikipedia.org>, <https://www.uwgb.edu> on July 2017). ..... 23
- Figure 11: Celestial sphere centered on the observer with the correlation between horizontal and equatorial coordinate systems. Where  $p$  is the North Pole,  $Z$  is the zenith,  $R$  is the location of the star,  $\varphi$  is the latitude of the observer,  $\Upsilon$  is the Vernal Equinox,  $\delta$  is the declination,  $\alpha$  is the right ascension,  $a$  is the altitude,  $A$  is the Azimuth, the tilted plane is the Celestial Equator and the horizon at the observer position is defined by the orange plane. The so called astronomical triangle is formed between the vertexes PZR (Image source: downloaded from <https://commons.wikimedia.org> on July 2017). ..... 24
- Figure 12: Location of the Cassegrain Focus on a Cassegrain reflecting telescope consisting of a parabolic primary mirror and a hyperbolic secondary mirror (Image source: downloaded from [https://en.wikipedia.org/wiki/Cassegrain\\_reflector](https://en.wikipedia.org/wiki/Cassegrain_reflector) on October 2017). ..... 25
- Figure 13: Location of the Nasmyth Focus on a Cassegrain reflecting telescope consisting of a parabolic primary mirror and a hyperbolic secondary mirror (Image source: downloaded from <https://en.wikipedia.org> on October 2017). . 27
- Figure 14: Field rotation trajectory, velocity and acceleration at ELT Nasmyth platform A (Cerro Armazones latitude  $\varphi = -24.6^\circ$ , Zenith limit =  $1.5^\circ$ ). ..... 29
- Figure 15: ELT global coordinate system showing the Nasmyth platform designations, the same coordinate system is used in the VLT (Image source: ELT Standard Coordinate Systems and Basic Conventions, document number: ESO-193058). ..... 30
- Figure 16: Pupil rotation at the ELT Nasmyth platform A. .... 31
- Figure 17: Effect of the telescope pointing error (middle plot) and the time delay (bottom plot) over some ideal field rotation trajectories (top plot) at the ELT Nasmyth platform A. .... 34
- Figure 18: Abbe type prisms (top) and LINC-NIRVANA K-mirror (bottom) (Image source: [https://en.wikipedia.org/wiki/Abbe%E2%80%93Koenig\\_prism#/media/File:Ab](https://en.wikipedia.org/wiki/Abbe%E2%80%93Koenig_prism#/media/File:Ab)

be-K%C3%B6nig_prism.svg on January 2018 and LINC-NIRVANA consortium). .....	36
Figure 19: LINC-NIRVANA science detector unit (Image source: LINC-NIRVANA consortium) .....	37
Figure 20: MICADO field of view showing the required image position stability at the corner of the focal plane.....	39
Figure 21: Slewing ball bearing (Image source: SKF slewing bearing catalog 2015). .....	41
Figure 22: Hydrostatic oil bearing. ....	42
Figure 23: Hydrostatic air bearing (Image source: Newway air bearing catalog 2011). .....	43
Figure 24: Magnetic bearings (Image source: downloaded from <a href="http://www.synchrony.com">http://www.synchrony.com</a> on December 2016). .....	43
Figure 25: LINC-NIRVANA Ground-Layer Wavefront Sensor derotator CAD model with the main components of the mechanism (Image source: LINC-NIRVANA consortium). .....	46
Figure 26: GRAAL CAD model showing the main components (Image source: downloaded from <a href="http://www.eso.org">www.eso.org</a> on December 2017). .....	47
Figure 27: US (right) and EU (left) ALMA antennas (Image source: downloaded from <a href="http://www.eso.org">www.eso.org</a> on December 2017). .....	48
Figure 28: LBT bent Gregorian rotators (Image source: downloaded from <a href="http://www.lbto.org">www.lbto.org</a> on December 2017). .....	49
Figure 29: DKIST Coudé laboratory derotator CAD model (top, image source: downloaded from <a href="http://dkist.nso.edu/node/903">http://dkist.nso.edu/node/903</a> on December 2017) and Linear motion curved guides (bottom, Image source: downloaded from <a href="http://www.indunorm.eu/produkte/thk-linearfuehrungen/linearfuehrungen-ohne-kugellkette/bogenfuehrung-hcr.html">http://www.indunorm.eu/produkte/thk-linearfuehrungen/linearfuehrungen-ohne-kugellkette/bogenfuehrung-hcr.html</a> on December 2017). .....	50
Figure 30: TMT IRIS CAD model (downloaded from <a href="http://oirlab.ucsd.edu/img/IRIS.png">http://oirlab.ucsd.edu/img/IRIS.png</a> on January 2018). .....	51
Figure 31: Typical Slewing bearings used in antenna applications. Single-row four-point contact ball bearing (left), crossed roller bearing (middle) and three-row	

## List of figures

---

roller bearing (right) (Image source: taken from ThyssenKrupp Rothe Erde slewing bearing catalog 2016).....	54
Figure 32: Custom designed single-row four-point contact ball bearing for the MICADO derotator (band encoder image source: Heidenhain catalog, 2014)..	56
Figure 33: Optimal bearing support structure geometry (left) and non-optimal option transferring the warping moment to the bearing (right). The vertical arrow represents the transmission of the axial load acting on the bearing, while the curved arrow illustrates the effect of the warping moment due to the translation of the axial load. A three-row roller bearing is used as example in this case (Image source: ThyssenKrupp Rothe Erde slewing bearing catalog 2016). .....	58
Figure 34: 3-point mechanical interface introduced after the beginning of phase B.	59
Figure 35: Original 6-point mechanical interface with the instrument support structure.....	60
Figure 36: Options developed for the conceptual design of the bearing support structure.....	62
Figure 37: FEA showing the total deformation of the options developed for the conceptual design of the bearing support structure.....	63
Figure 38: Boundary conditions applied to the model for the FEA. ....	64
Figure 39: Location of the maximal and minimal deformation considered for $I_A$ . ....	65
Figure 40: Performance of the proposed concepts according to $I_A$ .....	66
Figure 41: Location of the maximal X axis and maximal Y axis deformations considered for the optimization fiction $I_R$ . ....	67
Figure 42: Performance of the proposed concepts according to $I_R$ .....	68
Figure 43: CAD model of the MICADO derotator preliminary design. ....	69
Figure 44: Derotator mechanical interfaces. ....	70
Figure 45: Manufacturing proposal to build the bearing support structure (The upper plate is not shown in the figure). ....	72
Figure 46: Manufacturing concept using a self-assembly system and metallic inserts for the bolts (Image source: CarbonVision). ....	72
Figure 47: Boundary conditions applied to the bearing support structure FEM.....	73

---

Figure 48: Axial deformation (Y axis) of the bearing support structure using an equivalent quasi-isotropic material. ....	75
Figure 49: Radial deformation (X axis) of the bearing support structure using an equivalent quasi-isotropic material. ....	76
Figure 50: Mechanical interfaces towards materials with different CTE. ....	77
Figure 51: Optimization parameters. ....	79
Figure 52: Performance of the proposed thermal ring concepts according to $I_A$ . ....	79
Figure 53: Effect of the thermal compensation ring in the interface towards the cryostat. ....	80
Figure 54: CAD model of one derotator drive unit, at least two identical ones will be used. ....	81
Figure 55: Ideal drive unit arrangement for the backlash suppression mechanism. ..	82
Figure 56: CAD model of the scanning head mount (left) and scanning head/band encoder real hardware example (right) (band encoder image source: Heidenhain catalog, 2014). The scanning head mount provides translation in the Y and Z axes, and rotations in the X, Y, Z axes. ....	83
Figure 57: Proposal of the control system considered for the MICADO derotator preliminary design.....	85
Figure 58: Test bearing cross section.....	88
Figure 59: Boundary conditions and mesh used in the rings of the bearing. ....	89
Figure 60: Mesh implemented in the FEM using solid elements. ....	89
Figure 61: Bearing total deformation (left) and Von-Mises stress (right) using solid elements. ....	90
Figure 62: Bearing FEM using spring elements. ....	92
Figure 63: Bearing total deformation and Von-Mises stress using spring elements. ....	92
Figure 64: Bearing total deformation (left) and Von-Mises stress (right) using spring elements without face sizing on the raceways. ....	93
Figure 65: Bearing FEM using beam elements.....	94

## List of figures

---

Figure 66: Bearing total deformation (left) and Von-Mises stress (right) using beam elements.....	94
Figure 67: Bearing total deformation (left) and Von-Mises stress (right) using beam elements without face sizing on the raceways. ....	95
Figure 68: model of the bearing test setup cross section at ThyssenKrupp Rothe Erde. ....	97
Figure 69: Test setup for the axial load case at the ThyssenKrupp Rothe Erde factory. ....	97
Figure 70: FEM of the bearing test setup. ....	98
Figure 71: Bearing test setup total deformation for the axial force load case.....	98
Figure 72: Bearing test setup total deformation for the radial force load case. ....	99
Figure 73: Bearing test setup total deformation for tilting moment load case. ....	99
Figure 74: Boundary conditions used for the FEA of the MICADO derotator.....	101
Figure 75: Location of the control nodes used to estimate the deformations on the bearing. The image shows the derotator cross section where one of the drive units is located.....	103
Figure 76: FEM of the MICADO derotator. ....	103
Figure 77: Derotator total deformation. ....	104
Figure 78: Derotator Y axis (axial) deformation.....	104
Figure 79: Derotator X axis (radial) deformation. ....	105
Figure 80: Derotator Z axis (radial) deformation.....	105
Figure 81: Bearing total deformation. ....	106
Figure 82: Bearing Y axis (axial) deformation. ....	107
Figure 83: Bearing X axis (radial) deformation. ....	107
Figure 84: Bearing Z axis (radial) deformation. ....	108
Figure 85: First eigenfrequency mode (26.7 Hz) of the MICADO instrument with a 4-point interface for the derotator. ....	110

---

Figure 86: First eigenfrequency mode (22.5 Hz) of the MICADO instrument with a 8-point interface for the derotator. ....	110
Figure 87: Effect of the resulting warping moment over the cross section of a circular ring. (Image source: Hake & Meskouris, 2007).....	112
Figure 88: Location of the derotator cross section where the warping moment is calculated (the auxiliary octopod structure for the relay optics table is not show in this figure). ....	113
Figure 89: Location of the forces generating the warping moment according to the current position of the mechanical interfaces towards the upper and lower octopod structures. ....	114
Figure 90: Location of the forces generating the warping moment according to the proposal to relocate of the mechanical interfaces towards the upper and lower octopod structures. ....	114
Figure 91: MICADO instrument mechanical model.....	125
Figure 92: Equivalent MICADO instrument mechanical model where the Harmonic Drive gear is modeled as a pinion and gear wheel pair.....	127
Figure 93: Reduced equivalent MICADO instrument mechanical model. ....	128
Figure 94: Reduced Bristle interpretation of the friction according to the LuGre model (Image source: (Olsson, 1996)). The spring and the damper have been included into the figure for a better understanding of the model, but they do not belong to the original figure. ....	131
Figure 95: End-to-end model of the DKIST. Image source: (Dreyer, et al., 2014). ....	132
Figure 96: Current end-to-end model of the MICADO derotator.....	133
Figure 97: Simulink implementation of the MICADO derotator mechanical system. The input of the signal is represented in the case with an step signal block....	133
Figure 98: Simulink implementation of the LuGre friction model.....	134
Figure 99: Derotator test stand CAD model. ....	137
Figure 100: Derotator test stand CAD model cross section. ....	138
Figure 101: Support structure and dummy mass for the derotator prototype. ....	139

## List of figures

---

Figure 102: Alignment system between the cryostat dummy mass and the bearing of the derotator test stand. A similar alignment concept is proposed for the derotator of the MICADO instrument. ....	140
Figure 103: Proposal for the alignment mechanism with an radial indicator. ....	141
Figure 104: Test stand Drive unit cross section. ....	141
Figure 105: Test stand positioning measurement system.....	142
Figure 106: Test stand friction simulator. ....	143
Figure 107: Support with the bearing installed on top of it. ....	144
Figure 108: Fluid epoxy resin applied on top of the bearing outer ring as part of the liquid shimming process. Tape and plastic sheets are placed to protect other areas of the bearing.....	144
Figure 109: Bearing interface plate installed on top of the derotator. The alignment pins are shown in the lower corners. ....	145
Figure 110: Drive unit installed on top of the bearing interface plate. ....	145
Figure 111: Encoder ring installed on top of the bearing interface flange.....	146
Figure 112: Measurement of the encoder ring radial runout after the application of the alignment process described in section 6.1.2. ....	146
Figure 113: Band encoder and scanning head installed in the derotator test stand..	147
Figure 114: Verification of the scanning head's signal quality. The small reference marks represent the maximum values for a full rotation of 360°. According to Heidenhain, having signal quality within the yellow range is considered good. The green area corresponds to perfect signal quality. ....	147
Figure 115: Derotator test stand completely integrated in the MPIA assembly hall, electronic cabinet (bottom left corner) and friction simulator (bottom right corner). ....	148
Figure 116: Standard Drive unit (left) and drive unit with the torque sensor on top. ....	149
Figure 117: Identified Stribeck curve with the values referred to the bearing. ....	151
Figure 118: Frequency response of the derotator test stand.....	153



---

Figure 119: Sine velocity profile used for the relative angular positioning accuracy test. ....	154
Figure 120: Position trajectory used for the relative angular positioning accuracy test. ....	155
Figure 121: Position error of the test stand while following the test trajectory. ....	155
Figure 122: Position error of the test stand (bottom) with simulated friction torque changes(top). ....	156
Figure 123: Simulated vs measured friction torque for a motor velocity of 0.05 rpm. ....	157
Figure 124: Simulated vs measured friction torque for a motor velocity of 0.1 rpm. ....	158
Figure 125: Simulated Harmonic Drive gearing arrangement (Image source: Harmonic Drive AG, 2014). ....	167
Figure 126: Schematic representation of the band brake (Source: MathWorks online documentation ). ....	169
Figure 127: Steady state friction torque measurement for a motor velocity of 0.2 rpm. ....	171
Figure 128: Steady state friction torque measurement for a motor velocity of 0.3 rpm. ....	172
Figure 129: Steady state friction torque measurement for a motor velocity of 0.4 rpm. ....	172
Figure 130: Steady state friction torque measurement for a motor velocity of 0.5 rpm. ....	173
Figure 131: Steady state friction torque measurement for a motor velocity of 0.6 rpm. ....	173
Figure 132: Steady state friction torque measurement for a motor velocity of 0.7 rpm. ....	174
Figure 133: Steady state friction torque measurement for a motor velocity of 0.9 rpm. ....	174

## List of figures

---

# List of tables

Table 1: ELT instruments and adaptive optics modules (marked in blue) as proposed during the initial phase A conceptual study (Source: taken from <a href="http://www.eso.org">www.eso.org</a> on December 2016). The bold letters show the first light hardware approved for construction within the phase 1 of the ELT program.....	9
Table 2: Derotator performance and physical requirements.....	38
Table 3: Bearing technology trade-off summary.....	44
Table 4: Main dimensions and parameters of the custom designed single-row four-point contact ball bearing for the MICADO derotator.....	57
Table 5: Maximum allowed deformation of the bearing.....	58
Table 6: Numerical results of the optimization function $I_A$ .....	66
Table 7: Numerical results of the optimization function $I_R$ .....	67
Table 8: Results of the bearing support structure FEA using the detailed FEM considering the lamination sequence and the strength of different types of fibers. The deformation in the X and Z axes are very similar. Therefore, only the values for X and Y axis are shown.....	74
Table 9: Results of the bearing support structure FEA using an equivalent quasi-isotropic material where the lamination sequence and the strength of different types of fibers is not considered. The deformation in the X and Z axes are very similar. Therefore, only the values for X and Y axis are shown.....	75
Table 10: Properties of the equivalent quasi-isotropic material used in the FEM of the bearing support structure. The typical values for steel are given as reference.....	77

## List of tables

---

Table 11: Differential thermal deformation at the interface with the cryostat.....	78
Table 12: Differential thermal deformation at the interface with the bearing support structure.....	78
Table 13: Thermal ring concepts.....	79
Table 14: Derotator mass budget .....	86
Table 15: Bearing dimensions.....	88
Table 16: Comparison between the different FEMs. ....	95
Table 17: Validation of the bearing FEM, measured vs FEA deformations.....	99
Table 18: Deformations affecting the bearing according to the results of the FEA.	108
Table 19: Bearing Y axis deformations registered at the control nodes. ....	108
Table 20: Results of the modal analysis for the first six eigenfrequency modes. ....	111
Table 21: Results of the warping moment optimization. ....	115
Table 22: Difference between the standard test bearing and the high precision nominal bearing.....	136
Table 23: Identified parameters of the Stribeck curve. ....	151
Table 24: Parameters of the test stand mechanical model used for the end-to-end simulation. For the implementation of the end-to-end simulation at this first stage, linear friction is assumed ( $dGC \approx Fv$ ). ....	152
Table 25: Output data assumed for the selection of the Harmonic Drive gear. ....	167

# List of abbreviations

<b>CFRP</b>	Carbon Fiber Reinforced Plastic
<b>CTE</b>	Coefficient of Thermal Expansion
<b>DM</b>	Deformable Mirror
<b>ELT</b>	European Extremely Large Telescope
<b>ELTs</b>	Extremely Large Telescopes
<b>FEA</b>	Finite Element Analysis
<b>FEM</b>	Finite Element Model
<b>GMT</b>	Giant Magellan Telescope
<b>GTC</b>	Gran Telescopio Canarias
<b>GWS</b>	Gourd-layer Wavefront Sensor
<b>HARMONI</b>	High Angular Resolution Monolithic Optical and Near-infrared Integral field spectrograph
<b>LBT</b>	Large Binocular Telescope
<b>LGS</b>	Laser Guide Star
<b>MAORY</b>	Multi-Conjugate Adaptive Optics RelaY
<b>MCAO</b>	Multi-Conjugate Adaptive Optics
<b>METIS</b>	Mid-infrared ELT Imager and Spectrograph
<b>MICADO</b>	Multi-AO Imaging CAmera for Deep Observations
<b>NGS WFS</b>	Natural Guide Star Wavefront Sensor
<b>PFS</b>	Pre-Focal Station
<b>PSF</b>	Point Spread Function
<b>PtV</b>	Peak-to-Valley
<b>RE</b>	ThyssenKrupp Rothe Erde
<b>RMS</b>	Root Mean Square
<b>SCAO</b>	Single-Conjugate Adaptive Optics
<b>TMT</b>	Thirty Meter Telescope
<b>VLT</b>	Very Large Telescope
<b>WFS</b>	Wavefront Sensor
<b>WFS</b>	Wavefront Sensor

## List of abbreviations

---

# List of symbols

$\Delta$	Declination
$A$	Right ascension
$H$	Hour angel
$\omega_0$	Sidereal time
$A$	Altitude
$A$	Azimuth
$P$	Parallactic angle
$\Phi$	Observer latitude
$F_{Ca}$	Field rotation at Cassegrain focus
$F_N$	Field rotation at Nasmyth focus
$P_N$	Pupil rotation at Nasmyth focus
$M_r$	Bearing starting friction torque
$\mu$	Viscous friction coefficient
$M_K$	Tilting moment on the bearing
$F_A$	Axial force on the bearing
$F_r$	Radial force on the bearing
$D_L$	Bearing raceway diameter
$E$	Modulus of elasticity
$\nu$	Poisson's ratio
$\rho$	Density
$\delta_K$	Deformation of a ball at its contact areas with the raceways
$C_{KN}$	Stiffness constant at the contact areas of the ball with the raceways
$C_{KL}$	Linear stiffness constant at the contact areas of the ball with the raceways
$F_K$	Ball force
$d_K$	Ball diameter
$C_s$	Equivalent spring stiffness
$N_K$	Number of balls

## List of symbols

---

$N_T$	Number of spring pairs for the FEM
$K$	Stiffness matrix
$q$	Displacement vector
$\tilde{F}$	Load vector
$M$	Mass matrix
$D$	Damping matrix / dimensionless damping ratio
$\omega_0$	Undamped natural frequency
$\omega$	Damped natural frequency



# 1 Introduction

In order to tackle new scientific challenges and questions related to Exoplanets, Fundamental Physics, Black Holes, Stars, Galaxies and the Dark Ages (ESO, 2011), astronomers around the world are pushing the limits of technology even further. Those questions cannot be handled with the current generation of large telescopes, like the Very Large Telescope (comprising four telescopes with a monolithic 8.2 m primary mirror), the Large Binocular Telescope (carrying two monolithic 8.4 m primaries on the same mount) and the Gran Telescopio Canarias (using a segmented 10.4 m primary mirror). As a result, projects like the Giant Magellan Telescope (GMT) employing a 25 m primary mirror by means of circular segments (Johnsa et al., 2014), the Thirty Meter Telescope (TMT) with a 30 m segmented primary mirror (Nelson & Sanders, 2008) and the 39 m ELT (Tamai, Cirasuolo, González, Koehler, & Tuti, 2016); are being developed and should see first light within the next 10 years.

Having larger telescopes with better sensitivity and resolution has been the dream of scientists since the beginning of the astronomy as a science. The evolution in the size of the optical telescopes since its invention in the 17<sup>th</sup> century by Hans Lippershey<sup>1</sup> is the best proof of it (Racine, 2004). Even more than financial limitations, technological and technical constrains have slowed down the increase in the dimensions of optical telescopes in the last decades. This was due to the inability to cast monolithic mirrors with diameters larger than 8 m, until the technology to build and control segmented ones was available. This technology was first successfully

---

<sup>1</sup> Galileo's refractor telescope had a diameter of 1.5 cm.

## 1.1 The European Extremely Large Telescope

---

implemented in the Keck telescopes, each of which has a 10 m primary mirror (Nelson, Mast, & Faber, 1985).

Despite the progress with the segmented mirrors, the line of an 11-m-diameter primary mirror has not been crossed until now. The optical design on the ELT considers the implementation of ~800 segments to form its primary mirror.

Nowadays a similar phenomenon is occurring with the next generation of extremely large telescopes (ELTs), as the required technology to manufacture and control big deformable mirrors<sup>2</sup> to be used in the adaptive optics systems of those telescopes is just under development. A clear example is the deformable mirror of the ELT (Crepuy, et al., 2010; Vernet, et al., 2013).

Nevertheless, having an extremely large telescope is not enough to perform new cutting edge science. The next generation state-of-the-art astronomical instruments are required in parallel. The ELT will become “the world’s biggest eye on the sky”, and MICADO has been selected as one of its first light instruments together with METIS and HARMONI (Zeeuw, Tamai, & Liske, 2014). The development of such large telescopes, as well as its new suite of instruments is creating unprecedented challenges for the engineers around the world who are working with the astronomers to design, build and test those unique pieces of equipment. As the size of the telescopes increases, the requirements to realize the new astronomical instruments become even more demanding, since the increasingly large optomechanical components require higher levels of precision and accuracy. This thesis focuses on one of the many challenges in the design of the MICADO instrument, i.e. the derotator required to compensate for the field rotation of the ELT.

## 1.1 The European Extremely Large Telescope

The international effort to build an extremely large telescope dates back to 1999, when different ideas and possible concepts were collected in the Bäckaskog

---

<sup>2</sup> Deformable mirrors require a large quantity of high precision actuators, the proposed design for the ELT M4 has more than 5200 actuators and 6 segments.

Workshop on Extremely Large Telescopes. Ambitious projects like the 50 m Swedish extremely large telescope (Andersen, et al., 1999), the 35 m extremely large telescope (Sebring, Moretto, Bash, Ray, & Ramsey, 1999), the 50 m extremely large multiple mirror telescope (Beckers, 1999) and the 100 m Overwhelmingly Large Telescope (OWL) (Dierickx & Gilmozzi, 1999)<sup>3</sup> were presented in that conference. Being the European approach, the concept for the OWL Telescope quickly evolved and the progress of the project was published a year later (Dierickx & Gilmozzi, 2000). As financial and technological constraints became more clear, the diameter of OWL was reduced to the half by 2003, with the introduction of The Euro50 Extremely Large Telescope (Andersen, et al., 2003). Later the so called Euro50 telescope was renamed ELT (Ardeberg, et al., 2006) with an even smaller, 42 m primary mirror.

Afterwards the European Southern Observatory (ESO) in collaboration with industry, started to develop a more detailed design proposal of that big optical/infrared telescope, with a final design using a primary mirror with a diameter of 39 m (ESO, 2011). Since then, important milestones have been achieved as the project approaches the beginning of the construction of the telescope, at Cerro Armazones, Chile, after ESO started the final discussion with the winner of the tender process in February 2016. This important step was possible after the ESO council gave green light for the construction of the ELT phase 1 on December 2014 (Zeeuw, Tamai, & Liske, 2014). The phase 1 of the ELT construction will deliver a fully working telescope with a bigger central obscuration, an adaptive optics system (MAORY) and the three first light instruments already mentioned. ESO finally signed the “Largest Ever Ground-based Astronomy Contract for ELT Dome and Telescope Structure” at a ceremony in Garching, Germany on 26 May 2016 (ESO, 2016). Preparation works on the mountain are already complete, and the construction of the ELT at Cerro Armazones started in 2017. The ELT first light is planned for the end of 2024. Currently, there is no plan to build an optical telescope bigger than the ELT.

---

<sup>3</sup> The OWL presented by ESO in 1999 would eventually become what we know as ELT.

### 1.1.1 Location

As the number of clear nights per year and weather conditions is a key aspect for the success of such a facility, the location of the ELT is one of the most important aspects of the project. For that reason, considerable effort was dedicated to the analysis and selection of possible places around the world. The largest optical telescope in the world requires not only a site with the best possible conditions for astronomical observation, but also a robust infrastructure and services to operate and maintain it. No-less important are the political and economic stability of the country to host such a research facility, in order to ensure the long-term live of the project.

The decision on the ELT site was based on a large comparative meteorological investigation carried out during several years (Vernin, Muñoz-Tuñón, & Sarazin, 2008). The ELT Site Selection Committee started studying in great detail possible locations in Argentina, Chile, Maroco and Spain; while the final short list of possible places presented by the committee was reduced to four locations in Chile (Armazones, Ventarrones, Tolonchar and Vizcachas) and one in Spain (La Palma). All five possibilities offer excellent conditions for astronomical observation.

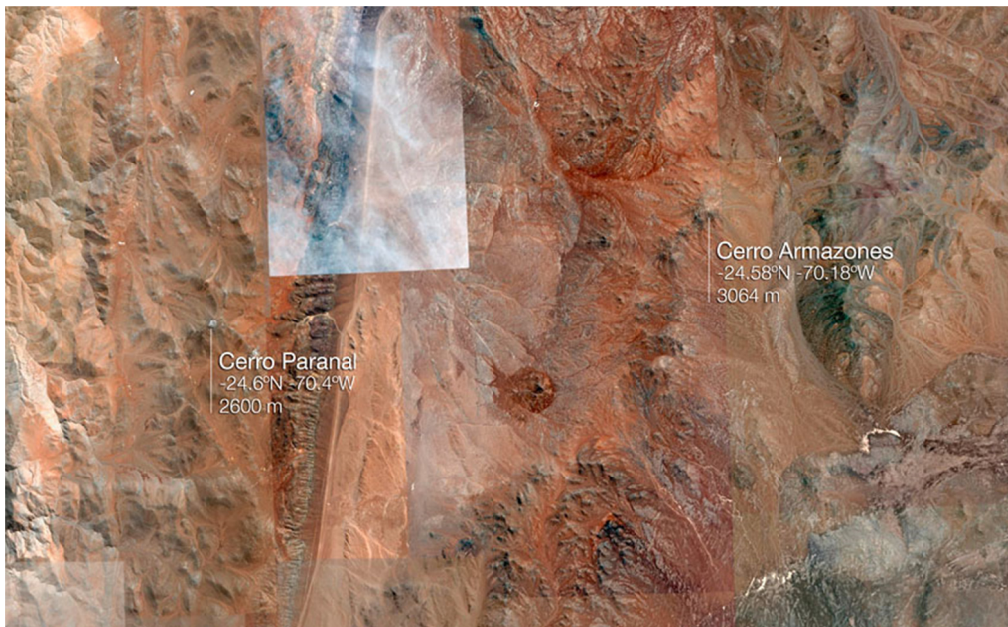


**Figure 1:** Cerro Armazones, ELT location in the Atacama Desert, Chile (Image source: downloaded from [www.eso.org](http://www.eso.org) on December 2016).

On 26 April 2010, the ESO council selected Cerro Armazones as the site for the construction of the ELT (ESO, 2010). This mountain with an altitude of 3060 m is located at the Atacama Desert in Chile, 130 km south of Antofagasta city in northern Chile and just 20 km east from Cerro Paranal, the location of ESO VLT (Figure 1). Its proximity to Paranal Observatory was finally one of the main reasons to select Cerro Armazones for the ELT, as most of the support infrastructure required to operate the telescope is already there. In addition, the strong and long diplomatic relationship between ESO and Chile (due to all ESO facilities already established in that country) is a guarantee of the required political stability to build the ELT. At this location the ELT will count with more than 320 clear nights per year, among many other excellent weather conditions i.e. seeing 0.67 arcsec at 500 nm, rainfall in one year 100 mm, relative humidity of 15%, usual wind speed of 7 m/s and average nighttime air temperature of 9°C.

### 1.1.2 Optical Design

The optical design of the ELT (Figure 2) combines a three-mirror anastigmatic telescope with two flat folding mirrors providing the adaptive optics correction. The second folding mirror is able to send the light towards the Nasmyth focus on two opposite sides of the telescope along the elevation axis. On the so called Nasmyth platforms the instruments are located.

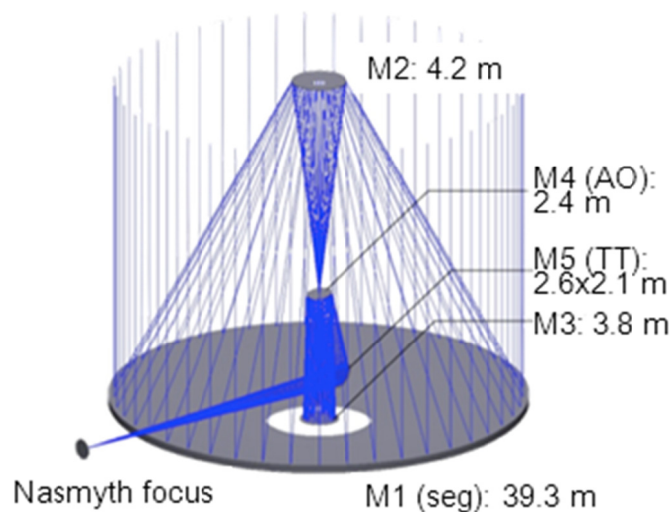


**Figure 2:** ELT five mirrors optical design (Image source: downloaded from [www.eso.org](http://www.eso.org) on December 2016).

## 1.1 The European Extremely Large Telescope

---

The primary mirror (M1) is a segmented 39 m active mirror using 798 hexagonal segments (corner to corner dimension 1.4 m) with a focal ratio of  $f/0.93$  and a central obstruction of 11.1 m. The monolithic 4.2 m secondary mirror (M2) is a thin meniscus which shape can be actively controlled by a set of axial actuators supporting it. The complete M2 cell is supported by a hexapod like structure providing the required degrees of freedom for the alignment capability of the mirror. The whole assembly of approximately 12 tons is suspended on top of the primary by the telescope main structure, directing the light through a hole in the quaternary mirror (M4) to the 3.8-m active tertiary mirror (M3) located at the vertex of M1. At this point the beam is sent to the adaptive optics system, composed of the flat deformable 2.4 m adaptive mirror (M4) providing shape correction with thousands of actuators at very high frequencies and the flat tip-tilt elliptical (2.6 x 2.1 m) fifth mirror (M5) as the field stabilization unit for low frequencies (Cayrel, 2012). As a result of this particular design, the telescope's field of view is limited to 10 arcmin (in diameter) by the hole in M4.

### 1.1.3 Mechanical Design

Since the beginning of the project, the structural design of the ELT has significantly evolved. The conceptual design of the 42 m ELT in 2007 is presented in Figure 3, while the current base line for the 39 m telescope is shown in Figure 4. One of the most important changes that helped to shape the current aspect of the telescope main structure came after the application of an optimization process, performed from the viewpoint of structural mechanics as learned from the principle of bridge building (Kärcher H. J., 2008). At the same time, a novel pyramidal load transmission principle known as the "Rocking-Chair Concept" conceived almost 30 years ago was implemented into the ELT structural design (Kärcher, Kühn, & Nicklas, 1988).

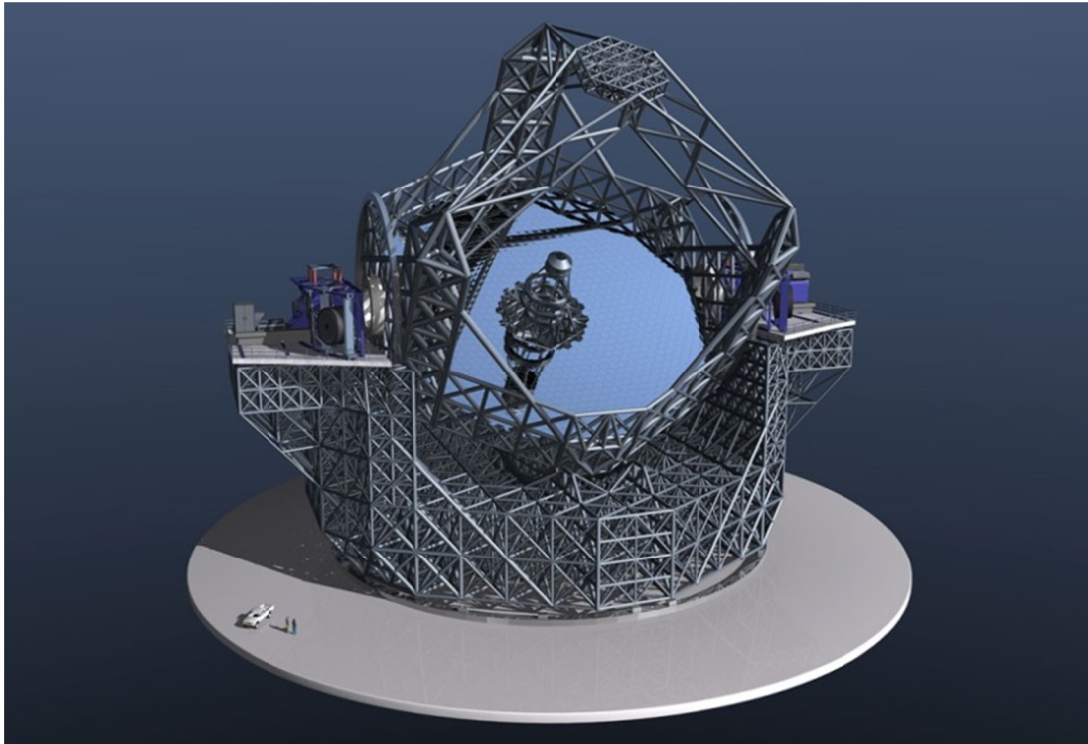


**Figure 3:** 42m ELT conceptual design in 2007 (Image source: downloaded from [www.eso.org](http://www.eso.org) on December 2016).

The ELT main structure (Figure 4) consists of an alt-azimuth mount with about 2800 ton of moving mass, which is separated in two main components: the azimuth structure (Figure 4, top left) including the two Nasmyth platform, providing rotation around the Zenith axis over three azimuth tracks and, the altitude structure (Figure 4, bottom left) plus the central tower carrying the whole telescope optics, allowing rotation around the elevation axis. Axial and radial hydrostatic bearings with direct drive motors are planned to operate the telescope. Two pre-focal stations (PFS) each able to hold up to three scientific instruments each are also part of the azimuth structure. The ELT has been designed to achieve diffraction limited performance with high precision pointing and tracking requirements, 1 arcsec and 0.1 arcsec respectively (ESO, 2011).



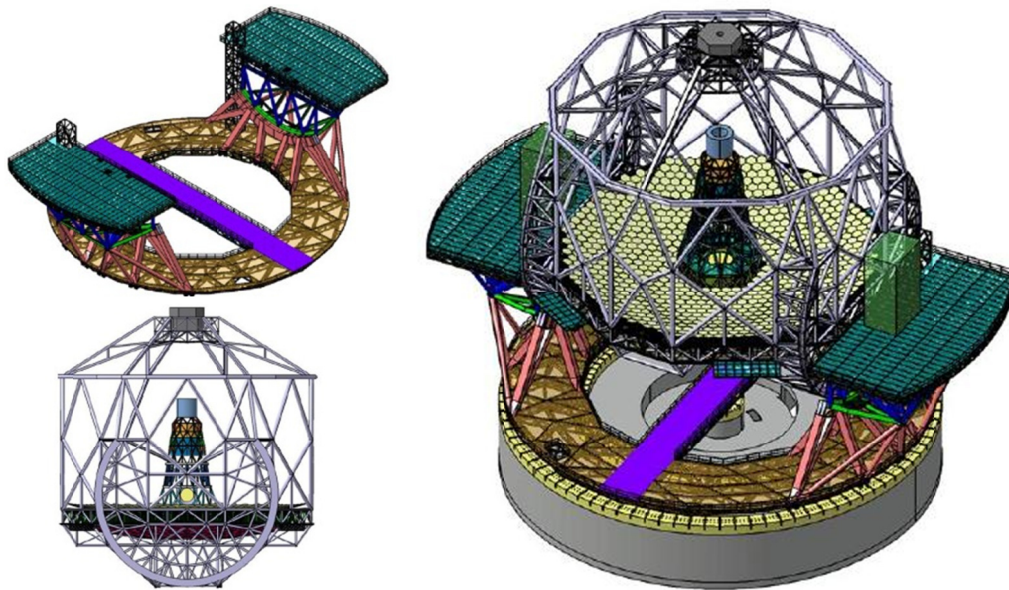


**Figure 4:** ELT azimuth structure (top left), altitude structure (bottom left) and complete main structure with pre-focal stations (right) (Image source: downloaded from [www.eso.org](http://www.eso.org) December 2016).

### 1.1.4 Instruments

Driven by the ELT science cases, a complete suite of instruments covering a wide wavelength range and different observing modes has been developed in parallel with the telescope as part of the ELT program. In total nine instruments and two Multi-Conjugate Adaptive Optics (MCAO) modules were proposed during the initial phase. A conceptual study of the ELT instrumentation program has been carried out between 2007 and 2010. The original list of instrument concepts is presented in Table 1. As described in the last update of the ELT instruments roadmap, the suite has been reduced to seven instruments keeping both MCAO modules, while the Phase A studies for two new instruments (MOSAIC and HIRES) have also started (Ramsay, et al., 2016).

After a difficult selection process based on the scientific impact, scientific flexibility and the scientific return, three instruments (HARMONI, MICADO and METIS) and one MCAO module (MAORY) have now been approved for construction and the memoranda of understanding to build the instruments has been signed between ESO and the respective consortia following the final approval of the ELT project (phase 1) in December 2014.



<b>Name</b>	<b>Instrument Type</b>	<b>Wavelength Range (<math>\mu\text{m}</math>)</b>	<b>Field of View</b>
CODEX	High Resolution, High Stability Visual Spectrograph	0.37 – 0.71	0.82"
EAGLE	AO-assisted Multi-integral Field NIR Spectrometer	0.8 – 2.45	IFU: 1.65" x 1.65"
EPICS	Planet Imager, Spectrograph and Imaging Polarimeter with Extreme Adaptive Optics	0.6 – 1.65	IFU: 0.8" x 0.8"
<b>HARMONI</b>	Single Field Integral-field Spectrograph	0.47 – 2.45	10" x 5" coarsest pixel scale
<b>METIS</b>	Mid-infrared Imager and Spectrograph with AO	2.9 – 14	17.6" x 17.6" (imager)
<b>MICADO</b>	Imager and Slit Spectrograph	0.8 – 2.5	up to 53"
OPTIMOS-DIORAMAS	Wide-Field Imager & Low-Medium Resolution Slit Spectrograph	0.37 – 1.6	6.78' x 6.78'
OPTIMOS-EVE	Optical-NIR Fibre-based MOS	0.37 – 1.7	Large field IFU: 7.8" x 13.5"
SIMPLE	Cross-dispersed Echelle Spectrograph, Long-slit Option	0.8 – 2.5	up to ~4" patrol field for slit viewer
ATLAS	Laser Tomography AO Module	0.35 – 13.5	60"
<b>MAORY</b>	Multi Conjugate AO Module	0.8 – 2.4	2'

**Table 1:** ELT instruments and adaptive optics modules (marked in blue) as proposed during the initial phase A conceptual study (Source: taken from [www.eso.org](http://www.eso.org) on December 2016). The bold letters show the first light hardware approved for construction within the phase 1 of the ELT program.

## 1.2 The MICADO Instrument

MICADO is the Multi-AO Imaging Camera for Deep Observations that will provide the ELT with a diffraction limited imaging capability at near-infrared wavelengths (0.8–2.4  $\mu\text{m}$ ) for the first light of the telescope (currently expected in 2024). The final use of the MICADO instrument is a configuration with the MCAO module MAORY in order to provide imaging over a large 50 arcsec field of view. Therefore, the instrument is being designed and optimized to work with MAORY using laser guide stars, while the MICADO cryostat is installed under the MAORY optical bench. MICADO and MAORY are two different systems and are mainly being designed separately. Nevertheless, at the end they will have to operate as one single instrument composed of the camera and the adaptive optics system. In order to reduce the risk at the first light, a phased approach has been agreed by ESO, MICADO and MAORY consortiums. Therefore, the MICADO-SCAO (Single-Conjugate Adaptive Optics) configuration delivering a smaller field of view, is being designed in parallel. As shown in Figure 5, the instrument will be located on top of the left Nasmyth platform, using the straight focus port of the PFS for the SCAO arrangement and, slightly shifted to the side due to the MAORY optical bench for the MCAO configuration (Davies, et al., 2016).

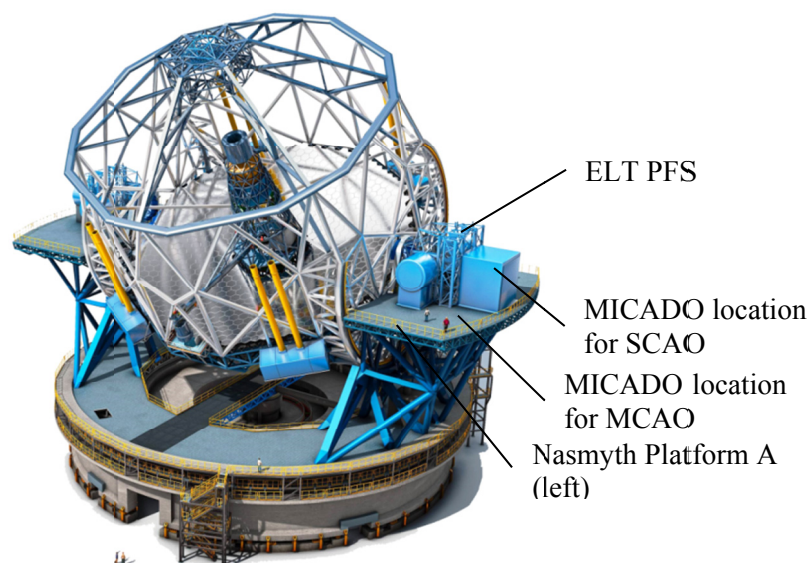


**Figure 5:** ELT rendering and the location of the MICADO instrument on top of the Nasmyth platform A (left side) for both SCAO and MCAO configurations (Image source: downloaded from [www.eso.org](http://www.eso.org) on December 2016).

The M6 mirror used to send the light to the lateral ports of the PFS is not required to operate MICADO. However, in order to keep the instrument in a gravity invariant arrangement a dedicated additional mirror (M7 or M11 for SCAO and MCAO respectively) is implemented in the optical design to send the light vertically down into the cryostat. MCAO corrects the atmospheric turbulence in three dimensions with more than one deformable mirror, while SCAO uses only one deformable mirror.

The design of MICADO has evolved considerably from the concept presented as result of the phase A study (Davies, et al., 2010), but it has kept one of its main advantages, a simple and robust design. As mentioned, the instrument can initially be operated with its own more simple adaptive optics system (SCAO) using a single natural guide star for on-axis diffraction limited performance. With this arrangement, high quality images for demonstration of the scientific capabilities of the ELT can be achieved more easily at first light.

The MICADO consortium is formed by more than eighty people from nine institutions in five European countries. More specifically, the Max Planck Institute for extraterrestrial Physics (MPE) as principal investigator (PI) institute, Max Planck Institute for Astronomy (MPIA), University Observatory of Munich and Institute for Astrophysics of the Georg-August-Universität Göttingen (IAG) in Germany; Netherlands Research School for Astronomy (represented by University of Groningen, the University of Leiden, and the NOVA optical/infrared instrumentation group based at ASTRON in Dwingeloo) in the Netherlands; National Institute for Astrophysics at the Observatory of Padova in Italy; Centre National de la Recherche Scientifique/Institut National des Sciences de l'Univers (represented by LESIA, GEPI and IPAG) in France and an Austrian partnership represented in MICADO by the University of Vienna, the University of Innsbruck, the University of Linz, and RICAM Linz (Austrian Academy of Sciences). ESO is also a fundamental member of the consortium, taking care of the high level project management and the detector array work package. The MICADO consortium achieved an important milestone in the project, where all partners agreed the transition into the preliminary design phase (phase B) with the kick-off meeting held in Vienna, October 2015 (MPE, 2015). As

part of the MICADO consortium MPIA is responsible for two sub-system of the instrument: the calibration unit and the derotator. This thesis is directly related to the derotator work package.

### 1.2.1 Key Capabilities of the Instrument

MICADO will offer key capabilities taking advantage of the distinctive characteristics of the ELT: great sensitivity and resolution, precision astrometry and spectroscopy. The main observing mode of the instrument is imaging focused on astrometry. Therefore one of the crucial components of the camera is the array of 3 x 3 infrared detectors (each of 4096 x 4096 pixels) to be used to cover the large focal plane of MICADO. In order to achieve the required stability to provide spatial resolution in the order of 10 milli-arcsec and astrometric precision lower than 50 micro-arcsec, the optical design is composed entirely of fixed mirrors, a novel atmospheric dispersion corrector is used and the instrument has its own astrometric calibration strategy. Coronagraphy, in order to provide a high contrast imaging capability, will be implemented using a different focal plane and/or pupil plane masks, is also considered in the design as one of the observing modes to be offered together with a slit spectroscopic mode. Finally, time resolved imaging is also contemplated in the current concept of MICADO.

The science cases that have motivated the design of this big camera are described by Davis et al. (2016) as follows: (i) galaxy evolution at high redshift, (ii) black holes in galaxy centres, including the Galactic Center, (iii) resolved stellar populations, including photometry in galactic nuclei, the initial mass function in young star clusters, and intermediate mass black holes in globular clusters, (iv) characterization of exoplanets and circumnuclear disks at small angular scales, (v) the solar system, and (vi) time resolved phenomena around neutron stars and stellar mass black holes.

### 1.2.2 The MICADO Concept

The MICADO instrument concept consists of a structural cryostat of about 2.1 m in diameter and a height of 2 m. The mass of the cryostat is around 5500 kg. All optical components are installed inside the so called “cold structure” that will work under

cryogenic conditions at temperatures between 40 K and 100 K. The internal cold structure is covered with a radiation shield and is fixed to the cryostat central flange through an isolating cylindrical structure made of G10 fibreglass. Given that the central flange is the structural support of the entire cryostat, the vessel to keep the vacuum inside the camera is also screwed on this part. The CAD model of the cryostat is presented in Figure 6.

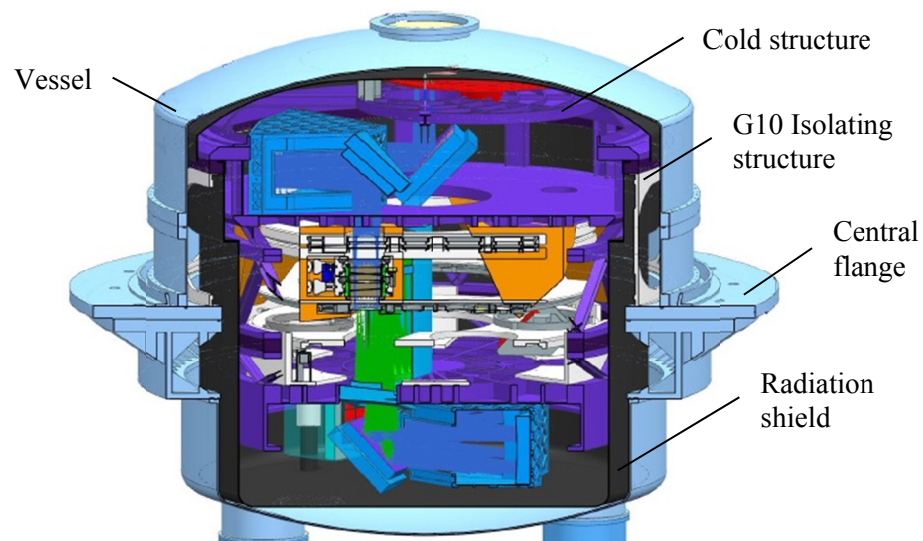


**Figure 6:** MICADO Cryostat CAD model (Image source: MICADO consortium).

The natural guide star wavefront sensor (NGS WFS) including the SCAO module with a mass around 1500 kg, is mounted on a dedicated optical bench located on top of the cryostat. The SCAO optical bench is held in place by a conical support structure also attached to the cryostat central flange. The SCAO subsystem is described in detail by Clénet, et al. (2016).

The whole group of the cryostat, NGS WFS and SCAO module with a mass of about 7000 kg, is mounted via the central flange to a large high-precision image derotator. The derotator holds the cryostat close to its center of gravity and becomes the structural support of the entire MICADO instrument. Field rotation compensation is accomplished by rotating the entire camera instead of using a K-mirror because of the large diagonal field of view (Davies, et al., 2016). The instrument support structure, with an octopod-like configuration must keep the complete assembly suspended at about 3.5 m (using the central flange as reference) above the ELT

## 1.2 The MICADO Instrument

---

Nasmyth platform (Figure 7 and Figure 8). Finally, some of the instrument electronics cabinets, the cable-wrap and the cooling system are placed on a separated coarse-precision co-rotating platform below the cryostat between the eight struts of the support structure. Other electronic cabinets, i.e. for the derotator and the calibration unit, are fixed on the telescope Nasmyth platform.

The instrument support structure has considerably evolved since the beginning of phase B and a previous concept is described elsewhere (Nicklas, Anwand-Heerwart, Schubert, & Rhode, 2016). The current proposal considers the installation of the cryostat from above, as baseline for the assembly, integration and verification (AIV) phase. Since the focal plane of the ELT straight-through port is located at 6 m above the Nasmyth platform and just 1m away of the PFS and, in order to provide the gravity invariant orientation for the camera, the focal plane must be reimaged using relay optics for any of the operational modes of MICADO (MCAO or SCAO). The current concept of the instrument support structure allows that a single design can be used in both configurations.

The MCAO configuration MICADO-MAORY is shown in Figure 7. In that case, all optical components related to the AO system (including two deformable mirrors) and the relay optics are placed on a big optical bench (Diolaiti, et al., 2016), while the MICADO cryostat is shifted to the side supported by its own structure. The last optical component on the MAORY module (M11) sends the light vertically down into the cryostat. The baseline design of the MAORY relay optics consists of two optical exit ports, which means that in addition to MICADO this MCAO module could be used with a second instrument as well (Lombini, et al., 2016). The MICADO-MAORY calibration unit is also located on the MCAO optical bench close to the focal plane of the telescope.

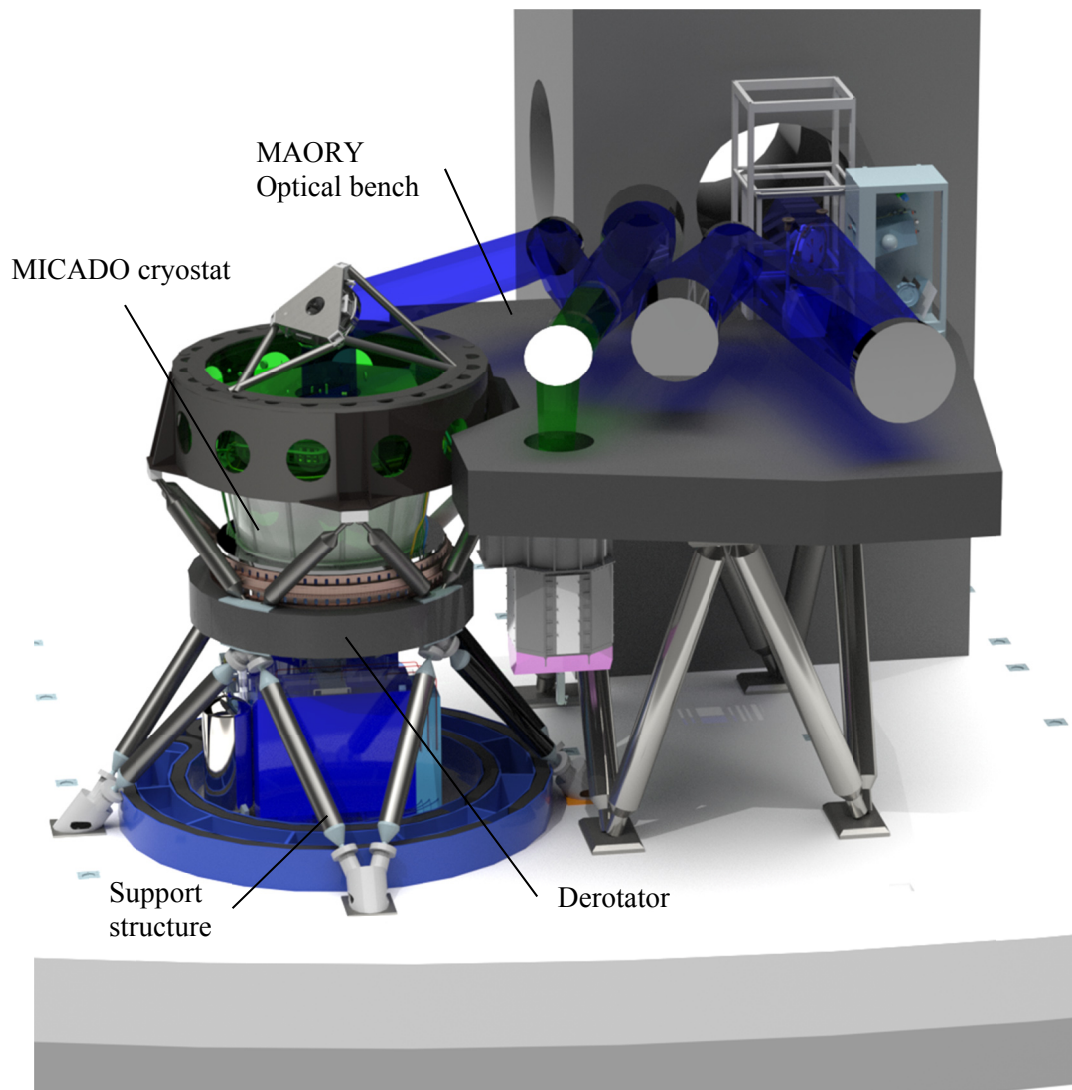


**Figure 7:** The MCAO configuration MICADO-MAORY (Image source: MICADO consortium).

For the MICADO stand-alone configuration (SCAO) shown in Figure 8, an additional optical bench is required to hold the optical relay system to match the focal plane of the telescope with the instrument, the M7 unit to send the light vertically down into the cryostat and the MICADO calibration unit. The auxiliary bench is located directly on top of the cryostat using a similar octopod-like support structure also attached to the static mechanical interface of the derotator.



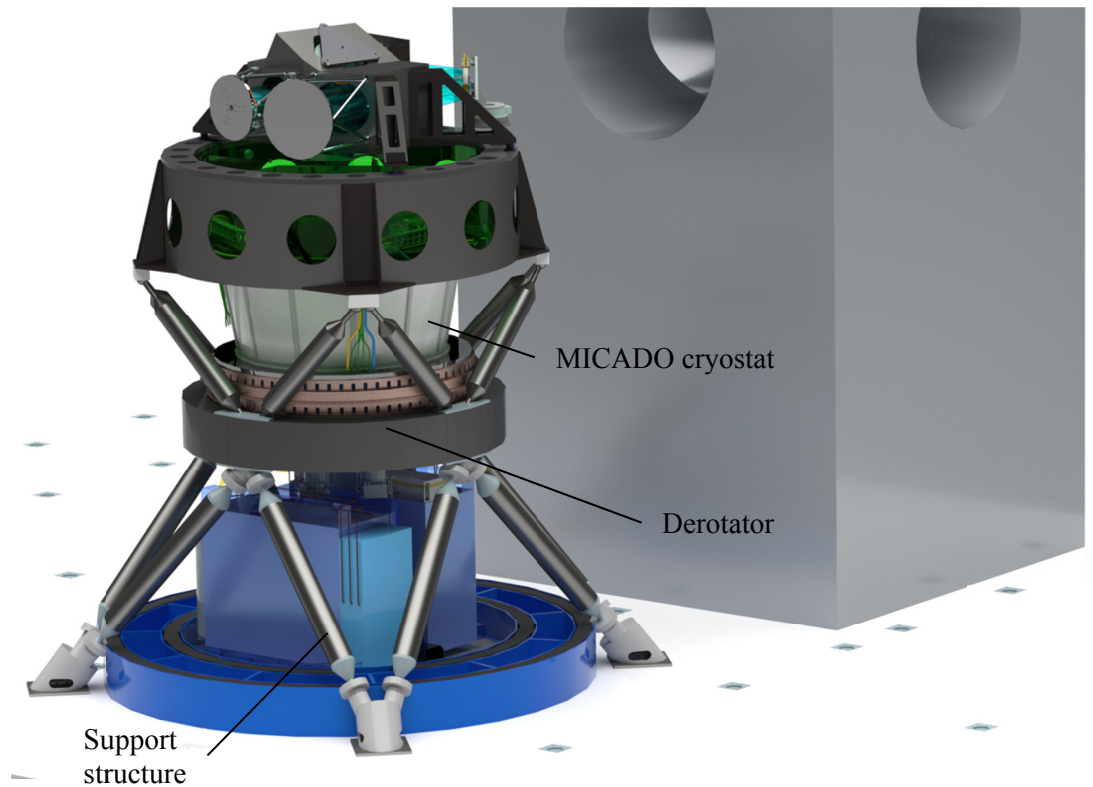


**Figure 8:** The SCAO configuration MICADO “stand alone” (Image source: MICADO consortium).

### 1.3 The Image Derotator

The Derotator work package comprises the design elaboration, manufacture/procurement and verification of MICADO’s sub-system for accurate field rotation compensation. As already mentioned this is due to the ELT’s alt-azimuth mounting structure. MPIA has included in the work package as well, the early built of representative prototypes to gain initial performance data and to minimize the risk of late interface and/or design flaws (the prototype of the MICADO derotator is called derotator test stand). The biggest challenge will be achieving an angular positioning control at the level of 2 arcsec (on the detector focal plane) during the exposure time (typically up to 120s) while the telescope tracks the scientific target. This critical requirement is understood as the difference (rms) between the ideal field rotation trajectory and the real trajectory measured by an encoder installed into the derotator. Up to now, the angular positioning accuracy is



the most critical requirement, while other key performance requirements like the radial/axial runout and wobble can be fulfilled more easily with the chosen bearing technology.

The current derotator concept consists of:

- A custom designed slewing bearing as the main component.
- The bearing support structure.
- The thermal compensation rings.
- Several drive units for backlash suppression.
- The angular positioning measurement system using a tape encoder with several scanning heads.
- The control system to operate the derotator in closed loop.

The overall concept of the derotator has remained essentially the same since the beginning of phase B, but the mechanical interfaces have changed considerably. A previous concept considering the installation of the cryostat from below is described elsewhere (Barboza, et al., 2016). The main risk of the current design proposal is the effect of the bearing friction over the required angular positioning accuracy while rotating at low velocities. Therefore, the derotator test stand will play a crucial role in verifying if this requirement can be achieved with the suggested bearing technology. Understanding the friction phenomena is the key to optimizing the control system working in closed loop. The goal is to apply methods for friction compensation if required.

## **1.4 Motivation and Thesis Objectives**

A derotator is a mechanism with one degree of freedom that must compensate for the field rotation of telescopes with alt-azimuth mounts. As an assembly of several components, i.e. a precision bearing, gears, motors, encoders, mechanical interfaces, controllers and software; the challenge is to develop a system in which all those components are able to work together in order to fulfil the high precision requirements demanded by the last generation of state-of-the-art astronomical instruments like MICADO. This thesis is mainly focused on the overall design of the

## 1.4 Motivation and Thesis Objectives

---

system and the selection of the required hardware. Thus, the design of the control system and software are not the central topic of this work.

This PhD project concentrates on a key mechanical component of the MICADO instrument and the task to design a feasible solution of such a device. The thesis runs parallel to the phase B (preliminary design phase) of MICADO. After that, if positively qualified and released during the final design review (FDR), the derotator will be manufactured based on the design proposal presented in this dissertation. Thus, the result of this work will represent a significant contribution to the preliminary design review of the instrument within the MICADO consortium planned for late 2018.

More specifically the objectives of the dissertation are defined as follows:

- Investigation and trading-off of available technologies and existing solutions.
- Selection of an appropriate bearing technology based on the available space, precision, expected performance and cost.
- Develop a preliminary design of the MICADO derotator based on the common mechanical interfaces.
- Perform finite element analysis to estimate the static performance of the proposed design.
- Setup an end-to-end simulation to estimate the dynamic performance of the derotator proposal.
- Development of adequate test procedure / facilities to verify the requirements of the derotator (derotator test stand).
  - Test the encoder-pinion solution.
  - Learn about the implementation and performance of the band encoder.
  - Proof the alignment procedure between the interface flange and the bearing.
  - Test backlash suppression system.
  - Understand the effects of the friction over the positioning accuracy.
  - Calibrate the parameters of the end-to-end model.
  - Compare the results of the end-to-end model with the performance of the real prototype.
  - Validate the Finite Element Model (FEM) of the bearing.

## 1.5 Thesis Outline

The research performed for this PhD thesis is structured and presented in the following:

The origin of the field rotation in telescopes with Alt-Azimuth mounts, the issue that this research work intends to solve for the MICADO instrument, is addressed in chapter 2. The mathematical background to derive the parallactic angle using the celestial sphere is given as introduction, to then focus in the specific field rotation trajectories that the MICADO derotator should follow at the ELT Nasmyth platform A. To conclude this chapter, some variables affecting the ideal field rotation trajectories are discussed as well.

Chapter 3 is dedicated to describing some possibilities to provide field rotation compensation in astronomical instruments and why this particular option (rotating the whole camera) was selected for the MICADO instrument. The most relevant requirements driving the design of the MICADO derotator are summarized in this chapter and a bearing technology trade-off is provided as well. An overview of existing technical solutions providing field rotation compensation for astronomical instruments is presented to conclude this section.

The proposal to provide field rotation compensation for the MICADO instrument is described in detail through chapter 4. Initially, the custom design slewing bearing is described. Afterwards the mechanical interfaces and the optimization process of the structural components are presented, to finish with the overall concept of the derotator. The static structural analysis and the verification of the bearing FEM are also presented in this chapter.

Chapter 5 is dedicated to providing the tools for developing the end-to-end simulation of the MICADO instrument, to be used for estimating its dynamic performance. The required basics of structural dynamics to develop the mathematical model of the MICADO mechanical system are provided as introduction, to continue with the implementation of the mechanical model in Matlab/Simulink. The approach used for modeling the bearing friction is also discussed in this chapter.

## 1.5 Thesis Outline

---

The experiment used as a technology demonstrator is finally described in chapter 6, including the AIV phase and the most relevant performance results of the test campaign carried out with the derotator test stand.

The conclusions about this research work are finally given in chapter 7, while some complementary calculations and experimental data are presented in the appendices.

## 2 Alt-Azimuth Telescopes Field Rotation

When pointing a telescope at a star, stability is very important, therefore the choice of a proper mount is crucial in telescope design. Until the 1980's, the preferred type was the equatorial mount, due to its mechanical simplicity and accuracy. This is because the telescope only needs to move one axis at constant velocity to track a star. This also means this type of support structure does not suffer from field rotation, as only the equatorial axis (parallel to the polar axis of the earth) must be rotated. Equatorial telescopes use the equatorial coordinate system (Figure 9), which is defined with respect to the center of the Earth. Here the Celestial Equator is used as the reference plane and the Vernal Equinox ( $\gamma$ ) as the reference direction. The equatorial coordinate system is not related to the position of the observer. The declination ( $\delta$ ) is used as the latitude coordinate and the right ascension ( $\alpha$ ) as the longitude coordinate, together these can be directly used to locate the celestial objects. To determine the position of the star at the moment of observation, the hour angle ( $h$ ) must be calculated using the sidereal time ( $\omega_0$ ).

## 2 Alt-Azimuth Telescopes Field Rotation

---

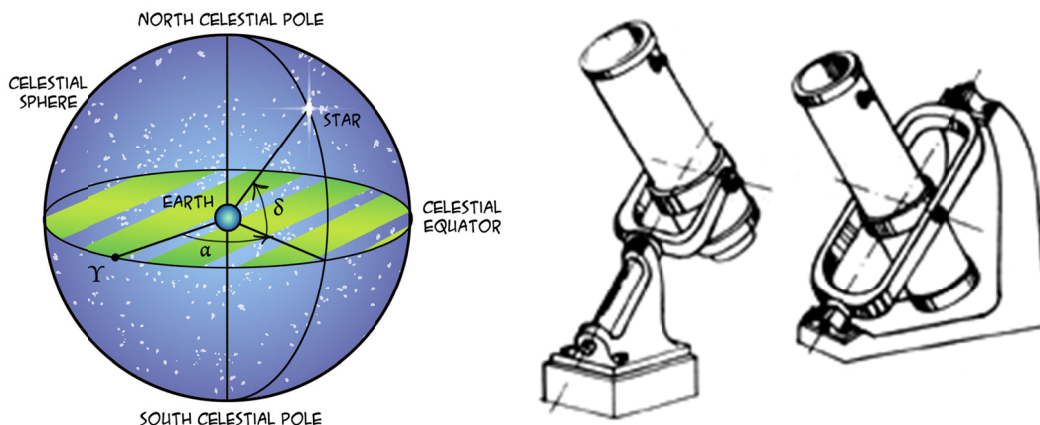


**Figure 9:** Equatorial coordinate system (left) and equatorial mounts (right) (image source downloaded from <https://quantumredpill.wordpress.com> and <http://bibliotecadigital.ilce.edu.mx> on July 2017).

Whilst equatorial mounts are simple and accurate they are fundamentally heavier. Due to the inclination of the polar axis, they must provide additional stiffness to the telescope. As the size of the primary mirror increased, the telescope builders had to move to the alt-azimuth mounts in order to make the weight of the structure manageable.

The telescopes using alt-azimuth mounts (Figure 10) are more efficient in terms of mass distribution (better load transmission) and thus are able to support bigger mirrors, but at the cost of introducing rotation of the field of view and a more complex two-axis tracking system. This kind of telescope uses a horizontal coordinate system, which is related to the position of the observer on the earth and therefore considered a local coordinate system. The horizon at the location of the observer is taken as reference plane and the north cardinal point is used as reference direction. To define the position of the celestial object the altitude ( $a$ ) is used as the latitude coordinate and the azimuth ( $A$ ) is used as the longitude coordinate. While observing using alt-azimuth telescopes where the axes of rotation are implemented vertically and horizontally, the hour angle ( $h$ ) and the declination ( $\delta$ ) as global coordinates, must be converted to altitude ( $a$ ) and azimuth ( $A$ ) as the local coordinates.

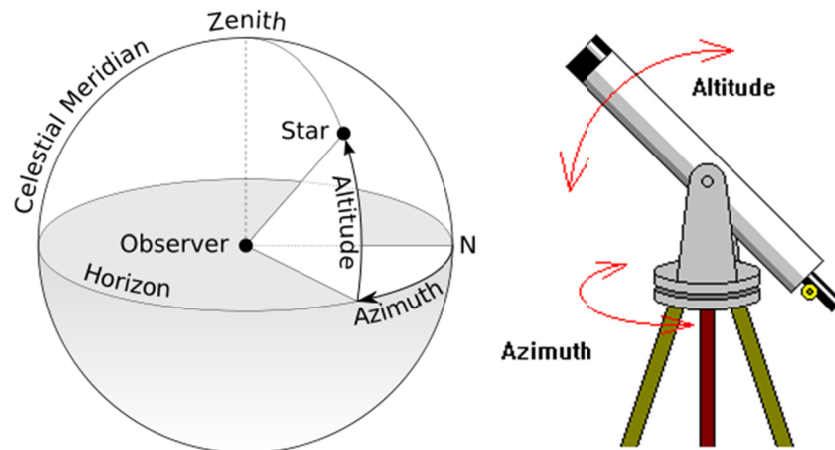


**Figure 10:** Horizontal coordinate system (left) and alt-azimuth mount (right) (Image source: downloaded from <https://en.wikipedia.org>, <https://www.uwgb.edu> on July 2017).

In this case, two axes must be rotated simultaneously at variable speeds in order to track a star and, the third one to compensate for the field rotation. The field rotation at the Cassegrain focus is then directly given by the negative parallactic angle ( $p$ ) (Bely, 2003), which is the angle formed between the great circle passing through the star and the zenith, and the hour circle of the celestial object (see Figure 11). The following sections are dedicated to explain the field rotation calculation.

## 2.1 Deriving the Parallactic Angle

The celestial sphere shown in Figure 11 is used to represent the parameters required to obtain the equations defining the parallactic angle. This figure describes the horizontal coordinate system centered on the observer (defined by  $A$ ,  $a$ ) and the relation to the equatorial coordinate system where  $\alpha$  (required to calculate  $h$ ) and  $\delta$  are used to locate the star. Despite the horizontal coordinate system is being used as reference in telescopes with alt-azimuth mounts, the parallactic angle must be expressed as a function of  $h$  and  $\delta$  (the parameters of the global Coordinate system).

## 2.1 Deriving the Parallax Angle

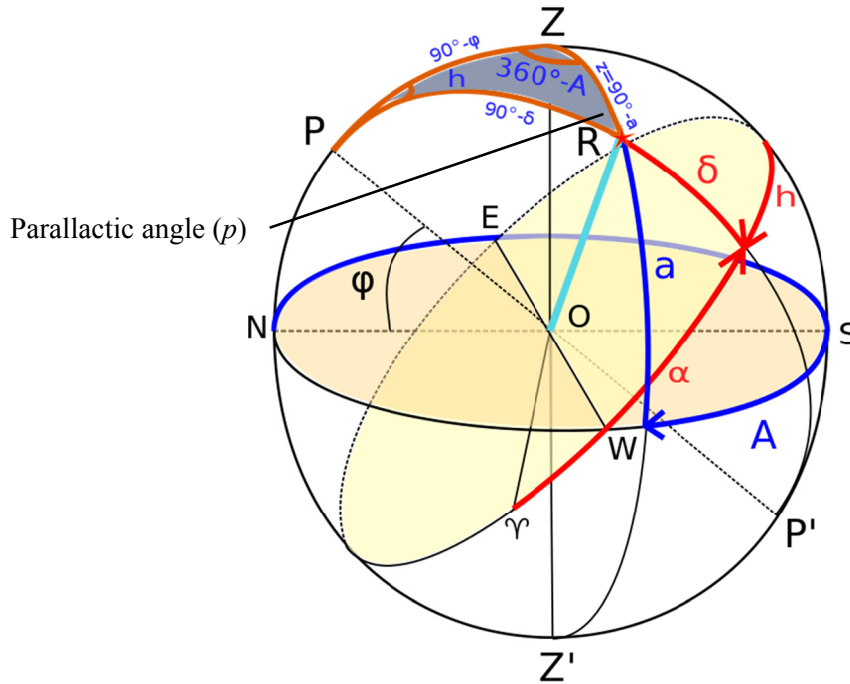


**Figure 11:** Celestial sphere centered on the observer with the correlation between horizontal and equatorial coordinate systems. Where  $p$  is the North Pole,  $Z$  is the zenith,  $R$  is the location of the star,  $\varphi$  is the latitude of the observer,  $\gamma$  is the Vernal Equinox,  $\delta$  is the declination,  $\alpha$  is the right ascension,  $a$  is the altitude,  $A$  is the Azimuth, the tilted plane is the Celestial Equator and the horizon at the observer position is defined by the orange plane. The so called astronomical triangle is formed between the vertexes PZR (Image source: downloaded from <https://commons.wikimedia.org> on July 2017).

The parallax angle can be calculated using the so called “Astronomical Triangle”, which is defined by the vertex PZR and the arc segments  $90^\circ - a$ ,  $90^\circ - \varphi$  and  $90^\circ - \delta$ , as shown in Figure 11. The internal angles of the triangle are then  $h$ ,  $360^\circ - A$  and the parallax angle  $p$ . An equation which directly describes the parallax angle can be found using spherical trigonometry (Todhunter & Leathem, 2006). Applying the sine rule to the Astronomical triangle the following equation (1) can be established

$$\frac{\sin p}{\sin(90^\circ - \varphi)} = \frac{\sin h}{\sin(90^\circ - a)}, \quad (1)$$

which can be simplified as

$$\sin p \cos a = \sin h \cos \varphi. \quad (2)$$

Using the so called “analogue formula” in spherical trigonometry (Green, 1985) the subsequent expression can be obtained



$$\cos p \cos a = \sin \varphi \cos \delta - \cos \varphi \sin \delta \cos h. \quad (3)$$

The function  $p(\delta, h)$  is found dividing equation (2) by equation (3)

$$\tan p = \frac{\sin h}{\tan \varphi \cos \delta - \sin \delta \cos h}, \quad (4)$$

where  $\varphi$  is the latitude of the telescope location,  $\delta$  (declination) is related to the star at which the telescope is pointing staying constant for a given observation and,  $h$  (hour angle) is the time variable typically represented in hours for a range of about 12 hours where an observation could take place during the night.

## 2.2 Field Rotation at Cassegrain Focus

Depending of the optical design of the telescope, different focal stations exist. As shown in Figure 12, the Cassegrain focus is the one located right behind the primary mirror of the telescope.

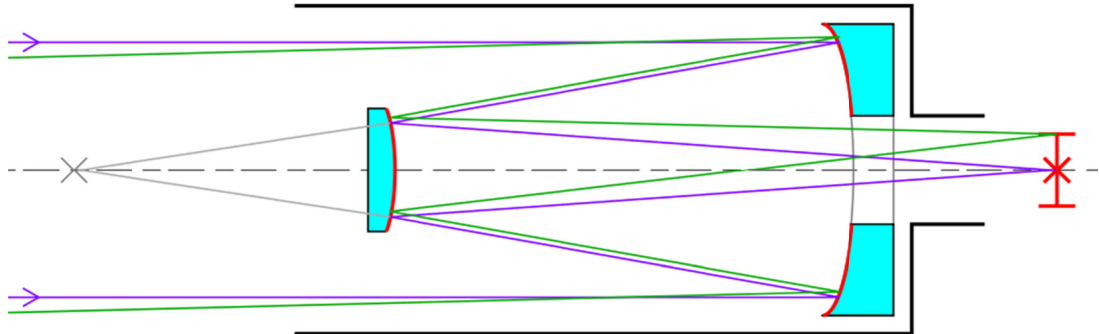


**Figure 12:** Location of the Cassegrain Focus on a Cassegrain reflecting telescope consisting of a parabolic primary mirror and a hyperbolic secondary mirror (Image source: downloaded from [https://en.wikipedia.org/wiki/Cassegrain\\_reflector](https://en.wikipedia.org/wiki/Cassegrain_reflector) on October 2017).

As the field rotation at the Cassegrain focus ( $F_{Ca}$ ) is represented by the negative parallactic angle the following relation can be established,

$$F_{Ca} = -p. \quad (5)$$

For tracking purposes the velocity and the acceleration of the field rotation are also required. Those parameters are represented by equations (6) and (7) as the first and second derivative of  $p$  with respect to the time.

## 2.2 Field Rotation at Cassegrain Focus

---

$$F_{Ca} = -\dot{p}, \quad (6)$$

$$F_{Ca} = -\ddot{p}. \quad (7)$$

The tracking rate or how the field rotation evolves with respect to the time is defined by the rotation of the earth, represented with the sidereal rate ( $\omega_0$ ). The sidereal rate is then 1 revolution/day,  $360^\circ/24$  hours or  $15^\circ/\text{hour}$ . The field rotation velocity can be found by differentiating equation (6) with respect to the hour angle and then multiplying the results by the sidereal rate as described in equation (8) (Shepherd, 2001)

$$\dot{p} = \frac{dp}{dt} = \frac{dp}{dh} \frac{dh}{dt} = \frac{dp}{dh} \omega_0. \quad (8)$$

After mathematical arrangement and simplification, the final equations for the field rotation velocity and acceleration can be written as follows using equations (11) and (12) which are described below

$$\frac{\dot{p}}{\omega_0} = \frac{\cos \varphi \cos A}{\cos a} \quad (9)$$

$$\frac{\ddot{p}}{\omega_0^2} = -\frac{\sin A \sin 2\varphi}{2 \cos a} - \frac{\sin a \sin 2A \cos^2 \varphi}{\cos^2 a}. \quad (10)$$

This is a normalized form using the sidereal rate ( $\omega_0$ ) and its square, as has been reported by ESO in the calculation of the field rotation for the VLT unit telescopes (Avila & Wirenstrand, 1991).

In this case the values used for the normalization are given by

$$\omega_0 = 15 \text{ arcsec/s}$$

$$\omega_0^2 = 1.091 \times 10^{-3} \text{ arcsec/s}^2$$

where  $\omega_0^2$  is obtained multiplying  $\omega_0$  in rad/s by  $\omega_0$  in arcsec/s (Avila & Wirenstrand, 1991).

The complementary expressions to calculate the altitude ( $a$ ) and the azimuth ( $A$ ) are finally described by equations (11) and (12)

$$\sin a = \sin \delta \sin \varphi + \cos \delta \cos h \cos \varphi \quad (11)$$

$$\tan A = \frac{\sin h}{\cos h \sin \varphi - \tan \delta \cos \varphi}. \quad (12)$$

## 2.3 Field Rotation at Nasmyth Focus

The Nasmyth focus is particularly important for the work in this thesis as this is the focal station where the MICADO instrument will be installed. The Nasmyth telescope is a modified version of the Cassegrain telescope, where the focus is located sideways by the introduction of an additional flat mirror. This optical concept is shown in Figure 13.

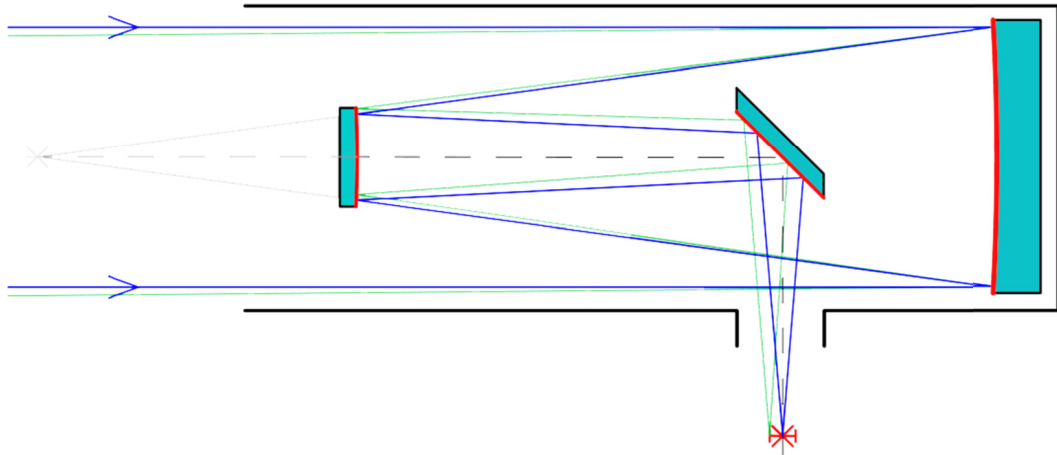


**Figure 13:** Location of the Nasmyth Focus on a Cassegrain reflecting telescope consisting of a parabolic primary mirror and a hyperbolic secondary mirror (Image source: downloaded from <https://en.wikipedia.org> on October 2017).

When the Nasmyth Focus is used in a telescope, the altitude angle  $a$  must be considered in the calculation of the field rotation. Thus, the field rotation at the Nasmyth focus  $F_N$ , as well as the corresponding velocity and acceleration are given by the following expressions

$$F_N = p \pm a, \quad (13)$$

$$\dot{F}_N = \dot{p} \pm \dot{a}, \quad (14)$$

$$\ddot{F}_N = \ddot{p} \pm \ddot{a}, \quad (15)$$

## 2.3 Field Rotation at Nasmyth Focus

---

where the sign + or – depends on which Nasmyth port is been used. The additional expressions required to obtain the altitude angle velocity and acceleration are described by equations (16), (17) and (18).

$$\frac{\dot{a}}{\omega_0} = -\sin A \cos \varphi, \quad (16)$$

$$\frac{\ddot{a}}{\omega_0^2} = -\frac{\dot{A}}{\omega_0} \cos A \cos \varphi, \quad (17)$$

$$\frac{\dot{A}}{\omega_0} = \sin \varphi + \tan a \cos A \cos \varphi. \quad (18)$$

### 2.3.1 Field rotation at ELT Nasmyth platform A

The MICADO instrument will be located at the ELT Nasmyth platform A (Frank, 2015). If the telescope is pointing close to the horizon and the observer is behind the primary mirror, the platform A is to the left side and the platform B to the right side. Thus, the sign minus (–) is used in the equations (13), (14) and (15), and the angle of rotation is defined as positive in the counterclockwise direction. The field rotation trajectories, velocities and accelerations corresponding to this port are presented in Figure 14. The plots are generated using the latitude at Cerro Armazones, several typical values of declination  $\delta$  around the Zenith and during a period of twelve hours for the hour angle  $h$ . As the VLT and the ELT share the same global coordinate system shown in Figure 15, the same assumption can be used for the sign of the equation describing the field rotation.

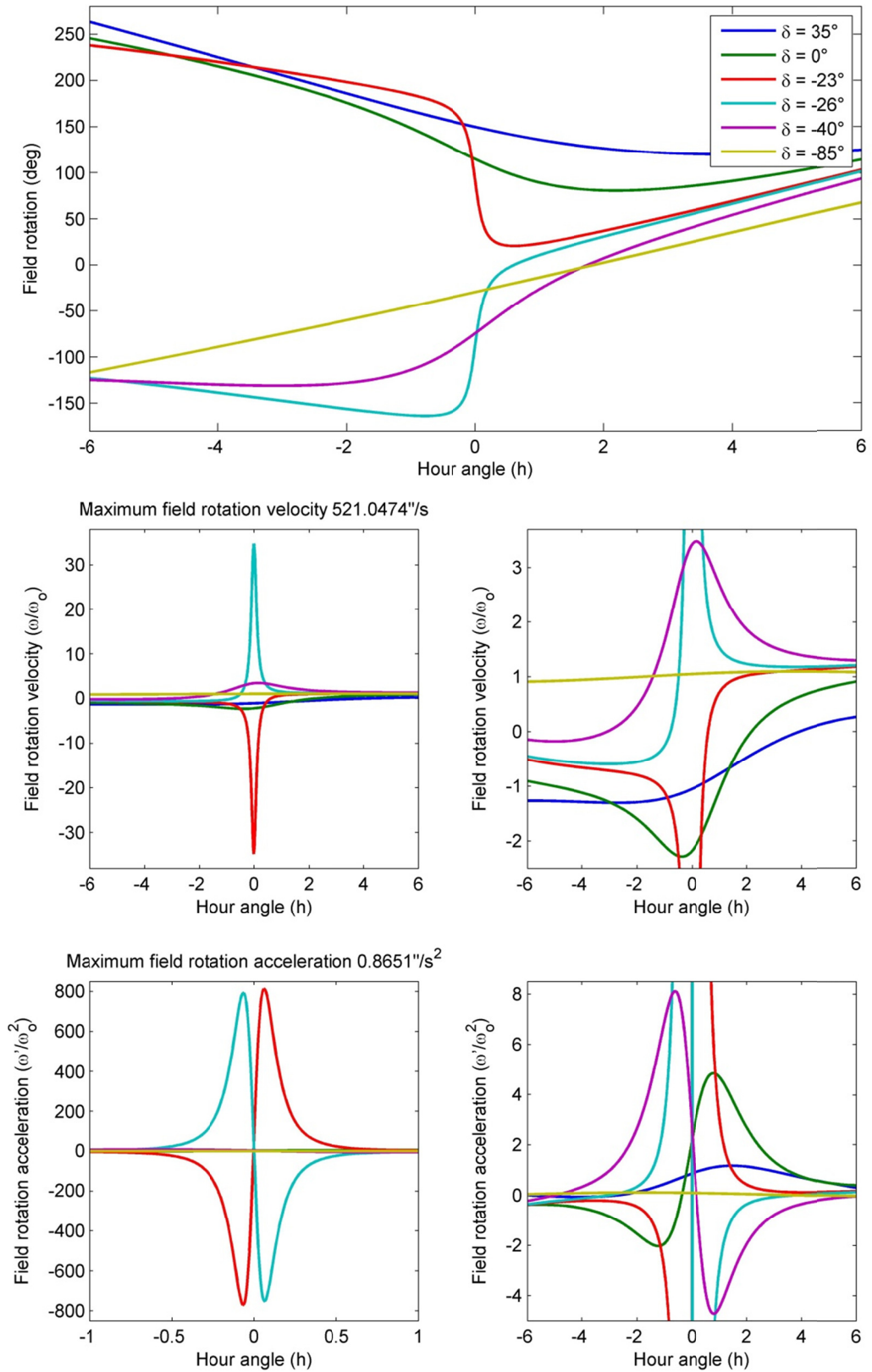


**Figure 14:** Field rotation trajectory, velocity and acceleration at ELT Nasmyth platform A (Cerro Armazones latitude  $\varphi = -24.6^\circ$ , Zenith limit =  $1.5^\circ$ ).

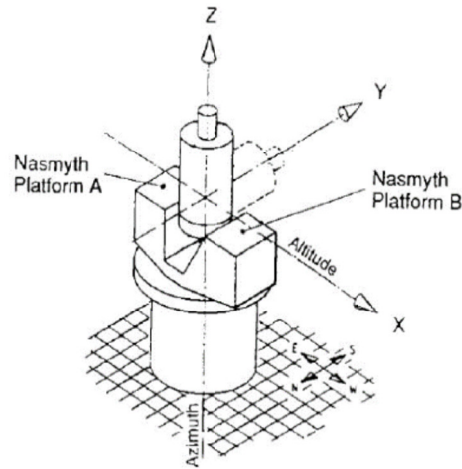


**Figure 15:** ELT global coordinate system showing the Nasmyth platform designations, the same coordinate system is used in the VLT (Image source: ELT Standard Coordinate Systems and Basic Conventions, document number: ESO-193058).

From equation (9) it can be seen that the field rotation velocity becomes infinite when the telescope is pointing to Zenith ( $a = 90^\circ$ ), and this effect is very clear in the velocity plots presented in Figure 14. For that reason, a Zenith limit of  $1.5^\circ$  ( $\pm 1.5^\circ$  around the Z axis) has been defined by ESO for the ELT (Zenith limit reference). With the defined Zenith limit, the maximum velocity is only 521 arcsec/s, while typical velocities will not exceed 52 arcsec/s. The trajectories of Figure 14 have been used as reference for the design of the MICADO Derotator.

## 2.4 Pupil Rotation at Nasmyth Focus

The MICADO instrument will be typically used in the standard imaging mode, where field rotation stabilization is required, i.e. the orientation of the sky must remain fixed on the focal plane where the science detectors are located. However, under certain conditions it is necessary that the pupil (“e.g. the wavefront aberrations from the telescope optics and the image of the spider holding the secondary mirror”) maintains a fixed orientation on the focal plane. This mode is called pupil rotation stabilization (Davies, Pott, & Tolstoy, 2017). The pupil rotation trajectories, velocities and accelerations at the Nasmyth platform A are presented in Figure 16, these calculations are performed using equations (19), (20) and (21). The plots are generated for the same values of declination as used in Figure 14.

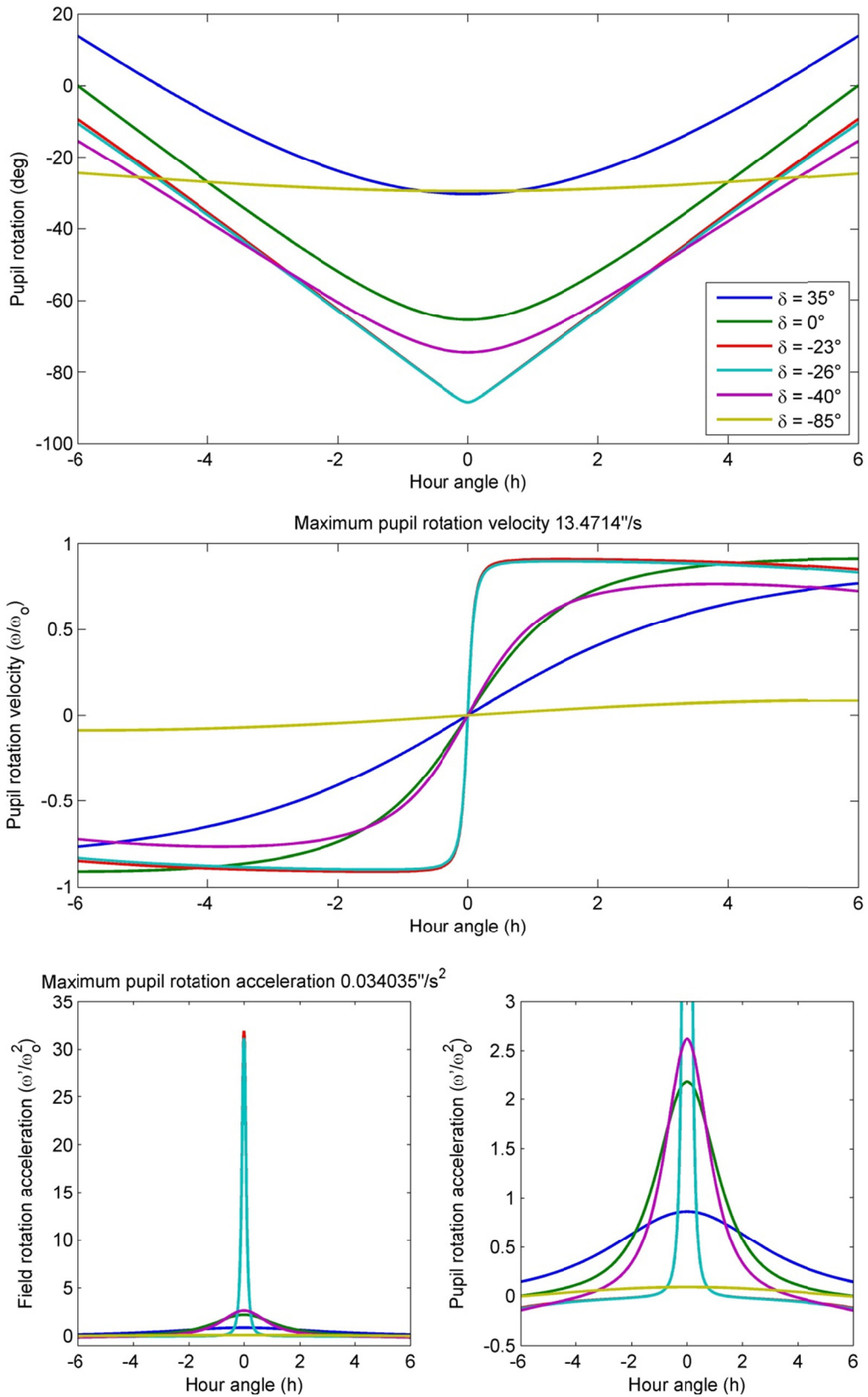


Figure 16: Pupil rotation at the ELT Nasmyth platform A.

## 2.5 Variables Affecting the Field Rotation Trajectory

---

At the Nasmyth platform the pupil rotates following the altitude angle (Avila & Wirenstrand, 1991). Thus the following expressions can be defined, where the negative sign (–) correspond to the Nasmyth platform A.

$$P_N = \pm a \quad (19)$$

$$\dot{P}_N = \pm \dot{a} \quad (20)$$

$$\ddot{P}_N = \pm \ddot{a} \quad (21)$$

## 2.5 Variables Affecting the Field Rotation Trajectory

The field rotation trajectories presented in Figure 14 are theoretically calculated ideal curves. However, in a real application several variables will introduce errors affecting those ideal trajectories. Hence it is necessary to create the real field rotation curves which the derotator should follow to provide the image stabilization. Some of the variables affecting the ideal field rotation trajectories are: the atmospheric refraction, the telescope miss-pointing and the time delay in addition to errors due to the misalignment of the instrument itself. The derotator will follow trajectories previously determined by the software of the instrument. If such external errors are not considered in the trajectory calculation, the device will not be able to provide the image stabilization even if the derotator follows the given trajectories with a very high accuracy. Atmospheric refraction deflects the light of any astronomical objects due to the variable air density in the different layers of the atmosphere. Introducing a bending of the incoming light as it passes through the atmosphere, leading to an apparent star which is higher in the sky than the true star. As the telescope tries to follow the apparent star, the error in the pointing direction will affect the field rotation trajectories. This problem can be interpreted as a pointing error, not coming from the telescope pointing control system. The effect created by the atmospheric refraction is strongly influenced by the altitude  $a$  and the meteorological conditions during the observation (Bely, 2003). The plots presented in Figure 17 shows the repercussion of the pointing error over the field rotation trajectories.



The errors introduced by the telescope pointing can be explained as the difference between two field rotation trajectories for a given declination ( $\delta$ ). The first trajectory calculated using the ideal declination of the star to be observed and the second one calculated using the same declination value plus the telescope pointing error (Egner & Bertram, 2009). As a result, the following expression can be established

$$\Delta F_N(\Delta\delta) = F_N(\delta) - F_N(\delta + \Delta\delta), \quad (22)$$

where  $\Delta F_N(\Delta\delta)$  is the residual field rotation due to the miss-pointing of the telescope  $\Delta\delta$ . Equation (22) is plotted in Figure 17 (middle plot) for six different values of zenith limit and for a telescope pointing error of  $\Delta\delta = 1$  arcsec. This calculation describes a linear behavior for different values of  $\Delta\delta$  and therefore the effect of the telescope pointing can be easily escalated. It can be observed that the error increases considerably while the telescope is pointing close to the zenith.

The effect generated by the time delay while starting the field rotation compensation can be represented in a similar way. In this case, the required two field rotation trajectories are calculated with exactly the same arbitrary value of declination but with different values of hour angle ( $h$ ). The reference trajectory is then calculated with the ideal value of  $h$ , while the second one is calculated considering the time delay. Equation (23) describes the created error

$$\Delta F_N(\Delta t) = F_N(h) - F_N(h + \Delta t), \quad (23)$$

where  $\Delta F_N(\Delta t)$  is the residual field rotation due to the time delay  $\Delta t$ . This effect is show in Figure 17 (bottom plot) for the same values of zenith limit and a time delay of  $\Delta t = 1s$ . The error described by equation (23) is also directly proportional to the  $\Delta t$  and the maximum values are obtained if the telescope is close to the zenith as well. The results obtained in this section are used to derive some of the requirements for the MICADO derotator, like the timing accuracy of the field rotation tracking and how the pointing/tracking accuracy of the ELT could affect the derotator performance. Section 3.1 is dedicated to this matter.

## 2.5 Variables Affecting the Field Rotation Trajectory

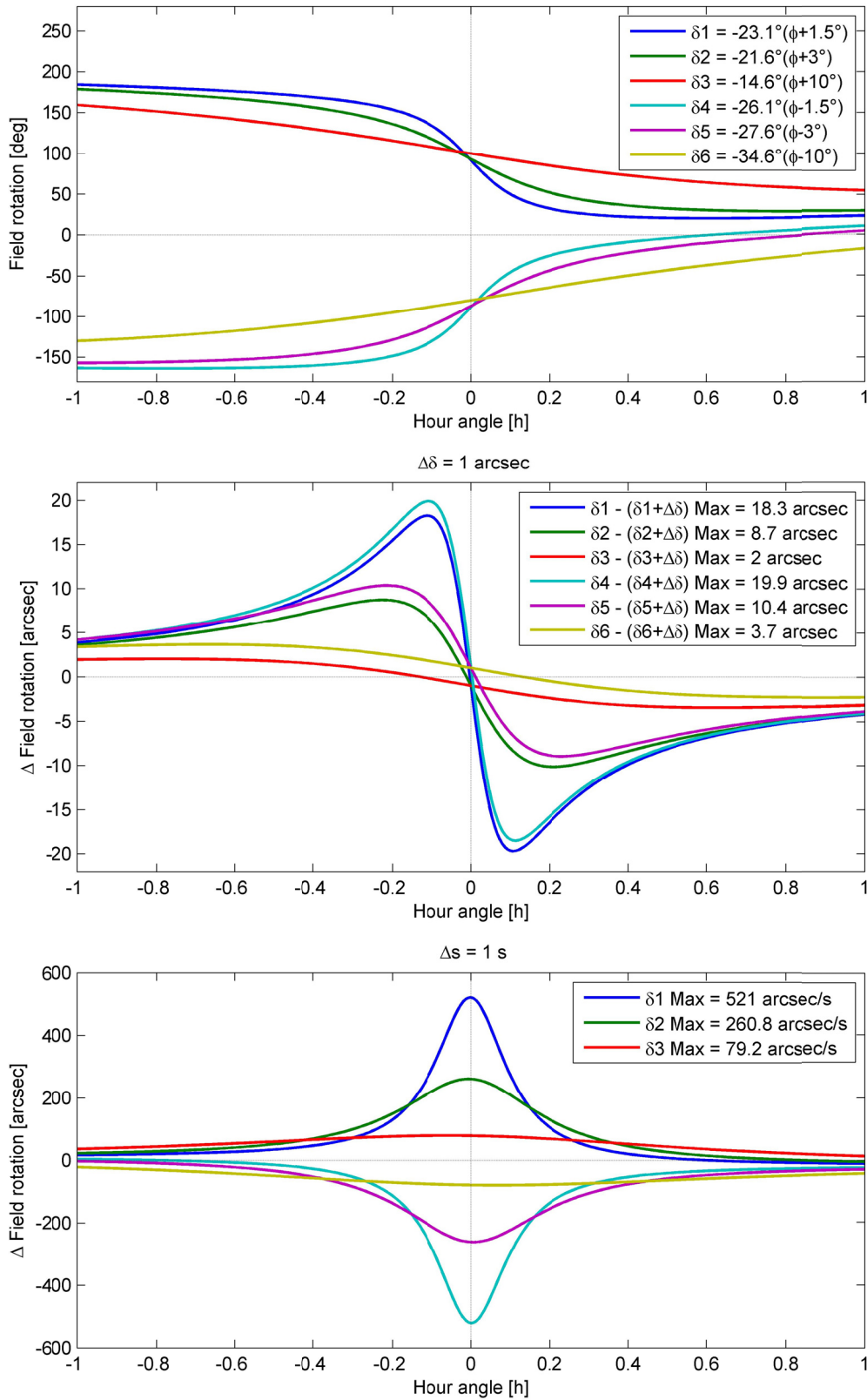


**Figure 17:** Effect of the telescope pointing error (middle plot) and the time delay (bottom plot) over some ideal field rotation trajectories (top plot) at the ELT Nasmyth platform A.

### **3 Field De-Rotation for MICADO**

After having introduced in the previous chapter the origin of the field rotation phenomenon, starting with a general approach on the matter in telescopes with alt-azimuth mounts and then focusing on the expected trajectories at the Nasmyth platform A of the ELT, it is necessary to define the requirements for the field de-rotation stabilization demanded by the MICADO instrument. This includes considering at the same time possible technical solutions matching the limitations imposed by this particular application. Potential restrictions are the location of the derotator, available space, and weight of the device. The problem to be solved finally reduces to designing, building and testing a derotator capable of following those field de-rotation trajectories with the required angular positioning accuracy.

The top level science goals (Liske, 2015) have shaped the overall concept of the MICADO instrument, while specific science cases and observation modes like standard imaging, astrometric imaging, coronagraphic imaging, time resolved imaging, slit spectroscopy and pupil imaging (Davies, Pott, & Tolstoy, 2017) are driving the design of the instrument subsystems on a more detailed level. The requirements for the MICADO derotator are mainly derived from those observation modes.

One possibility to compensate for the field rotation is using an optical derotator. Such a device can provide the required image stabilization by rotating a set of flat mirrors around the axis of the light beam entering the instrument. In this optical setup, the reflection surfaces must be arranged in a very specific way, like the Abbe type rotator (Swift, 1972). That kind of optical arrangement is also known as K-mirror (see Figure 18) and has been implemented in other astronomical instruments,

such as the MCAO optical bench of LINC-NIRVANA (Schreiber, et al., 2008) and VLT GRAVITY using metallic mirrors (Gebhardt, et al., 2012).

This is also the chosen alternative to provide field rotation stabilization in the ELT instrument METIS (Brandl, et al., 2012). For MICADO a K-mirror is implemented for pupil stabilization in the MICADO SCAO module as well.

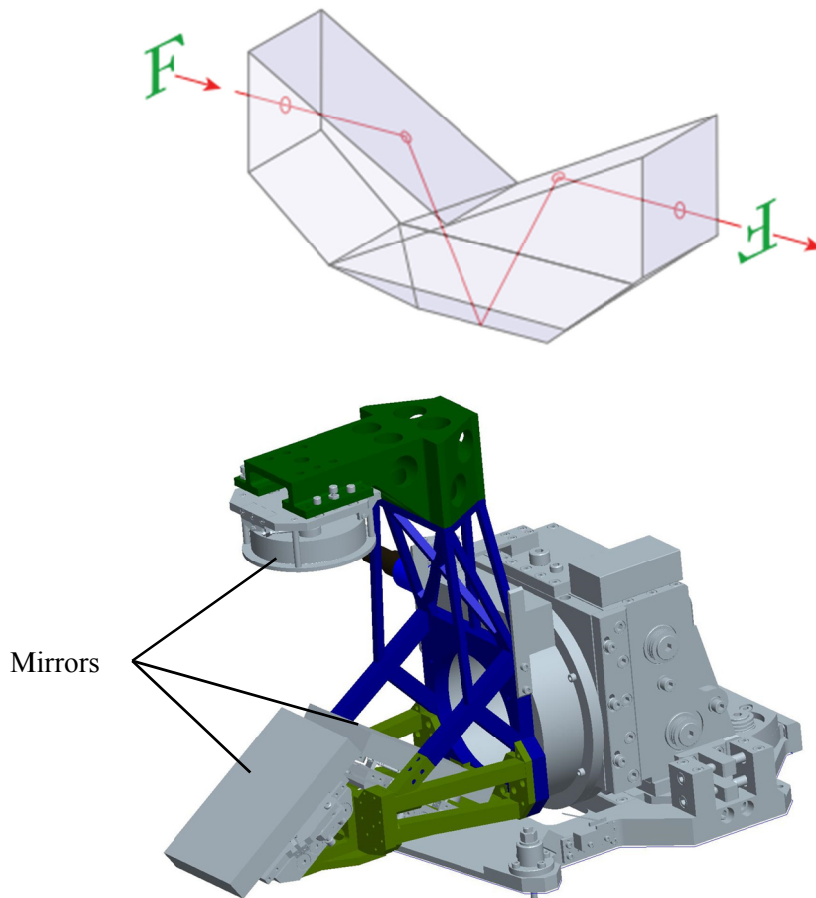


**Figure 18:** Abbe type prisms (top) and LINC-NIRVANA K-mirror (bottom) (Image source: [https://en.wikipedia.org/wiki/Abbe%E2%80%93Koenig\\_prism#/media/File:Abbe-K%C3%B6nig\\_prism.svg](https://en.wikipedia.org/wiki/Abbe%E2%80%93Koenig_prism#/media/File:Abbe-K%C3%B6nig_prism.svg) on January 2018 and LINC-NIRVANA consortium).

Another possibility is to provide field rotation stabilization by physically counter rotating the detector (or array of detectors) located at the focal plane of the instrument. This can be achieved, for example, by turning the detector itself as realized inside the LINC-NIRVANA cryostat (Bizenberger, et al., 2012), or by rotating the whole camera as it will be implemented in the MICADO instrument. The main disadvantage of a warm K-mirror is that three warm reflections are added to the

fore-optics which will make observations significantly less sensitive. Then the easiest way to implement a cold field derotator is the LINC-NIRVANA solution with the science detector (see Figure 19), but this comes at the price of rotating the detector against the optics/aberrations, which should be avoided for astrometry. The next option would be to have a cold K-mirror inside the MICADO cryostat, which was also avoided, because the intention is to rotate actually not only the MICADO field, but also the MAORY patrol field and WFS. The only solution for this is a common warm derotator. Additionally, by rotating the whole camera as planned with the current MICADO opto-mechanical concept, only one derotator is needed due to the fact that the WFS are mechanically fixed to the rotating cryostat. Thus avoiding relative differential movement between these components.

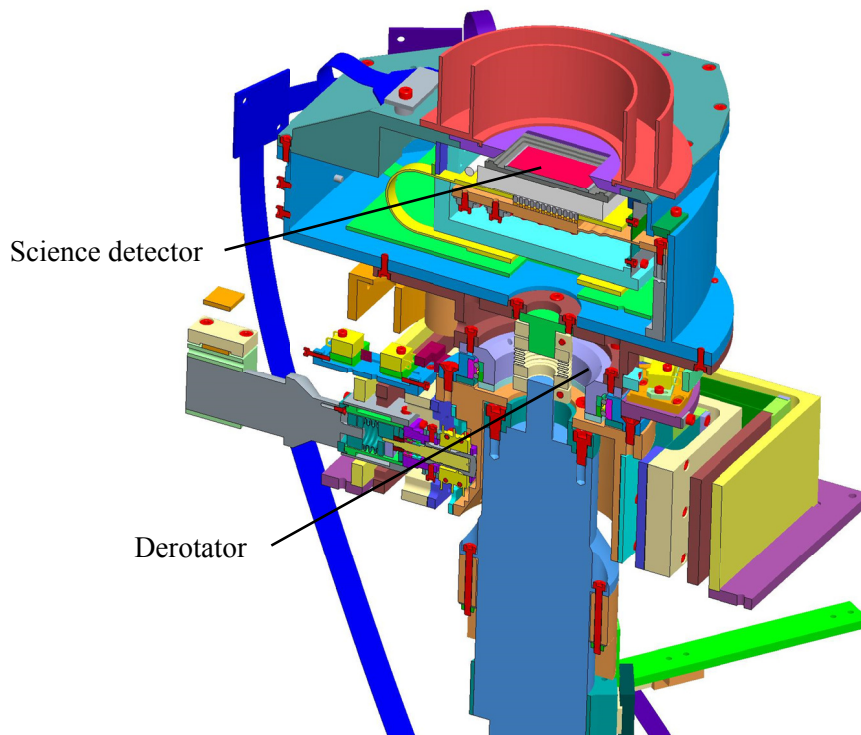


**Figure 19:** LINC-NIRVANA science detector unit (Image source: LINC-NIRVANA consortium)

### 3.1 Derotator Requirements

As a subsystem of the MICADO instrument, the derotator has to fulfill requirements internally outlined by the MICADO consortium defining the required image stabilization at the focal plane, but it must also satisfy general requirements defined by ESO for all instruments to be installed on the ELT. The complete list including general, functional, operational, physical, performance, interface and environmental requirements is quite big and therefore described in detail elsewhere (Mueller, 2017). This section summarizes the requirement which most critically drive the design of the derotator, as developed during this dissertation project; see Table 2.

Parameter	Value (PtV)	Value (RMS)
Axial runout	< 0.1 mm	< 0.035 mm
Radial runout	< 0.3 mm	< 0.1 mm
Wobble	< 30 arcsec	< 10 arcsec
Relative angular position accuracy <sup>4</sup>	$\leq 6$ arcsec	$\leq 2$ arcsec
Moving mass		$\leq 7000$ kg
Inner diameter		$> 2500$ mm
Operating temperature		0°C to 15°C
Max. angular velocity		$\leq 3$ deg/s
Derotator mass		$< 1800$ kg (TBC)

**Table 2:** Derotator performance and physical requirements.

According to the science requirements previously mentioned, the position stability of the image at the focal plane of the instrument can be derived. During a typical observation, the worst case for the derotator is defined by taking an image with an exposure time of 120 s, at a  $1.5^\circ$  zenith distance and a wavelength of  $1 \mu\text{m}$ . The motion of the center of the Point Spread Function <sup>5</sup> (PSF) induced by the hardware should be better than 1/16 of the PSF (Pott & Barboza, 2017). The axial runout, radial runout, wobble and the relative angular position accuracy are derived from that requirement. The relative angular position accuracy is defined as follow.

<sup>4</sup> With respect to the preset de-rotation trajectory.

<sup>5</sup> The PSF represents the response of an optical system to a light point source like a star on the sky.

The diffraction limited resolution of the ELT is calculated using the Rayleigh criterion. It corresponds to 6.4 miliarcsec for an observing wavelength of 1  $\mu\text{m}$ , which represent a worst case for the most demanding astrometric observations. The image position stability under the requirement mentioned above (1/16 of the PSF) translates to 0.4 miliarcsec, which should be guarantee over the whole field of view, as shown in Figure 20.

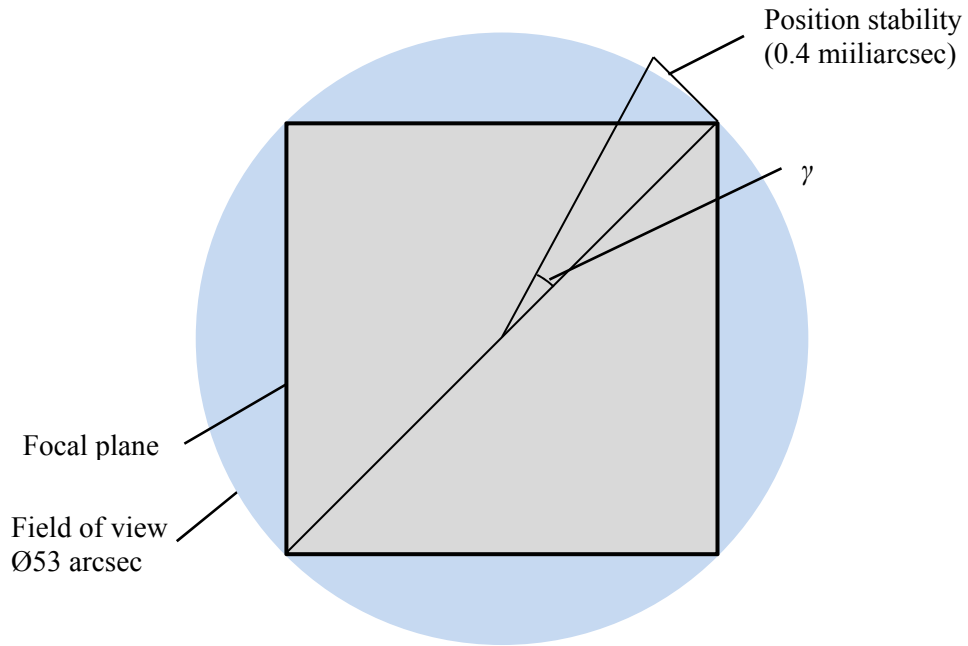


**Figure 20:** MICADO field of view showing the required image position stability at the corner of the focal plane.

The angular position accuracy corresponds to the arctangent of the angle ( $\gamma$ ) show in Figure 20, where a safety buffer factor of 1.5 is used for the diameter of the MICADO field of view. The calculation is given as follow

$$\arctan \gamma = \frac{0.4e - 3}{1.5 \times 26.5} \cong 2.1 \text{ arcsec}. \quad (24)$$

At this point, it becomes clear that the key component of the MICADO derotator is a large high-precision bearing. Such a bearing must have the adequate technology to guarantee the required running accuracy (axial runout, radial runout, wobble). On the other hand, the relative angular position accuracy is a performance parameter delivered by the whole derotator as a system. For that reason, it cannot be guaranteed

by the bearing itself. The relative angular position accuracy is being understood as the difference between the preset input field rotation trajectory (input of the system) and the real measured trajectory of the cryostat (output of the system), during the exposure time while an image is being taken tracking a scientific object. In an ideal perfect system with no disturbance and errors, this difference should be zero.

## 3.2 Bearing Technology Trade-off

As the main component of the whole derotator, the selection of the bearing requires special attention. At this time, there are several commercial bearing technologies that could meet the high precision running accuracy requirements of the MICADO derotator presented in Table 2. Some of those technologies used in high precision applications are: Slewing bearings (with balls, rollers or a combination of them), hydrostatic bearings that use oil or air as the fluid to operate them, and magnetic bearings. In this sense, it is very important to understand the working principle, advantages and disadvantages of these different kinds of bearing technologies. This is the first step before the selection of the bearing to be used in the MICADO derotator.

The main drivers for the selection of the bearing are the accuracy, the maintainability, the simplicity, the weight and the costs; these represent one of the major restrictions in state-of-the-art projects like the MICADO instrument. The trade-off analysis based on wide background information will help to make the right decision about the selection of the bearing, in order to achieve the expected performance with the most effective solution. For simplicity, the trade-off analysis is based on a qualitative comparative study.

### 3.2.1 Slewing Bearings

Slewing bearings like that in Figure 21 basically consists of an inner ring (a) and an outer ring (b) joined together by rolling elements (balls (c) or cylindrical rollers), that are separated by spacers or a cage (d). The rings, one of which usually incorporates a gear (e), are provided with holes (f) to accommodate attachment bolts. Generally,



only the raceways in the rings (g) are hardened and precision-ground to improve the running accuracy of the bearing. Integral seals (h) keep the lubricant in, and contaminants out of the bearing. Slewing bearings are re-lubricated through grease fittings (i) to reduce maintenance and operating costs. Slewing bearings offer a compact and ready to use solution where additional auxiliary equipment is not required. They also require very low maintenance, limited to periodically provide the bearing and the gear with fresh grease (the period of re-lubrication depends of the bearing operating conditions). The main disadvantage is however, the relative high friction typical in this kind of bearing.

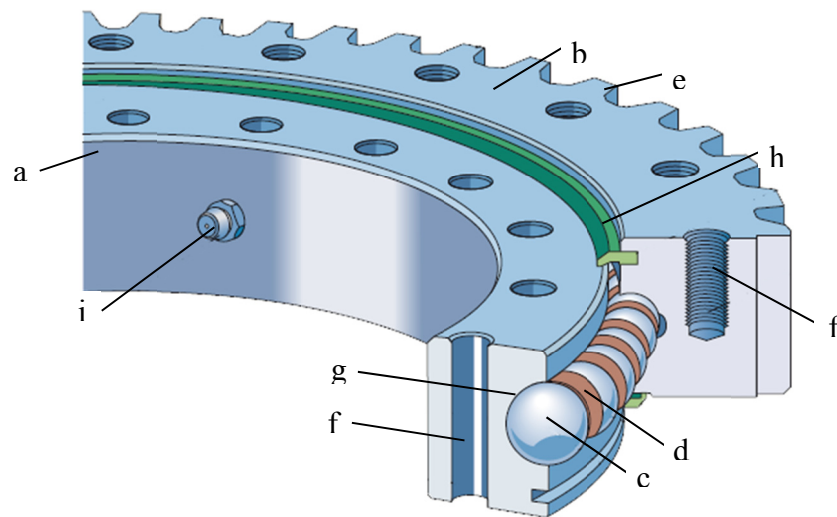


**Figure 21:** Slewing ball bearing (Image source: SKF slewing bearing catalog 2015).

### 3.2.2 Hydrostatic Oil Bearings

Following the hydrostatic principle, oil is injected by a pump system into the pockets formed between the sliding pads and the girth ring conforming the bearing (see Figure 22). The pressure accumulated in the pocket causes the girth ring to lift until a gap is created between both surfaces and the oil can freely escape through the gap to a collecting area. Due to a continuous flow of oil, the surfaces remain separated and the girth ring can slide (nearly friction-less) without restrictions over the pads. No contact takes place between the surfaces.

In order to obtain a bearing using this principle, most applications use two sets of sliding pads to restrict the movement of the girth ring in both axial and radial

directions. The main advantage here is the very low friction values due to the lack of contact between the surfaces. On the other hand, the fact that high precision machining is required in the large contact surfaces of the girth ring and the pads, the risk of oil pollution, and the required auxiliary equipment including an active control system to provide the oil flow are the main disadvantage of this kind of bearing.

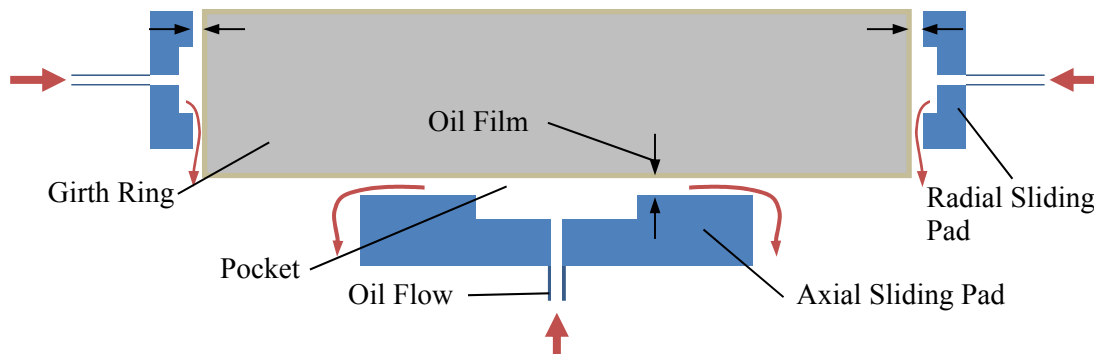


**Figure 22:** Hydrostatic oil bearing.

### 3.2.3 Hydrostatic Air Bearings

Hydrostatic air bearings work with the same hydrostatic principle explained in the previous section, but in this case a gas is used to operate the bearing. Thus, pressurized air is injected through the sliding pads to create the gap between the contact surfaces and suspend the girth ring on a thin air film, providing also a non-contact nearly friction-less running system. The last generation of sliding pads for air bearings utilizes porous materials in the contact surface, which offers a uniform distribution of the air flow through the complete area of the sliding pad. Axial and radial pads are also usually implemented in the same way as for oil bearings.

This kind of bearing is generally used for high speed applications due to its nearly friction-less operating principle. The advantage and disadvantage are similar to the hydrostatic oil bearings, with the additional remark that the risk of oil pollution is removed, but the required clean pressurized air could create local turbulence. In astronomical instrumentation this is an effect not desired close to the camera optics and WFS. Air bearing are also susceptible to dirty operational environments. An illustration of this kind of bearing is presented in Figure 23.

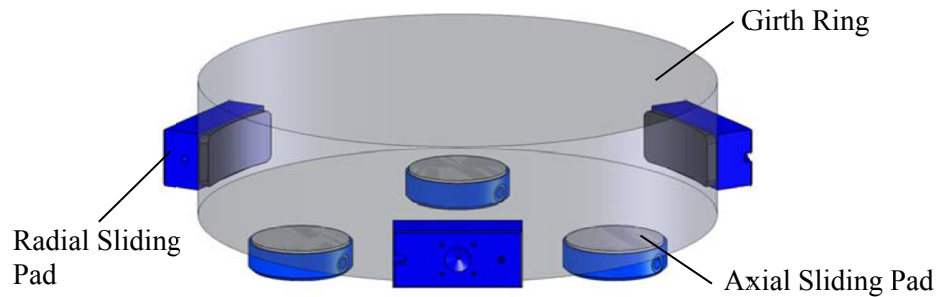


**Figure 23:** Hydrostatic air bearing (Image source: Newway air bearing catalog 2011).

### 3.2.4 Magnetic Bearings

In the case of magnetic bearings, a constant supply of current creates electromagnetic forces that are used to levitate the rotating part of the bearing, providing also a non-contact nearly friction-less running device. A typical magnetic bearing includes: the stator (carrying the electromagnets), the rotor, the electromagnets, position sensor and the active position control system. Two different sets of electromagnets are normally used to limit the movement of the rotor in the radial and axial directions (see Figure 24). The main disadvantages are the requirement of a constant current supply and an active control system to operate the electromagnets monitoring the gap between the rotor and the stator with a position sensor. Electromagnetic pollution could also be a potential problem to the camera itself and to the people in the surrounding area.

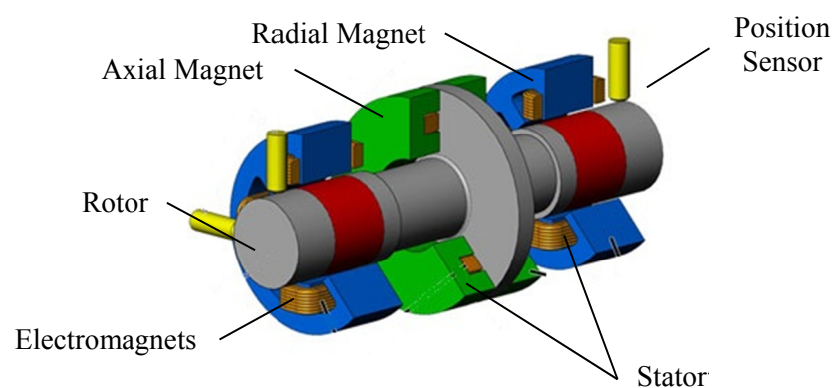


**Figure 24:** Magnetic bearings (Image source: downloaded from <http://www.synchrony.com> on December 2016).

### 3.2.5 Bearing Technology Trade-off Comparative Summary

Hydrostatic oil bearings were finally banned by ESO due to the high risk of oil pollution close to the telescope optics. Therefore, ESO will not provide the required infrastructure for its operations. After checking with possible providers for the remaining alternatives, it can be confirmed that all of them are able to achieve the required running accuracy for the MICADO derotator, which is the main decision criteria for the selection of the bearing. Therefore, those variables (axial/radial runout and wobble) are not considered in the summary presented in Table 3.

Hydrostatic air bearings can achieve an axial/radial runout in the order of 0.010 mm (New Way Air Bearings, 2011) and slewing bearing are able to achieve up to 0.015 mm (Krüsemann, 2015).

Bearing type	Advantage	Disadvantage
Slewing bearings	<ul style="list-style-type: none"> <li>- Low maintenance</li> <li>- No oil pollution</li> <li>- Integrated gearwheel</li> </ul>	<ul style="list-style-type: none"> <li>- Friction</li> <li>- Limited rigidity</li> <li>- Limited positioning accuracy</li> </ul>
Hydrostatic oil bearings	<ul style="list-style-type: none"> <li>- Low Friction</li> <li>- Higher positioning accuracy</li> <li>- High load capacity</li> </ul>	<ul style="list-style-type: none"> <li>- Oil Pollution</li> <li>- Require auxiliary equipment</li> <li>- Maintenance</li> </ul>
Hydrostatic air bearings	<ul style="list-style-type: none"> <li>- Very low Friction</li> <li>- Higher positioning accuracy</li> <li>- No oil pollution</li> </ul>	<ul style="list-style-type: none"> <li>- High precision manufacture</li> <li>- Require auxiliary equipment</li> <li>- Maintenance and local seeing</li> </ul>
Magnetic bearings	<ul style="list-style-type: none"> <li>- Very low Friction</li> <li>- Higher positioning accuracy</li> <li>- No oil or air pollution</li> </ul>	<ul style="list-style-type: none"> <li>- Power consumption</li> <li>- Complex active control</li> <li>- Magnetic pollution</li> </ul>

**Table 3:** Bearing technology trade-off summary.

According to the results of the trade-off, due to the lower cost, less complexity and simpler maintenance, the slewing bearings are taken as the initial choice offering the lightest and more compact solution. However, the relative angular positioning accuracy of the MICADO derotator must be carefully analyzed, to ensure that the required value of 2 arcsec can be achieved with this kind of bearing technology. This is a parameter that depends on the performance delivered by the complete unit as an assembly of all components of the mechanisms; including the motors, the positioning

measurement device and the control system. It has to be said that the friction of slewing bearings is a particular concern, due to the very low rotation velocities and the related stick-slip effects (the friction phenomenon is discussed in detail in chapter 5), which will require also a more sophisticated controller architecture (cascaded position-velocity control, with feed-forward elements, see section 4.3.5).

### **3.3 Existing Technical Solutions**

As the rotation of the field of view is an issue present in all telescopes with alt-azimuth mounts, there are existing technical solutions that can be taken as reference for the design of the MICADO derotator. Some of the most recent developments in astronomical instrumentation are considered here in order to understand how the field stabilization problem has been solved in other telescopes and instruments. This compilation focuses on collecting the main characteristics and performance figures achieved (or expected) by different mechanisms providing rotational motion, which have of course diverse physical requirements in terms of running accuracy, dimensions and moving mass but a common goal of high angular positioning accuracy. All technical solutions described below use the same (or similar) bearing technology selected for the MICADO derotator, i.e. a slewing bearing with rollers or balls. As the running accuracy must be guaranteed by the bearing manufacturer, these parameters are not considered here.

#### **3.3.1 LINC-NIRVANA Ground-Layer Wavefront Sensor**

The derotator of the LINC-NIRVANA ground layer wavefront sensor (GWS) has a diameter of 0.9 m (bearing outer diameter). It uses a single row crossed cylindrical roller bearing disposed in a vertical configuration (see Figure 25), carrying about 300 kg corresponding to the GWS optics and mechanics (not shown in the figure). The drive system consists of a spur gear (integrated to the bearing) with two pinions for backlash suppression, while the pinions are driven by stepper motors through a Harmonic Drive gear transmission. The GWS derotator operates in open-loop and is able to achieve an angular positioning accuracy lower than 20 arcsec rms (Bertram, 2015).

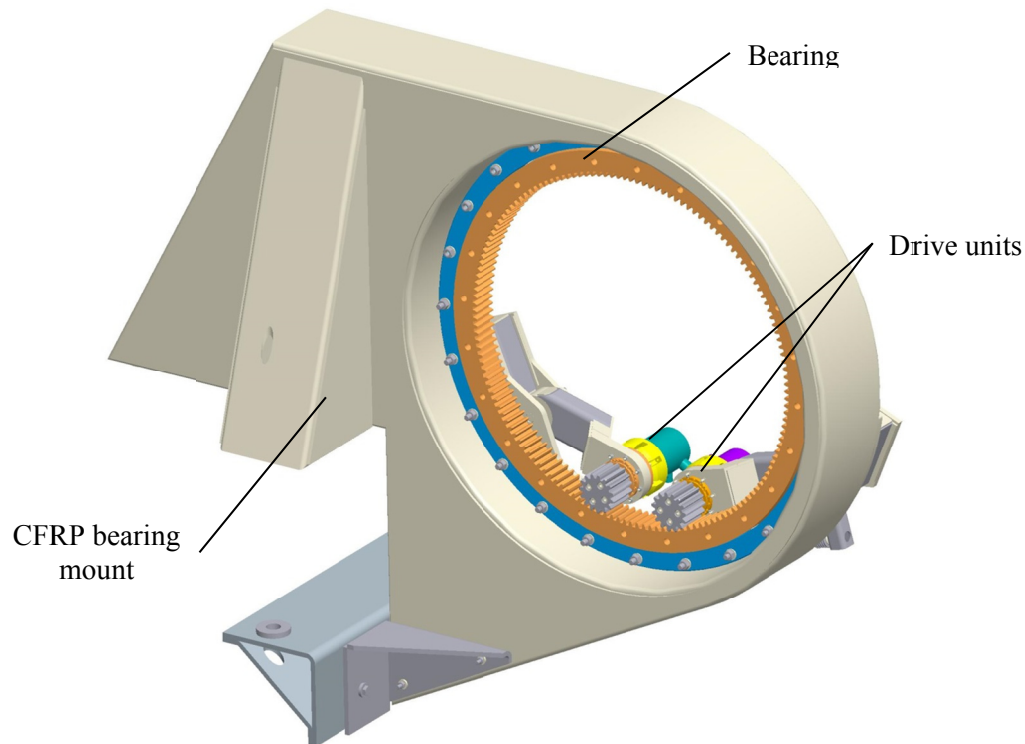


**Figure 25:** LINC-NIRVANA Ground-Layer Wavefront Sensor derotator CAD model with the main components of the mechanism (Image source: LINC-NIRVANA consortium).

### 3.3.2 The Ground-Layer Adaptive Optics Assisted by Laser

The **GR**ound-layer Adaptive optics Assisted by Laser (GRAAL) is an adaptive optics module developed for the HAWK-I instrument on the VLT. Its derotator has a diameter of 1.2 m (bearing outer diameter), using also a single row crossed cylindrical roller bearings disposed in a vertical configuration as shown in Figure 26. It carries about 250 kg of equipment related to the wavefront sensor opto-mechanical components. The drive system consists of a direct drive torque motor integrated in the bearing, i.e. where no gears are used. The main advantage of a direct drive system is that a backlash suppression mechanism is not required. The GRAAL derotator can maintain an angular positioning accuracy lower than 10 arcsec rms, while working in closed-loop (Paufique, et al., 2010).

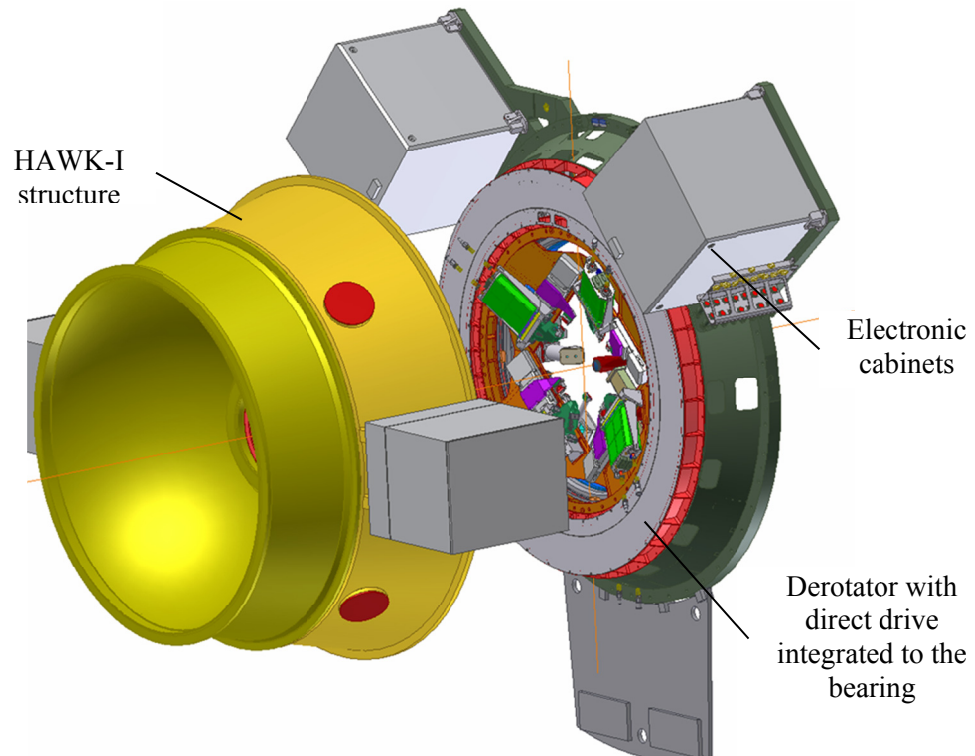


**Figure 26:** GRAAL CAD model showing the main components (Image source: downloaded from [www.eso.org](http://www.eso.org) on December 2017).

### 3.3.3 The ALMA Antenna Azimuth Mechanism

The azimuth mechanism of the US (Mangum, 2015) and the European (Laing, 2015) ALMA antennas share some similarities, like the kind of bearing and the geometry of the support structure but they also have some fundamental differences, like the diameter of the bearing and the drive system. Nevertheless, both designs managed to achieve the high precision pointing requirements of the ALMA project. Absolute pointing  $< 2$  arcsec and offset pointing  $< 0.6$  arcsec rms. Both US and EU antennas use single-row four-point contact ball bearing and three-row roller bearing, but with diameters of  $\sim 2.6$  m and  $\sim 4.3$  m respectively. The US antenna uses a pair of servo motors with gear and pinions as drive units, while the EU antenna uses a gear-less direct drive torque motor integrated to the bearing. See Figure 27.



3.3 Existing Technical Solutions

---



**Figure 27:** US (right) and EU (left) ALMA antennas (Image source: downloaded from [www.eso.org](http://www.eso.org) on December 2017).



### 3.3.4 LBT Gregorian Focus Rotator

The LBT has two different sets of derotators for the direct and bent secondary Gregorian focus stations, with diameters of  $\sim 3.3$  m and  $\sim 1.7$  m respectively. Both mechanisms were designed with a two row angular contact ball bearing and these derotators also use a pair of servo motors with pinions as drive units to provide backlash compensation. The specified (long term) positioning accuracy on-sky error is defined as 0.1 arcsec (Ashby & Meeks, 2007). The bent Gregorian derotators are shown in Figure 28, while the bigger direct focus devices are located below the primary mirrors.

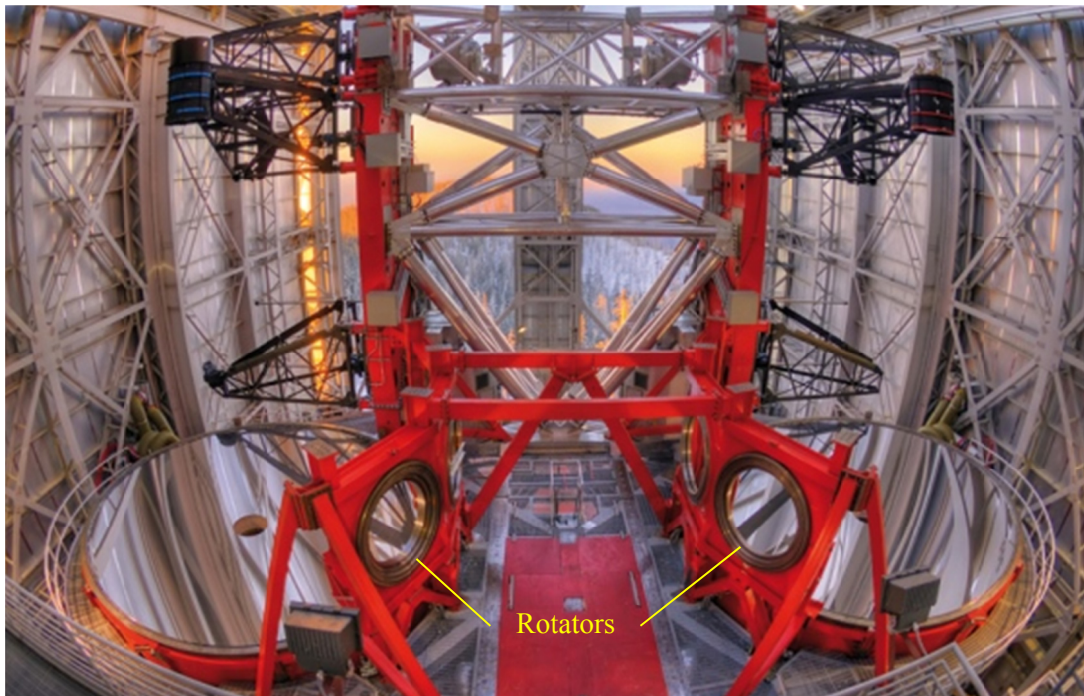


**Figure 28:** LBT bent Gregorian rotators (Image source: downloaded from [www.lbto.org](http://www.lbto.org) on December 2017).

### 3.3.5 Daniel K. Inouye Solar Telescope Coudé Rotator

The Coudé rotator of the Daniel K. Inouye Solar Telescope (DKIST) has a diameter of  $\sim 9$  m (Figure 29). It uses a different kind of bearing technology that consists of linear motion curved guides, carrying several ton of equipment in the Coudé laboratory of the telescope. The drive units consist of a helical gear with two pairs of torque motors for the backlash suppression system, where the motors are arranged in two pairs opposite to each other. The Coudé rotator can achieve an angular

### 3.3 Existing Technical Solutions

---

positioning accuracy lower than 0.1 arcsec (rms) working in a double cascade closed-loop considering velocity and position feedback simultaneously with friction compensation (Kärcher, Weis, Dreyer, Jeffers, & Bonomi, 2012). This is the controller architecture to be implemented on the MICADO derotator as well.

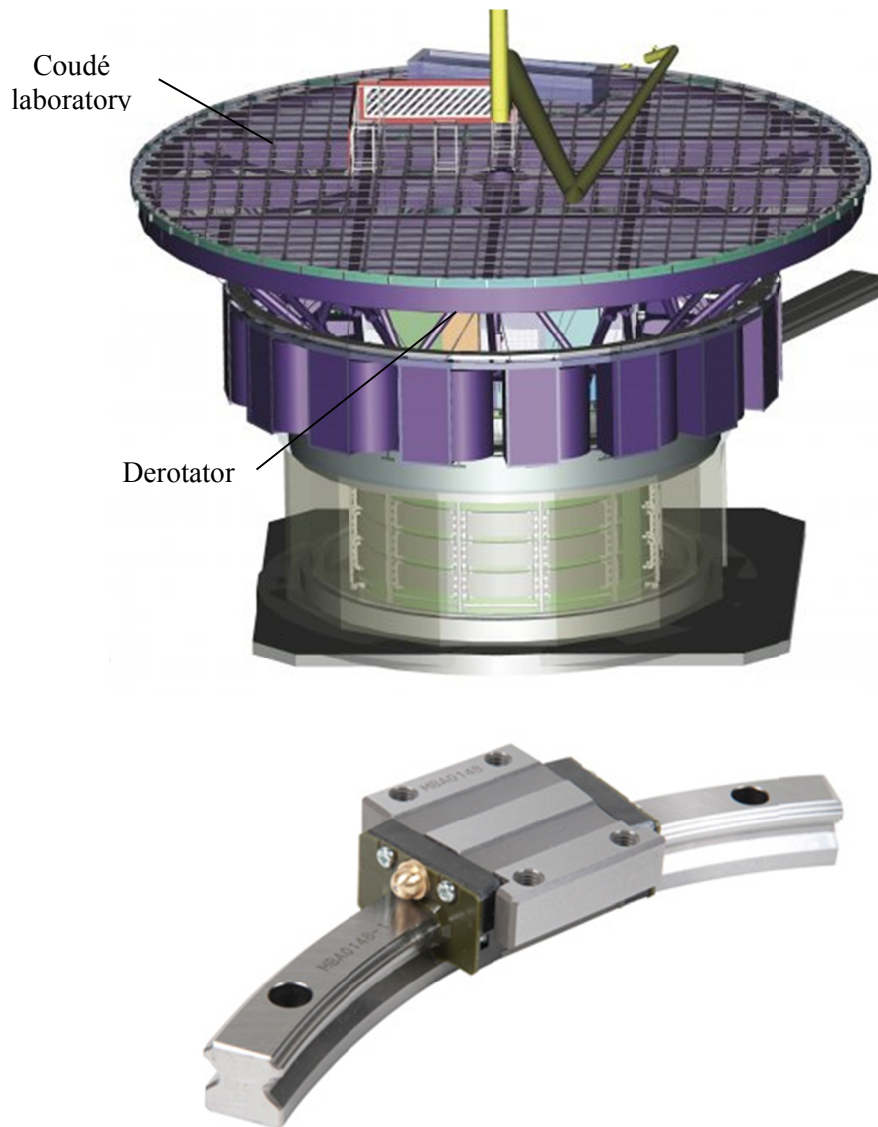


**Figure 29:** DKIST Coudé laboratory derotator CAD model (top, image source: downloaded from <http://dkist.nso.edu/node/903> on December 2017) and Linear motion curved guides (bottom, Image source: downloaded from <http://www.indunorm.eu/produkte/thk-linearfuehrungen/linearfuehrungen-ohne-kugelkette/bogenfuehrung-hcr.html> on December 2017).

### 3.3.6 TMT Infrared Imaging Spectrograph (IRIS) Rotator

The IRIS instrument is currently under development for the TMT, but its current concept represents a good reference where a slewing bearing is also considered in the design to provide smooth rotation for field rotation compensation. TMT / IRIS is the comparable US project to ELT/MICADO. In this case, a cross-roller bearing with a diameter of 1.5 m is implemented into the rotator, while a direct drive torque motor will be used to move the bearing. The mass to be carried by the bearing is about 4500 kg. The instrument support structure is a key component to provide the required stiffness on the bearing Figure 30 and additional thermal compensation rings are included in the design due to the differential expansion between the aluminum stator and the steel bearing (Dunn, et al., 2016).

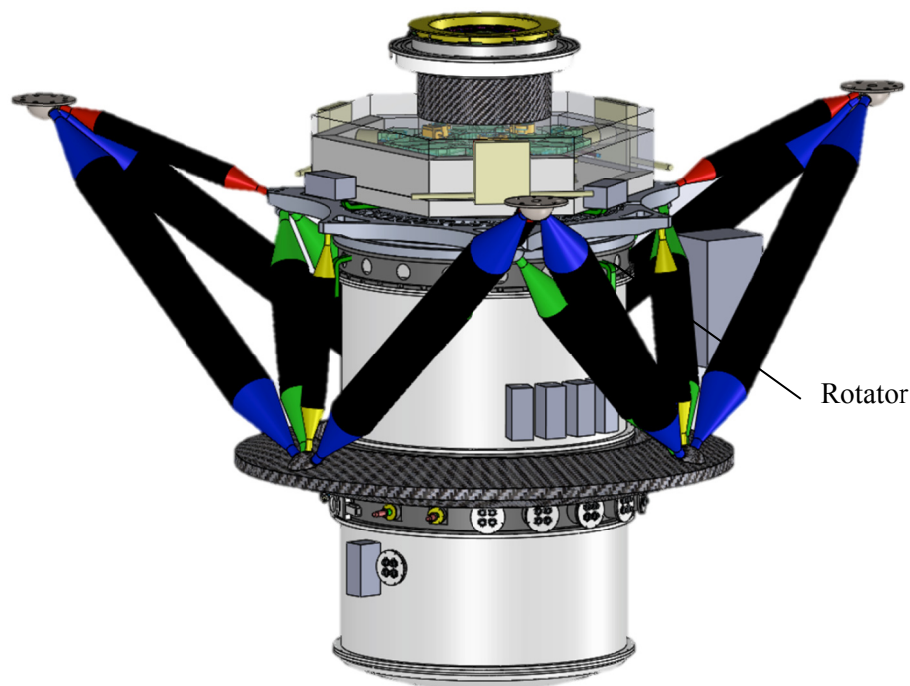


**Figure 30:** TMT IRIS CAD model (downloaded from <http://oirlab.ucsd.edu/img/IRIS.png> on January 2018).

Section 3.3 provides even more confidence about the correct selection of slewing bearing as a suitable bearing technology for the MICADO derotator. To the knowledge of the author, all devices cited have achieved the expected performance. Additionally, the fact that future instruments plan to use that technology as well, ratify the selection of this kind of bearings.

### 3.3 Existing Technical Solutions

---

## 4 The MICADO Derotator

The problem to be solved as the main goal of this research work has been explained in detail and is clearly defined by a complete set of performance and physical requirements in chapters 2 and 3. A tentative bearing technology has been selected as result of the trade-off analysis: slewing bearings, which can use balls or cylindrical rollers as the elements to provide the rotational movement. Furthermore, several existing technical solutions to provide field rotation compensation using that bearing technology (or similar, like the Linear motion curved guides) were briefly discussed as reference.

The proposal to provide field rotation stabilization for the MICADO instrument is developed around a custom designed slewing bearing, which is the result of several design iterations through the partnership with the bearing provider during the course of the project. Other structural components, i.e. the bearing support structure and the thermal compensation rings are adapted to the bearing size and the mechanical interfaces toward the cryostat and the instrument support structure. The definition of these mechanical interfaces was a significant part of this thesis and is based on an intensive discussion with other members of the MICADO consortium at MPE and IAG, responsible for the cryostat and the instrument support structure respectively. The designs for other components like the drive units and the position measurement system, as internal subsystem of the derotator, were developed internally at MPIA as part of the PhD work. The control concept is been designed in collaboration with the Institute for System Dynamics (ISYS) at the University of Stuttgart.

Accordingly, this chapter is dedicated to describing the design process and the current technical proposal of the MICADO derotator, including the calculations and

optimization process that led to the results presented here. Finally, some suggestions to improve the mechanical interfaces from the structural point of view are given as well. The focus in this chapter is the static performance of the suggested design, while the dynamic performance, especially velocity dependent friction effects, is addressed in chapter 5.

### 4.1 The Custom Designed Slewing Bearing

The bearing is the main component of the derotator in order to provide smooth angular movement. Therefore, after the selection of slewing bearings as the possible technology for the MICADO derotator, the attention is shifted to the bearing type itself. There are several possibilities offering high precision running accuracy for this kind of application: single-row four-point contact ball bearing, crossed roller bearing and three-row roller bearing. They are presented in Figure 31.

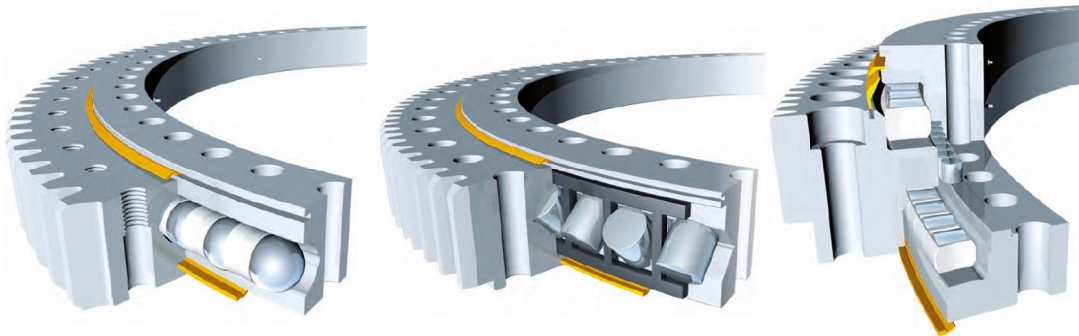


**Figure 31:** Typical Slewing bearings used in antenna applications. Single-row four-point contact ball bearing (left), crossed roller bearing (middle) and three-row roller bearing (right) (Image source: taken from ThyssenKrupp Rothe Erde slewing bearing catalog 2016).

Two bearing providers were contacted with the requirements defined in Table 2 (with exception of the angular positioning accuracy which cannot be guaranteed by the bearing itself, but by the whole derotator including the control system)<sup>6</sup>. Both of them confirmed the feasibility of providing such a slewing bearing, offering however in their technical proposals different types of bearings. The first provider consulted, SKF, offered a crossed roller bearing; while ThyssenKrupp Rothe Erde proposed a

---

<sup>6</sup> The bearing size has considerably increased during phase B, the inner diameter requirement went from >2100 mm to >2500 mm and it will be fixed after the final design review of the MICADO project in 2020.

single-row four-point contact ball bearing. As both types of slewing bearings are able to achieve the required high precision running accuracy, extensive discussions have been carried out to identify which one will offer a better performance in term of friction values and the related stick-slip effects. The friction is the main disadvantage of this bearing technology and a critical aspect for the required angular position accuracy of the MICADO derotator.

The bearing friction is a non-linear effect difficult to estimate, because it can be influenced by many different parameters, such as the rolling friction coefficient, the seals, the load distribution, the out-of-flatness of the bearing support structure, the lubrication used and the variation in the bearing's clearance resulting from installation, only to mention some of them (Krüseemann, 2015). During the design process of the bearing, the starting friction torque  $M_r$  can be roughly estimated assuming a constant value for the friction coefficient with the following expression (in the case of ball bearings)

$$M_r = \frac{\mu}{2}(4.4M_K + F_a D_L + 3.81F_r D_L), \quad (25)$$

where  $M_K$  is the resulting tilting moment,  $F_a$  the axial load and  $F_r$  the radial load acting on the bearing,  $\mu$  is the friction coefficient and  $D_L$  is the bearing raceway diameter (Thyssenkrupp Rothe Erde, 2017). A fluctuation range of  $\pm 20\%$  must be considered when equation (25) is used to estimate the friction torque. A more precise value can only be determined through measurements on the bearing. The proposal of ThyssenKrupp Rothe Erde using a single-row four-point contact ball bearing has been taken as base line for the design of the MICADO derotator. This is the most robust (less sensitive against warping moments) and least expensive of the three types of bearing shown in Figure 31, but has a starting friction torque usually slightly higher. The offered bearing can achieve an axial runout  $< 0.05$  mm, a radial runout  $< 0.1$  mm and a wobble  $< 10$  arcsec. The estimated starting friction torque for the current moving mass of  $< 7000$  kg is 1700 Nm ( $\pm 20\%$ ). The design of the bearing already includes the high precision mechanical interfaces for the installation of the band encoder (this positioning measuring system is explained in detail on section 4.3) and its tensioning cleat. The slot for the metallic tape must be machined to



## 4.1 The Custom Designed Slewing Bearing

---

perfectly match the inner tape diameter, 2801.91 mm in this case. The CAD model of this bearing is presented in Figure 32, while the main dimensions and parameters are given in Table 4.

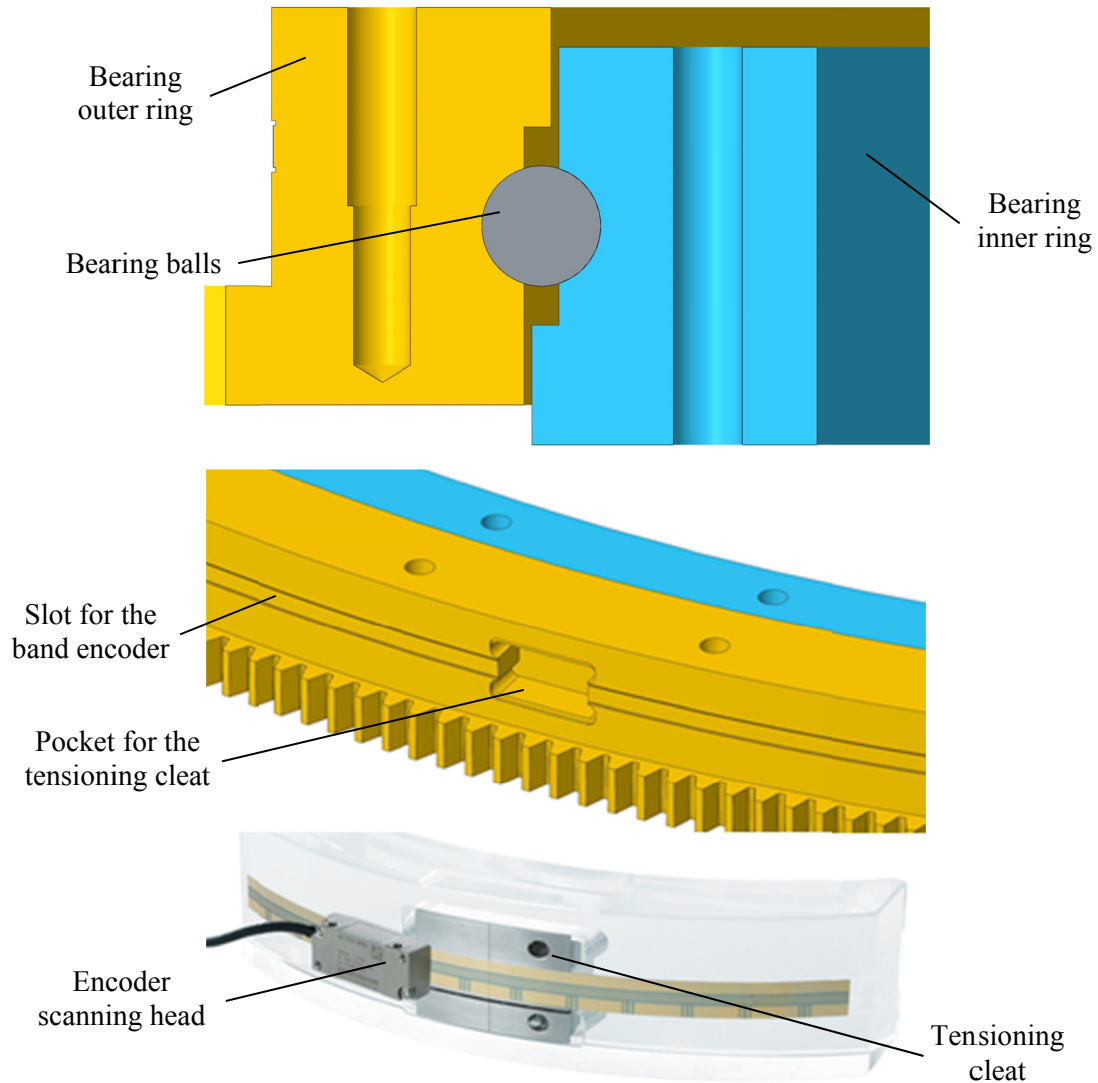


**Figure 32:** Custom designed single-row four-point contact ball bearing for the MICADO derotator (band encoder image source: Heidenhain catalog, 2014).



<b>Parameter</b>	<b>Value</b>
Weight	882 kg
Outer diameter	2826 mm
Inner diameter	2528 mm
Raceway diameter	2667 mm
Overall height	110 mm
Number of external bolt holes	44
External bolt size	M16
External bolt circle diameter	2747 mm
Number of internal bolt holes	44
Internal bolt size	M16
Internal bolt circle diameter	2583 mm
Gear module	6
Number of teeth	471

**Table 4:** Main dimensions and parameters of the custom designed single-row four-point contact ball bearing for the MICADO derotator.

### 4.1.1 Bearing Mechanical Interfaces

Due to their small cross sectional height and width compared to its diameter, slewing bearings have limited stiffness. For that reason, the bearing support structures (upper and lower) should be designed for maximum axial, radial and warping stiffness. The performance of the bearing depends on these stiff and distortion-resistant support rings, which to a large extent will prevent deformations on the bearing under the maximum operating loads. Additionally, the contact surfaces of the support rings must always be as flat as possible, in order to prevent the bearing from becoming deformed when it is bolted down. Thus, careful machining process of the contact surfaces is absolutely essential. Surface grinding is normally used in these large pieces to achieve the required flatness tolerances. The remaining out-of-flatness can be corrected using liquid shimming (Brickwood, 2016), where a special liquid epoxy resins is used to fill the gap between two surfaces in contact. The geometry of the bearing support rings should include a vertical structural reinforcement close to the track diameter in order to allow the load distribution via the raceway system of the bearing, thus minimizing the deformations of the contact surfaces. In addition, using that configuration the warping moment (German term “Krempelmoment”) generated by the translation of the axial load to the raceway diameter, is not directly

## 4.1 The Custom Designed Slewing Bearing

transmitted to the bearing (Hake & Meskouris, 2007). The optimal geometry for the bearing support structure is shown in Figure 33.

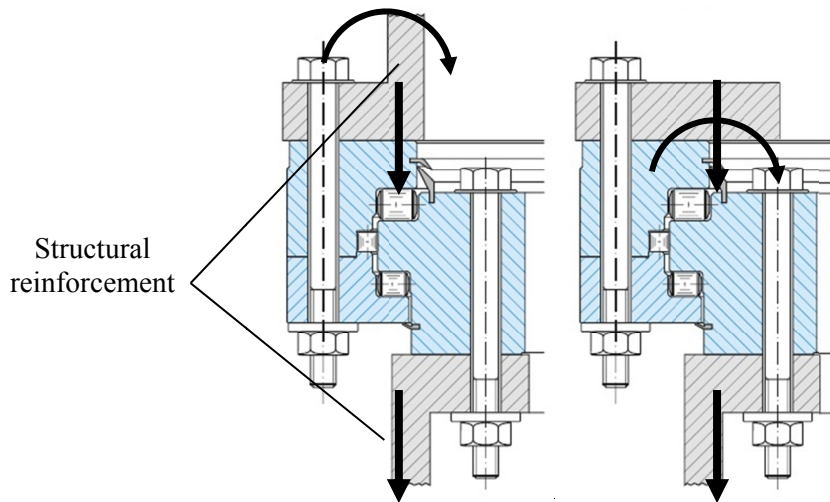


**Figure 33:** Optimal bearing support structure geometry (left) and non-optimal option transferring the warping moment to the bearing (right). The vertical arrow represents the transmission of the axial load acting on the bearing, while the curved arrow illustrates the effect of the warping moment due to the translation of the axial load. A three-row roller bearing is used as example in this case (Image source: ThyssenKrupp Rothe Erde slewing bearing catalog 2016).

The requirements for the stiffness and flatness of the support structures are derived from the axial/radial runout of the bearing. Consequently, the stiffness of the support structures must be such that the deformations on the bearing, including thermal gradient and the tension generated by the vacuum inside the cryostat do not exceed the values shown in Table 5 under maximum operating load. This value represents a conservative approach corresponding to the axial runout of the bearing described on page 55.

Parameter	Value
Maximal differential axial deformation	0.050 mm
Maximal differential radial deformation	0.050 mm
Maximum torsional deformation	110 arcsec

**Table 5:** Maximum allowed deformation of the bearing.

A flat mounting surface free of grease, oil and any other contaminant is essential for the upper and lower rings of the bearing to seat firmly, and the bearing must be completely supported by the connecting structure. The contact surface must be

measured before the installation of the bearing and the flatness deviation must be lower than the axial runout of the bearing ( $< 0.030$  mm). To avoid the existence of peaks in small sectors, any flatness deviation in the range of  $0^\circ - 180^\circ$  may only rise evenly once and fall again.

## 4.2 Bearing Support Structure Optimization

Shortly after the beginning of the phase B in 2016, a 3-point mechanical interface between the derotator and the instrument support structure was defined as baseline for the design of the MICADO instrument (see Figure 34). The change of the original 6-point mechanical interface<sup>7</sup> (see Figure 35) to the 3-points option was done in order to increase the instrument's eigenfrequency using a hexapod-like instrument support structure (ideally 6 struts joined at their ends). This change has a huge impact on the structural behavior of the derotator support structure. Therefore, developing the conceptual design of this part supported by an optimization process was essential.

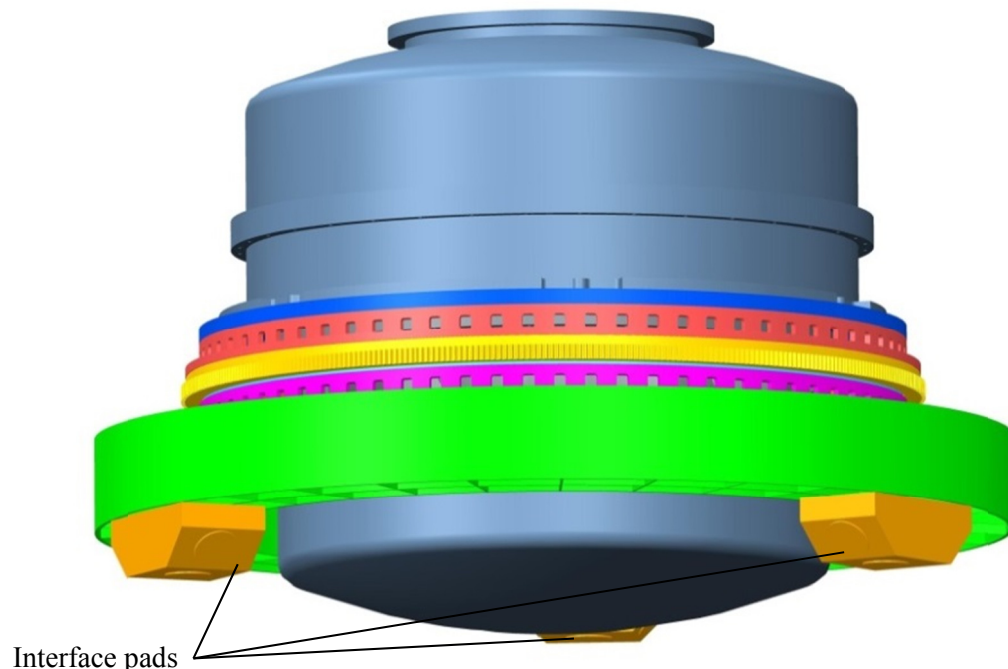


**Figure 34:** 3-point mechanical interface introduced after the beginning of phase B.

<sup>7</sup> The 6-point interface is included in the optimization results as reference.

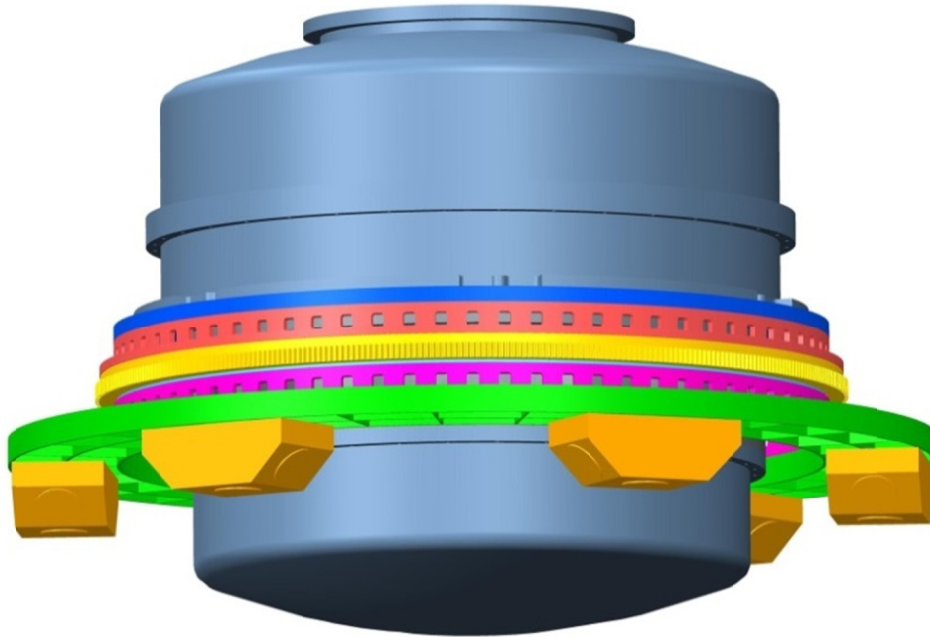


**Figure 35:** Original 6-point mechanical interface with the instrument support structure.

There are two possible strategies that can be followed to develop the design of the derotator support structure: (i) the conservative approach (easier to model) where the stiffness of the bearing/cryostat is not considered and, (ii) a more realistic approach (complex to model) where the stiffness of the bearing/cryostat is considered.

The derotator team at MPIA decided to follow the conservative approach to develop the conceptual design of the derotator support structure in this early phase of the project. This means that only the structural elements below the bearing are considered in the FEA for the optimization process (the bearing support structure and lower thermal compensation support ring, described in sections 4.3.1 and 4.3.2 respectively). The more realistic approach will be later implemented for the static analysis of the whole derotator including the bearing/cryostat and the instrument support structure. The reasons to take such a decision are as follows:

- The cryostat should not accommodate any stresses to achieve the required stiffness of the bearing support structure interface once the bolts are tightened. It would be difficult to determine the varying cryostat deformation and the resulting optical errors.

- The bearing support structure shall provide enough stiffness to guarantee a flat contact surface once the bearing is installed without bolt pre-load. This will guarantee for a most reliable derotator system performance.
- A complex FEM of the bearing including frictional contact and bolt pre-load is required to follow the most realistic approach.
- An over designed bearing support structure can be easily re-designed to achieved a thinner, lighter and less rigid part if required.

Using the three contact points equally distributed over a constant previously agreed diameter representing the instrument support structure, 18 different concepts of the derotator support structure were developed. These models are presented in Figure 36, and the results of FEA corresponding to the total deformation are showed in Figure 37. The load case for Figure 37 is described below.

4.2 Bearing Support Structure Optimization

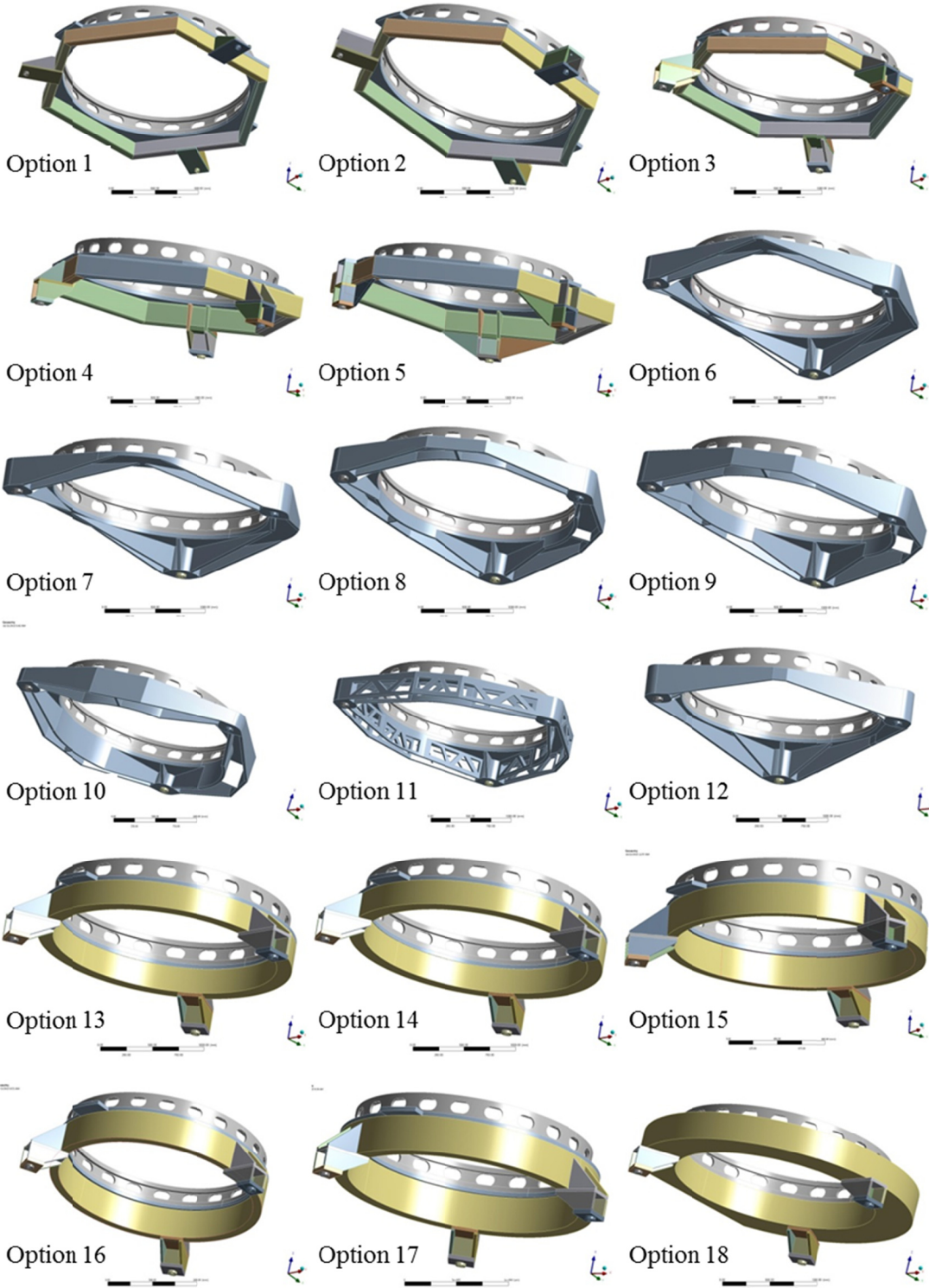
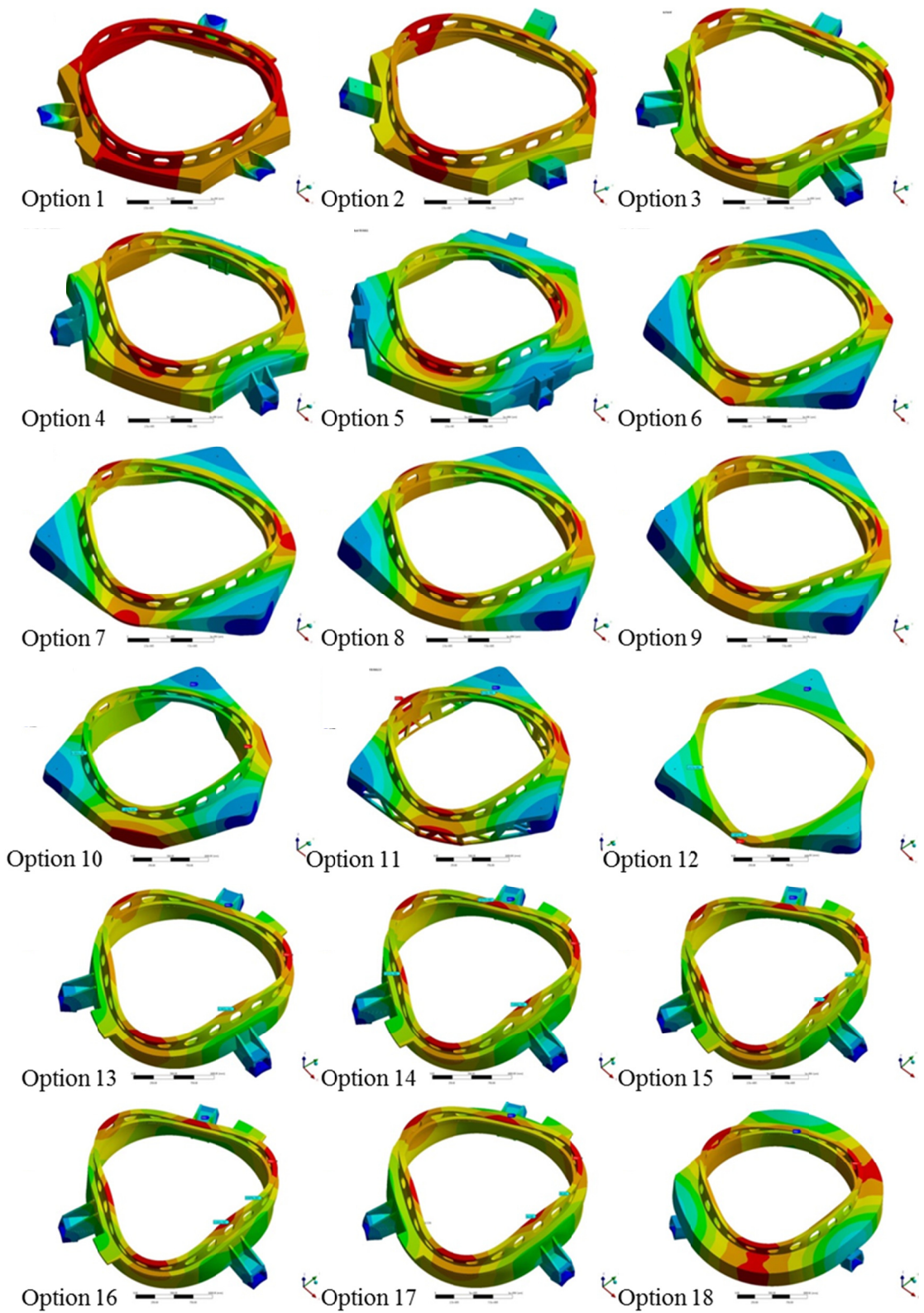


Figure 36: Options developed for the conceptual design of the bearing support structure.





**Figure 37:** FEA showing the total deformation of the options developed for the conceptual design of the bearing support structure.

## 4.2 Bearing Support Structure Optimization

---

All concepts were analyzed using the same material (structural steel), mesh quality and boundary conditions. An equally distributed remote load of 35 kN (at that point 3000 kg was the expected mass of the cryostat) located in the center of the ring and the three support pads as fixed contact areas were assumed. The remote force feature instead of the standard one, allows the transmission of the warping moment. Bonded contact<sup>8</sup> is used to simulate the connection between the bearing support structure and the structural ring (ANSYS, 2018). These boundary conditions are shown in Figure 38, where only option 9 is presented as an example. The total deformation is useful to quickly have a general idea about the performance of each concept, but in order to accurately select the best option a more detailed comparison method had to be implemented through the optimization process.

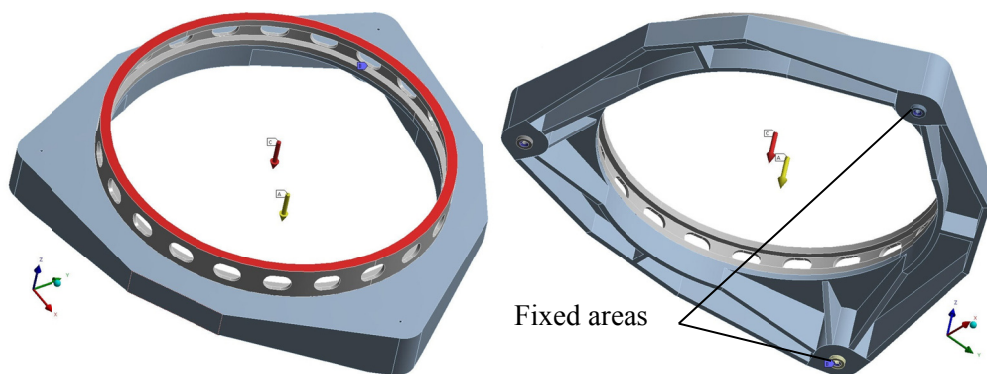


**Figure 38:** Boundary conditions applied to the model for the FEA.

The guidelines to properly perform an optimization process described by Wagner & Mlejnek (2015) were followed here. Accordingly, the most relevant elements of the optimization process can be listed in four steps:

1. Definition of the optimization criterion, which is related to the design goal.
2. Designation of the design variable, representing what is changeable on the design through the optimization process.
3. Definition of the restrictions and limitations that should be considered in the design.
4. Identification of the design model, meaning how the design can be described using a mathematical expression to be optimized.

---

<sup>8</sup> In a bonded contact no sliding or separation between faces or edges is allowed.



Applying these steps to the optimization process of the derotator support structure, the resulting aspects can be identified: low weight and high stiffness as optimization criterion, the geometry of the derotator support structure as design variable and the mass limit along with the maximal allowed deformation as the restriction for the design. At the moment of the optimization process, the mass limit for the derotator subsystem had not been defined. As the design model, two different optimization functions were defined for the axial and radial deformations respectively. The torsional deformation due to the warping moment was not considered for the optimization process, as it should represent a small contribution to the deformation.

The optimization functions are defined by the equations (26) and (27)

$$I_A = Mass * (Max. Axial Def. - Min. Axial Def.), \quad (26)$$

$$I_R = Mass * \sqrt{Max. X Axis Def.^2 + Max. Y Axis Def.^2}, \quad (27)$$

where the mass is expressed in kg and the deformations in  $\mu\text{m}$ . The goal of the optimization process is to find the minimum of those functions.

#### 4.2.1 Results of the Optimization Function $I_A$

The locations where the maximal and minimal axial deformation is measured to calculate  $I_A$  are show on Figure 39. The results of the optimization process are presented numerically in Table 6 and graphically in Figure 40.

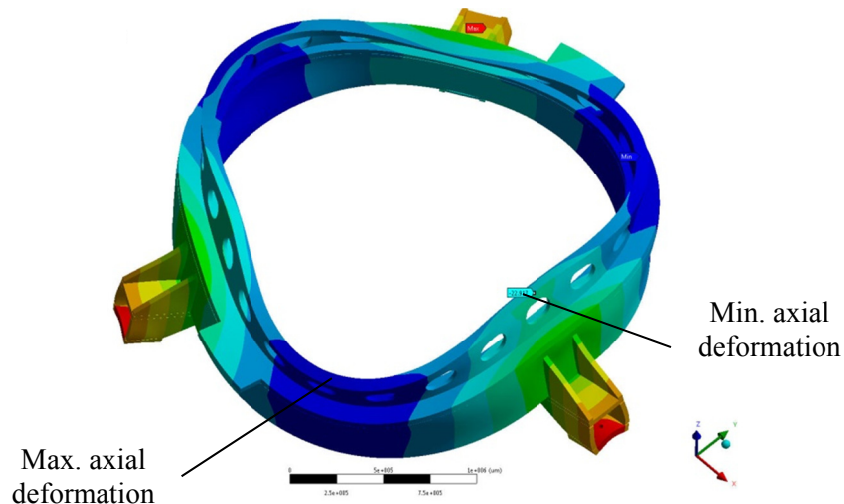


**Figure 39:** Location of the maximal and minimal deformation considered for  $I_A$ .

## 4.2 Bearing Support Structure Optimization

Concept	Mass (Kg)	Max. Axial Def. ( $\mu\text{m}$ )	Min. Axial Def. ( $\mu\text{m}$ )	Difference ( $\mu\text{m}$ )	$I_A$
Option 1	1174.5	300.46	269.72	30.74	36.10
Option 2	1324.7	175.97	135.13	40.84	54.10
Option 3	1527.7	71.09	44.54	26.55	40.56
Option 4	1933.9	42.71	21.91	20.80	40.23
Option 5	2363.9	46.55	16.31	30.24	71.48
Option 6	2393.8	46.24	20.68	25.56	61.19
Option 7	2333.1	46.08	21.10	24.98	58.28
Option 8	2517.0	48.34	22.37	25.97	65.37
Option 9	2855.3	35.57	18.09	17.48	49.91
Option 10	2841	65.19	30.78	34.41	97.77
Option 11	2447	48.35	23.63	24.72	60.50
Option 12	2198	45.79	27.96	17.83	39.18
Option 13	1636	53.34	30.17	23.17	37.90
Option 14	1591	55.35	33.80	21.55	34.29
Option 15	1794	51.45	31.62	19.83	35.57
Option 16	1894	45.76	29.32	16.44	31.13
Option 17	2057	35.24	22.92	12.32	25.34
Option 18	2013	31.55	18.32	13.23	26.63
6 Point interface <sup>9</sup>	1976	11.5	5.1	6.40	12.65

**Table 6:** Numerical results of the optimization function  $I_A$ .

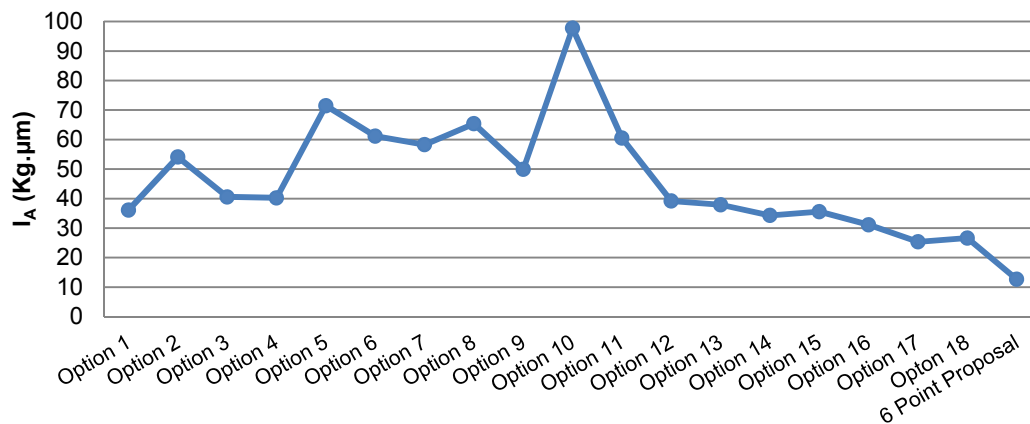


**Figure 40:** Performance of the proposed concepts according to  $I_A$ .

<sup>9</sup> This concept is not shown in Figure 33, but it consists of the same geometry used for the option 18 with three more supporting pads.

## 4.2.2 Results of the Optimization Function $I_R$

The points where the maximal X and Y axis deformations are measured to calculate  $I_R$  are shown on Figure 41, while the results of the optimization process are presented numerically in Table 7 and graphically in Figure 42.

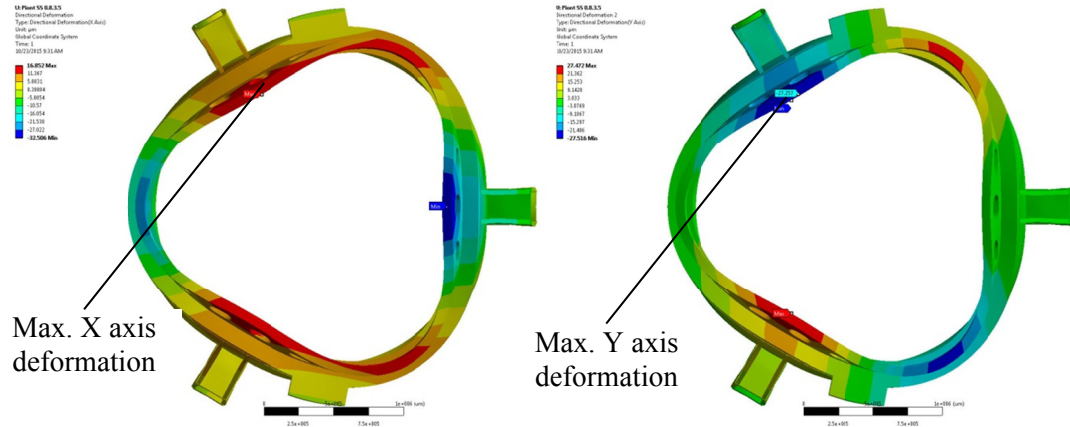


**Figure 41:** Location of the maximal X axis and maximal Y axis deformations considered for the optimization function  $I_R$ .

Concept	Mass (Kg)	Max. Def. X axis ( $\mu\text{m}$ )	Max. Def. Y axis ( $\mu\text{m}$ )	Radial Def. ( $\mu\text{m}$ )	$I_R$
Option 1	1174.5	61.95	106.44	123.16	144.65
Option 2	1324.7	57.33	98.53	114.00	151.01
Option 3	1527.7	34.45	57.92	67.39	102.95
Option 4	1933.9	13.42	22.98	26.61	51.46
Option 5	2363.9	15.16	17.62	23.24	54.95
Option 6	2393.8	17.69	27.24	32.48	77.75
Option 7	2333.1	17.37	27.27	32.33	75.43
Option 8	2517.0	15.89	24.77	29.43	74.07
Option 9	2855.3	12.32	19.77	23.29	66.51
Option 10	2841	20.05	32.03	37.79	107.37
Option 11	2447	17.77	29.11	34.11	83.47
Option 12	2198	21.63	37.60	43.38	95.33
Option 13	1636	26.20	42.21	49.68	81.27
Option 14	1591	33.00	53.40	62.77	99.88
Option 15	1794	30.31	49.10	57.70	103.51
Option 16	1894	28.22	45.36	53.42	101.16
Option 17	2057	16.85	27.26	32.05	65.91
<b>Option 18</b>	<b>2013</b>	<b>10.48</b>	<b>17.13</b>	<b>20.08</b>	<b>40.42</b>
<b>6 Point Proposal</b>	<b>1976</b>	<b>4.04</b>	<b>4.55</b>	<b>6.08</b>	<b>12.02</b>

**Table 7:** Numerical results of the optimization function  $I_R$ .

## 4.2 Bearing Support Structure Optimization

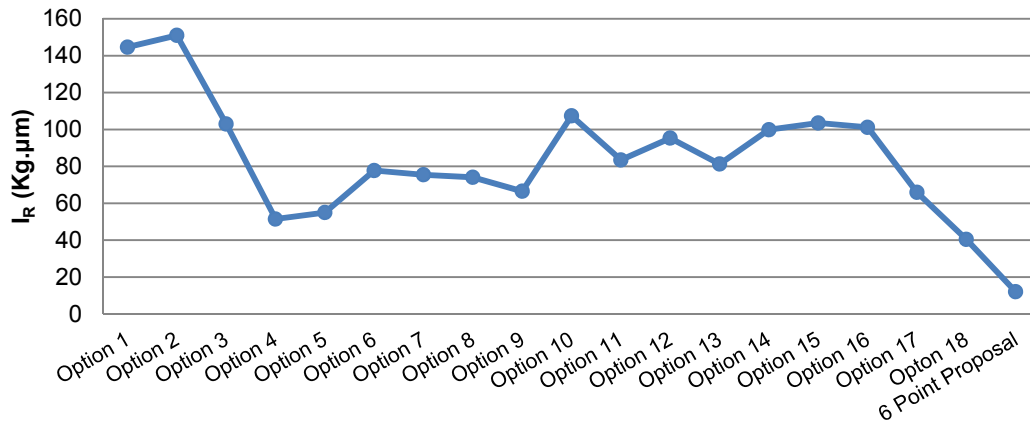


**Figure 42:** Performance of the proposed concepts according to  $I_R$ .

### 4.2.3 Discussion of the Optimization Process Results

According to the results of the optimization process defined by the functions  $I_A$  and  $I_R$ , only the options 17 and 18 were able to achieve the required 15 µm of maximal axial deformation, but these concepts are not able to meet the requirement of the maximal radial deformation. The best performance in the radial direction is achieved by option 18, but with radial deformation close to 20 µm. As bonded contact is used for the FEA, those deformation values are expected to increase once frictional contact is implemented. The option 18 consists of a ring with rectangular cross section and internal ribs for structural reinforcement.

The analysis shows that a 3-points mechanical interface between the derotator and the instrument support structure is not the proper solution from the structural point of view. Increasing the numbers of supporting points has a huge impact in the structural performance of the bearing support structure. This fact can be clearly seen in the results of both optimization functions with the option to use a 6-point mechanical interface.

The original 6-point mechanical interface is able to achieve a better performance within the requirements for both axial and radial directions. Based on these results, MPIA requested to have an interface towards the instrument support structure with a minimum of 6 supporting points. However, the recommendation was not

implemented by the MICADO consortium due to the reduction in the instrument eigenfrequency. This issue is discussed in detail in section 4.6.

### 4.3 Derotator design proposal

The preliminary design of the derotator is presented in Figure 43. It consists of the custom designed single-row four-point contact ball bearing previously described, the thermal compensations rings (upper and lower, which are going to be built with the same type of steel used in the bearing, see section 4.3.2) and the bearing support structure. Additionally, it has the drive system with at least two drive units and the positioning measurement system composed of a band encoder with at least two scanning heads. The control and electronic system to operate the derotator in closed-loop is also a fundamental part of the current proposal.

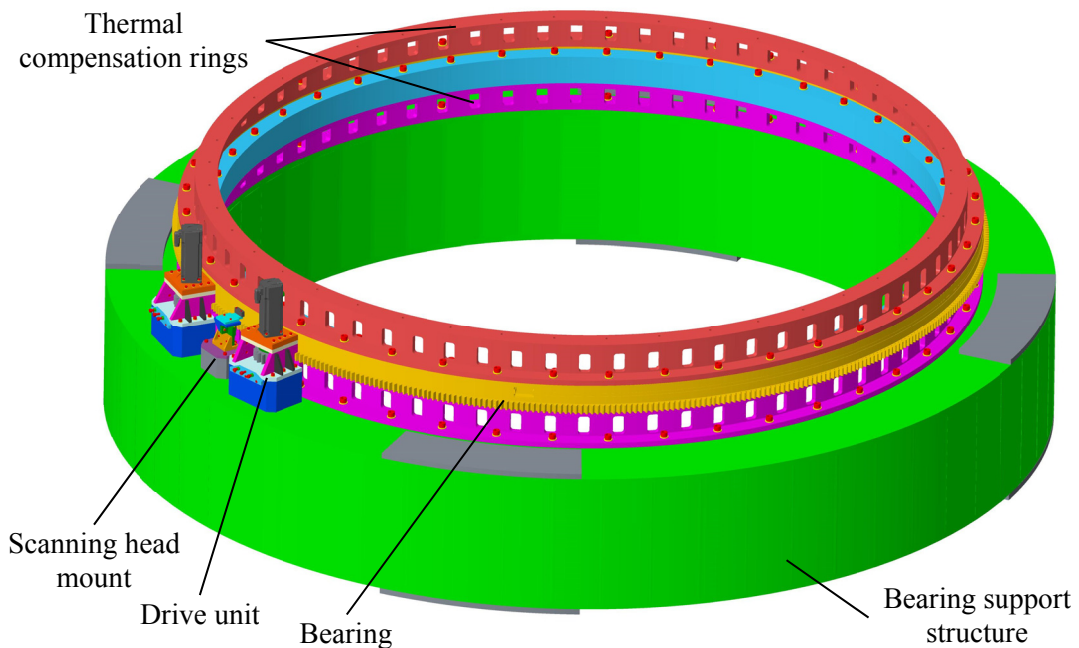


**Figure 43:** CAD model of the MICADO derotator preliminary design.

The derotator has mechanical interfaces with three MICADO subsystems, i.e. the cryostat, the instrument support structure and the relay optics support structure (see section 1.2.2). The interface towards the cryostat is defined by the contact surface between the cryostat central flange and the upper thermal compensation ring. It is a bolted connection where the alignment system between the cryostat optical axis and

the derotator axis of rotation will be implemented<sup>10</sup> (the alignment concept is described in 6.1.2). The interface with the instrument support structure has been changed and the current base line is defined by 4 supporting points with an octopod-like instrument support structure, which is better than the previous 3-points interface but not the optimal solution from the structural point of view. Lastly, the interface to the relay optics support structure considers also 4 supporting points located exactly on top of the instrument support structure interface pads. Both are bolted joints as well, where the interface pads are bolted down to the bearing support structure. The derotator mechanical interfaces are shown in Figure 44.

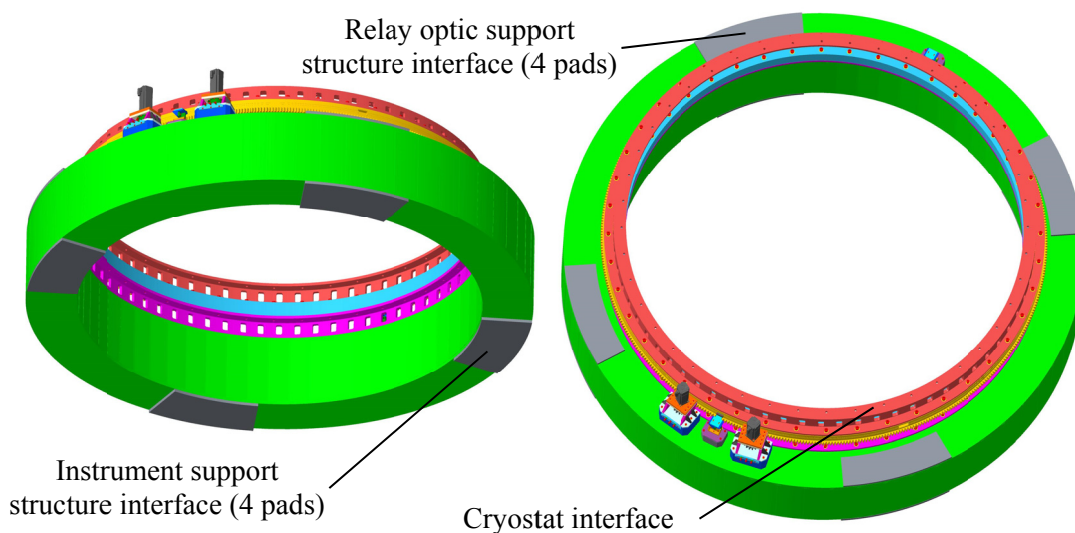


**Figure 44:** Derotator mechanical interfaces.

### 4.3.1 Bearing Support Structure

Following the results of the optimization process, the bearing support structure was developed following the geometry of concept 18 which offered the best performance. Due to the restriction of the derotator mass requirement (1800 kg TBC), it became clear that using steel for such a large part was not an option. As the bearing support structure would be already heavier than the mass limit. For that reason, carbon fiber reinforced plastic (CFRP) is considered as first choice to manufacture the bearing

---

<sup>10</sup> The alignment system considers only adjustment for the lateral shifting between the axes. No tip-tilt correction is provided in this interface.

support structure. This material has been successfully implemented to build large structures for applications related to astronomical instrumentation. Several alternatives can be implemented to build such CFRP components, i.e. (i) laminating CFRP plates with other materials like aluminum in the form of honeycomb structure plates or, (ii) using pure CFRP to build the whole structure. For instance the LINC-NIRVANA optical bench was built following the first approach (Rohloff, et al., 2006), while the support structure for the slewing bearing of the LINC-NIRVANA GWS was built using the second alternative (Ingenieurbüro SCHLOSSMACHER, 2006). Another example where pure CFRP was used is the PFS SUMIRE Bench (CarbonVision, 2014). As the second option offers a better specific stiffness, that method will be implemented to build the bearing support structure of the MICADO derotator.

The manufacturing proposal of building the bearing support structure is presented in Figure 45 (CarbonVision, 2017). Preliminary dimensions have been defined according to the bearing size with an outer diameter of 3300 mm, an inner diameter of 2647 mm and a tentative height of 500 mm. The height of the structure, the thickness of the plates and the type of fibers are the parameter that can be adjusted to increase or decrease the stiffness of this part. It consist of two plates (upper and lower) build as single pieces with a thickness of 20.64 mm, the outer and inner cylindrical shells using 60 10.32-mm-thick plates and 60 ribs with a thickness of 10.32 mm conforming the internal structure. All parts are joined using a self-assembly system<sup>11</sup> and then glued together with a special resin. Through the manufacturing process, metallic inserts can be installed to bolt down all other components and to join the derotator with the instrument support structure interface pads (see Figure 46). These details will be included during the final design phase of the project.

---

<sup>11</sup> The small plates forming the cylindrical shell and the ribs are manufactured with inserts that are introduced into slots in the upper and lower large plates.



### 4.3 Derotator design proposal

---

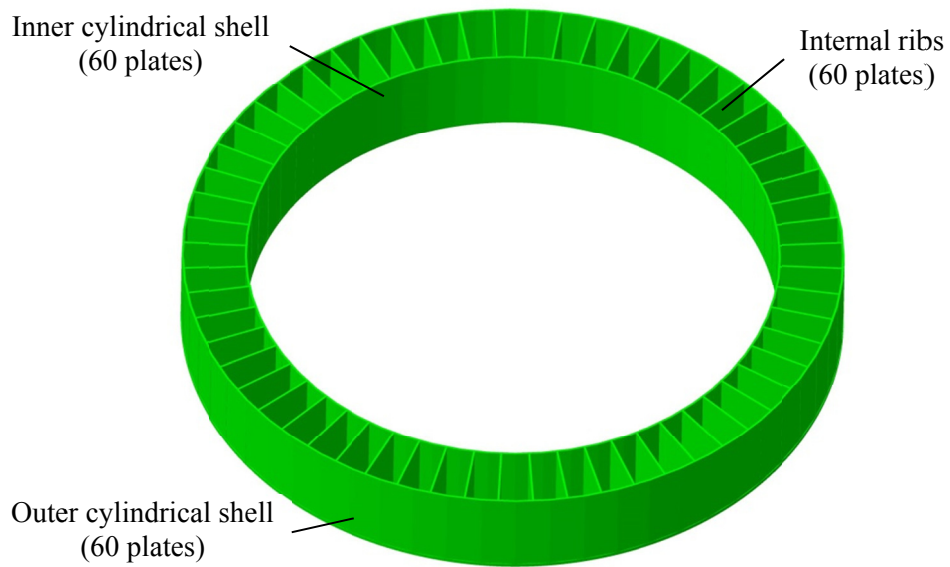


**Figure 45:** Manufacturing proposal to build the bearing support structure (The upper plate is not shown in the figure).

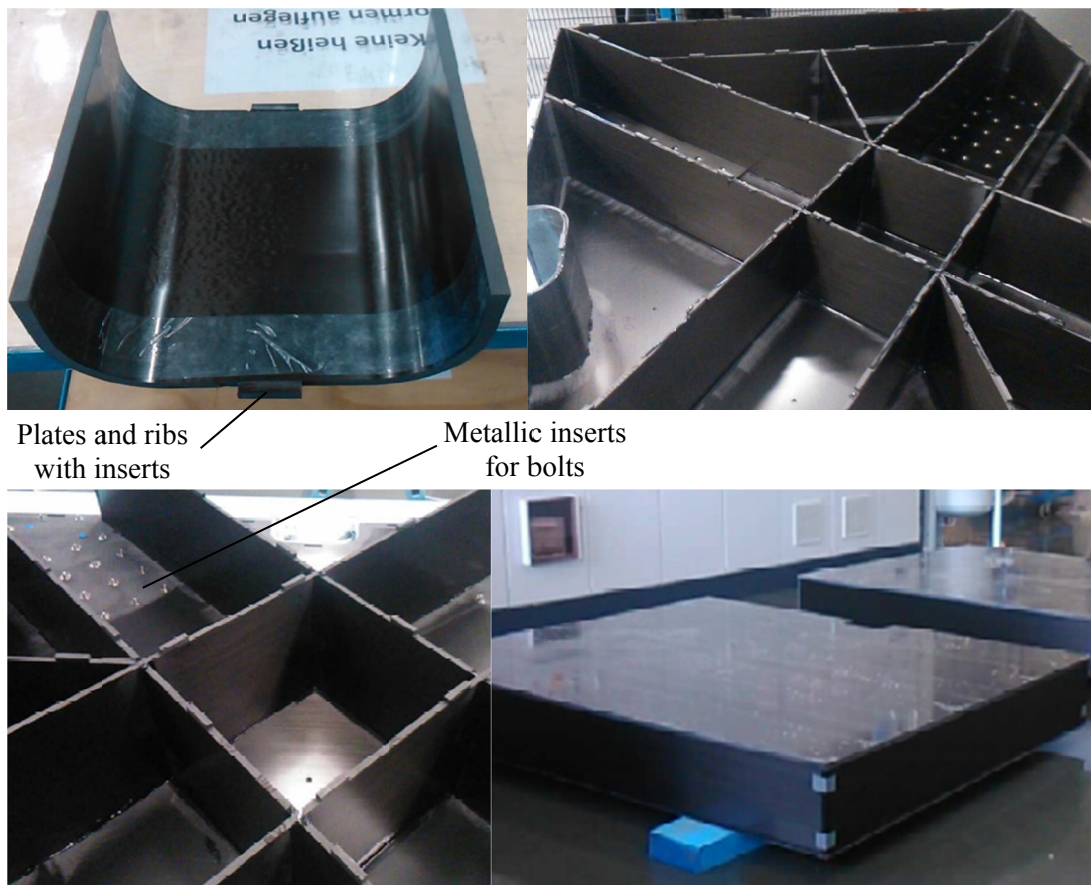


**Figure 46:** Manufacturing concept using a self-assembly system and metallic inserts for the bolts (Image source: CarbonVision).



The CFRP is by definition an anisotropic material, but if the correct lamination sequence is used, a material with quasi-isotropic properties can be obtained (Beckwith, 2012). The final FEA of the bearing support structure will be performed using a detailed FEM, where the lamination sequences and the strength of the fibers are considered in the calculations. However, as the implementation of such a FEM requires high levels of effort, for the design phase of the derotator an equivalent material with quasi-isotropic properties will be used for the FEA. This approach corresponds to conservative case, because the estimated deformations are about twice as large in absolute terms, as the ones obtained with the detailed FEM.

In order to quantify the expected deformations while using CFRP for the bearing support structure, a first detailed FEM was performed for comparison by that company (CarbonVision) which could eventually manufacture this part. The boundary conditions defined for that FEA are show in Figure 47.

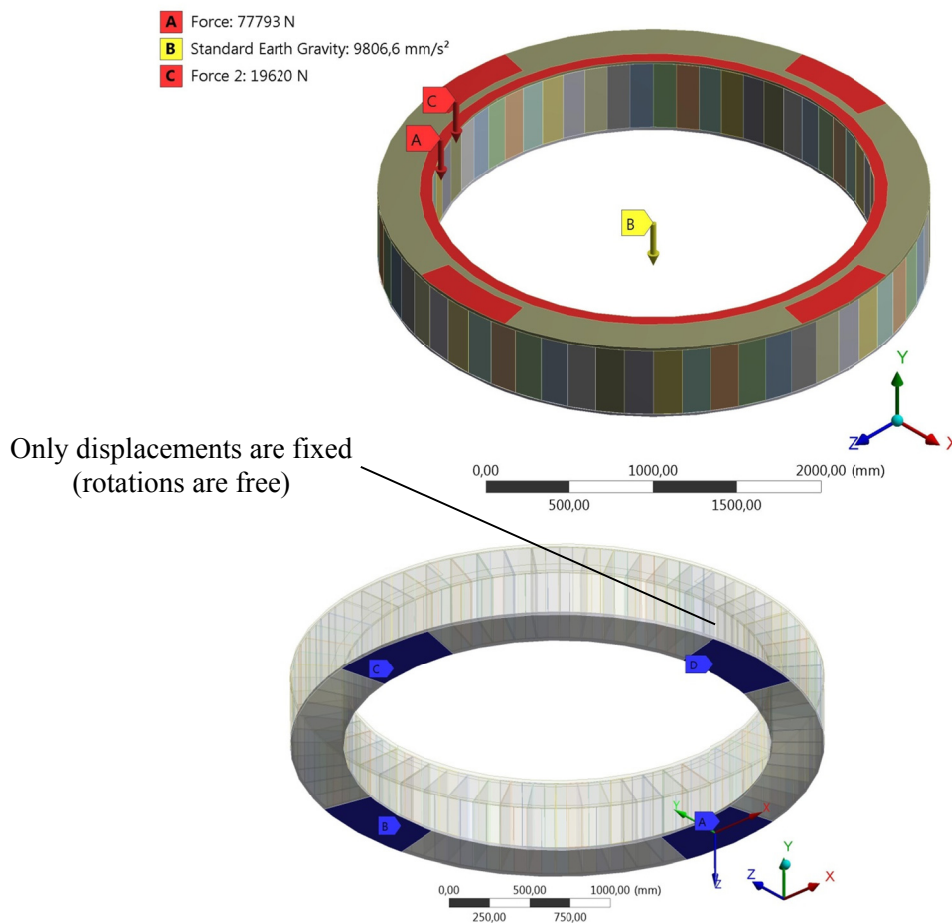


**Figure 47:** Boundary conditions applied to the bearing support structure FEM.

### 4.3 Derotator design proposal

---

Force A corresponds to the mass of all components to be installed on top of the bearing support structure (about 7850 kg TBC) and is applied on a ring defined by the contact surfaces of the lower thermal compensation ring. Force B represents the mass of the relay optic support structure (about 2000 kg TBC) and acts on the corresponding four upper interface pads. Finally, the connection with the instrument support structure is simulated with spherical joints, where the displacements of the interface pads are fixed but the rotations are kept free. The results of the first detailed FEA are presented in Table 8. Different types of fibers were considered in this structural calculation, High Tenacity and Strength (HTS) and a combination of HST with High Modulus fibers (HM). The estimated mass of the bearing support structure made of CFRP is about 500 kg (CarbonVision, 2017).

Parameter	HTS Fibers	HTS+HM Fibers
Max. axial deformation (Y axis)	-0.051 mm	-0.018 mm
Min. axial deformation (Y axis)	0.011 mm	0.004 mm
Max. radial deformation (X axis)	0.020 mm	0.009 mm
Min. radial deformation (X axis)	-0.022 mm	-0.010 mm

**Table 8:** Results of the bearing support structure FEA using the detailed FEM considering the lamination sequence and the strength of different types of fibers. The deformation in the X and Z axes are very similar. Therefore, only the values for X and Y axis are shown.

In order to define the properties of the equivalent quasi-isotropic material, a validation FEA must be performed to guarantee that the structural behavior matches the detailed FEM. The results of this FEA using exactly the same boundary conditions previously explained are presented in Table 9 (see also Table 10). Both the calculation provided by the company CarbonVison and the values obtained as parts of this research work are given. The FEA performed by CarbonVision was executed using shell elements, while the calculation carried on at MPIA was performed using solid elements. However, a very small discrepancy between both FEA was achieved. The plots corresponding to the axial and radial deformations (MPIA FEA) are presented in Figure 48 and Figure 49 respectively.

Parameter	CarbonVision FEA	MPIA FEA
Max. axial deformation (Y axis)	-0.042 mm	-0.043 mm
Min. axial deformation (Y axis)	0.010 mm	0.008 mm
Max. radial deformation (X axis)	0.020 mm	0.022 mm
Min. radial deformation (X axis)	-0.022 mm	-0.022 mm

**Table 9:** Results of the bearing support structure FEA using an equivalent quasi-isotropic material where the lamination sequence and the strength of different types of fibers is not considered. The deformation in the X and Z axes are very similar. Therefore, only the values for X and Y axis are shown.

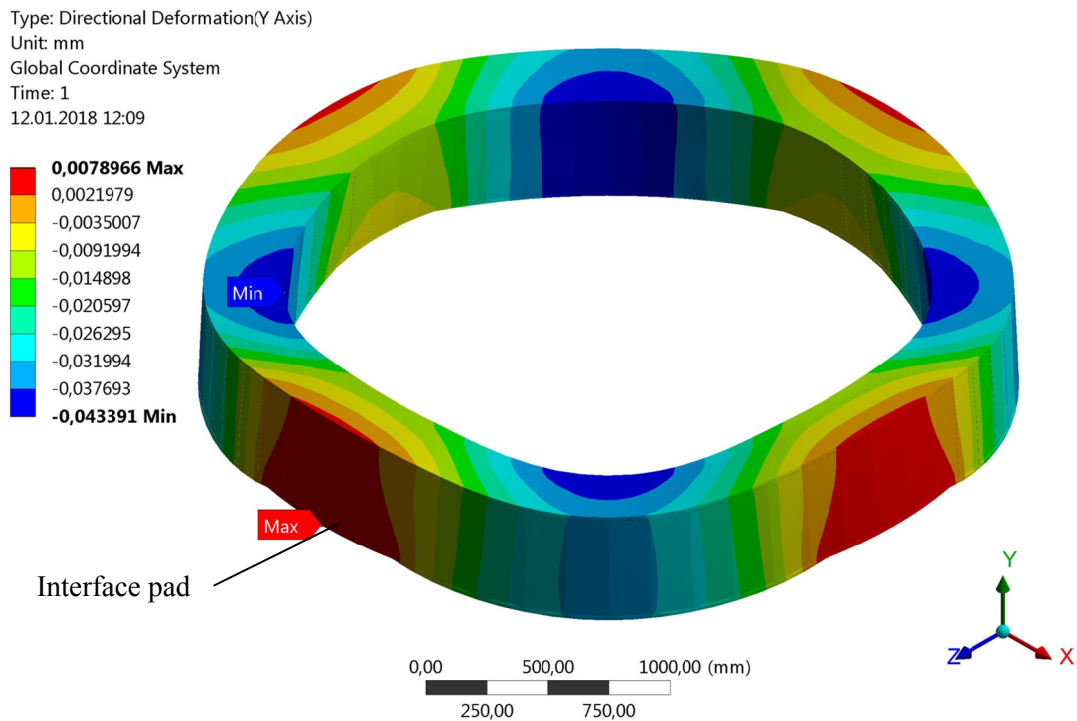


**Figure 48:** Axial deformation (Y axis) of the bearing support structure using an equivalent quasi-isotropic material.

### 4.3 Derotator design proposal

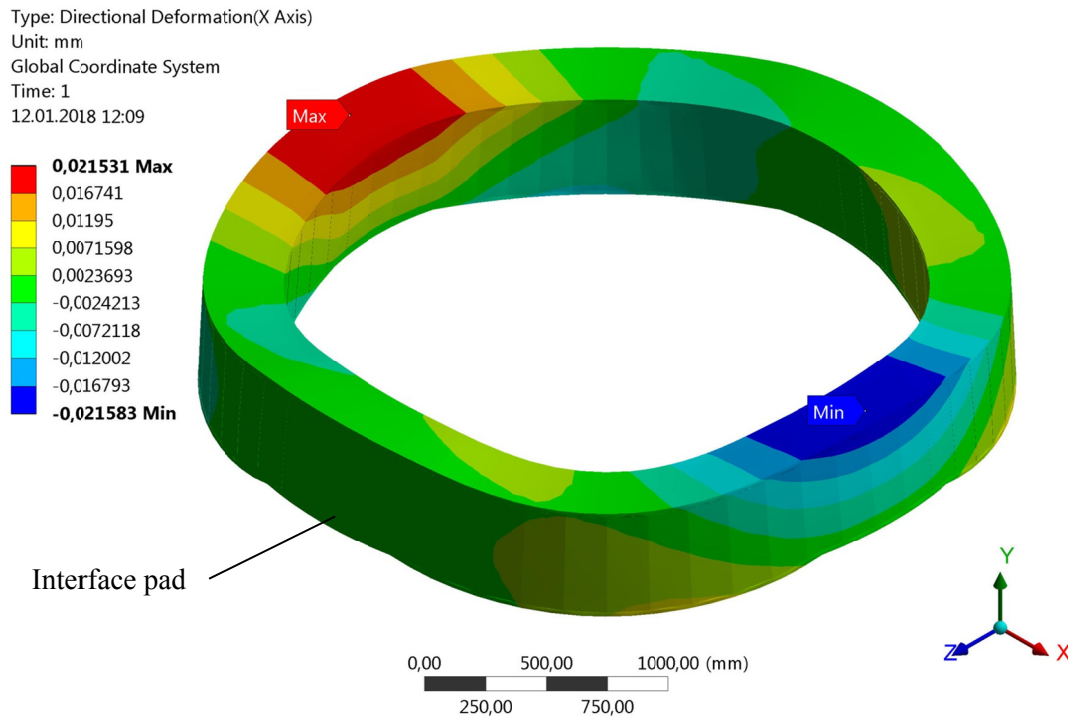


**Figure 49:** Radial deformation (X axis) of the bearing support structure using an equivalent quasi-isotropic material.

According to the results of the FEA of the bearing support structure, it can be demonstrated that an equivalent material with quasi-isotropic properties may be used to estimate the relevant structural performance of the CFRP. Therefore this approach will be used for the design process of the MICADO derotator. The bearing support structure will be manufactured using a combination of HTS and HM fibers, because with that method the deformations of the structure can be considerably reduced. The properties of the equivalent quasi-isotropic material used for the FEA are finally given in Table 10.

Annotation: The basic fiber has a modulus of elasticity of 200 GPa. With 60% of fiber content in the laminate the modulus of elasticity becomes 120 GPa. The layer structure was chosen in order to have high shear stiffness ( $\pm 45^\circ$ ). Therefore with this orientation, the equivalent modulus of elasticity comes down to  $\sim 39$  GPa for the replacement quasi-isotropic material.

Parameter	CFRP	Steel
Modulus of elasticity (E)	39 GPa	200 GPa
Poisson's ratio ( $\nu$ )	0.492	0.26
Density ( $\rho$ )	1560 kg/m <sup>3</sup>	7800 kg/m <sup>3</sup>

**Table 10:** Properties of the equivalent quasi-isotropic material used in the FEM of the bearing support structure. The typical values for steel are given as reference.

### 4.3.2 Bearing Thermal Compensation Rings

In addition to providing supplementary stiffness to the bearing, the support rings will help to compensate for possible deformations due to the CTE difference of the materials used in the bearing mechanical interfaces. Those support rings should preserve the axial stiffness, while allowing some degree of radial flexibility to absorb thermal deformations. In the interface with the cryostat, two different types of steel (with dissimilar CTEs) are implemented; whereas in the interface to the bearing support structure, a combination of steel and CFRP exist, see Figure 50.

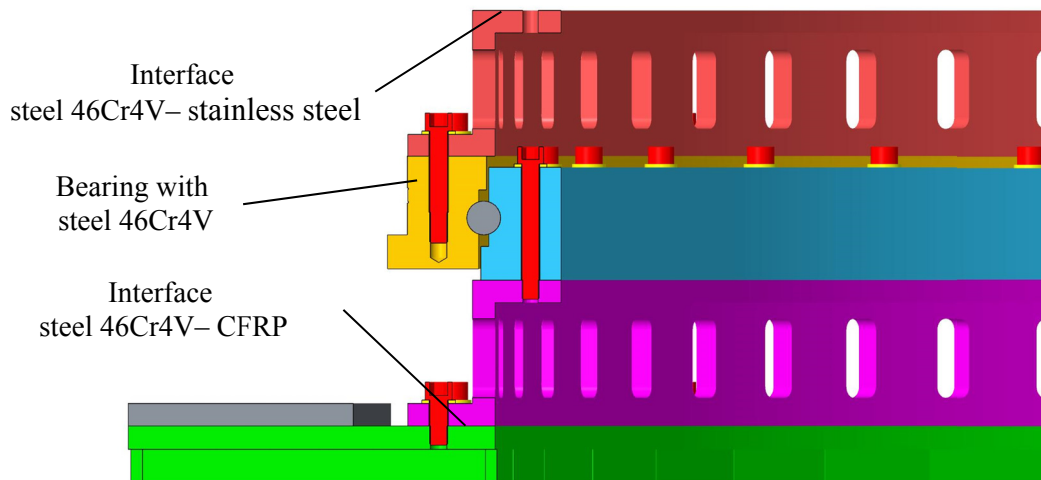


**Figure 50:** Mechanical interfaces towards materials with different CTE.

Thus the aim of the thermal compensation rings is to avoid the bimetallic strip effect deformations being transferred to the bearing (Kandpal, 1997). A calculation of the expected differential thermal deformation for the operational  $\Delta T$  in the interface towards the cryostat is given in Table 11. This effect is even worse at the interface with the bearing support structure made of CFRP, which has a CTE of  $2 \times 10^{-6}$  mm/mm C<sup>o</sup> (see Table 12).

### 4.3 Derotator design proposal

Parameter	Central Flange	Bearing
Diameter	2803 mm	
Material	Stainless Steel 1.4301	Steel 46Cr4V
CTE	$16,0 \times 10^{-6} \text{ mm/mm C}^\circ$	$11,7 \times 10^{-6} \text{ mm/mm C}^\circ$
Operational $\Delta T$	15 C $^\circ$	
Difference in diameter ( $\Delta\emptyset$ )	0.673 mm	0.492 mm
$\Delta\emptyset_{\text{flange}} - \Delta\emptyset_{\text{bearing}}$	0.18 mm	

**Table 11:** Differential thermal deformation at the interface with the cryostat.

Parameter	Support structure	Bearing
Diameter	2528 mm	
Material	CFRP	Steel 46Cr4V
CTE	$2 \times 10^{-6} \text{ mm/mm C}^\circ$	$11,7 \times 10^{-6} \text{ mm/mm C}^\circ$
Operational $\Delta T$	15 C $^\circ$	
Difference in diameter ( $\Delta\emptyset$ )	0.076 mm	0.444 mm
$\Delta\emptyset_{\text{bearing}} - \Delta\emptyset_{\text{support structure}}$	0.37 mm	

**Table 12:** Differential thermal deformation at the interface with the bearing support structure.

In order to define the adequate geometry for the support ring, an optimization process has also been carried out, but in this case focused only in the axial stiffness. The same optimization function  $I_A$  as well as the same design criteria like in section 4.2 are used here. As the general geometry of this part is already defined by the bearing size, the optimization is based on the parameters described in Figure 51. The different options considered are presented in Table 13 and the results of the optimization process are given graphically in Figure 52. The optimization process is performed with an arbitrary axial load and the 4-points interface on the bearing support structure.

Parameter (mm)	Concept
t1=30, t2=20, h=60	Option 1
t1=25, t2=20, h=60	Option 2
t1=20, t2=20, h=60	Option 3
t1=25, t2=15, h=60	Option 4
t1=25, t2=10, h=60	Option 5
t1=25, t2=20, h=50	Option 6
t1=25, t2=20, h=70	Option 7
t1=25, t2=20, h=80	Option 8
t1=20, t2=20, h=90	Option 9
t1=20, t2=15, h=90	Option 10

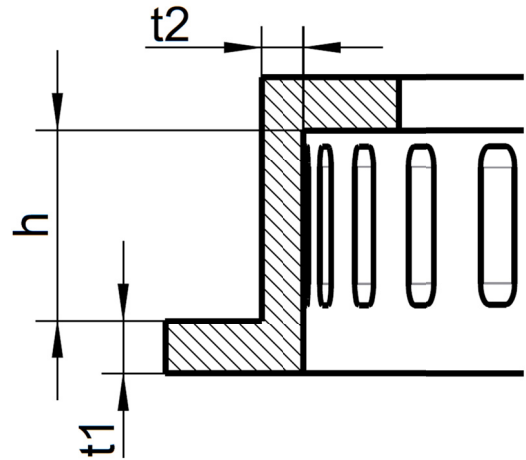


**Table 13:** Thermal ring concepts.

**Figure 51:** Optimization parameters.

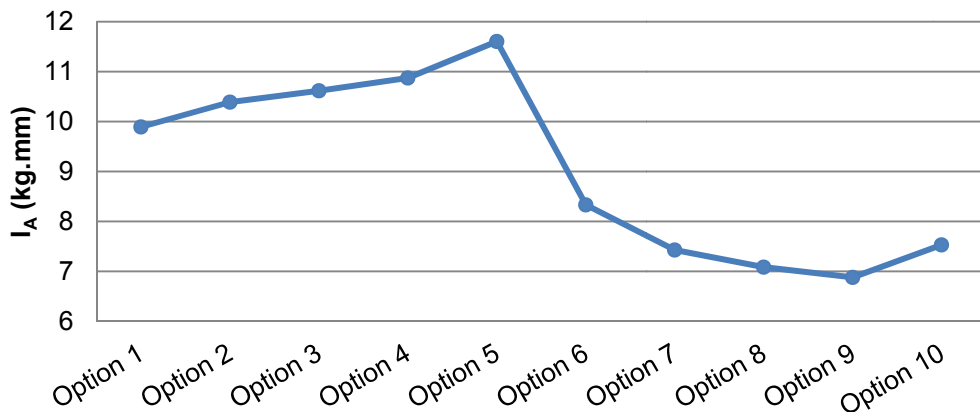


**Figure 52:** Performance of the proposed thermal ring concepts according to  $I_A$ .

Using the geometry of option 9, the effect of the thermal compensation rings can be observed with the corresponding FEA for the interface towards the cryostat, which is presented in Figure 53. The operational  $\Delta T$  of  $15\text{ C}^\circ$  is used for this calculation. Frictional contact and bolt pretension are implemented at the interface with the cryostat and free displacement in the radial direction is used as boundary condition in the contact surface of the thermal compensation ring with the bearing (this is assuming that the bearing deforms in the same amount than the thermal compensation ring). As result of the optimization process, option 9 is the geometry of the thermal compensation ring included in the preliminary design of the MICADO derotator. The rectangular holes in the vertical wall of the ring are intended to reduce

## 4.3 Derotator design proposal

the mass and increase the radial flexibility. If necessary, further options could be considered during the final design phase to increase even more the radial flexibility of this part, i.e. slitting the upper part of the ring in the radial direction.

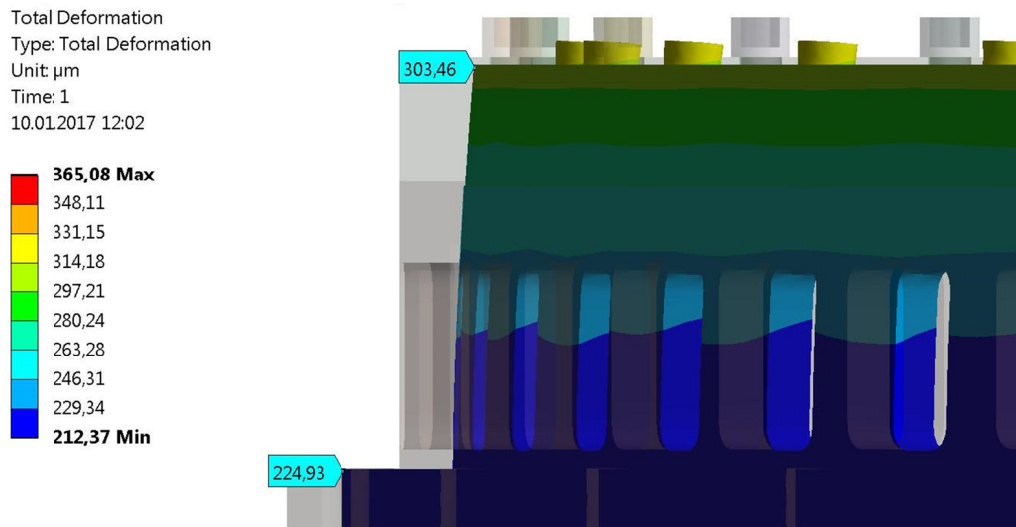


**Figure 53:** Effect of the thermal compensation ring in the interface towards the cryostat.

### 4.3.3 Drive System

The proposed drive system for the MICADO derotator consists of at least two drive units (the option using four drive units has not yet been discarded) for the backlash suppression mechanism. Each drive unit is composed of a servomotor, a Harmonic Drive gear and a pinion which is driving the gearwheel integrated into the slewing bearing (see Figure 54). The servomotor and the Harmonic Drive gear are screwed to a single mounting plate with the adequate tolerances to guarantee the correct centering of both components. The pinion is bolted down to the harmonic drive gear using a pin to keep the alignment, and in order to increase the stiffness of the unit a counter bearing is implemented into the opposite side of the pinion through a centering pin as well. In an L shape movement, the motor mounting plate is installed on top of the drive unit bracket by means of a circular concentric reference to keep the centering of the motor with the counter bearing. The drive unit bracket is finally bolted down to a spacer to match the height of the thermal compensation ring, where the correct gear-pinion center distance can be set with the radial adjustment mechanism (sliding guides are built in between the spacer and the unit bracket



interface plate). The spacer is then fixed to the CFRP bearing support structure. With exception of the pinion, aluminum is planned to be used to build all parts of the drive units, while the spacer could be manufacture using CRFP as well.

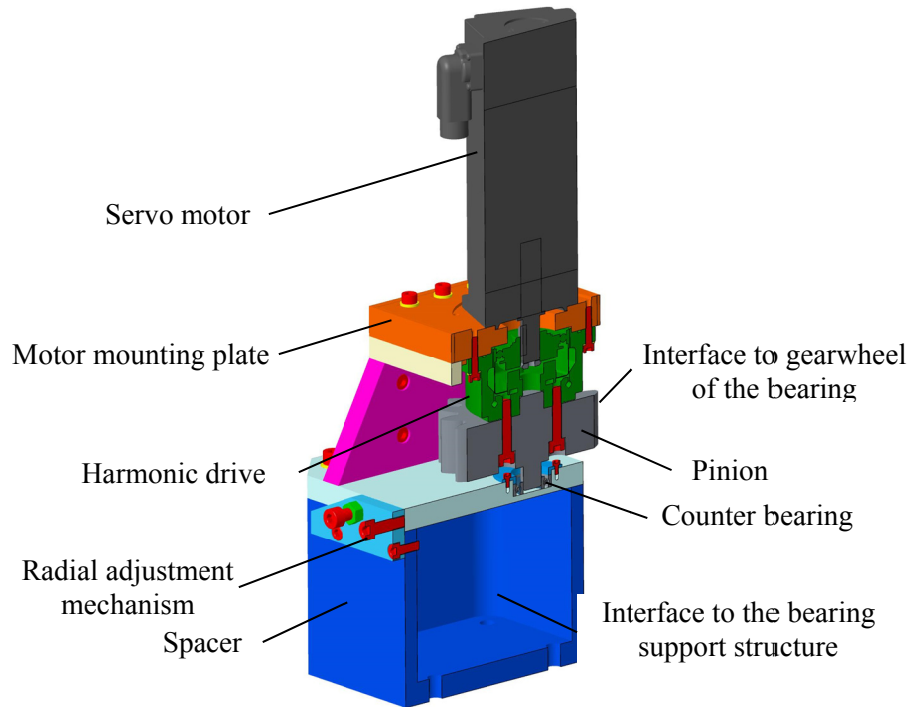


**Figure 54:** CAD model of one derotator drive unit, at least two identical ones will be used.

The required torque to overcome the bearing friction, the moment of inertia of all moving parts and the Harmonic Drive gear friction, referred to the motor axis is about 0.8 Nm (the gear ratios of the pinion and the Harmonic Drive gear are 27.7 and 160 respectively, for a total gear ratio of 1:4432). A conservative safety factor of 2.5 has been defined for the required torque to drive the slewing bearing, which means that the servo motor should be able to deliver an output torque of a least 2 Nm (the complete calculation of the required torque at the motor axis and the selection of the corresponding Harmonic Drive gear are given in appendix A). According to this value, the servomotor Beckhoff AM8532E with a rated output torque of 2.2 Nm (BECKHOFF, 2015) and a rated maximal speed of 6000 rpm, and the Harmonic Drive HFUC-25-160-2UH (Harmonic Drive AG, 2014) were chosen for the drive unit of the MICADO derotator.

### 4.3 Derotator design proposal

---

The distribution of the drive units for the backlash suppression mechanism is a relevant aspect for the performance of the derotator. Ideally four drive units arranged in two pairs opposite to each other should be used for the backlash suppression system. This configuration allows canceling the reaction force generated by the preload applied between the two drive units to remove the backlash of the gear. This concept is described in Figure 55.

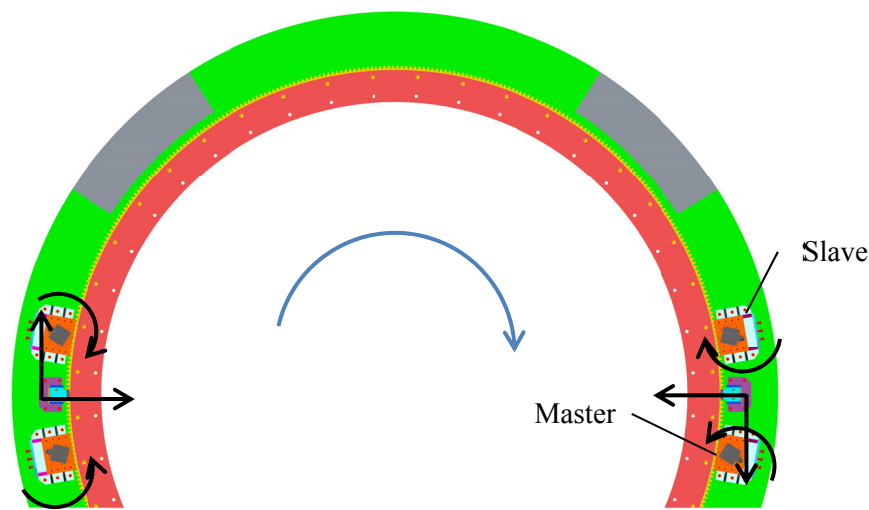


**Figure 55:** Ideal drive unit arrangement for the backlash suppression mechanism.

The motors are running in a synchronized master-slave configuration, where the master operates with a higher torque (100%) to overcome the slave, which is pushing (with a lower torque  $\sim 40\%$ ) in the opposite direction. In this way, the required preload to remove the mechanical play between the gear wheel and the pinion is generated, allowing a smooth rotation while a change of direction is happening in the field rotation trajectory. In order to concentrate the preload in a small section of the bearing, the motors must be placed close to each other.

Some of the technical solutions previously described in section 3.3 are operating only with one pair of drive units. Therefore, this option is tentatively implemented for the MICADO derotator preliminary design. In this case the reaction force created by the unique pair of drive units must be considered for the calculation of the bearing starting friction torque. The possibility to upgrade the drive system to operate with four drive units is always possible if required.

### 4.3.4 Positioning Measurement System

Having an accurate measurement of the position of the cryostat is a key aspect to achieve the positioning accuracy demanded by the MICADO derotator. The positioning measuring system proposed here consists of a custom made HEIDENHAIN scale tape incremental angle encoder (without integral bearing) for high accuracy and at least two scanning heads. Images of the hardware to be used, as well as the CAD model of the scanning head mount are presented in Figure 56. The model selected for this application is the MSB ERA 8400C full circle version with the corresponding scanning head AK ERA 8480. The metallic scale tape has a precise inner diameter of 2801.91 mm, which comes as result of the 220000 reference marks printed on it.

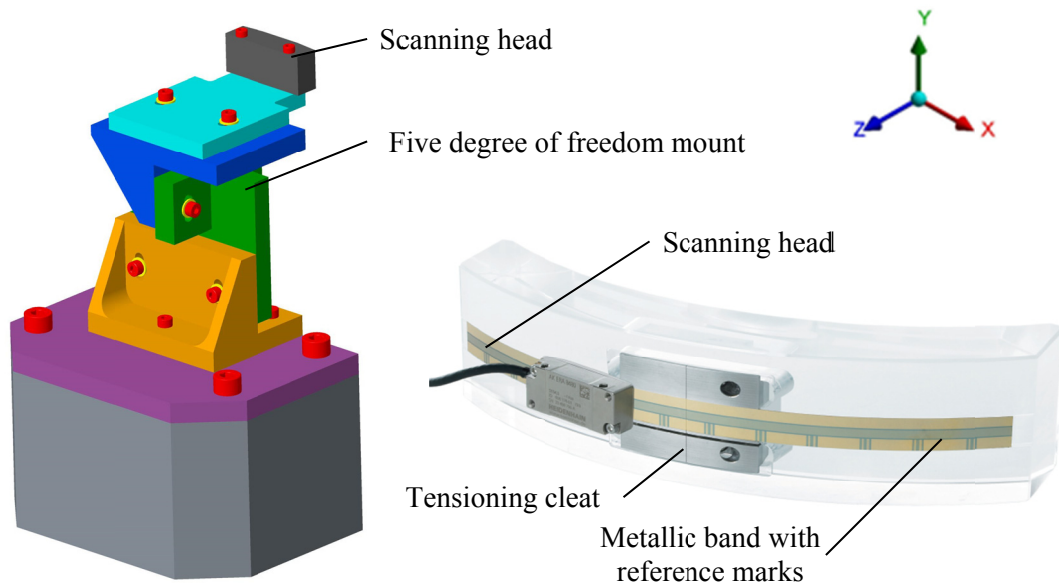


**Figure 56:** CAD model of the scanning head mount (left) and scanning head/band encoder real hardware example (right) (band encoder image source: Heidenhain catalog, 2014). The scanning head mount provides translation in the Y and Z axes, and rotations in the X, Y, Z axes.

The nominal position error between two marks is  $\pm 0.1$  arcsec and the accuracy of the graduation in the scale tape is  $\pm 1.9$  arcsec. The encoder-specific position error for one full revolution is the combination of those two parameters (HEIDENHAIN, 2014). According to HEIDENHAIN, the expected encoder-specific error for the configuration selected for the derotator is about 1.6 arcsec (RMS in  $360^\circ$ ). However, that error can be reduced by introducing more scanning heads in the measurement system. The estimated value with two equidistant scanning heads is around 1.1

arcsec (RMS in  $360^\circ$ ) and could be reduced up to 0.3 arcsec when using six equidistant scanning heads if necessary (Sändig, 2016). As HEIDENHAIN offers an off-the-shelf solution to combine the signal of two scanning heads into one single output signal, this option has been implemented as base line in the derotator preliminary design. Other sources of errors affecting the encoder performance are described in detail by Häberle (2017).

The metallic band goes into the slot machined in the bearing and is secured only using its tensioning cleat, for that reason the manufacturing tolerances of the mechanical interfaces on the bearing are extremely tight. The scanning head is supported by a self-aligning five degree of freedom mount (HEIDENHAIN, 2011), where the correct alignment is achieved using a dummy scanning head which has an insert that fixes into the band slot machined on the bearing.

#### 4.3.5 Controller Architecture

Applying the adequate control strategy will have a huge impact on the performance of the derotator. This is a key aspect that must be considered with the goal of achieving the required differential angular positioning accuracy at the level of 2 arcsec (RMS). The control system proposed for the preliminary design of the MICADO derotator has been successfully used in other applications related to astronomical instrumentation, where high precision positioning accuracy was required as well (Dreyer et al., 2014). The control system is based on a cascaded architecture, with the inner current/torque loop and the middle velocity loop, embedded into the outer position loop. Additionally, a velocity feedforward and a torque feedforward are also implemented in the controller. A friction compensation feature could also be applied if necessary. In this case, the friction torque must be estimated using a dedicated mathematical model. Then, a signal that compensates the predicted friction torque can be added to the controller in the inner current/torque loop (Olsson, Aström, Caudas de Wit, Gäfvert, & Lischinsky, 1998).

Due to the positioning accuracy required for the MICADO derotator, this option is being considered for the design of the controller. The scheme of the proposed control system as part of the preliminary design is presented in Figure 57.

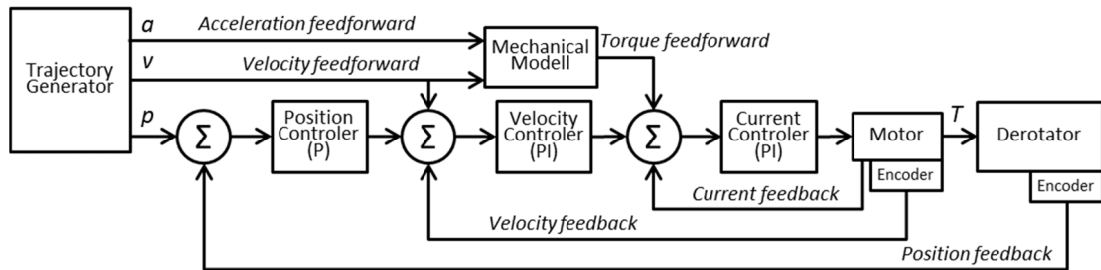


**Figure 57:** Proposal of the control system considered for the MICADO derotator preliminary design.

The trajectory generator produces the required signals of position, velocity and acceleration to be used in the controller. Those calculations are made based on the field rotation equations described in chapter 2. The position error signal, which is calculated as the difference between the given trajectory and the actual position feedback coming from the band encoder signal installed in the bearing, is fed into the proportional (P) position controller where the corresponding velocity command is generated. The velocity error signal, calculated considering the velocity feedback (calculated with the derivative of the position signal from the encoder in the motor) and the velocity feedforward signal, is then fed into the proportional-integral (PI) velocity controller where the corresponding current command is derived. Finally, the current error signal, which has been obtained taking into account the torque feedforward (the torque feedforward is calculated using the inverse of the MICADO instrument mechanical model) and the current feedback, is fed into the proportional-integral (PI) current controller, which delivers the correct current signal to the motor. The required torque to drive the slewing bearing through the given position trajectory at the precise required velocity is then generated by the motor. The control concept is described in more detail by Glück (2019).

### 4.3.6 Derotator Mass Budget

The estimated mass of the derotator according to the preliminary design is given in Table 14. The total mass of 2160 kg is slightly higher than the previously defined mass limit (Mueller, 2017). Therefore if the total mass cannot be further reduced, an official change request will be necessary to increase this limit of the mass requirement.

## 4.4 Derotator Static Structural Analysis

---

<b>Item</b>	<b>Mass (kg)</b>
Bearing support structure	500
Thermal compensation ring (2x)	600
Bearing	890
Drive units (4x)	100
Encoder unit	20
Bolts and washers	50
<b>Total</b>	<b>2160</b>

**Table 14:** Derotator mass budget

## 4.4 Derotator Static Structural Analysis

Nowadays, numerical analysis methods like the FEA are becoming especially relevant during the design phase of complex systems. Therefore efficient and reliable numerical simulations are crucial for the development of high precision instruments like MICADO. The derotator is a central structural part of the MICADO instrument, connecting the cryostat with the instrument support structure, where the single-row four-point contact ball bearing has a key role as its main component. For that reason, developing an adequate FEM of the bearing will allow not only an accurate static FEA of the derotator itself, but also the calculations of the whole MICADO instrument for other aspects like the modal and the earthquake analyses.

### 4.4.1 Modeling a Four-Point Contact Ball Bearing

Most industrial applications where large slewing bearings are used, like cranes or civil engineering machines, must deal with heavy load and therefore high stress values. In those cases relative large deflections are tolerable and the change in the bearing friction is overcome by applying a higher torque to the mechanism. On the other hand, in applications like astronomical instrumentation the loads involved are relatively small. As a result, the stress values are not the driver of the design. In these circumstances, where high precision and accuracy are essential, the main goal is to minimize deformations in order to keep the instrument as stable as possible while the bearing is rotating.

The first approach that could be used to model a large four-point contact ball bearing, and maybe the easiest to implement, is simply using 3D solid elements in all of its components, i.e. the inner ring, the outer ring, and the balls inside the bearing. However, due to the size of these kinds of bearings (typically up to 8 m manufactured as one piece) this method is not the most efficient in terms of computation time and the required computing power. In order to obtain faster results with less computing power, several other alternatives have been proposed to simplify the FEM of large slewing bearings. For instance, using springs elements (Gao, Huang, Wang, & Chen, 2010), beams elements (Daidié, Chaib, & Ghosn, 2008) or a combination of them to replace the rolling elements in the slewing bearing (Krynke, Selejdak, & Borkowski, 2013).

This section is dedicated to comparing these different ball bearing modeling techniques with the intention of analyzing their advantage and disadvantages. In this context, two additional alternatives were selected to perform the study. The first replaces the 3D modelling of the balls inside the bearing with spring elements and a second method uses beam elements instead. In all three cases the rings of the bearing are modeled using 3D solid elements (Barboza, et al., 2017). A schematic drawing of the bearing cross section used in the derotator prototype, which is taken as reference for this calculation is presented in Figure 58, while the main dimensions are presented in **Table 15**. The CAD model of the bearing was generated following those dimensions, where the diameter of the balls is 20.5 mm. For simplicity, the seals of the bearing are not considered in the FEA. The same image (Figure 58) is also used to show the load transmission (red arrows) through the bearing for the case of an axial load under compression.

#### 4.4 Derotator Static Structural Analysis

Parameter	Value
$D_L$	Ø 1094 mm
$O$	Ø 1092.5 mm
$D_i$	Ø 1022 mm
$U$	Ø 1095.5 mm
$D_a$	Ø 1198.4 mm
$H$	56 mm
$H_1$	45.5 mm
$H_2$	45.5 mm
$t$	20 mm
$M$	12
$B$	Ø 13.5

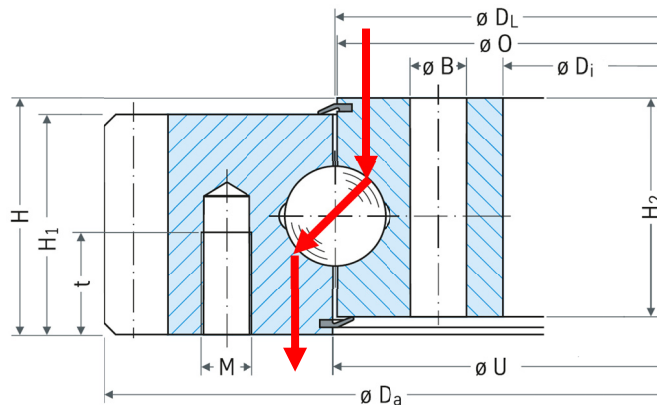


**Table 15:** Bearing dimensions. **Figure 58:** Test bearing cross section.

The same boundary conditions are used for the three models to be compared. They consist of a fixed support at the lower contact surface of the inner ring and an axial load of 30 kN (7.5 kN after reducing the model to a quarter ring due to its symmetry) at the upper contact surface of the outer ring. It is important to note, that the bearing is installed on the test stand with the outer ring upwards, the opposite orientation shown in Figure 58. An additional boundary condition is used to restrict the rotation of the bearing outer ring, which in a real case is prevented due to the friction torque. The “displacement support” feature offered in ANSYS Workbench is used for this purpose. With the intention of focusing the comparative analysis on the three different methods implemented for the balls of the bearings, the mesh using solid elements for the inner and outer rings is kept constant. The boundary conditions, as well as the mesh used in the rings are shown in Figure 59. The mesh of the rings is made using tetrahedrons and the “face sizing” feature is implemented on the raceway contact surfaces to allow a higher density of nodes in those areas of interest. This FEM is the base line for the following comparative FEA where the balls are modeled using the three different approaches previously mentioned.



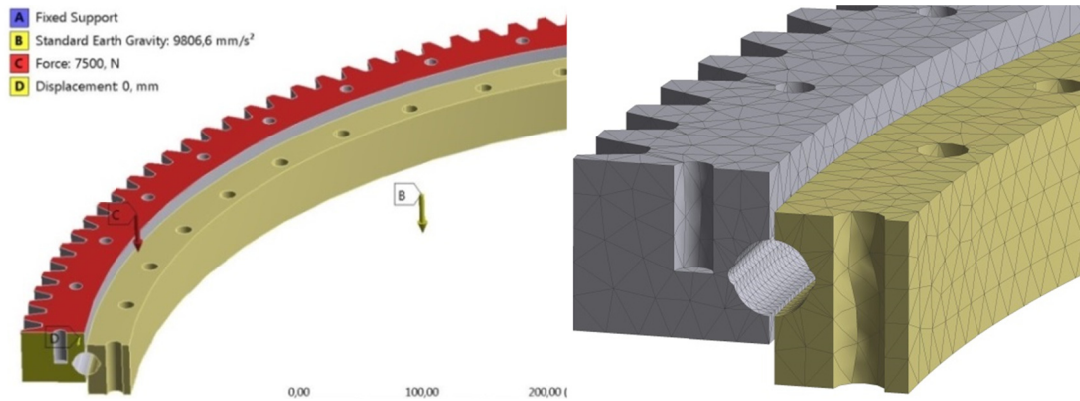


**Figure 59:** Boundary conditions and mesh used in the rings of the bearing.

#### 4.4.1.1 Bearing FEM Using Solid Elements

The balls are inserted into the FEM of the bearing shown in Figure 56, where the mesh of the spheres is also generated using tetrahedral elements. “Frictional contact” is used to simulate the connection between the balls and the rings. As the balls can still rotate/slide inside the raceway, an additional boundary condition is required to restrict this degree of freedom on each sphere. In this case, the “displacement support” is used as well. The whole bearing contains a total of 144 balls, therefore 36 balls are included in the FEM where only a quarter of the bearing is implemented. Figure 60 shows the meshed model used for this FEA.

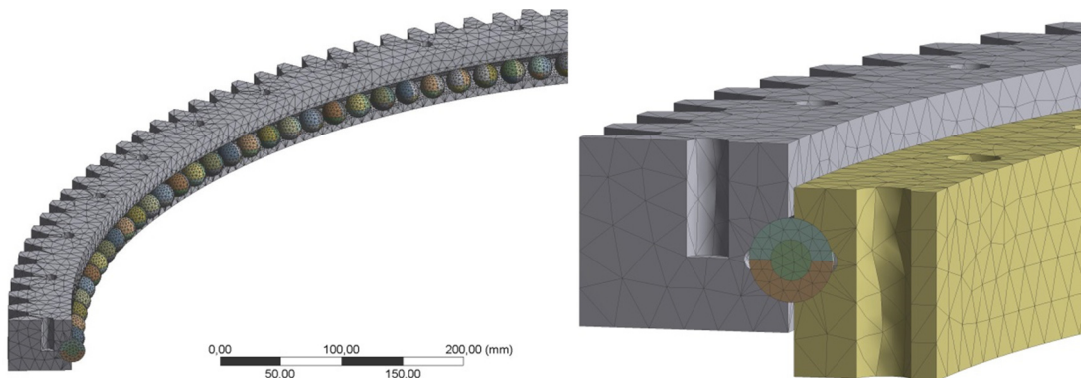


**Figure 60:** Mesh implemented in the FEM using solid elements.

The results of the total deformation and the Von-Mises stress corresponding to this FEA are presented in Figure 61. The computing time is 8 min for a total of 215322 nodes, and 5 GB of memory are required for this calculation. Due to all the details considered in this approach, it might be considered the most accurate one. However,

## 4.4 Derotator Static Structural Analysis

the results are considerably sensible to changes in the friction coefficient parameter used in the definition of the frictional contact. In this case a friction coefficient of 0.025 is used. A higher friction coefficient will reduce the total deformation and increase the stress values.

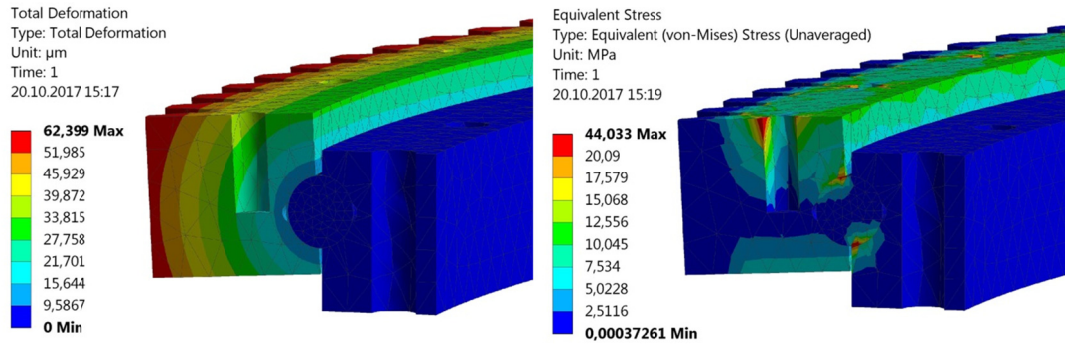


**Figure 61:** Bearing total deformation (left) and Von-Mises stress (right) using solid elements.

In the image showing the stress values it can be observed that the load transmission occurs only through two of the four contact areas, which is the expected behavior in this kind of bearings (see Figure 58). The contact points engaged for the load transmission are different depending on the axial load applied to the bearing, tension or compression. A loss of contact can be seen in the two points that are not involved in the load transmission; no values of stress are registered in those areas.

### 4.4.1.2 Bearing FEM Using Spring Elements

The second approach to be analyzed consists of replacing the balls inside the bearing with a pair of spring elements tilted  $\pm 45^\circ$ . All other boundary conditions are kept constant. The main parameter to be identified in this case is the stiffness of the springs to be used in the FEM. The bibliography for such a calculation is provided by the bearing manufacturer (ThyssenKrupp Rothe Erde, 2015). The required equations are presented as follow:

$$\delta_K = \left( \frac{F_K}{C_{KN}} \right)^{2/3} \quad (28)$$

$$C_{KN} = 34300 \frac{\sqrt{d_K}}{K^{0.35}} \quad (29)$$

$$F_K = \frac{F_A}{N_K}. \quad (30)$$

Equation (28) represents the deformation behavior of a ball at its contact areas with the raceways, denoted by  $\delta_K$ , where  $F_K$  is the ball force and  $C_{KN}$  is the stiffness constant at the contact areas of the ball with the raceways, described by equation (29). The ball diameter is represented by  $d_K$  and  $K$  is the osculation factor in the bearing (the standard value of  $K = 0.04$  is used in this calculation). The ball force  $F_K$  can be obtained with equation (30), where  $F_A$  is the axial force acting on the bearing and  $N_K$  is the number of balls. The stiffness constant  $C_{KN}$  describes non-linear behavior, but for the implementation of the FEM a linear force-deformation relation is generally desired. The idealized linear stiffness constant for a ball is represented by equation (31) and denoted by  $C_{KL}$  (ThyssenKrupp Rothe Erde, 2015),

$$C_{KL} = \frac{F_K}{\delta_K}. \quad (31)$$

Depending on the size, the number of balls inside a four-point contact ball bearing can be large. Therefore, it is useful to reduce the number of required spring pairs by defining an equivalent stiffness  $C_s$ , which can be obtained with equation (32).

$$C_s = C_{KL} \frac{N_K}{N_T}, \quad (32)$$

where  $N_T$  is the number of spring pairs to be implemented into the FEM of the bearing. The value of  $C_s$  used in this FEA corresponds to 87.1 kN/mm with 60 spring pairs (for the whole bearing), which is the minimum number of spring pairs recommended by ThyssenKrupp Rothe Erde. The assembly of the springs into the FEM is shown in Figure 62.

4.4 Derotator Static Structural Analysis

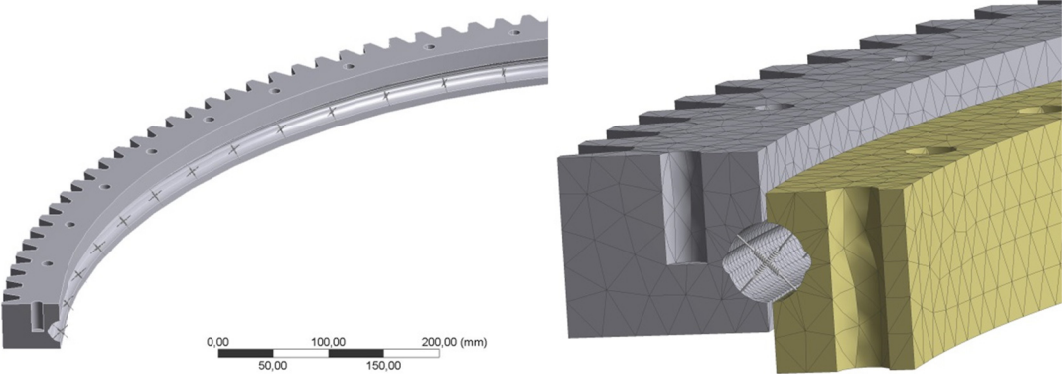


Figure 62: Bearing FEM using spring elements.

Figure 63 shows the results of the total deformation and the Von-Mises stress corresponding to this modeling alternative. The computing time required for this calculation is 4.5 min for a total of 127432 nodes and 0.7 GB of memory were used. The overall behavior of the deformed FEM using springs is very similar to the one described while using pure solid elements. However, the maximum value of deformation is 17.9% higher (the deformation value of the FEM using solid element is taken as reference for the calculation of the discrepancy). The stress values are also considerably higher. This is because the springs are acting as stress concentrators, transferring the load through a very small area on the raceway of the bearing. In addition, the total load on the bearing is distributed in only 60 pairs of springs. Checking the spring forces, it can be confirmed that the spring engaged with the load transfer is under compression, while the second one is under tension. This corresponds with the loss of contact between the balls and the raceway previously shown while using pure solid elements.

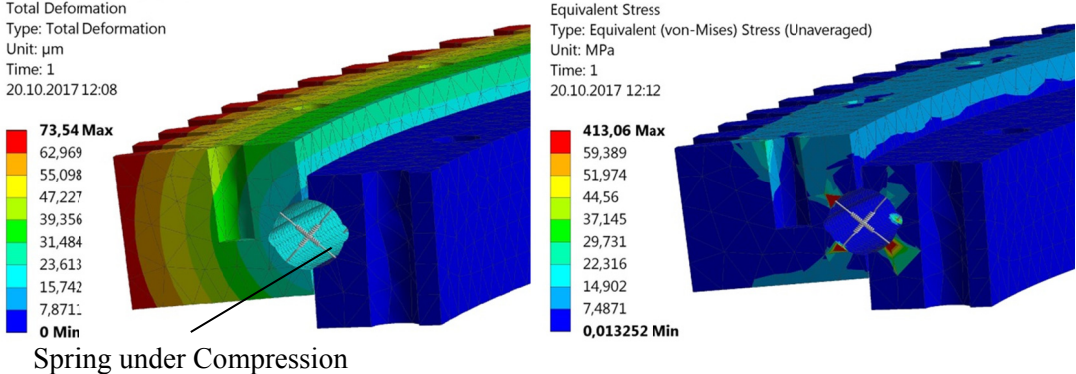
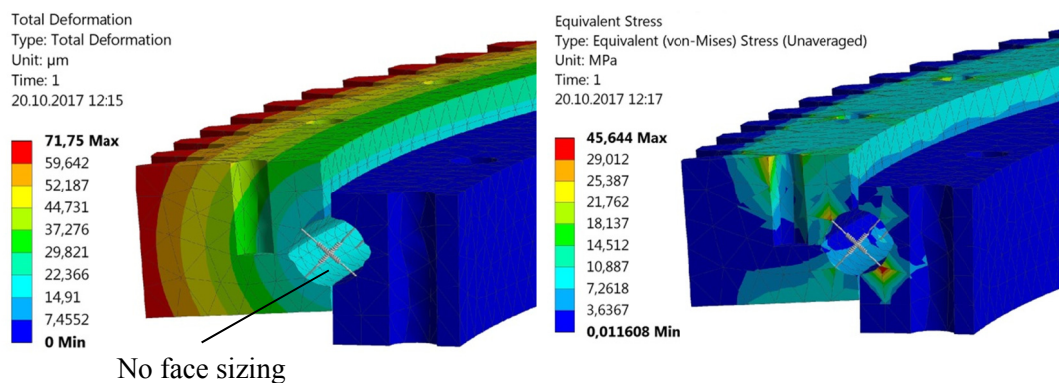


Figure 63: Bearing total deformation and Von-Mises stress using spring elements.

The “face sizing” feature was kept constant for the results presented in Figure 63. Nevertheless, as the balls are not included in the model, a higher density of nodes in the raceway is not really required. This alternative was investigated and the results without “face sizing” are presented in Figure 64. The calculation is considerably faster, with a computing time of 0.5 min for a total of 57882 nodes and the required memory was 0.3 GB. The deformation values are very similar, whereas the discrepancy reduces to 15%. The maximum value of stress is considerably lower, which means that the effects of the stress concentrators are not registered while a coarse mesh is implemented.



**Figure 64:** Bearing total deformation (left) and Von-Mises stress (right) using spring elements without face sizing on the raceways.

#### 4.4.1.3 Bearing FEM Using Beam Elements

Modeling the balls inside the bearing with beam elements is the second FEM alternative to be considered in this comparative analysis. As shown in Figure 65, only the contact areas involved with the load transfer are used to connect the rings of the bearings with the beam elements. If the other two contact areas are also linked with beam elements, the stiffness of the FEM becomes unrealistically high (representing a “bonded contact” between the balls and the raceways where the separation is not allowed, this behavior is not correct). The reason is that the axial stiffness of the beam element is extensively higher than a spring with similar dimensions.



4.4 Derotator Static Structural Analysis

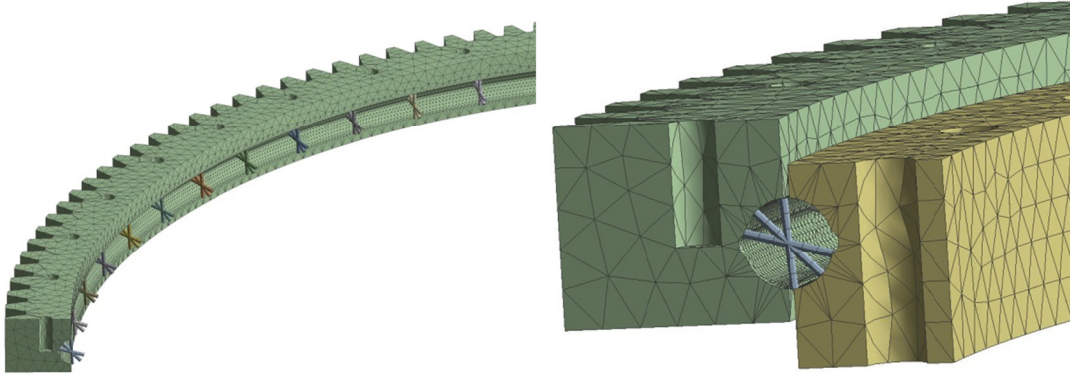


Figure 65: Bearing FEM using beam elements.

The relevant parameters to be defined for this method are: the geometry of the cross section, the dimensions and the quantity of beam elements to be used. For this calculation, a circular cross section with a diameter of 3 mm is selected for the beams, while three beams connected at the ball center are implemented into the FEM. These parameters were established taking the FEM using pure solid elements as reference.

The results of the FEA using beam elements are presented in Figure 66. The total deformation (left) matches the overall behavior of the deformed FEM described in the two previous alternatives, while the discrepancy to the first model reaches 9.5%. Similarly, the stress values are considerably higher than the ones obtained using solid elements, but slightly lower than the values registered using spring elements. This is consistent with the fact that the load on each raceway is distributed on three beam elements. The computing time required for this calculation is 0.5 min with a total of 129453 nodes and 2 GB of memory were used.

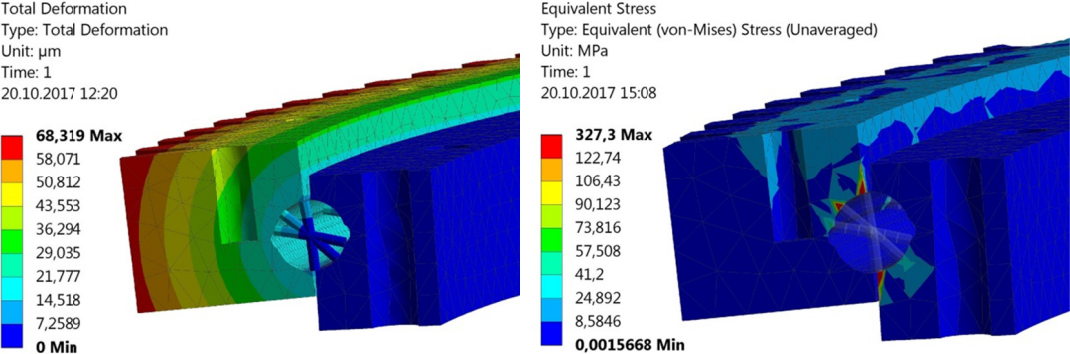
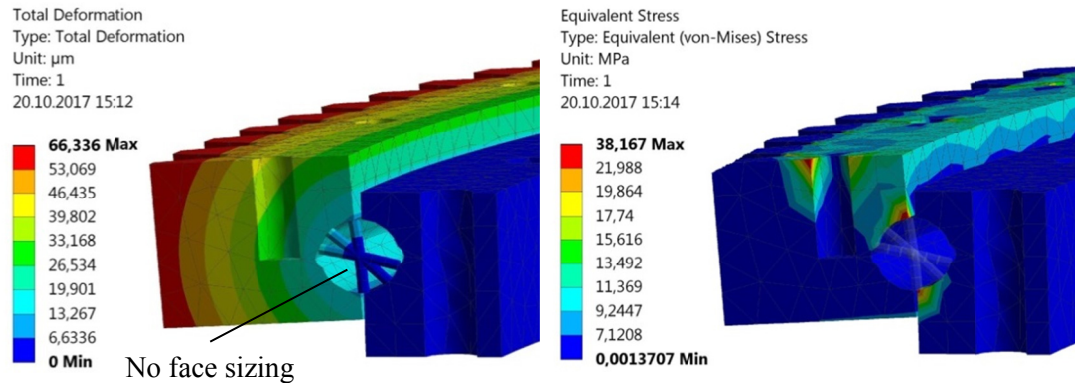


Figure 66: Bearing total deformation (left) and Von-Mises stress (right) using beam elements.

The alternative removing the “face sizing” (coarse mesh) on the raceway was also investigated while using beam elements and the results are presented in Figure 67. The computing time required in this case is 0.2 min for a total of 58524 nodes and 0.9 GB of memory were used. A summary of the bearing FEA with the three different FEMs and its variants is presented in section 4.4.2.



**Figure 67:** Bearing total deformation (left) and Von-Mises stress (right) using beam elements without face sizing on the raceways.

#### 4.4.2 Summary of the Bearing FEM Comparative Analysis

The relevant parameters of the comparative analysis for the bearing FEMs are presented in Table 16.

FEM	Nodes	Calc. time (min)	Time Reduction (%)	Memory (GB)	Def. ( $\mu\text{m}$ )	Def. Discrepancy (%)	Stress (MPa)
Solid	215322	8	--	5	62.4	--	44
Solid+springs (fine mesh)	127432	4.5	43.8%	0.7	73.5	17.9	413
Solid+springs (coarse mesh)	57882	0.5	93.8%	0.3	71.8	15	45.6
Solid+beams (fine mesh)	129453	0.5	93.8%	2	68.3	9.5	327.3
Solid+beams (coarse mesh)	58524	0.2	97.5%	0.9	66.3	6.3	38.2

**Table 16:** Comparison between the different FEMs.

The bearing FEM with solid elements is taken as reference for the analysis. Thus, the deformation discrepancy and the calculation time reduction for all FEM alternatives

are calculated with respect to the values  $62.4 \mu\text{m}$  and  $8 \text{ min}$ , respectively. As previously commented, the stress values are relatively low and therefore not relevant for this particular application, where the deformations are the drivers of the overall design. For that reason, the discrepancy is not calculated for the stress variable. Based on the result obtained, the bearing FEM using spring elements (with coarse mesh) is chosen to be implemented for the derotator FEA. This FEM was also successfully used for the validation of the bearing FEA. The option using beam elements is faster in the calculation time but requires three times as much memory to perform the same analysis.

### 4.4.3 Validation of the Bearing FEA

The initial idea was to validate the FEA using the derotator test stand itself (see chapter 6). However, after some discussions it was concluded that such a validation was not possible using the whole test stand assembly. There are several factors that could influence the measurements of the deformations, like the flatness of the floor and the additional bolted connections, making it very difficult to identify the stiffness of single components separately, i.e. the bearing, the support structure, and the struts. For that reason, it was decided to request a dedicated stiffness test on the bearing. Such a test can be performed at the bearing supplier factory under controlled conditions. Three different load cases were considered for the stiffness test: axial force ( $F_A$ ) of  $45 \text{ kN}$  (including the mass of the upper plate on top of the bearing), radial force ( $F_R$ ) of  $45 \text{ kN}$  and tilting moment ( $M$ ) of  $18 \text{ kNm}$ .

The CAD model of the setup used to identify the stiffness of the bearing, as well as the location of the dial gauges to measure the deformations are shown in Figure 68. The bearing is bolted down on a  $86\text{-mm}$ -thick steel ground plate with a diameter of  $1395 \text{ mm}$ , while an additional  $68\text{-mm}$ -thick steel upper plate with  $1195 \text{ mm}$  in diameter is mounted on top of it. A spacer with a thickness of  $10 \text{ mm}$  is placed between the upper plate and the bearing. The bolts were fastened with a nominal tightening torque of  $117 \text{ Nm}$ .

For the axial deformation measurement, three dial gauges were placed equally spaced ( $3 \times 120^\circ$ ) on top of the upper plate, for the radial deformation a dial gauge



was placed opposite to the radial force, and for the tilting deformation two dial gauges were placed opposite to each other on top of the upper plate (distance between dial gauges 1245 mm). The load application was performed using a hydraulic actuator and/or dummy masses.

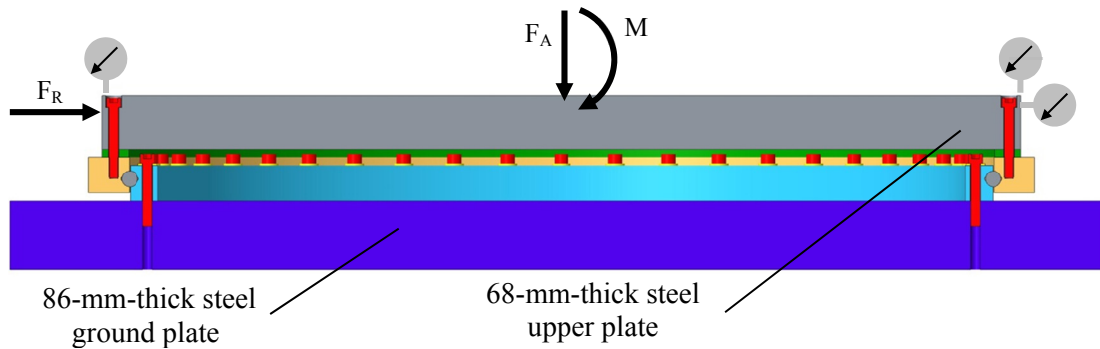


**Figure 68:** model of the bearing test setup cross section at ThyssenKrupp Rothe Erde.

Figure 69 shows the axial load case setup, where the ground plate is bolted down to a rotating table. A similar set up is also used for the fiction torque test of the bearing.

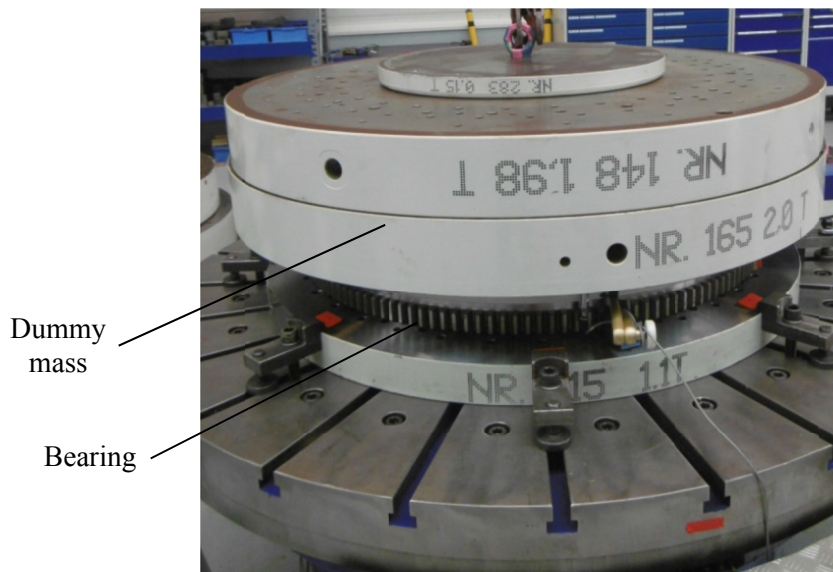


**Figure 69:** Test setup for the axial load case at the ThyssenKrupp Rothe Erde factory.

The whole test setup was duplicated in ANSYS with the corresponding boundary conditions in order to simulate the three load cases previously commented. Frictional contact ( $\mu = 0.2$ ) and bolt pretension (50 kN corresponding to 117 Nm) were included in the FEM as well. With the purpose of estimating the required calculation time for such a FEA, no symmetry condition was implemented. Therefore, also a relative coarse mesh was used in the upper and lower plates. The simulation was

#### 4.4 Derotator Static Structural Analysis

performed in two steps, the first step where only the bolt pretention are applied and the second one for the load application depending of each load case ( $F_A$ ,  $F_R$ ,  $M$ ). The FEM of the bearing test setup is shown in Figure 70.

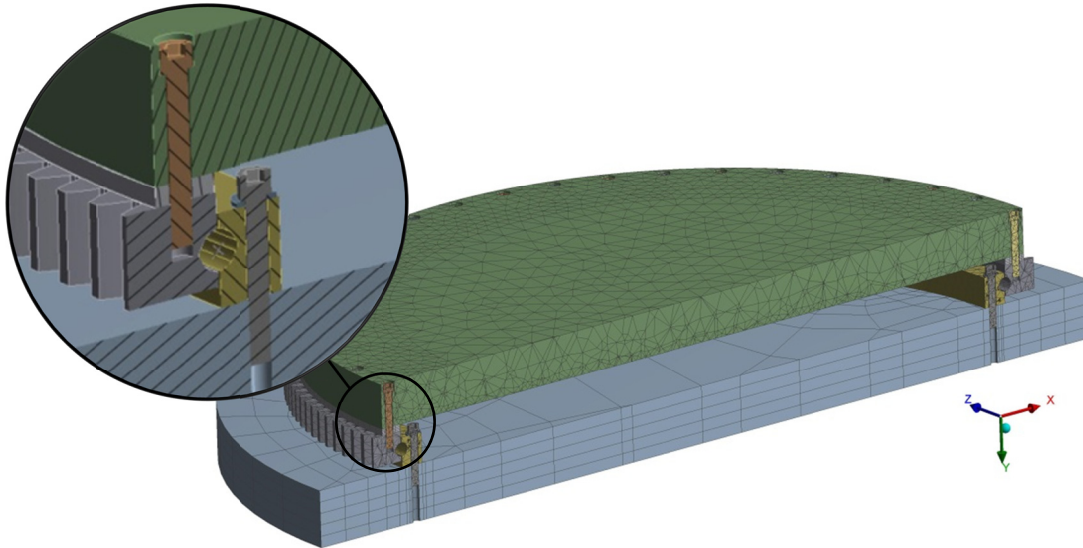


**Figure 70:** FEM of the bearing test setup.

The results of the FEA corresponding to the axial force, radial force and tilting moment load cases are presented in Figure 71, Figure 72, and Figure 73 respectively (left step 1, right step 2). As the maximum stress values are registered in the bolts due to the pretension, the stress plots are not shown. The measured deformations provided by Rothe Erde (Windgassen, 2017), as well as the corresponding values from the FEA are summarized in Table 17.

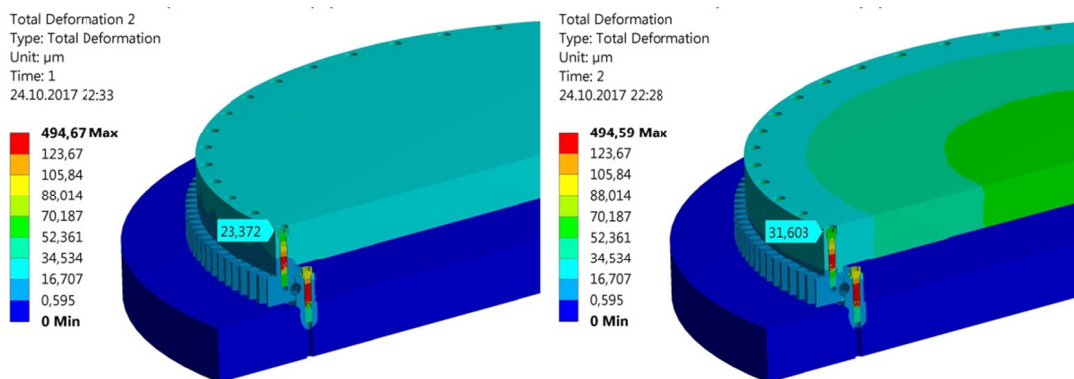


**Figure 71:** Bearing test setup total deformation for the axial force load case.

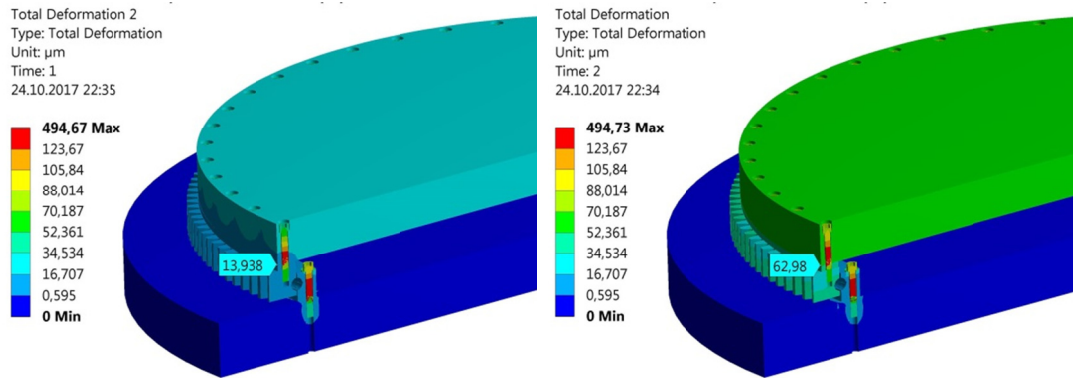


Figure 72: Bearing test setup total deformation for the radial force load case.

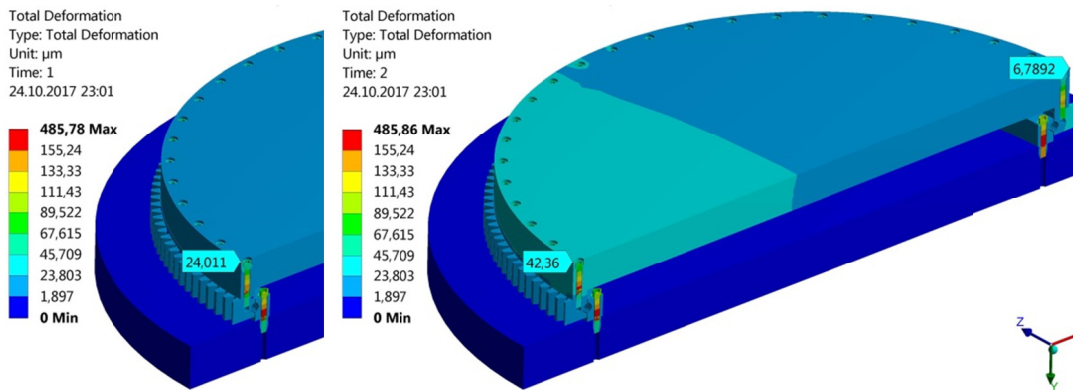


Figure 73: Bearing test setup total deformation for tilting moment load case.

Load Case	Measured Deformation (μm)				FEA Deformation (μm)		
	Dial gauge position 0°	Dial gauge position 120°	Dial gauge position 240°	Avg.	Bolt pretension	Load	Dif.
Axial Force 45 kN	20.74	9.21	13.1	14.4	23.3	31.6	8.3
Radial Force 45 kN	Bearing position 0°: 52	Bearing position 120°: 64	Bearing position 240°: 47	Bearing position Avg.: 54.3	Bolt pretension: 13.9	Load: 63	Dif.: 49.1
Tilting Moment 45 kNm	Dial gauge position 0°: 69.6	Dial gauge position 180°: -37.3	Sum.: 106.9	Sum.: 106.9	Measured point 0°: 18.4	Measured point 180°: -17.2	Sum.: 35.6
	Dial gauge distance: 1245 mm	Angle: 4.9°x10 <sup>-3</sup>	Measured point dist.: 1195 mm	Angle: 1.7°x10 <sup>-3</sup>			

Table 17: Validation of the bearing FEM, measured vs FEA deformations.

## 4.5 Results of the Derotator FEA

---

In the FEA the deformation generated by the load corresponds only to the difference between step 2 (simulating the application of the load) vs step 1 (representing only the application of the bolt pretension). Therefore both sets of values are required for the comparison with the experimental data. In the axial force load case, the deformation was experimentally measured for only one bearing position and the values registered by the three dial gauges are considerably different. For that reason, it may not be appropriate to directly compare the average measured deformation of  $14.4\ \mu\text{m}$  with the  $8.3\ \mu\text{m}$  obtained in the FEA. Indeed, the discrepancy is noticeably high, about 58%. However, both experimental and simulated deformations have the same order of magnitude, which can be considered an acceptable match, taking into account the size of the test setup and the small deformations registered by the dial gauges. For the radial force load case, the deformation of the bearing was measured for three different positions, which should provide better experimental data. In that case, the discrepancy between the average measured deformation and the FEA results is considerably smaller, less than 10%. Similarly as for the axial force load case, only one measurement was taken for the tilting moment load case. Therefore the same argument can be used to explain the difference between the experimental and simulated results.

## 4.5 Results of the Derotator FEA

Now, the alternative selected as result of the comparative analysis, using spring elements to replace the balls inside the slewing bearing, is applied on the nominal bearing for the MICADO derotator described in section 4.1. The stiffness of the spring elements is calculated according to the equations (28) to (32), where 60 equivalent spring pairs are implemented in the FEM as well. Using an osculation factor  $K = 0.08$  (which was defined by Rothe Erde for this special bearing), the equivalent stiffness of the springs used for the FEA of the MICADO derotator corresponds to  $161\ \text{kN/mm}$ . The boundary conditions applied to this calculation are similar to the ones used for the FEA of the CFRP bearing support structure. These boundary conditions are presented in Figure 74.

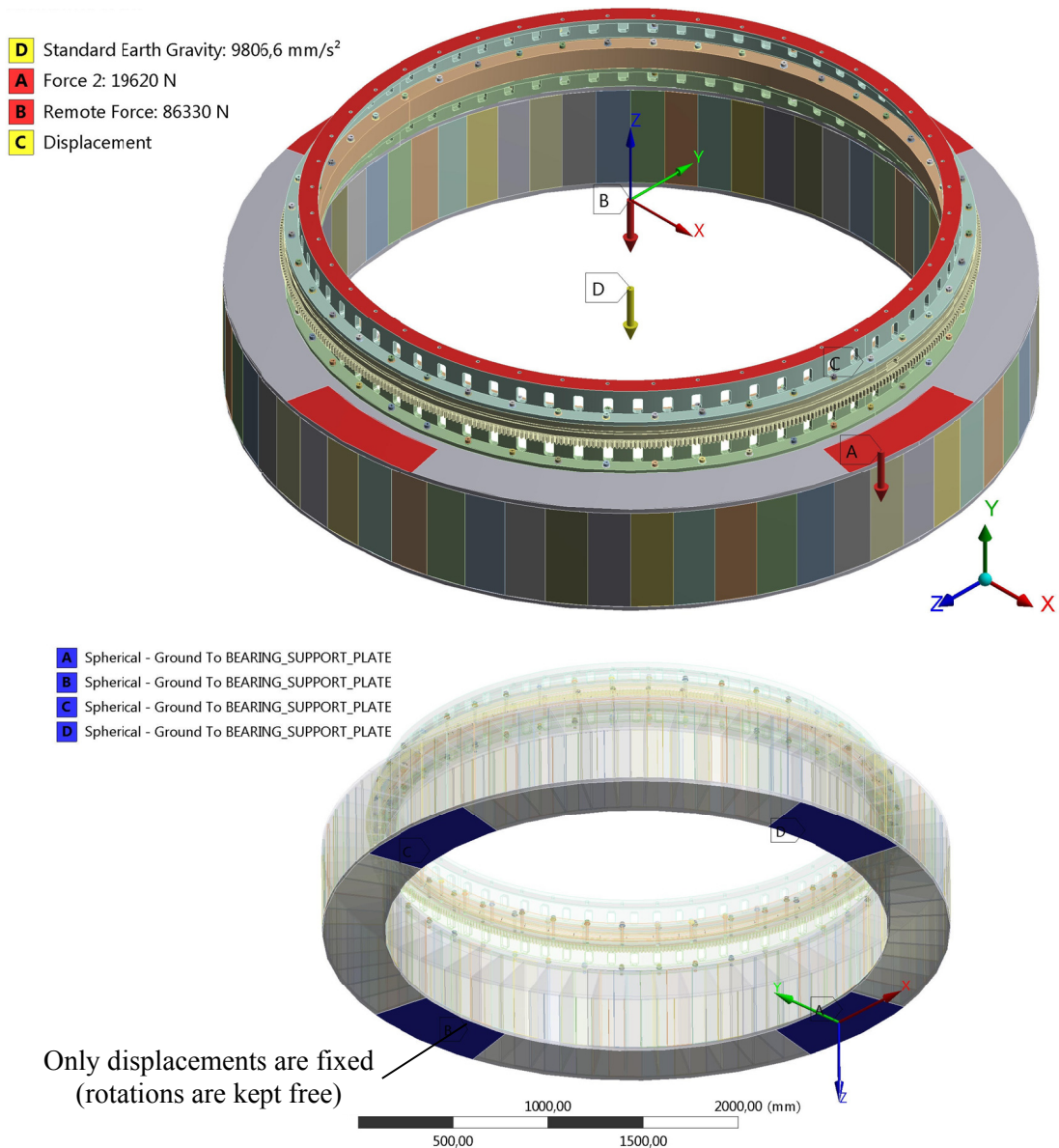


**Figure 74:** Boundary conditions used for the FEA of the MICADO derotator.

Now the difference in the boundary conditions is that the force representing the mass of the cryostat (Force B in this case), with a magnitude of 86.33 kN (corresponding to 8800 kg which is the current estimated mass for the cryostat plus the WFS module including 30% contingency), is applied on the contact surface of the upper thermal compensation ring, simulating the mechanical interface towards the cryostat. The “remote force” feature is used here, with the load located in the axis of rotation of the derotator (axis Z of the local coordinate system shown in Figure 74). The remote force allows the transmission of the moments generated by the location of the

#### 4.5 Results of the Derotator FEA

---

cryostat center of gravity. Additionally, the “displacement support” feature is also used in this calculation to restrict the rotation of the bearing outer ring with respect to the inner ring. In reality this degree of freedom is limited by the friction torque of the bearing. The connection between the bearing support ring and the instrument support structure is simulated in the same way using spherical joints, where only the displacements are fixed but the rotations are kept free.

All bolt connections in the derotator are simulated using bolt pretension and frictional contact, with values of 62.5 kN for the bolt pretension (which corresponds to a bolt pretension torque of 200 Nm for bolts strength class 8.8) and 0.2 for the friction coefficient respectively. In order to better mimic the reality, a multi steps analysis is also performed in this case. First the bolt pretension is applied, generating stresses and deformations in the model (first step) and then, once the bolt pretension has been “locked”, the additional loads are applied in the second step. As the mass of the drive units and the scanning heads mounts is negligible compared to the rotating mass and the weight of the relay optic support structure, they are not considered in the FEA.

In order to compare the results of the FEA with the requirements of the allowed axial and radial deformations into the bearing, the deformation plots corresponding to the axes of the global coordinate system can be directly used. However, to check the torsional deformation several control nodes are needed. Those control nodes are located at the bearing interfaces where the maximum (location 1) and minimum deformations (location 2) occur. The location of these control nodes are given in Figure 75. Location 1 corresponds to the area of the derotator which is not supported, between two supporting pads and, the location 2 corresponds to the area where the supporting pads are located (see Figure 77).



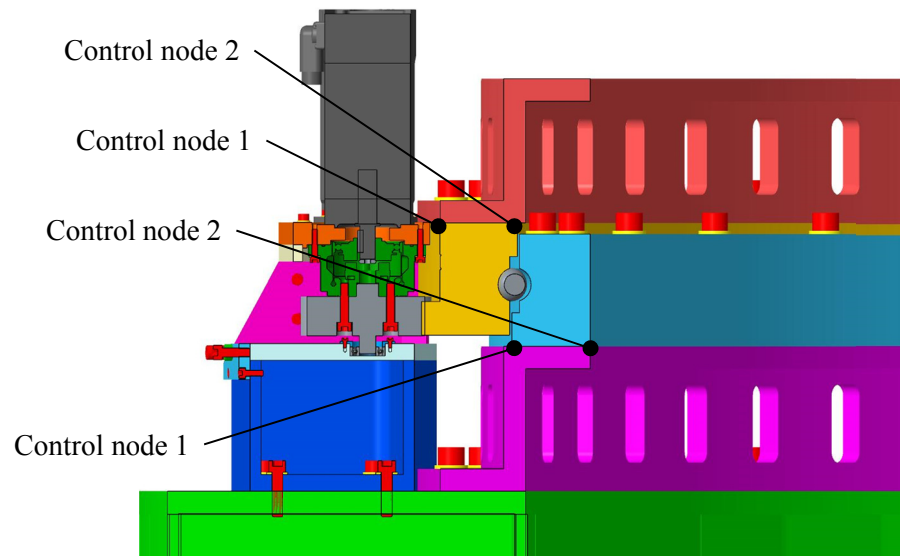


**Figure 75:** Location of the control nodes used to estimate the deformations on the bearing. The image shows the derotator cross section where one of the drive units is located.

The FEM of the MICADO derotator consist of 289057 nodes and the mesh used for this calculation is shown in Figure 76. The computing time required to run the simulation was ~10 min and ~9 GB of memory were used. As the FEM is not too large, more details can be included in future analyses. The results of the FEA corresponding to the complete derotator are given graphically in Figure 77 to Figure 80. Values for the total deformation as well as dedicated plots for the axes X, Y and Z of the global coordinate system are provided.

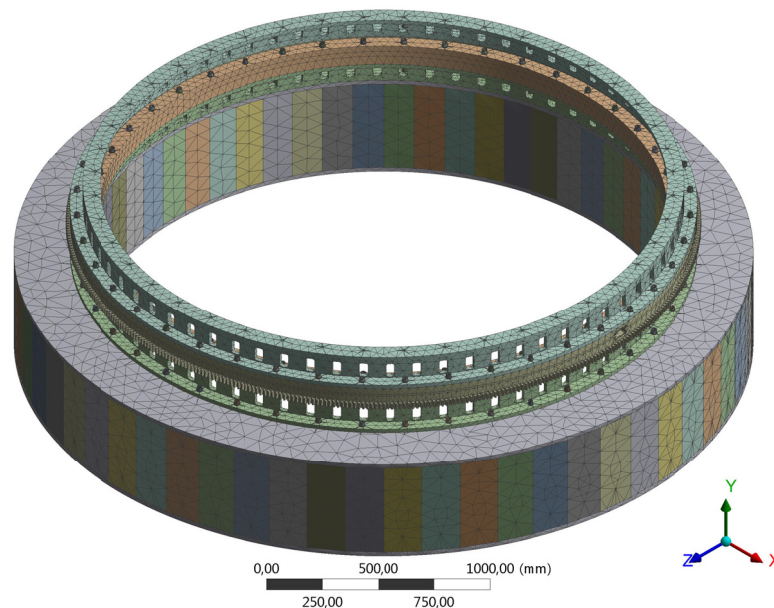


**Figure 76:** FEM of the MICADO derotator.

## 4.5 Results of the Derotator FEA

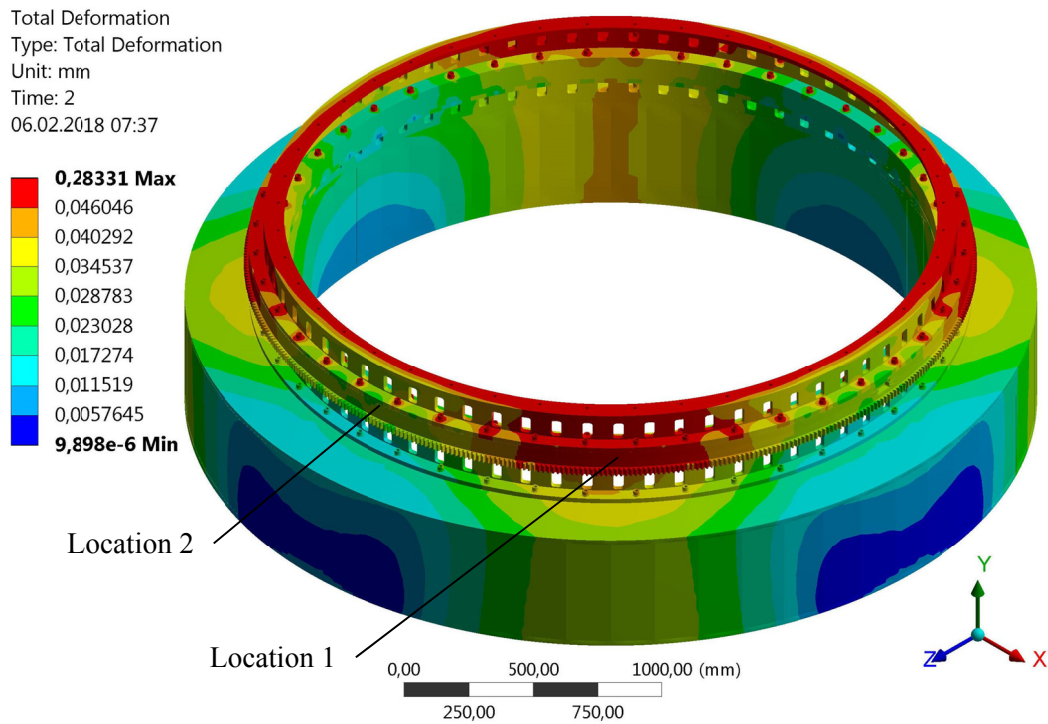


**Figure 77:** Derotator total deformation.

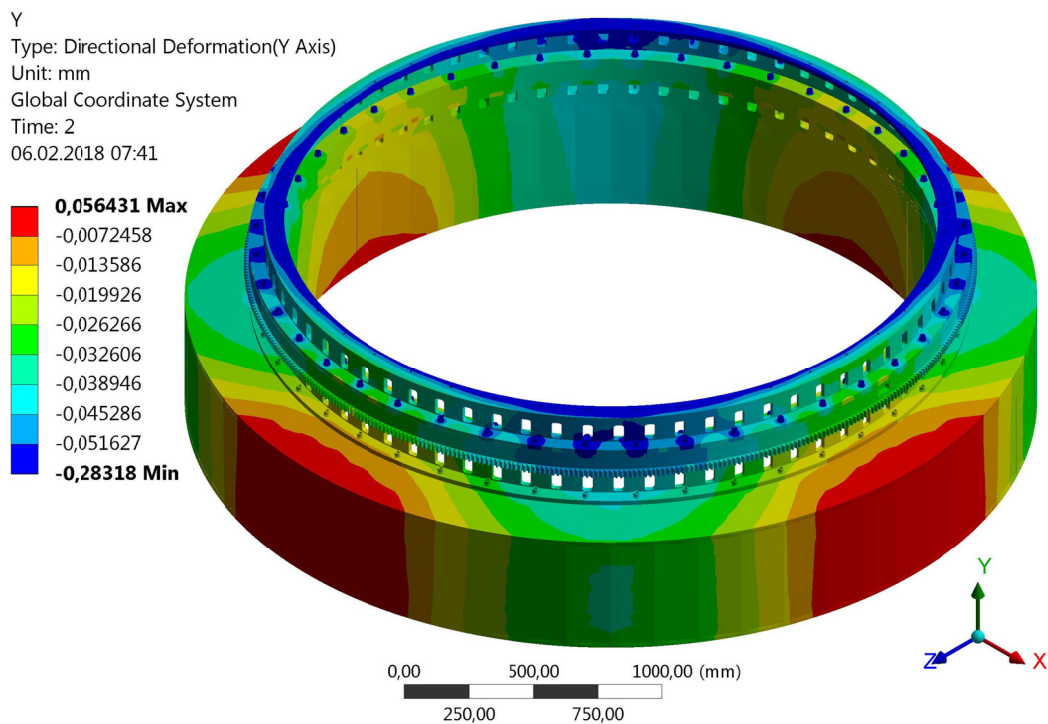


**Figure 78:** Derotator Y axis (axial) deformation.



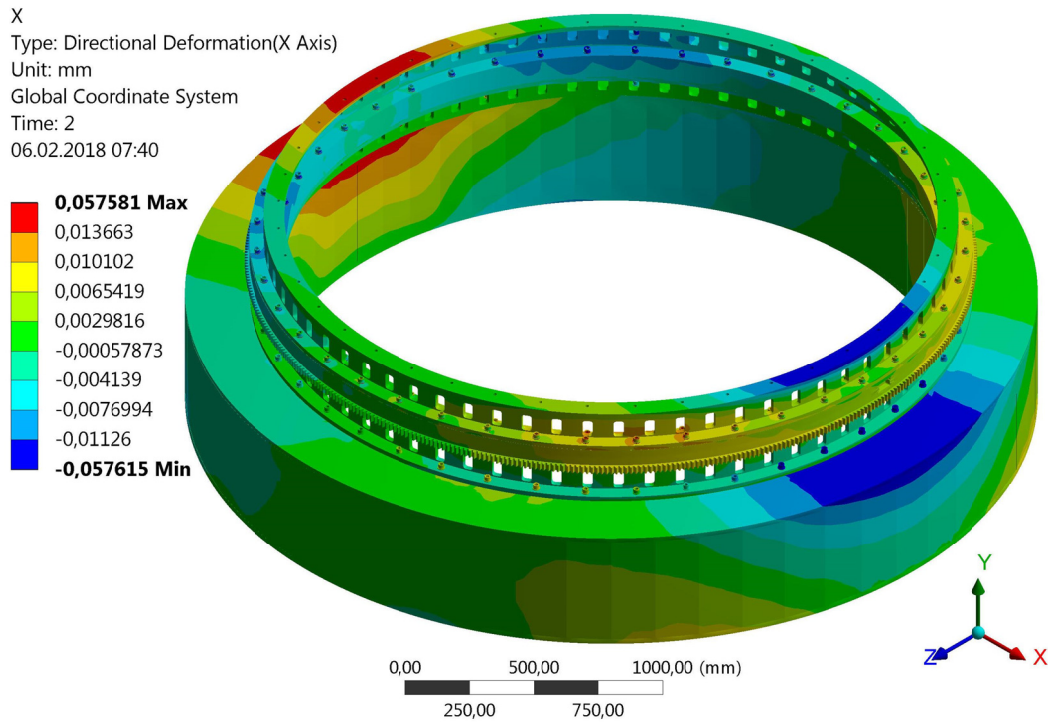


**Figure 79:** Derotator X axis (radial) deformation.

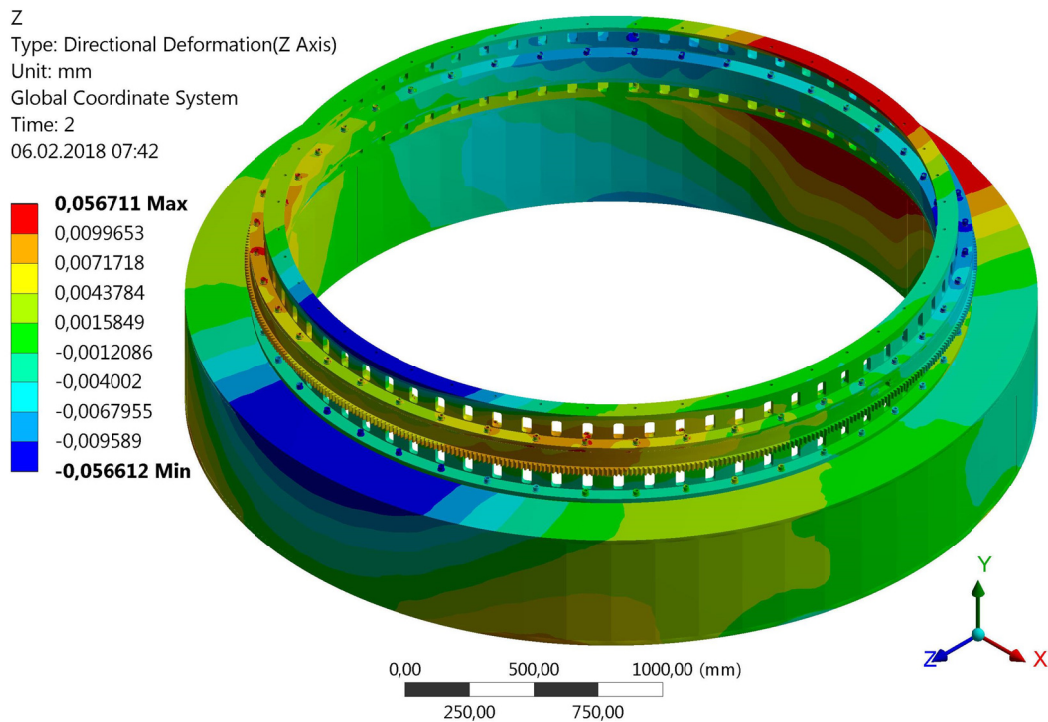


**Figure 80:** Derotator Z axis (radial) deformation.

## 4.5 Results of the Derotator FEA

The results previously presented (Figure 77 to Figure 80) give an overview of the general structural behavior of the derotator including all its components. Therefore the maximum values of deformations and stress are registered in the bolt connections due to the applied pretension. As earlier mentioned, the values of stress are not relevant for this application, consequently they are not discussed here.

On the other hand, in order to check the deformations introduced on the bearing itself, the outcome of the FEA must be evaluated focused only on this component. The results corresponding to the bearing total deformation and the values for the axes Y, X and Z are presented graphically in Figure 81 to Figure 84. The maximal axial deformation affecting the bearing can be directly retrieved from the Y axis deformation plot, corresponding to the difference between the maximum (location 1) and minimum (location 2) values registered in Figure 82. Otherwise, the maximal radial deformation is calculated as the magnitude of a vector defined by the components in the X and Z axes, which corresponds to the maximum (or minimum) deformation registered in Figure 83 and Figure 84 respectively. The maximal radial deformation is taking place in the location 1. Finally, the maximal torsional deformation is derived through the values in the Y axis registered at the control nodes defined in Figure 75. The results are summarized in Table 19.

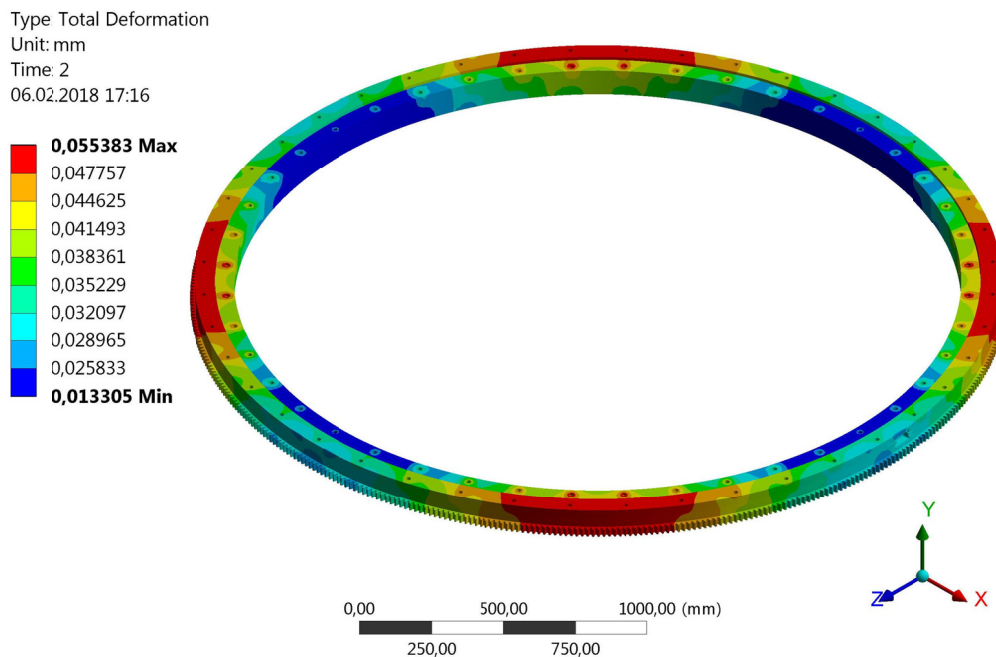


**Figure 81:** Bearing total deformation.

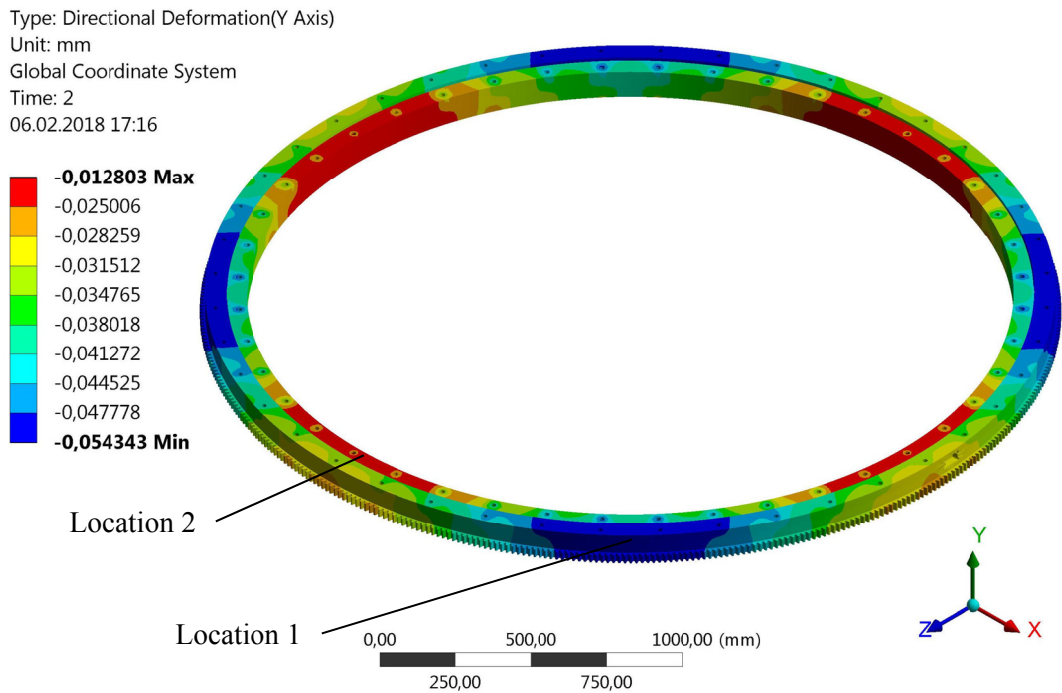


**Figure 82:** Bearing Y axis (axial) deformation.

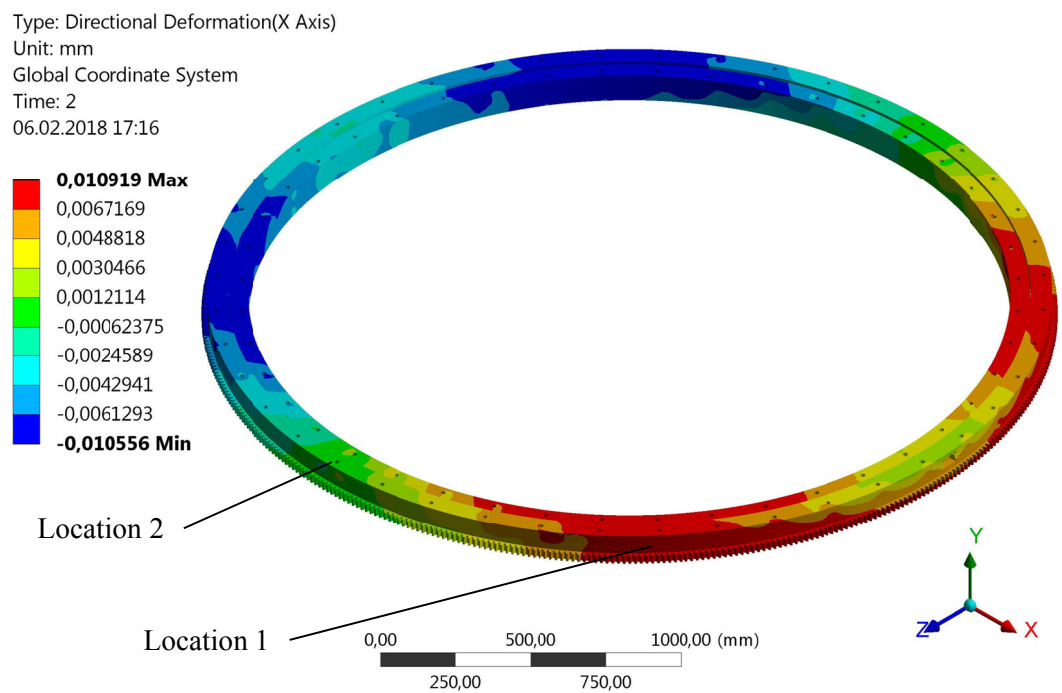


**Figure 83:** Bearing X axis (radial) deformation.

## 4.5 Results of the Derotator FEA

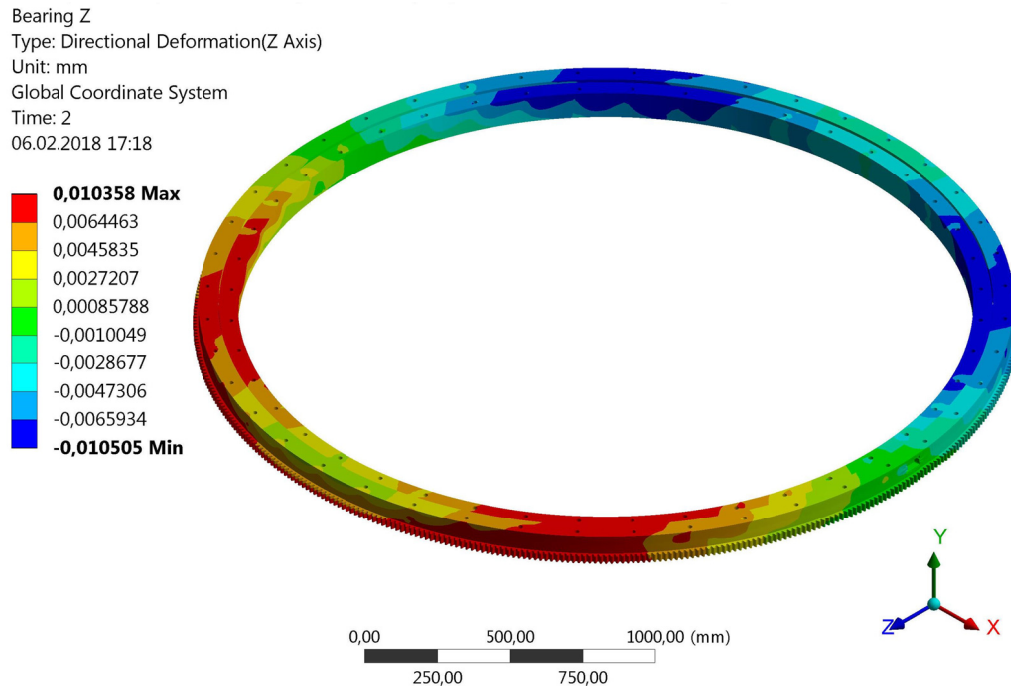


**Figure 84:** Bearing Z axis (radial) deformation.

Parameter	Value
Maximal axial deformation	0.042 mm
Maximal radial deformation	0.015 mm
Maximal torsional deformation	10.2 arcsec

**Table 18:** Deformations affecting the bearing according to the results of the FEA.

Part	Deformation	Location 1	Location 2	
Bearing Outer ring	Node 1	Axis Y	-0.051 mm	-0.032 mm
	Node 2	Axis Y	-0.052 mm	-0.034 mm
		Torsional	-2.06 arcsec	-5.76 arcsec
Bearing Inner ring	Node 1	Axis Y	-0.042 mm	-0.017 mm
	Node 2	Axis Y	-0.039 mm	-0.014 mm
		Torsional	10.20 arcsec	8.47 arcsec

**Table 19:** Bearing Y axis deformations registered at the control nodes.

According to the preliminary results provided in Table 19, the current design proposal is able to satisfy the requirement for the maximal axial deformation allowed into the bearing defined in Table 5. It is important to remember that when the quasi-

isotropic equivalent material is used, the estimated deformations are about twice as large in absolute terms, when compared to those obtained with the detailed CFRP FEM.

## 4.6 MICADO Instrument Eigenfrequency

The eigenfrequency of the whole MICADO instrument is a design aspect that must be carefully monitored. A requirement of 14 Hz (which already includes a safety factor of 2 over the minimum allowed value of 7 Hz) has been defined as the minimum for the first natural frequency of vibration (Schmid, 2015). Through the design process of the instrument support structure, it has been identified that the configuration of the mechanical interfaces towards the derotator has a considerable impact on the eigenfrequency of the instrument. For that reason, a dedicated modal analysis has been performed to estimate the impact of an interface with 8 supporting points instead of 4, which is the current baseline for the overall design of MICADO. The 8-points interface towards the bearing support structure can be obtained by splitting the supporting pads in the upper part of the octopod instrument support structure. This option provides a better load distribution for the derotator, which also has a significant impact with respect to the deformations coming into the bearing. Despite the results obtained with the derotator structural analysis, which in principle shows that the 4-points interface could work, the option with 8 supporting pads is seen as a better solution from the structural point of view.

The corresponding FEA is performed using a dummy single-piece cryostat to simulate the whole mass that the derotator must carry. The total mass of the derotator-cryostat assembly used for this simulation is about 12 tons. In addition, the structural effect of the relay optics group is also simulated here. In this case, a 2 ton dummy mass suspended above the cryostat by the supplementary octopod support structure of the relay optics table is used. The results of the modal analysis corresponding to the first eigenfrequency mode for both options are presented in Figure 85 and Figure 86, while the values for the next five Eigenfrequency modes are given numerically in Table 20.

## 4.6 MICADO Instrument Eigenfrequency

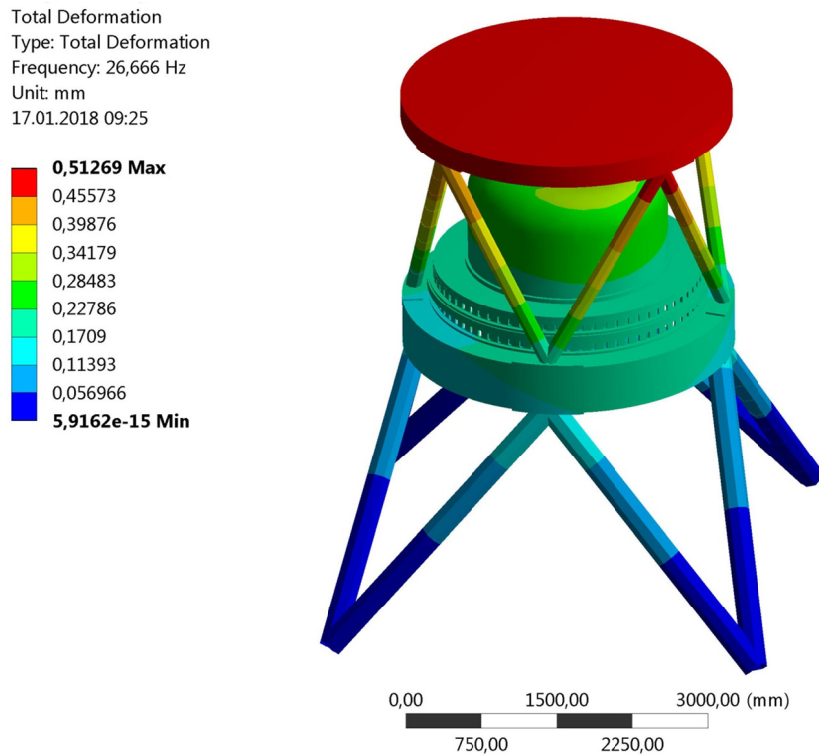


**Figure 85:** First eigenfrequency mode (26.7 Hz) of the MICADO instrument with a 4-point interface for the derotator.

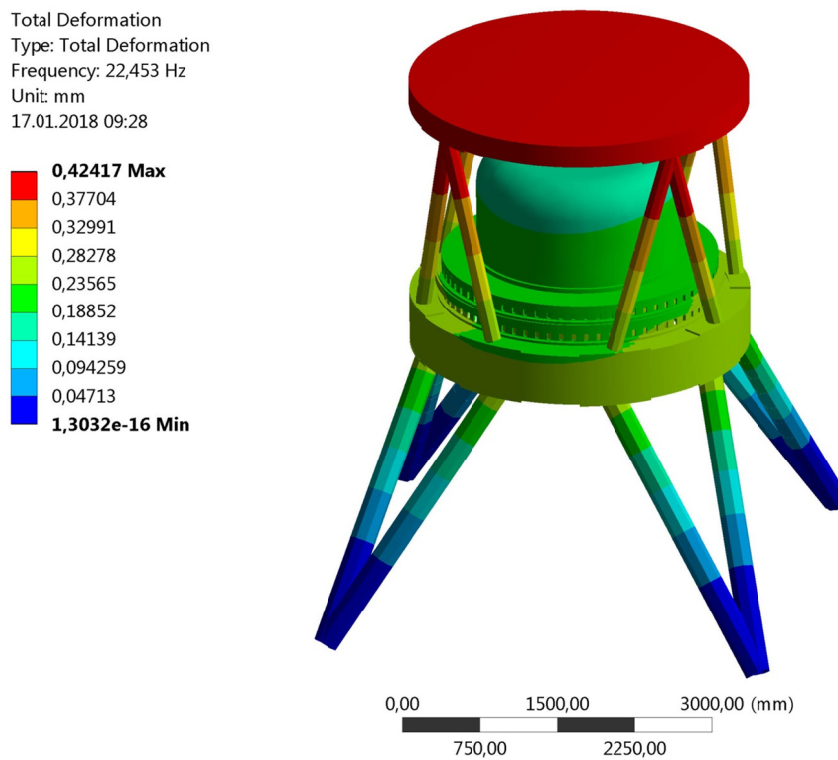


**Figure 86:** First eigenfrequency mode (22.5 Hz) of the MICADO instrument with a 8-point interface for the derotator.

Mode	Frequency 4-points (Hz)	Mode shape	Frequency 8-points (Hz)	Mode shape
1	26.7	Lateral movement	22.5	Lateral movement
2	26.7	Lateral movement	22.5	Lateral movement
3	45.8	Lateral movement	26.4	Lateral movement
4	45.8	Lateral movement	26.4	Lateral movement
5	48.2	Piston movement	30.5	Rotation
6	53.7	Rotation	49	Lateral movement

**Table 20:** Results of the modal analysis for the first six eigenfrequency modes.

In accordance with the results of the modal analysis for the whole MICADO instrument, the reduction of the first eigenfrequency as a consequence of the implementation of the 8-points interface corresponds only to 16%. Based on these results, it was recommended to the MICADO consortium to implement the 8-points interface, which delivers a better load distribution for the derotator-cryostat assembly. The interface option with 8 supporting points will contribute to the risk mitigation related to the overall performance of the MICADO instrument as well, providing a more stable mechanical setup while the cryostat is rotating on top of the derotator. The modal analysis has also demonstrated that the weakest part of the instrument, with respect to the Eigenfrequency, is the auxiliary octopod for the relay optics table.

## 4.7 Optimization of the Warping Moment Effect

The warping moment ( $W$ ) acting on the bearing support structure should be completely removed or at least reduced to its minimum. Nevertheless, this task must be carried out within the constraints imposed by the common mechanical interfaces of the derotator towards both (upper and lower) octopod support structures. A large warping moment over the derotator will introduce warping deformations on the bearing, which are not desired for the performance of the mechanism and could affect its angular positioning accuracy. The goal of the optimization of the warping moment is to achieve the static equilibrium of the bearing support structure cross section, where the sum of the moments (at the cross section centroid or center of gravity) should be minimized. An example with general rotationally symmetric load,



## 4.7 Optimization of the Warping Moment Effect

where the resulting warping moment is different to zero is given in Figure 87. This is the situation that should be avoided or minimized taking into account some correct design considerations. Strictly speaking, the behavior shown in Figure 87 is valid when the circular ring is supported with a full rotational symmetry, which is not the case of the bearing support structure supported only by 4 points. This principle is used to estimate the warping moment at the cross section of the bearing support ring where the interface pads are located, but is not applicable to the full circumference.

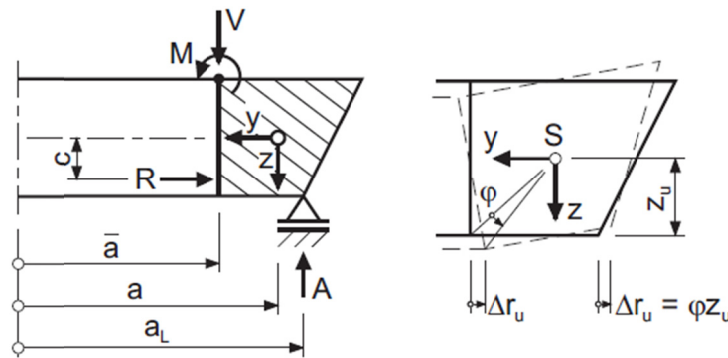


**Figure 87:** Effect of the resulting warping moment over the cross section of a circular ring. (Image source: Hake & Meskouris, 2007).

In order to better understand how the geometry of the cross section used for this calculation is obtained, both the full CAD model and the relevant cross section of the whole instrument are shown in Figure 88. Only the part of the cross section marked in the figure is used as reference for the estimation of the warping moment. The location of the centroid is performed using the CAD software. The location of the forces generating the warping moments are given in Figure 89 and Figure 90 for both cases, the current interface configuration and the proposal to reduce  $W$ . The results of the optimization process are presented in Table 21.



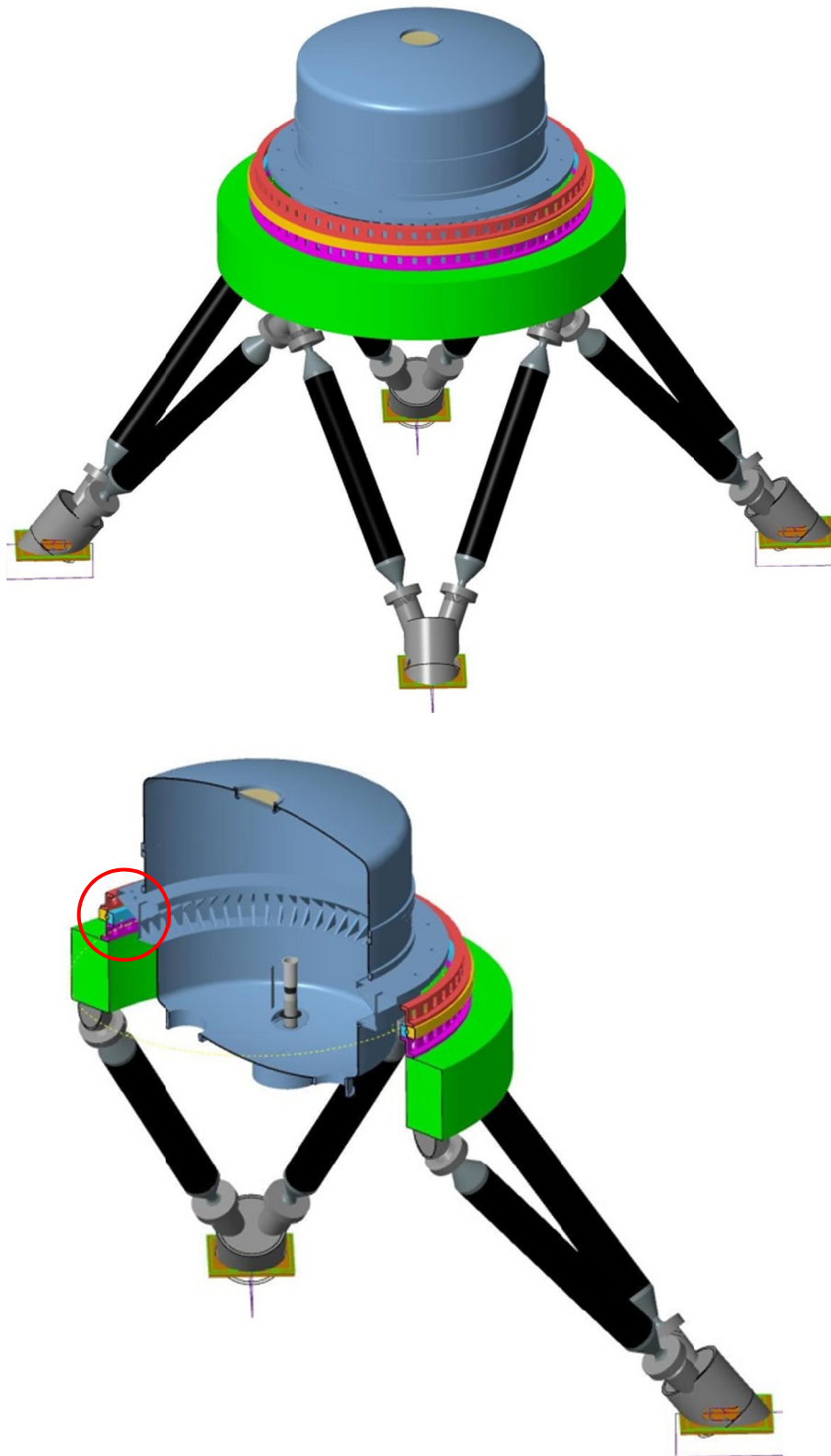


**Figure 88:** Location of the derotator cross section where the warping moment is calculated (the auxiliary octopod structure for the relay optics table is not show in this figure).

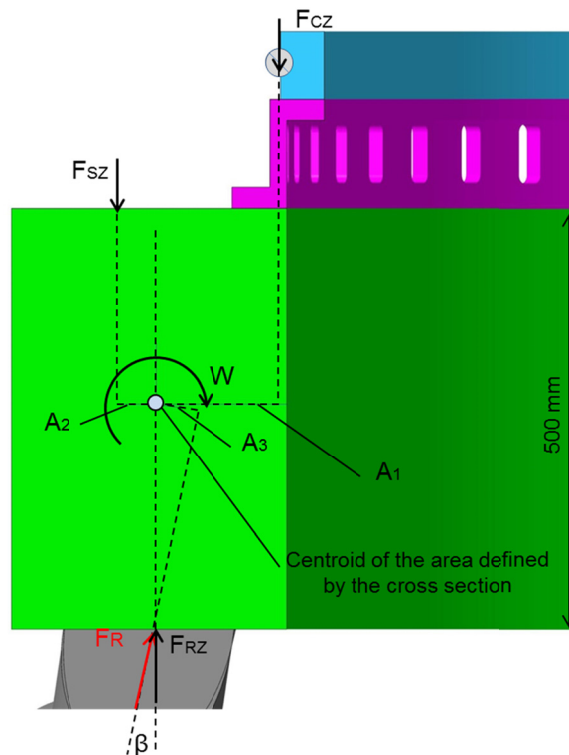


**Figure 89:** Location of the forces generating the warping moment according to the current position of the mechanical interfaces towards the upper and lower octopod structures.

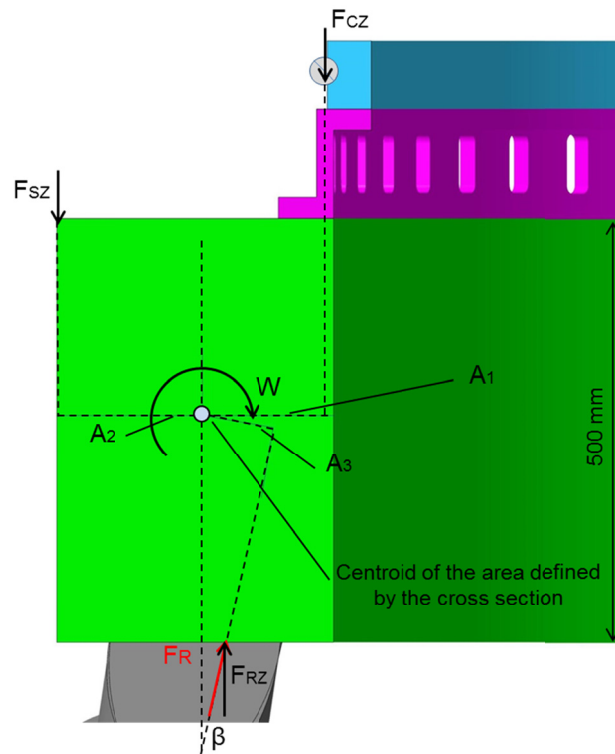


**Figure 90:** Location of the forces generating the warping moment according to the proposal to relocate of the mechanical interfaces towards the upper and lower octopod structures.

Parameter	Current interfaces	Proposed interfaces	Units
<b><math>W_1</math></b>			
Mass Cryostat	8.800	8.800	kg
Mass CTE Ring	300	300	kg
Mass Bearing/2	440	440	kg
Total mass	9.540	9.540	kg
For the calculation total mass/4	2.385	2.385	kg
F <sub>cz</sub>	23	23	kN
<b>A<sub>1</sub></b>	<b>0.155</b>	<b>0.155</b>	<b>m</b>
<b><math>W_1 = F_c A_1</math></b>	<b>3.63</b>	<b>3.63</b>	<b>kNm</b>
<b><math>W_2</math></b>			
Mass Relay Structure	2100	2100	kg
For the calculation total mass/4	525	525	kg
<b>F<sub>sz</sub></b>	<b>5.15</b>	<b>5.15</b>	<b>kN</b>
<b>A<sub>2</sub></b>	<b>0.040</b>	<b>0.172</b>	<b>m</b>
<b><math>W_2 = F_{sz} A_2</math></b>	<b>0.2</b>	<b>0.9</b>	<b>kNm</b>
<b><math>W_3</math></b>			
Mass Cryostat	8.800	8.800	kg
Mass Derotator	2.140	2.140	kg
Mass Relay Structure	2.100	2.100	kg
Total mass	13.040	13.040	kg
For the calculation total mass/4	3.260	3.260	kg
<b>F<sub>RZ</sub></b>	<b>32.0</b>	<b>32.0</b>	<b>kN</b>
<b>β</b>	<b>8.4</b>	<b>9.5</b>	<b>°</b>
<b><math>F_R = F_{RZ}/\cos\alpha</math></b>	<b>32.33</b>	<b>32.43</b>	<b>kN</b>
<b>A<sub>3</sub></b>	<b>0.031</b>	<b>0.85</b>	<b>m</b>
<b><math>W_3 = F_{RZ} A_2</math></b>	<b>1.0</b>	<b>2.76</b>	<b>kNm</b>
<b><math>W = W_1 - W_2 - W_3</math></b>	<b>2.42</b>	<b>-0.02</b>	<b>kNm</b>

**Table 21:** Results of the warping moment optimization.

Ideally in order to reduce  $W$ , the interface pads of the instrument support structure should be moved radially inwards towards the derotator axis of rotation. The interfaces pads of the relay optics support structure should be moved radially outwards away from the derotator axis of rotation. Nevertheless this task is clearly limited by the available space to locate both sets of interface pads. This, however, is only valid in the case of ideal rotational symmetry with constant support, which is not given for the envisaged octopod. Here, the intermediate sections between the struts experience different kind of deformations and the effects of the warping moment optimization need to be verified via FEA. In order to preserve the

#### 4.7 Optimization of the Warping Moment Effect

---

advantages of a lower warping moment for the bearing, the always favored 8-point-mounting (of the same octopod) is strongly recommended. This not only reduces the deformations along the circumference of the bearing (axial direction), but also additional perpendicular deformations in the radial direction. This is for the cost of only ~21.5% (15.8% with relay optics table) of eigenfrequency reduction and with >23Hz well above the 14Hz requirement (14Hz already including a safety factor of 2).

## 5 The end-to-end simulation

An end-to-end simulation allows considering all essential elements and effects between the input and the output of a dynamic system. So far, mainly the static performance of the MICADO derotator preliminary design has been discussed and analyzed in detail in chapter 4. The static FEA considered here focuses on the linear relation that exists between the displacements, the stiffness of a body or mechanical system (in this case the derotator) and the external forces applied to it. This relation can be described for a mechanical system in generalized coordinates by an algebraic equation or by a linear system of equations in matrix form (in the case of several degrees of freedom) with the following expression

$$Kq = \tilde{F}, \quad (33)$$

where  $K$  is the stiffness matrix of the mechanical system,  $q$  is a vector representing the displacements of the degrees of freedom in generalized coordinates and  $\tilde{F}$  is the load or external excitation applied to the system. Equation (33) is mostly used to solve elastostatic problems, but it can be also used for other stationary phenomena (Bathe, 2014). For problems involving structural dynamics, however, other effects like the structural damping or viscous friction and the effects of inertia of the system must be considered in the analysis (see section 5.1).

This chapter provides the basic tools to develop the end-to-end simulation of the MICADO derotator, where its dynamical structural performance can be combined with the controller architecture, in order to estimate the performance of the derotator as a complete system. The contribution of this research work for the full end-to-end simulation of the derotator is focused only on the mathematical modelling of the mechanical system and the friction phenomenon of the bearing. The modelling of the

control system was developed in parallel, implemented in the test stand (chapter 6) and will be described in Glück (2019).

### 5.1 Basics of structural dynamics

Real technical systems can be simulated by idealized equivalent systems defined through mathematical expressions. In this case, the key task of the engineers is to identify the influential aspects (parameters) of the real technical problem and appropriately reproduce them in the idealized equivalent mathematical model. In order to represent a multibody mechanical system lumped mass models are typically used, which consist of single masses (or bodies with a defined moment of inertia in the case of rotational movement) joined together e.g. with dampers and springs. This ideal equivalent model will not provide an exact representation of the real physical system, but it will deliver an approximation which in most of the cases is good enough for the task under analysis (Wagner & Mlejnek, 2012). For the given particular application, it is estimating the dynamic performance of the MICADO derotator.

Representing the dynamic behavior of a mechanical system by means of a mathematical model can often be accomplished by extending equation (33), which was used to represent the static performance of a mechanical system (in that case, velocities and accelerations are zero, therefore the damping effect and inertial effects, respectively, are not considered in the equation). So, the dynamic behavior of a mechanical system with multiple degrees of freedom can be represented as follow

$$M\ddot{q} + D\dot{q} + Kq = \tilde{F}, \quad (34)$$

where  $\ddot{q}$ ,  $\dot{q}$ ,  $q$  are the vectors of acceleration, velocity and displacements in generalized coordinates and,  $M, D, K$  are the mass, damping and stiffness matrices. Equation (34) is a second order differential equation that can be analytically solved and has exact basic solutions for especial cases depending on the damping ratio value.

Equation (34) can be written for the special case of a linear system with one degree of freedom following the same general form

$$m\ddot{q} + d\dot{q} + kq = \tilde{F}, \quad (35)$$

where  $m$  is the mass or moment of inertia in case of rotational displacements,  $d$  damping coefficient (translational or rotational),  $k$  is the stiffness (translational or rotational),  $q$  is the degree of freedom (displacement or rotation) and  $\tilde{F}$  is the load, that could be represented by a force or a moment depending on the case.

If the general mathematical expression describing a mechanical system with one degree of freedom (35) is divided by  $m$ , the following standard form can be obtained

$$\ddot{q} + 2D\omega_0\dot{q} + \omega_0^2q = \frac{\omega_0^2}{k}\tilde{F}, \quad (36)$$

where  $D$  is the dimensionless damping ratio and  $\omega_0$  is the undamped natural frequency expressed in Hz. These two system parameters are defined as follow:

$$\omega_0 = \sqrt{\frac{k}{m}}, \quad (37)$$

$$D = \frac{d}{2\sqrt{mk}}. \quad (38)$$

As a first step to use equation (36) for the analysis of mechanical systems, the solution of a simplified case where  $\tilde{F}(t) = 0$  (system under free oscillations) is initially discussed. This is known as the homogeneous solution and is also used to describe the different possible solutions according to the damping ratio  $D$ . The special case of an undamped system is not of interest for this application and therefore is not discussed here. Afterwards, the so called particular solution with  $\tilde{F}(t) \neq 0$  (system under forced oscillations) is briefly introduced, to finally obtain the general overall solution. More elaborated information about the analysis of equation (36) and the corresponding solutions is provided by Wagner & Mlejnek (2012).

### 5.1.1 Body under Free Oscillations with Damping

Equation (36) is describing the standard form of the equation of motion, with  $\tilde{F}(t) = 0$  it can be written as

$$\ddot{q} + 2D\omega_0\dot{q} + \omega_0^2q = 0. \quad (39)$$

For the case of a system with damping ( $D > 0$ ) three different cases can be defined, i.e. underdamped ( $D < 1$ ), critically damped ( $D = 1$ ) and overdamped ( $D > 1$ ). As the underdamped case is the relevant one for metal structures analysis, this is the only case discussed here. A typical value for the damping ratio in this kind of structures is  $D = 0.05$  (Wagner & Mlejnek, 2012). The solution  $q(t)$  for equation (39) with  $D < 1$  is defined by equation (40)

$$q(t) = e^{-D\omega_0 t}(\hat{q}_c \cos \omega t + \hat{q}_s \sin \omega t), \quad (40)$$

where the parameters  $\hat{q}_c$  and  $\hat{q}_s$  are constants that can be determined with the initial conditions applied to the system:

$$q(t_0 = 0) = q_0 \text{ and } \dot{q}(t_0 = 0) = \dot{q}_0. \quad (41)$$

Using the subsequent equations (42) and (43)

$$\hat{q} = \sqrt{\hat{q}_c^2 + \hat{q}_s^2} \quad (42)$$

$$\tan \varphi = \frac{\hat{q}_s}{\hat{q}_c} \quad (43)$$

the homogeneous solution can be reformulated in the form

$$q(t) = e^{-D\omega_0 t} \hat{q} \cos(\omega t - \varphi), \quad (44)$$

where the parameter  $\hat{q}$  represents the amplitude and  $\varphi$  the phase shift. The damped natural frequency  $\omega$  is then defined as follow

$$\omega = \omega_0 \sqrt{1 - D^2}. \quad (45)$$



### 5.1.2 Body under Forced Oscillations with Damping

The situation of bodies under the effects of external forces is the most relevant for the analysis of real applications. Following the same approach as in the previous section, only the solution for the underdamped ( $D < 1$ ) case is discussed here. Using the superposition principle, the general overall solution of equation (36) can be obtained by adding the particular solution ( $q_p$ ), to the previously described homogeneous solution presented in equation (40). This results in the following expression

$$q(t) = e^{-D\omega_0 t}(\hat{q}_c \cos \omega t + \hat{q}_s \sin \omega t) + q_p(t). \quad (46)$$

The general case of a harmonic excitation is used as input for the equation of motion defined by equation (36), in which  $\tilde{F}$  is represented by a force of the form

$$\tilde{F}(t) = \hat{F} \cos \Omega t, \quad (47)$$

where  $\hat{F}$  is the excitation amplitude in N or Nm and  $\Omega$  is the excitation frequency in Hz. The particular solution  $q_p(t)$  corresponding to the harmonic excitation  $\tilde{F}(t)$  is (Wagner & Mlejnek, 2012):

$$q_p(t) = \frac{\hat{F}}{k} V(\eta) \cos(\Omega t - \varphi_0(\eta)) \quad (48)$$

with

$$\eta = \frac{\Omega}{\omega_0} \quad (49)$$

$$V(\eta) = \frac{1}{\sqrt{(1 - \eta^2)^2 + 4D^2\eta^2}} \quad (50)$$

$$\varphi_0(\eta) = \arctan \frac{2D\eta}{1 - \eta^2} \quad (51)$$

In practice, the differential equation or system of differential equations for arbitrary functions of  $\tilde{F}(t)$  defining the equations of motions of a mechanical system are solved with software of numerical analysis like MATLAB and Simulink. For this

purpose, the general equation of motion in matrix form (a second order differential equation) described by equation (34), is normally rearranged multiplying the whole equation by the term  $M^{-1}$  as follows

$$\ddot{q} = -M^{-1}D\dot{q} - M^{-1}Kq + M^{-1}\tilde{F}. \quad (52)$$

The second order differential equation as described in Equation (52) can be directly solved in Simulink (Herman, 2017), either as a single equation for a mechanical system with one degree of freedom or in matrix form for a system with multiple degrees of freedom. Simulink is also the tool used to simulate the dynamic performance of the derotator mechanical system in this thesis. As systems become more complex, in some cases the state-space representation of a dynamic system is more convenient. Another alternative of representing a dynamic system is by its transfer function. These approaches are discussed in the next sections.

### 5.1.3 State-Space Representation

The state-space representation of a mechanical system is normally used to simplify its mathematical model. It results from transforming the second order differential equation representing its dynamic performance (52), into a single first order matrix differential equation. This can be done with the introduction of the so called state variables  $x, \dot{x}$ , that will fully describe the system and its response to external excitations. The state variables are defined as follows

$$x = \begin{bmatrix} q \\ \dot{q} \end{bmatrix} \quad (53)$$

$$\dot{x} = \begin{bmatrix} \dot{q} \\ \ddot{q} \end{bmatrix}. \quad (54)$$

The general state-space representation of a dynamic system is then given by the following equations

$$\dot{x} = Ax + Bu \quad (55)$$

$$y = Cx + Du, \quad (56)$$

where  $A$  is called the state or system matrix,  $B$  is the input matrix,  $C$  output matrix and  $D$  is the feedforward matrix. All four matrices are constant and represent the characteristics of the system. The parameter  $u$  represents the input vector of the system and  $y$  describes the output vector (Åström & Murray, 2009).

Taking the general equation of motion (52), the dynamic system in state-space representation is defined as

$$\dot{x} = \begin{bmatrix} 0 & 1 \\ -M^{-1}K & -M^{-1}D \end{bmatrix} x + \begin{bmatrix} 0 \\ M^{-1}\tilde{F} \end{bmatrix} u \quad (57)$$

$$y = [1 \quad 0]x. \quad (58)$$

As most mechanical system models do not have a direct feedforward, the  $D$  matrix is often zero. Typically, the feedforward is part of the control system, it does not belong to the mechanical system itself.

### 5.1.4 Structural Transfer Function

The transfer function is also a commonly used method to describe a dynamic system. Generally speaking, it describes the input-output relation of the system, in other words, how the system reacts to any given input like an external force. If the dynamic system is represented by a differential equation, as in the case of the mechanical system with one degree of freedom defined by equation (35), the transfer function can be obtained taking the Laplace Transform of the differential equation with zero initial conditions. Recalling equation (35)

$$m\ddot{q} + d\dot{q} + kq = \tilde{F}, \quad (35)$$

the Laplace Transform of this differential equation can be written as

$$(ms^2 + ds + k)q(s) = \tilde{F}(s). \quad (59)$$

The transfer function of the system is the ratio between the output and the input, normally denoted by  $G(s)$  or  $H(s)$

$$H(s) = \frac{q(s)}{\tilde{F}(s)} = \frac{1}{(ms^2 + ds + k)}, \quad (60)$$

where  $\tilde{F}(s)$  represents the input and  $q(s)$  the output of the system.

The transfer function is frequently used for characterizing existing dynamic systems and for the parameter identification or verification of dynamic system models in the frequency domain. This method is also called the frequency response or harmonic response of the system. In this case, the output describing the behavior of the system (calculated through its transfer function) is registered by its response to a harmonic sine or cosine steady state input signal. The results of the frequency response of a dynamic system are normally presented in the so called Bode plot, where the amplitude and the phase shift are plotted as a function of the input signal frequency.

In some applications, deriving the mathematical model of a dynamic system can be difficult. The frequency response can be here a powerful tool to experimentally obtain the transfer function of a dynamic system. This technique is called sine sweep method, where the frequency response is obtained over the desired frequency range. The analytical transfer function is then obtained by curve fitting the experimental data (Åström & Murray, 2009).

## 5.2 Specific challenges of modelling the derotator

As the derotator is a subsystem of the whole MICADO instrument, which connects the cryostat with the instrument support structure, the dynamic performance of the derotator cannot be analyzed as an independent subsystem. The effects of the instrument support structure, the relay optics support structure and the cryostat, must be considered in the mechanical model. This means, that the mathematical model of the whole MICADO instrument mechanical system is required to estimate the dynamic performance of the derotator. For the end-to-end simulation a lumped mass model equivalent to the MICADO instrument is presented in Figure 91 (as the relay optic table is still not determined, this element has not yet been included in the model), where the relevant rotational degree of freedom is defined by the parameter  $\theta$ .

The mechanical model includes the servo motor (yellow box), the Harmonic Drive gear (green box), the bearing (which is divided into two parts, i.e. the outer and inner

ring for a better implementation of the model), the bearing support structure, the cryostat and the internal cold structure of the cryostat. All these elements represent single bodies with a defined moment of inertia  $j$ , which are adequately joined with a combination of spring and dampers to simulated the MICADO instrument.

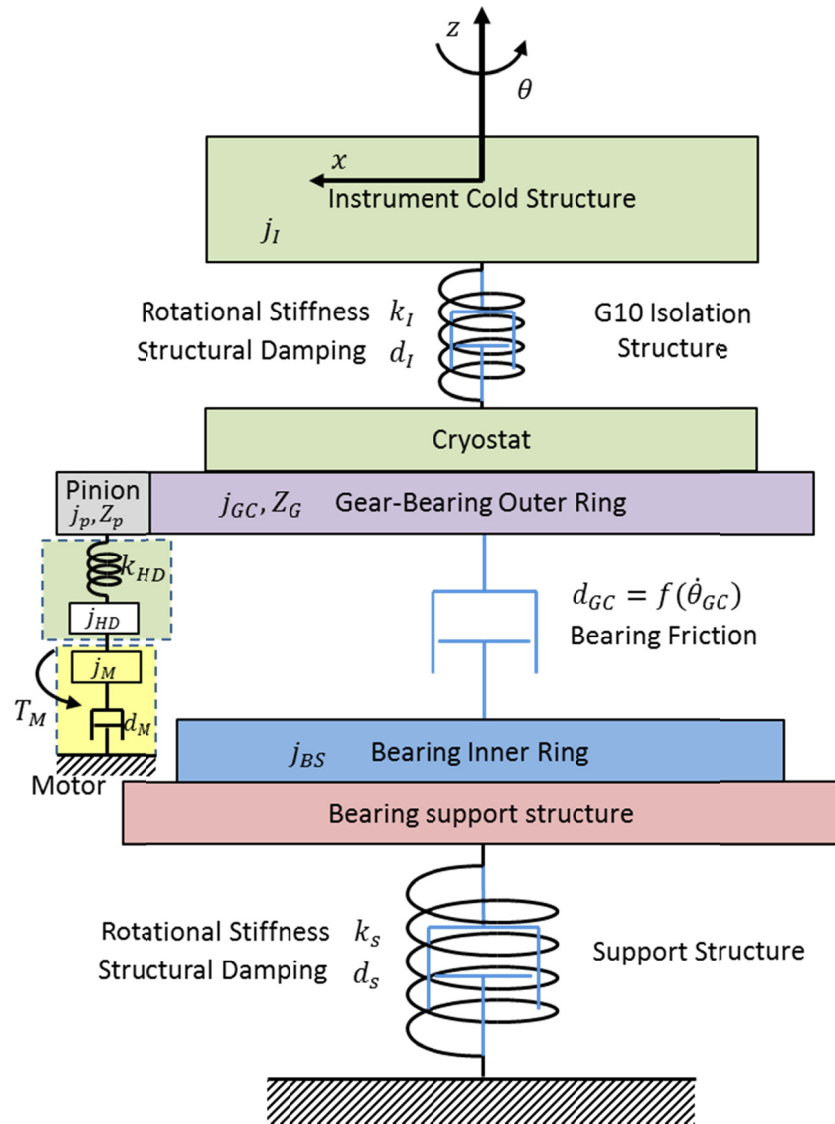


**Figure 91:** MICADO instrument mechanical model.

Starting with the instrument from the bottom up, the first body (with moment of inertia  $j_{BS}$ ) representing the bearing support structure and bearing inner ring (including the lower thermal compensation ring) is joined to the ground by a spring ( $k_s$ ) and a damper ( $d_s$ ) serving as the instrument support structure. The second body (with moment of inertia  $j_{GC}$ ), representing the cryostat vessel and bearing outer ring

(including the upper thermal compensation ring) is joined to the first body by means of a damper ( $d_{GC}$ ) as substitute of the bearing friction. The bearing friction is not a constant variable and is actually a nonlinear phenomenon which is not trivial to model (see section 5.3), therefore this parameter is represented as a function of the bearing angular velocity  $d_{GC} = f(\dot{\theta}_{GC})$ . The third body (with moment of inertia  $j_I$ ) representing the cryostat internal cold structure is joined to the second body by a spring ( $k_I$ ) and a damper ( $d_I$ ) as the isolating structure. Finally, the drive unit is modeled with the following configuration: the body representing the servomotor (with moment of inertia  $j_M$ ) is joined to the ground by a damper ( $d_M$ ), the body representing the Harmonic Drive gear (with moment of inertia  $j_{HD}$ ) is joined to the element representing the motor by an ideal stiff connection and consequently no spring is implemented here, the last body representing the pinion (with moment of inertia  $j_P$ ) is joined to the element describing the Harmonic Drive gear by a spring ( $k_{HD}$ ). The Harmonic drive is a complex element itself and the simplest possible representation has been selected for the MICADO mechanical model, which consist of modeling it as a pinion and a gear wheel pair. The equivalent system using this approach is presented in Figure 92. More detailed models are given by Tuttle (1992) and Taghirad (1995).

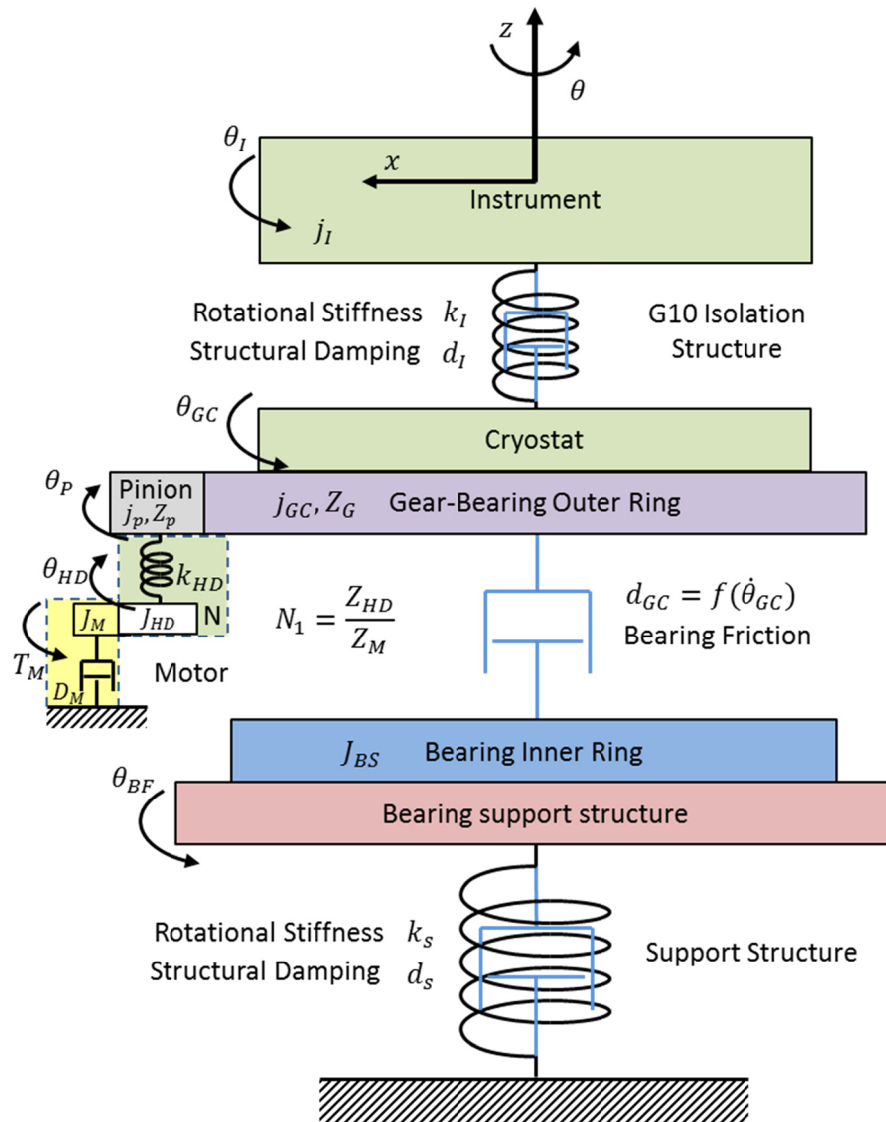


**Figure 92:** Equivalent MICADO instrument mechanical model where the Harmonic Drive gear is modeled as a pinion and gear wheel pair.

The equivalent model described in Figure 92 consists of a six degrees of freedom mechanical system. By means of some mathematical manipulation the motor degree of freedom ( $\theta_M$ ) can be eliminated (Turner, 2011), where the effects generated by the Harmonic Drive Gear ratio ( $N_1$ ) are represented in a new equivalent body defined by  $j_{E1}$ . This reduced equivalent MICADO mechanical model is presented in Figure 93 and the new equivalent parameters are defined by equations (61) to (64).

## 5.2 Specific challenges of modelling the derotator

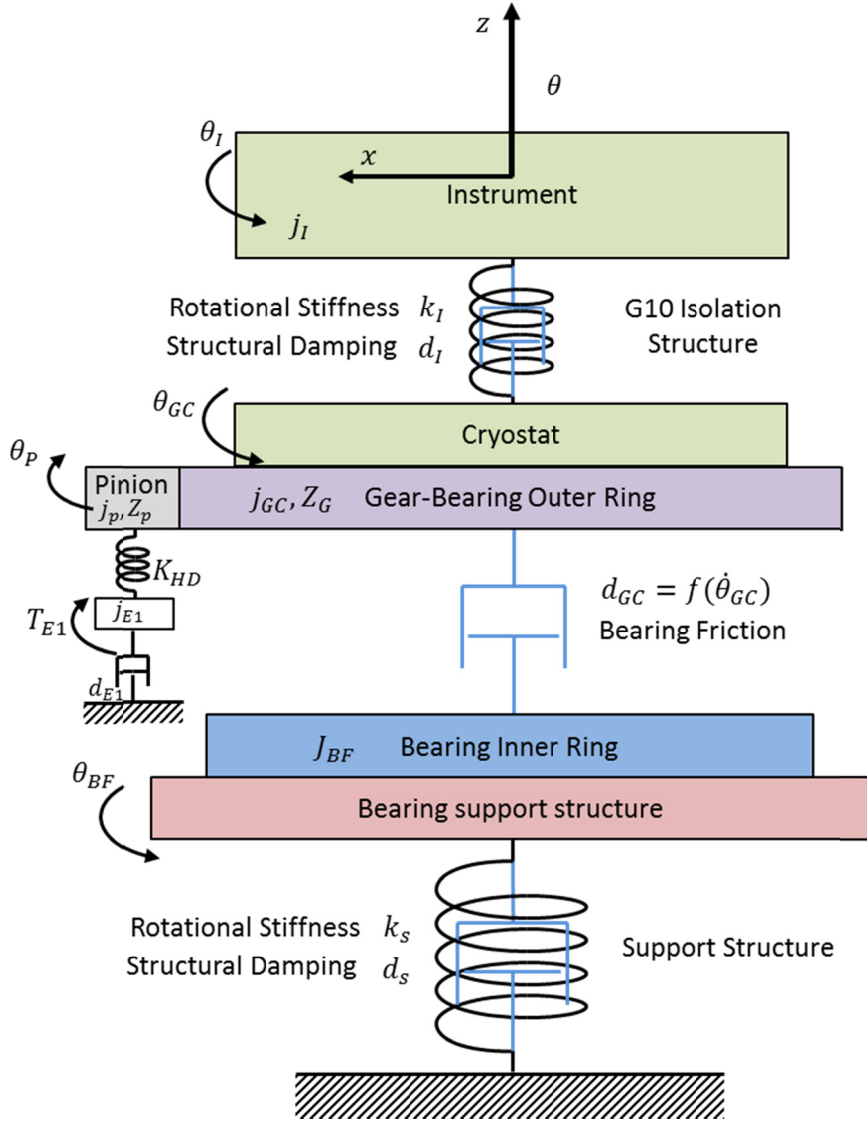


**Figure 93:** Reduced equivalent MICADO instrument mechanical model.

$$\theta_M = \theta_{E1} N_1 \quad (61)$$

$$T_{E1} = T_M N_1 \quad (62)$$

$$j_{E1} = j_{HD} + j_M (N_1)^2 \quad (63)$$

$$d_{E1} = d_M (N_1)^2 \quad (64)$$



Through the free body diagrams of each of the element considered in the reduced MICADO mechanical model, the following equations of motion can be established:

$$-j_{E1}\ddot{\theta}_{E1} - d_{E1}\dot{\theta}_{E1} - k_{HD}\theta_{E1} + k_{HD}N_2\theta_{GC} = -T_{E1} \quad (65)$$

$$-j_P\ddot{\theta}_P - k_{HD}\theta_P + k_{HD}\theta_{E1} + F_c R_P = 0 \quad (66)$$

$$j_{GC}\ddot{\theta}_{GC} + (d_{GC} + d_I)\dot{\theta}_{GC} + k_I\theta_{GC} - d_I\dot{\theta}_I - d_{GC}\dot{\theta}_{BF} - k_I\theta_I + F_c R_G = 0 \quad (67)$$

$$j_{BF}\ddot{\theta}_{BF} + (d_S + d_{GC})\dot{\theta}_{BF} - d_{GC}\dot{\theta}_{GC} + k_S\theta_{BF} = 0 \quad (68)$$

$$j_I\ddot{\theta}_I + d_I\dot{\theta}_I + k_I\theta_I - d_I\dot{\theta}_{GC} - k_I\theta_{GC} = 0. \quad (69)$$

By means of mathematical arrangement equations (66) and (67) can be combined in one single equation of the form

$$j_{E2}\ddot{\theta}_{GC} + (d_{GC} + d_I)\dot{\theta}_{GC} - d_I\dot{\theta}_I - d_{GC}\dot{\theta}_{BF} + k_{E2}\theta_{GC} - k_I\theta_I - N_2 k_{HD}\theta_{E1} = 0 \quad (70)$$

where  $N_2$  is the gear ratio between the gear wheel and the pinion and

$$j_{E2} = j_{GC} + j_P(N_1)^2 \quad (71)$$

$$k_{E2} = k_I + K_{HD}(N_1)^2. \quad (72)$$

This operation reduces the mathematical model to a system of four second order differential equations and that system of four equations can also be written in matrix form as follows

$$\begin{bmatrix} -j_{E1} & 0 & 0 & 0 \\ 0 & j_{E2} & 0 & 0 \\ 0 & 0 & j_{BF} & 0 \\ 0 & 0 & 0 & j_I \end{bmatrix} \begin{bmatrix} \ddot{\theta}_{E1} \\ \ddot{\theta}_{GC} \\ \ddot{\theta}_{BF} \\ \ddot{\theta}_I \end{bmatrix} + \begin{bmatrix} -d_{E1} & 0 & 0 & 0 \\ 0 & d_{GC} + d_I & -d_{GC} & -d_I \\ 0 & -d_{GC} & d_S + d_{GC} & 0 \\ 0 & -d_I & 0 & d_I \end{bmatrix} \begin{bmatrix} \dot{\theta}_{E1} \\ \dot{\theta}_{GC} \\ \dot{\theta}_{BF} \\ \dot{\theta}_I \end{bmatrix} + \begin{bmatrix} -k_{HD} & k_{HD}N_2 & 0 & 0 \\ -k_{HD}N_2 & k_{E2} & 0 & -k_I \\ 0 & 0 & k_S & 0 \\ 0 & -k_I & 0 & k_I \end{bmatrix} \begin{bmatrix} \theta_{E1} \\ \theta_{GC} \\ \theta_{BF} \\ \theta_I \end{bmatrix} = \begin{bmatrix} -T_{E1} \\ 0 \\ 0 \\ 0 \end{bmatrix}. \quad (73)$$

A simplified version of the mathematical model describing the MICADO mechanical system is implemented to simulate the dynamic behavior of the derotator prototype, which is described in chapter 6. With exception of the bearing friction ( $d_{GC}$ ), all parameters of the model are constants which can be either taken from catalogues (like the Harmonic Drive gear stiffness and the servomotor viscous friction) or estimated using equations (37) and (38) once the relevant eigenfrequency has been calculated through a FEA.

## 5.3 Modeling the bearing friction

As previously mentioned (see section 4.1 and 4.3.5), the bearing friction is a highly nonlinear phenomenon that can be influenced by many factors and therefore is difficult to simulate through a mathematical model. Several friction models, static and dynamic ones, have been proposed to estimate and predict the friction related stick-slip effects, which degrades the performance of mechanical systems influenced by high friction values. Some of these models are discussed in detail by Armstrong-Hélouvry, Dupont, & Canudas de Wit (1994), Dupont, Armstrong, & Hayward (2000), Olsson, Aström, Caudas de Wit, Gäfvert, & Lischinsky (1998). Friction compensation on the other hand is a powerful control tool to improve the performance of mechanical systems highly influenced by the friction related stick-slip effects, where high positioning accuracy is required.

The LuGre representation (Canudas de Wit, Olsson, Aström, & Lischinsky, 1995), as dynamic friction model has been previously used in applications related to astronomical instrumentation (Dreyer, et al., 2014). This model has also been chosen to simulate the friction phenomenon of the slewing bearing for the MICADO derotator end-to-end simulation and the eventual friction compensation through the control system. The notation used by Olsson (1996) is used here for the description of the friction model.

The LuGre model is based on the bristle interpretation of the friction, assuming that on microscopy level surfaces are irregular and therefore the contact between two surfaces occur through asperities, supposed to elastic bristles. The friction force ( $F$ )

is estimated by the average deflection of these bristles ( $Z$ ), where the bristles are considered in the mathematical model as elastic springs, with stiffness ( $\sigma_0$ ) and damping coefficient ( $\sigma_1$ ). If the deflection is large enough, the bristles will start to slip. This interpretation of the friction phenomena is schematized in Figure 94.

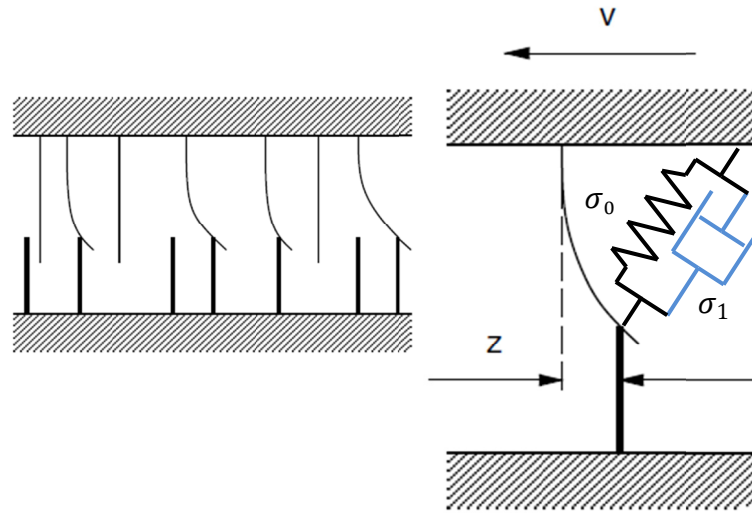


**Figure 94:** Reduced Bristle interpretation of the friction according to the LuGre model (Image source: (Olsson, 1996)). The spring and the damper have been included into the figure for a better understanding of the model, but they do not belong to the original figure.

The friction force is estimated with the following expression

$$F = \sigma_0 z + \sigma_1 \frac{dz}{dt} + F_v v \quad (74)$$

where ( $v$ ) is the velocity and ( $F_v$ ) is a constant representing the viscous friction.

The term ( $dz/dt$ ) representing the rate of change of the bristle deflection is defined as

$$\frac{dz}{dt} = v - \frac{|v|}{g(v)} z \quad (75)$$

in which the function  $g(v)$  is characterized by the following expression

$$g(v) = \frac{1}{\sigma_0} (F_c + (F_s - F_c) e^{-(v/v_s)^{\delta_s}}) \quad (76)$$

where  $v_s$  is the so called Stribeck velocity,  $F_s$  is the stiction friction force and  $F_c$  the Coulomb friction force. Equations (74), (75) and (76) define the simplified version of

## 5.4 Implementation of the end-to-end model

the LuGre standard model. The parameters  $F_v$ ,  $F_c$  and  $F_s$  dependent on the application and for that reason they must be experimentally identified. Recommended values are given by Olson (1996) for the rest of the parameters:  $\delta_s = 2$ ,  $v_s = 0.01$ ,  $\sigma_o = 10^3 - 10^5$  and  $\sigma_1 = 2\sqrt{\sigma_0 m}$ , where  $m$  is the mass of the inertia of the body under friction. The parameter identification of the friction model used here is described in chapter 6.

## 5.4 Implementation of the end-to-end model

One main aim of end-to-end simulation is to consider in the mathematical model all essential effects and perturbations between the input and the output of the system. The implementation of the simulation is done here in MATLAB/Simulink. A step-by-step approach is being followed to develop the end-to-end simulation of the MICADO derotator. This means that the different elements of the simulation are included one by one, which help to identify possible errors through the implementation process in an easier way. At its final stage, an end-to-end simulation as complete as the one performed for the DKIST (Dreyer, et al., 2014) should have been achieved for the MICADO derotator. The schematic representation of the DKIST end-to-end model is shown in Figure 95.

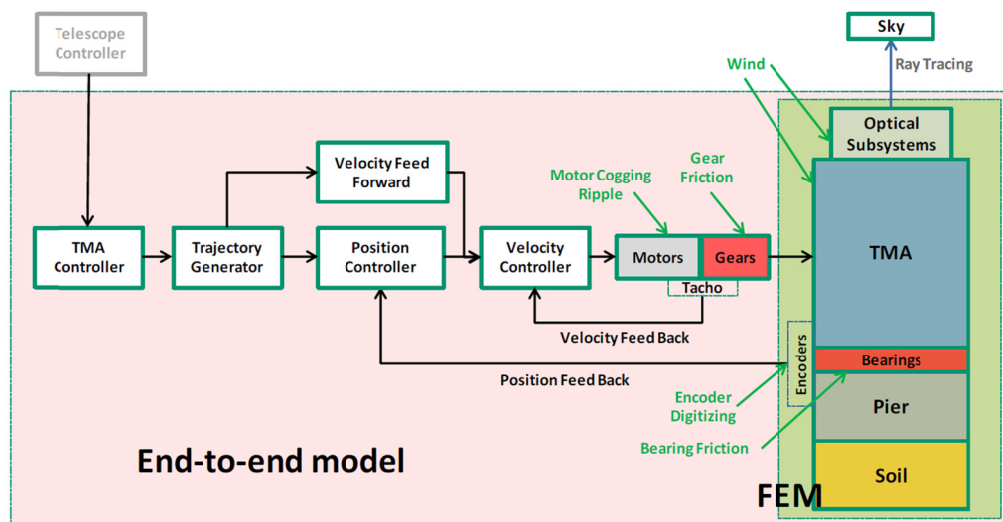


**Figure 95:** End-to-end model of the DKIST. Image source: (Dreyer, et al., 2014).

Following the same schematic representation as shown in Figure 95, the reached status of the end-to-end model for the MICADO derotator is presented in Figure 96.

As previously mentioned, only the elements of the mechanical system and the bearing friction (red box) are considered in this thesis. The trajectory generator and the controller (blue box) are described by Glück (2019). Other effects not considered so far are the modeling of the electrical part of the motor, the motor cogging, the motor ripple, the encoder digitizing, as well as external disturbances like residual torque from the cable wrap and wind effects. They can be included into the end-to-end model in a later stage if necessary. As shown later in section 6.3.2, including those effects should not change the dynamic behavior of the mechanical system.

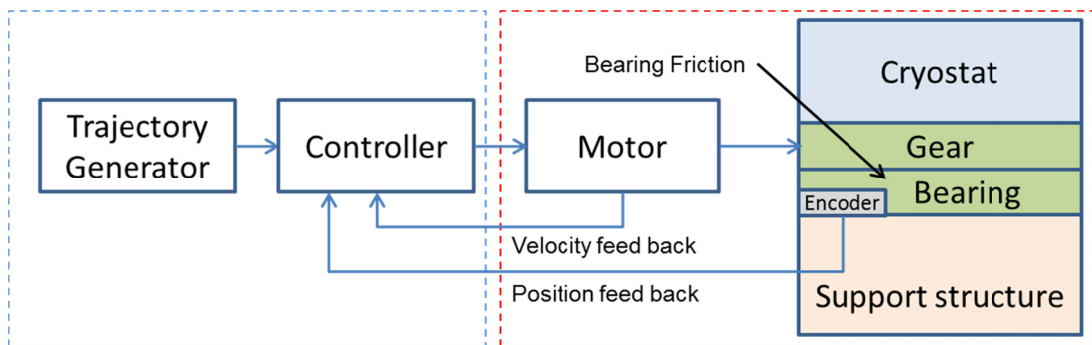


**Figure 96:** Current end-to-end model of the MICADO derotator.

Once the equation of motion of the mechanical system (73) is arranged in the form of equation (52), the simulation can be implemented in Simulink. This is a model-based design graphical programming tool integrated with MATLAB. The implementation of the simulation is given in Figure 97. All parameters of the mechanical model corresponding to the matrices  $J$ ,  $D$ , and  $K$  are defined in a separate MATLAB script.

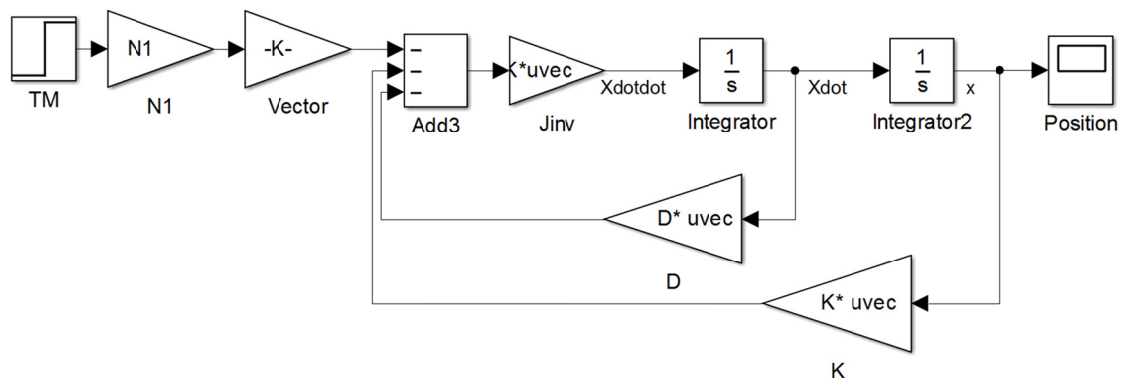


**Figure 97:** Simulink implementation of the MICADO derotator mechanical system. The input of the signal is represented in the case with an step signal block.

5.4 Implementation of the end-to-end model

The input of the signal corresponds to the torque applied by the motor and the output is represented by the positions of all four degrees of freedom defined in equation (73). The friction model is embedded in the block representing the damping matrix  $D$  and the corresponding Simulink implementation of the LuGre model is given in Figure 98. The input of the friction model is the velocity and the output is the friction force.

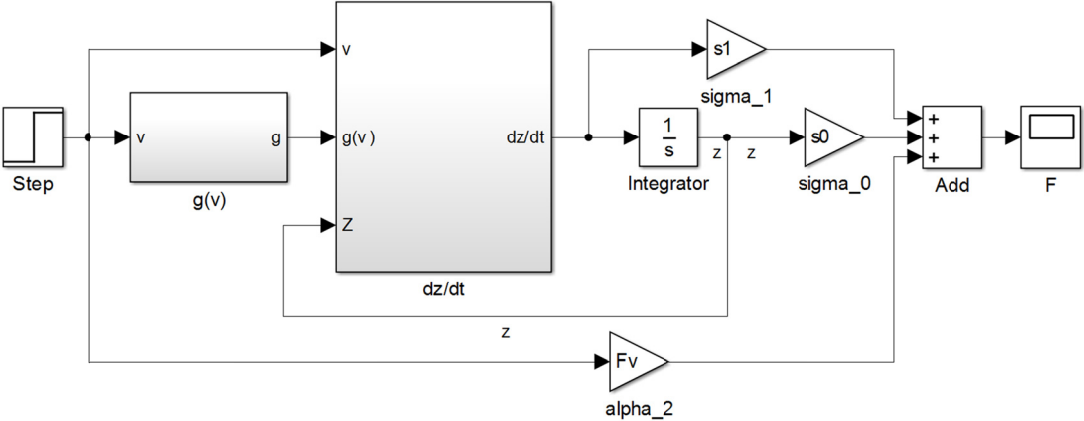


Figure 98: Simulink implementation of the LuGre friction model.

The implementation of the end-to-end simulation for the derotator test stand mechanical system following the tools provided in this chapter is presented in chapter 6.

## 6 The experiment: Derotator test stand

The derotator is a key subsystem of the MICADO instrument. For that reason, in order to reduce the risk of possible design flaws and due to the demanding positioning accuracy requirement, a prototype as technology demonstrator is essential in the early stage of the project. The main goal of the derotator test stand is to probe the proposed concept of providing field rotation compensation for the MICADO instrument with the chosen bearing technology, i.e. slewing bearings, specifically a four-point contact ball bearing. However, the experiment has been designed in such a way that all components (with exception of the bearing and the band encoder with a smaller diameter but exactly the same type to be used later in the nominal size) could be eventually used in the nominal MICADO derotator. These are: the servomotor, the Harmonic Drive gear, the encoder scanning heads, and all the electronics hardware used to power and control the derotator test stand.

This representative design approach will allow not only testing of the general concept, but also verifying, with nominal hardware, features like the backlash suppression system and the whole controller architecture optimization. Furthermore, understanding the impact of the bearing friction over the angular positioning accuracy of the system and how to compensate the related stick-slip effects is a crucial task to be carried out with the derotator test stand. Last but not least, the derotator test stand will allow the identification and verification of the mechanical system model described in chapter 5. In a final stage of the test campaign, the experimental results obtained with the prototype will allow to upscale the results given by the end-to-end simulation. Other technical aspects like the Assembly, Integration and Verification (AIV) procedure and the implementation of the liquid

shimming (see section 4.1.1) can be also put in practice with the derotator prototype. Chapter 6 collects the most relevant aspects and results obtained so far with the experiment.

## 6.1 Design of the experiment

The derotator test stand was designed based on a standard four-point contact ball bearing offered by Rothe Erde. The selection of the bearing was driven by its size and therefore, the selected one was the biggest off-the-shelf bearing available. The intention was to minimize the delivery time of the bearing in order to accelerate the manufacturing process of the whole experiment.

The main differences between the standard bearing used in the test stand and the high precision one considered for the MICADO derotator are presented in Table 22. The friction torque values for the test bearing were calculated for an axial load of 30 kN, which was the expected mass of the cryostat assembly at the time when the experiment was designed and built. The friction torque values of the nominal bearing are calculated for an axial load of 70 kN, which is the current estimation for the mass that the derotator should carry on top of it. Due to the difference in the friction torque between the test bearing and the nominal bearing (mainly due to the diameter), a friction simulator has been included in the design of the prototype.

<b>Parameter</b>	<b>Test Bearing</b>	<b>Nominal Bearing</b>
Raceway diameter	1094 mm	2667 mm
Axial runout	$\leq 50 \mu\text{m}$	$\leq 30 \mu\text{m}$
Radial runout	$\leq 60 \mu\text{m}$	$\leq 30 \mu\text{m}$
Gear module	8 mm	6 mm
Number of teeth	148	471
Starting friction torque (0 rpm)	1000 Nm	1700 Nm
Running friction torque (1 rpm)	900 Nm	1500 Nm
Raceway configuration	Spacers	Cage
Class quality	0 (worst)	5 (best)

**Table 22:** Difference between the standard test bearing and the high precision nominal bearing.

The test stand consists of the support structure, the dummy mass with interface flange (simulating the MICADO cryostat), the alignment system (see Figure 102



below), the drive system, the angular positioning measurement system and the friction simulator. Additionally, the electronics and control system also form part of the prototype. The CAD model of the derotator test stand showing all its components is presented in Figure 99 and Figure 100.

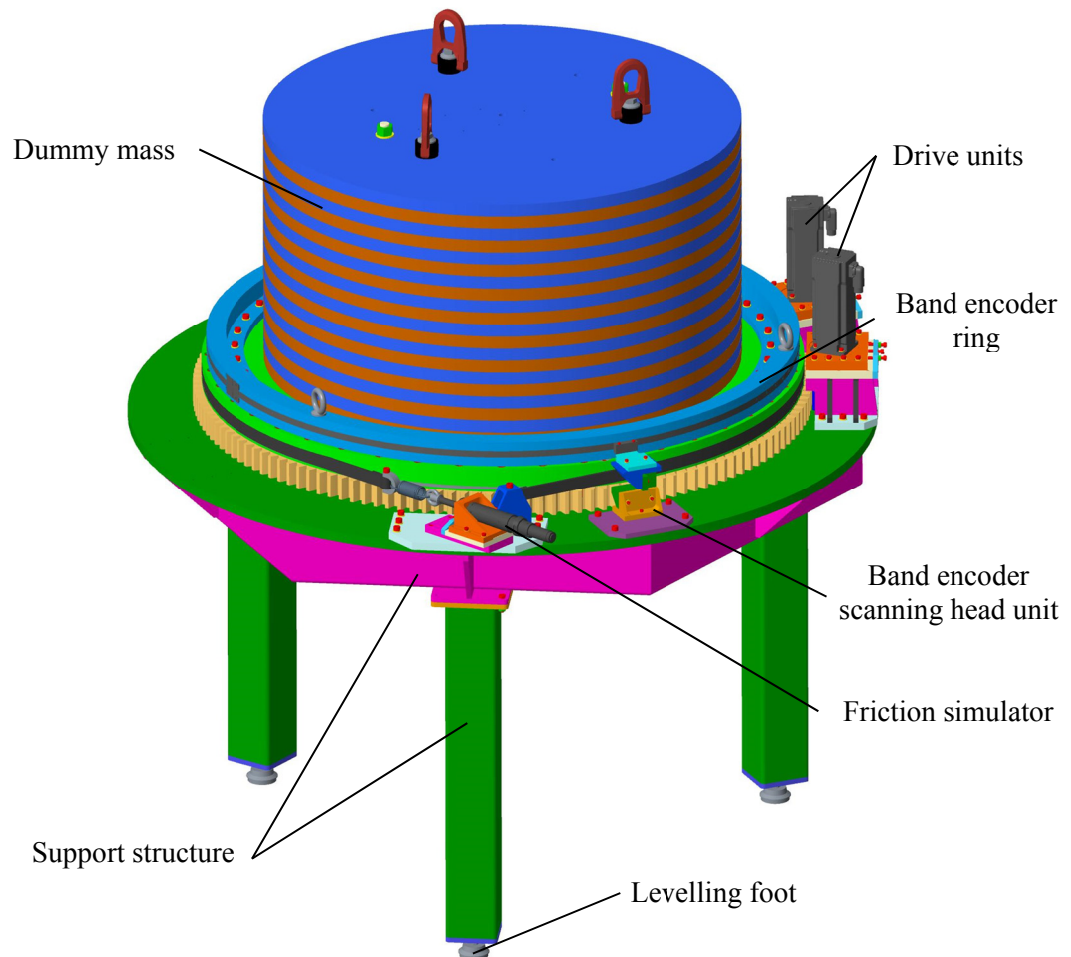


**Figure 99:** Derotator test stand CAD model.

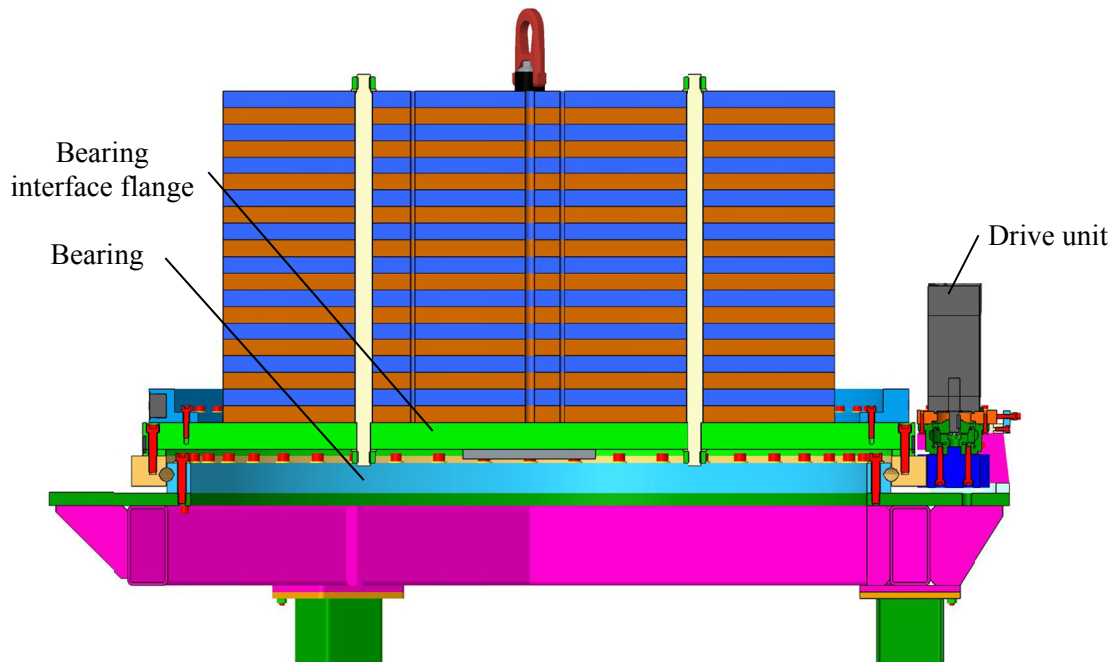


**Figure 100:** Derotator test stand CAD model cross section.

### 6.1.1 Support structure and dummy mass

The support structure consists of a hexagonal structural frame (see Figure 101) supported by three legs. Commercial structural steel profiles are used in this assembly. A steel plate on top of the hexagonal frame is used as mechanical interface to the bearing, the drive units and the encoder scanning head mount. Several ribs are placed on key points for additional structural reinforcement. In order to guarantee a flat contact surface, the upper face of the interface plate as well as the lower face of the interface pads towards the legs, must be machined after the whole frame is welded together. The dummy mass consists of 20 steel plates with a thickness of 25 mm and 925 mm in diameter, placed on top of the 50mm thick bearing interface flange (which simulates the cryostat central flange, see Figure 101). The FEA corresponding to the derotator test stand is described in detail by Barboza, et al., (2017), where the FEM using springs elements to simulate the balls inside the bearing was also used for this calculation, see section 4.4.1.

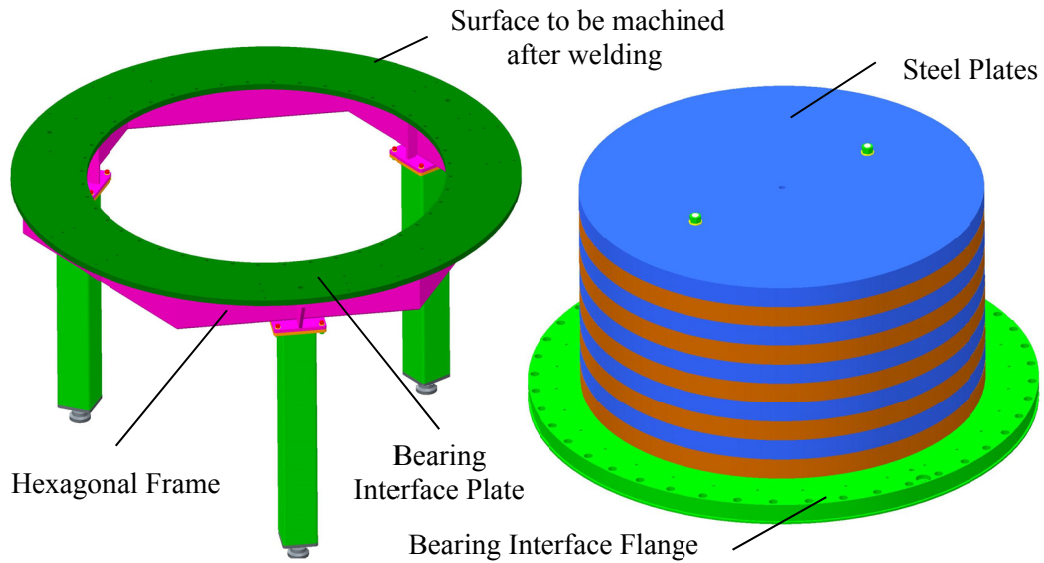


**Figure 101:** Support structure and dummy mass for the derotator prototype.

### 6.1.2 Alignment system

The alignment system consists of two pins placed opposite each other (180 degree) on the interface flange to the bearing (see Figure 102). Two special holes are machined into the interface flange to allow the installation of the pins. In order to adjust the final position during the alignment, the interface flange can move around the pins  $\pm 1$  mm in all directions within a plane parallel to the bearing. The pins must go into a hole and a slot, respectively, previously machined into the test bearing to fix the relative position between both parts. The implementation of the slot is necessary to absorb expansion or contractions of the interface flange (representing the central flange of the MCIADO cryostat, which is made of different steel than the bearing, see section 4.3.2). After the alignment procedure is finished, the pins can be fixed at the final position in the interface flange through several dedicated screws.

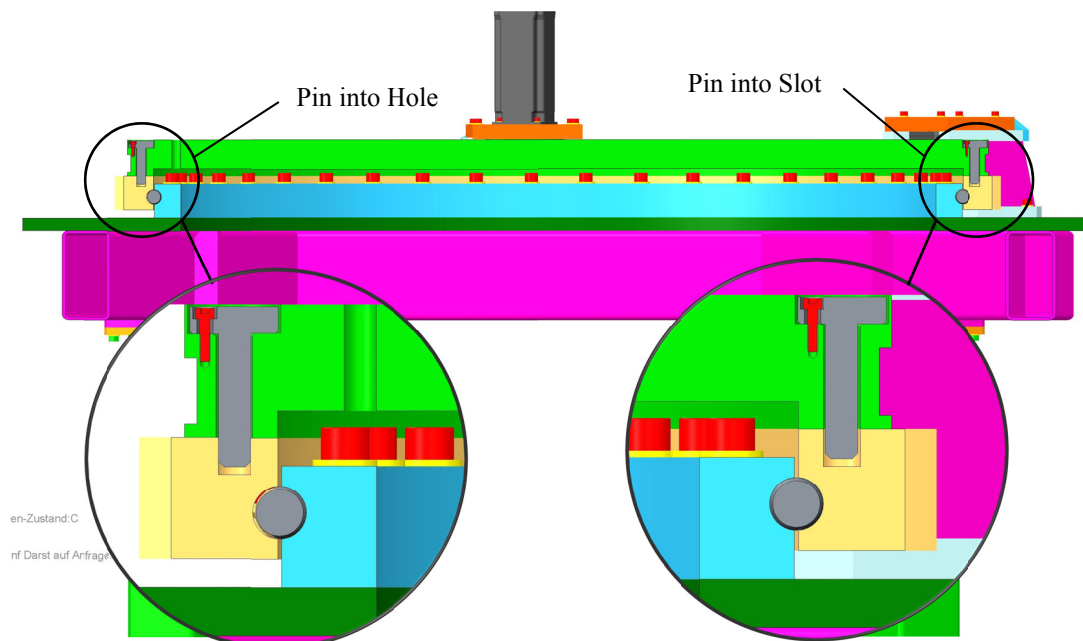


**Figure 102:** Alignment system between the cryostat dummy mass and the bearing of the derotator test stand. A similar alignment concept is proposed for the derotator of the MICADO instrument.

The alignment procedure must be performed only with the interface flange (empty central flange of the MICADO cryostat) and without the dummy mass to facilitate the positioning of this part. To set the position of the interface flange, a pushing screw is fixed to the bearing interface plate, this is placed opposite to a dial gauge that is measuring the difference between two reference points (opposite to each other). The bearing must be rotated and this difference must be minimized for any angular position of the interface flange. The reference surface chosen to implement the alignment procedure is the outer surface of the interface flange. Later the outer surface of the MICADO cryostat central flange could be used (see Figure 103). Later on, the cold structure carrying all optical components inside the MICADO cryostat must be aligned taking as reference the same surface used in this procedure. For the particular case of the test stand, the same process must be repeated for the alignment between the tape encoder ring and the interface flange.

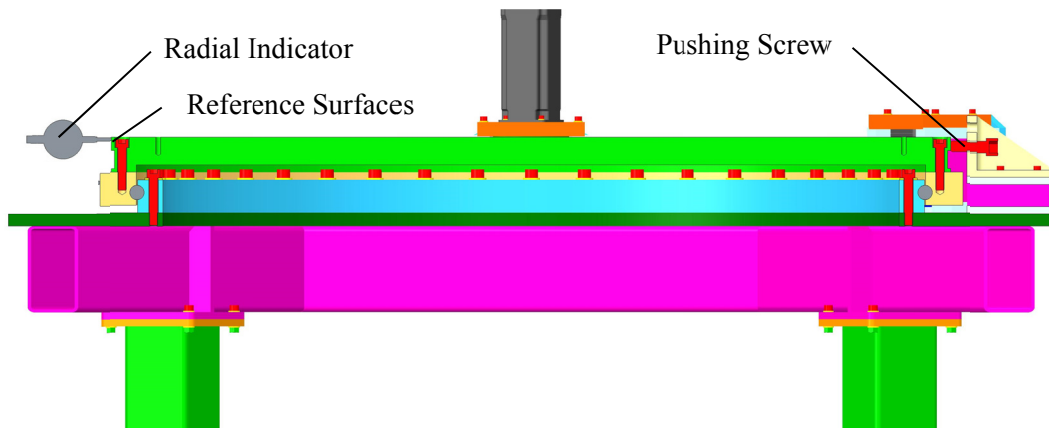


**Figure 103:** Proposal for the alignment mechanism with an radial indicator.

### 6.1.3 Test Stand Drive System

The drive system implemented in the derotator prototype corresponds exactly to the concept proposed for the derotator preliminary design (see section 4.3.3). It has only two minor differences, the absence of the spacer due to the fact that the thermal compensation rings are not included in the derotator test stand (the drive unit is directly fixed to the bearing interface plate) and a different pinion as result of the bigger module used for the gear wheel of the test bearing. The test stand drive unit is shown in Figure 104. Due to lack of space, the counter bearing for the pinion is not implemented here.

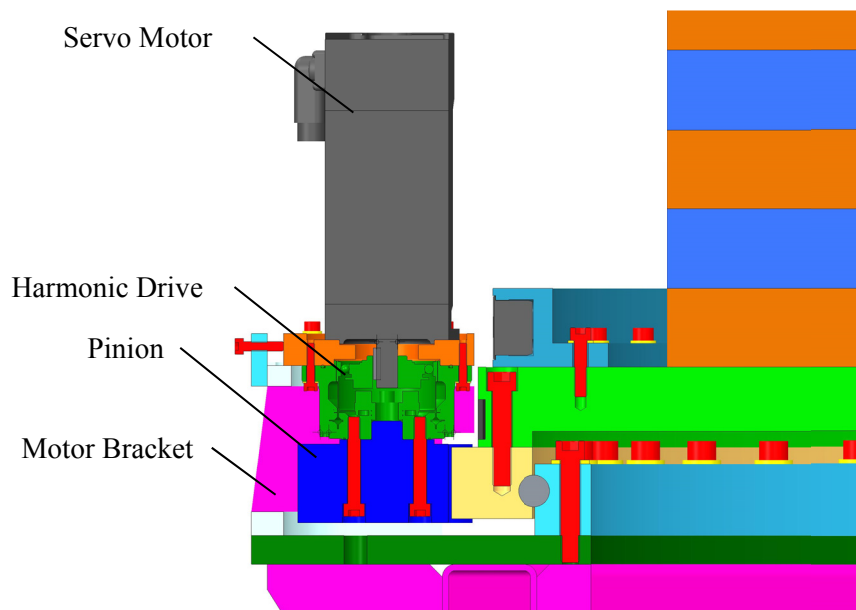


**Figure 104:** Test stand Drive unit cross section.

### 6.1.4 Test Stand Positioning measurement system

The positioning measurement system implemented in the test stand also corresponds to the concept proposed for the derotator preliminary design (see section 4.3.4). The unique fundamental difference is the diameter of the metallic scale tape, which in this case, has an inner diameter of 1145.73 mm and a total of 90000 reference marks printed on it. This is a standard encoder with an accuracy of the graduation of  $\pm 1.9$  arcsec and a position error per signal period of  $\pm 0.1$  arcsec. In the case of the derotator test stand, the band encoder is installed on a dedicated ring on top of the bearing interface flange, see Figure 105.

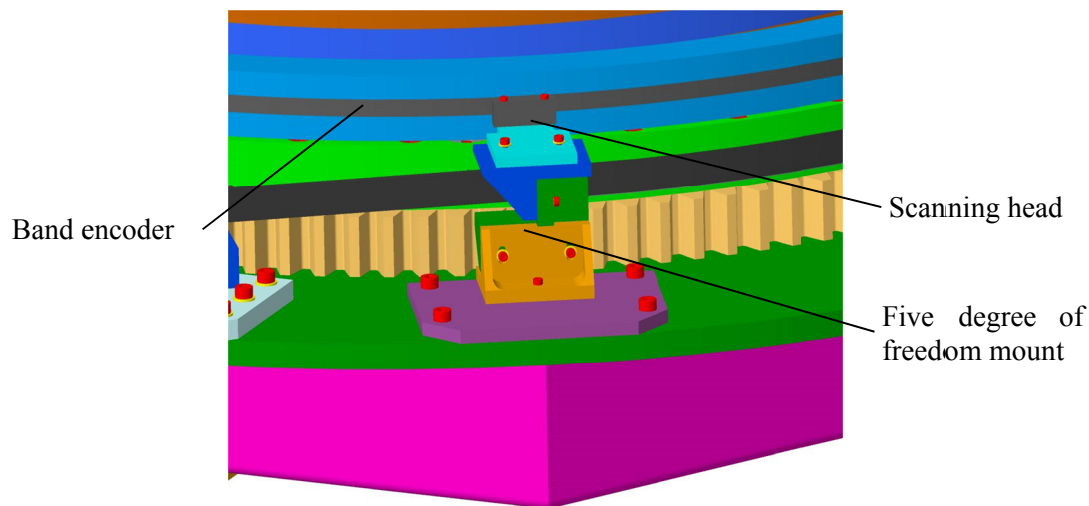


**Figure 105:** Test stand positioning measurement system.

### 6.1.5 Test Stand Friction Simulator

Understanding the effects of friction over the positioning accuracy of the derotator is one of the key goals of the prototype. Having a friction simulator will allow us to represent bad case scenarios for the positioning accuracy. In addition, as the test bearing has less friction torque than the nominal bearing for the MICADO derotator (mainly due to the difference in diameter), the missing amount of friction torque had to be externally generated. This is another reason for the inclusion of a friction simulator in the design of the experiment. The friction will be simulated using a band brake, consisting of a band of friction material that tightens concentrically around the interface flange to the bearing. The force to operate the brake is applied by a linear

actuator connected to the brake band via a spring, as shown in Figure 106. The calculation of the required force for the linear actuator is given in appendix B.

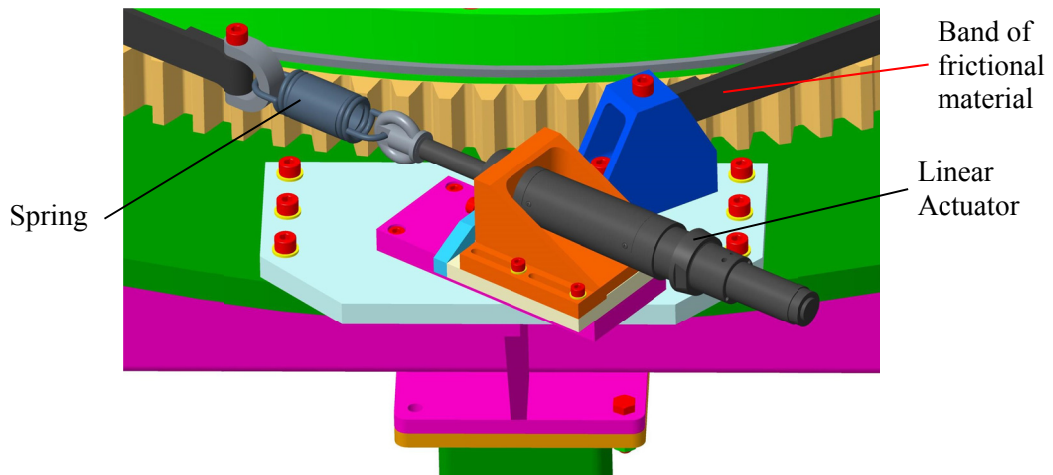


**Figure 106:** Test stand friction simulator.

## 6.2 Assembly, integration and verification (AIV)

The initial test campaign with the derotator test stand should provide preliminary results for the upcoming PDR of the MICADO project scheduled for October 2018. The derotator prototype has been integrated in the MPIA assembly hall in Heidelberg.

The complete AIV plan and procedure is described in detail in a dedicated document (Barboza, 2017). Here, however, only the most relevant steps are summarized. The AIV plan will be implemented on the nominal MICADO derotator in a very similar (or identical) way. Therefore it serves as training for the final stages of the project. Possible issues discovered during the AIV phase of the derotator test stand, can then be corrected and re-implemented for the nominal derotator. The AIV plan consists of the following steps:

1. Assembly of the support structure and bearing (See Figure 107).
2. Application of the liquid shimming (See section 4.1.1 and Figure 108).
3. Integration of the bearing interface plate (See Figure 109).
4. Assembly of the drive unit (See Figure 110).
5. Alignment of the interface plate.
6. Integration of the encoder ring (See Figure 111).
7. Alignment of the encoder ring (See Figure 112).



## 6.2 Assembly, integration and verification (AIV)

---

8. Integration of the encoder tape and scanning heads (See Figure 113).
9. Verification of the scanning heads signal quality (See Figure 114).
10. Integration of the dummy mass (See Figure 115).
11. Assembly of the friction simulator (See Figure 115).

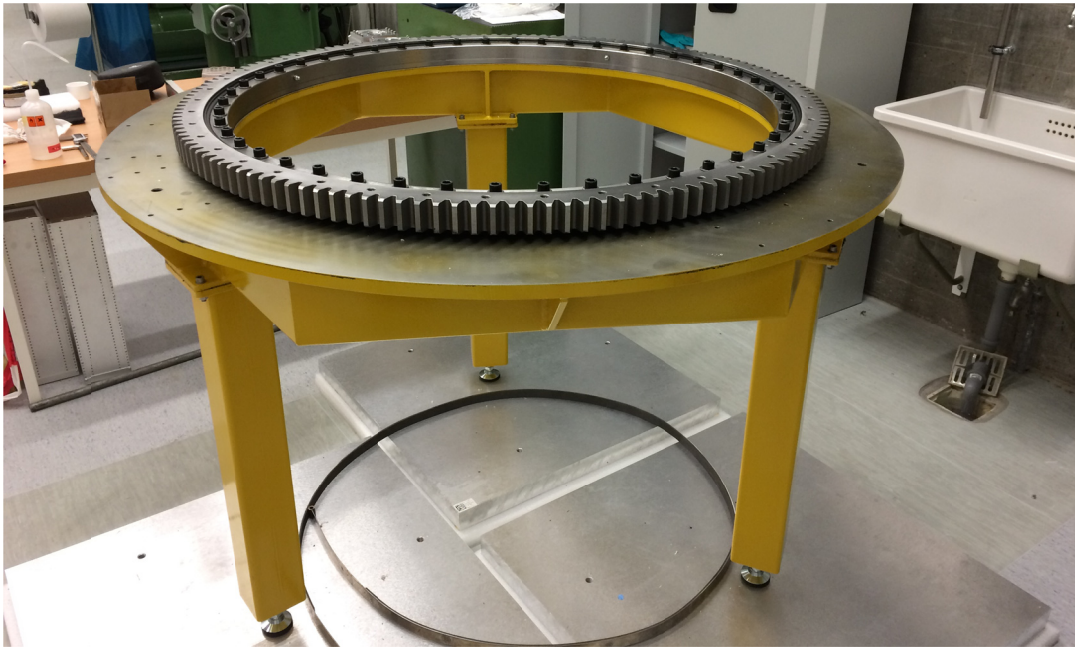


**Figure 107:** Support with the bearing installed on top of it.

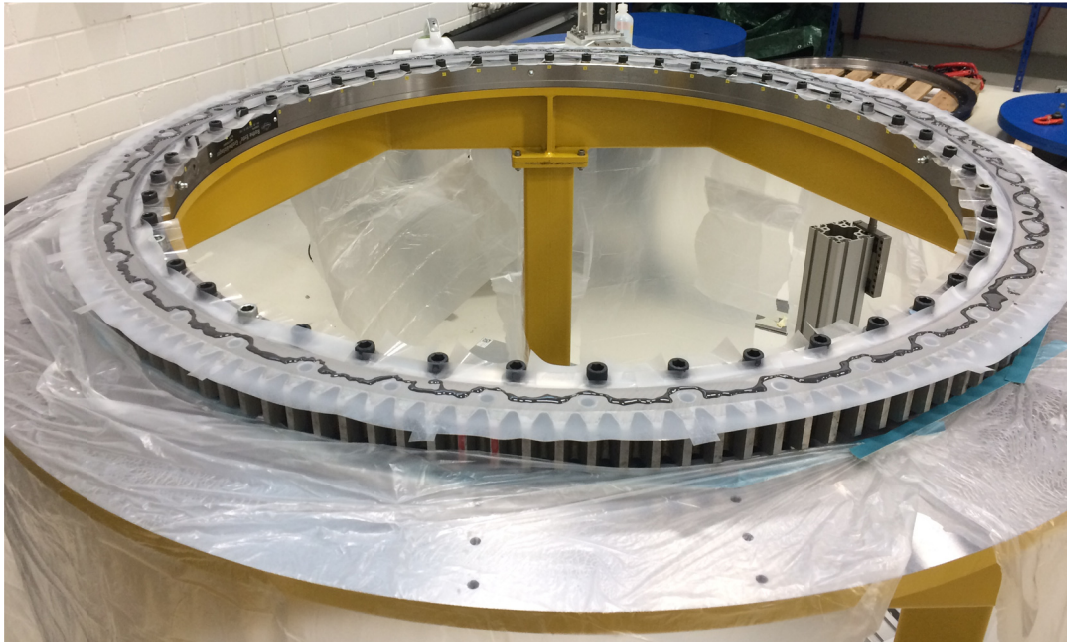


**Figure 108:** Fluid epoxy resin applied on top of the bearing outer ring as part of the liquid shimming process. Tape and plastic sheets are placed to protect other areas of the bearing.



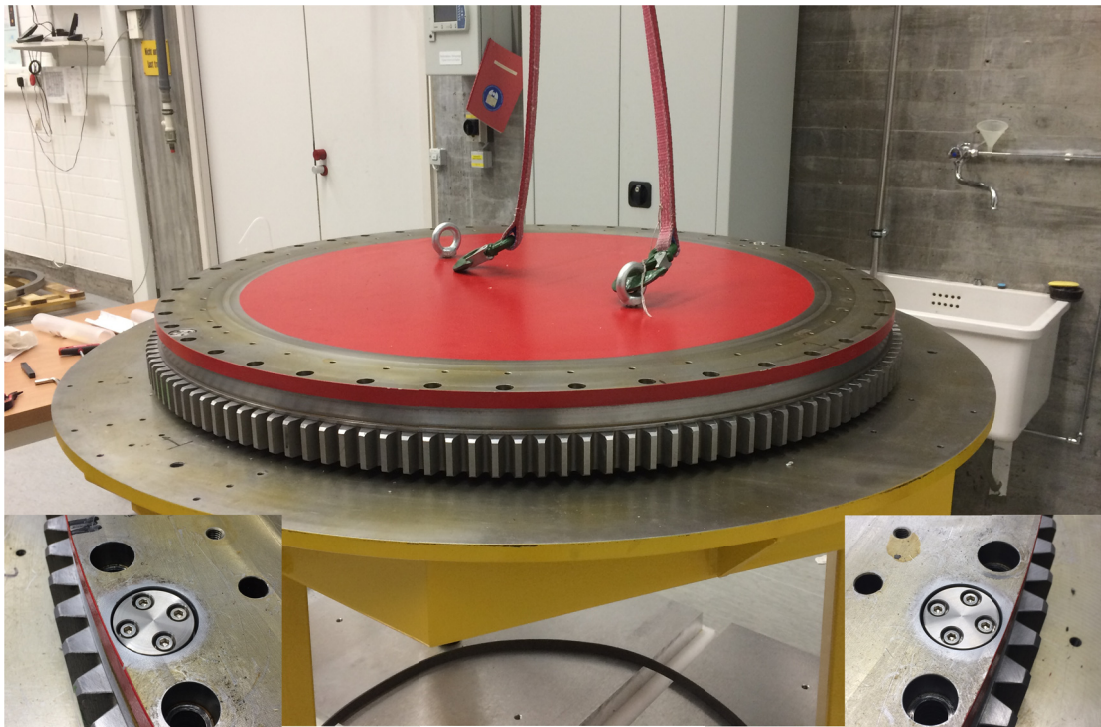


**Figure 109:** Bearing interface plate installed on top of the derotator. The alignment pins are shown in the lower corners.

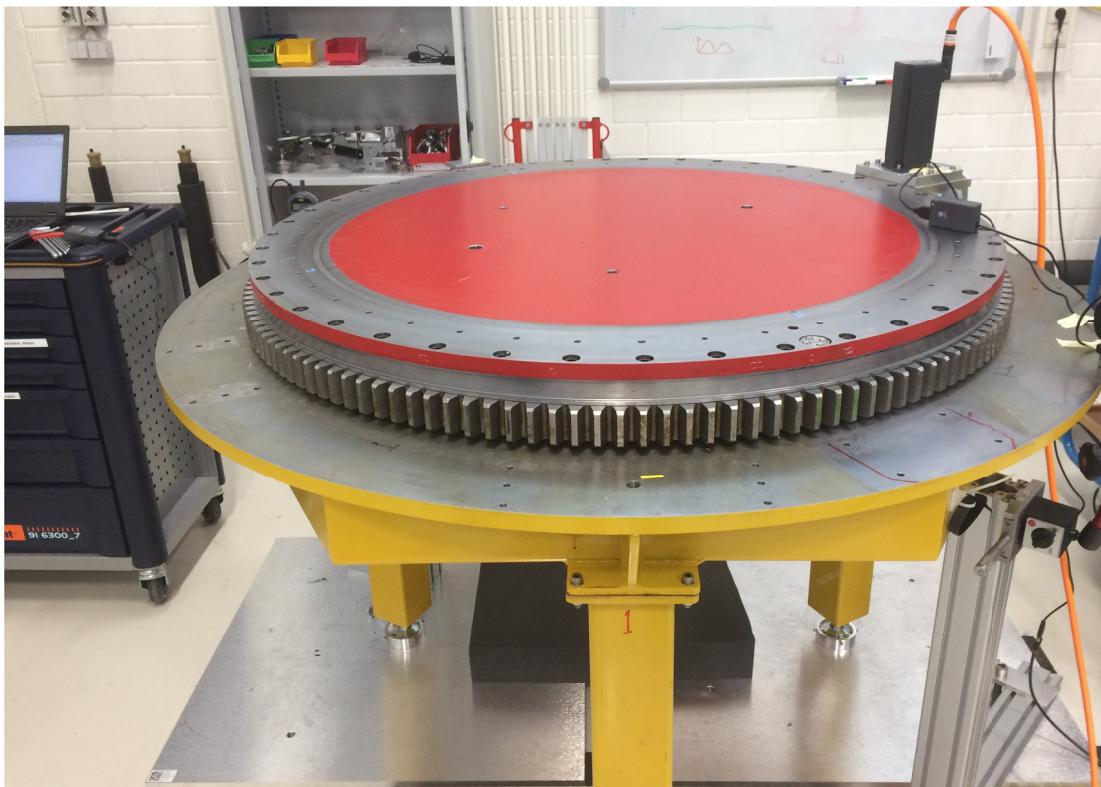


**Figure 110:** Drive unit installed on top of the bearing interface plate.

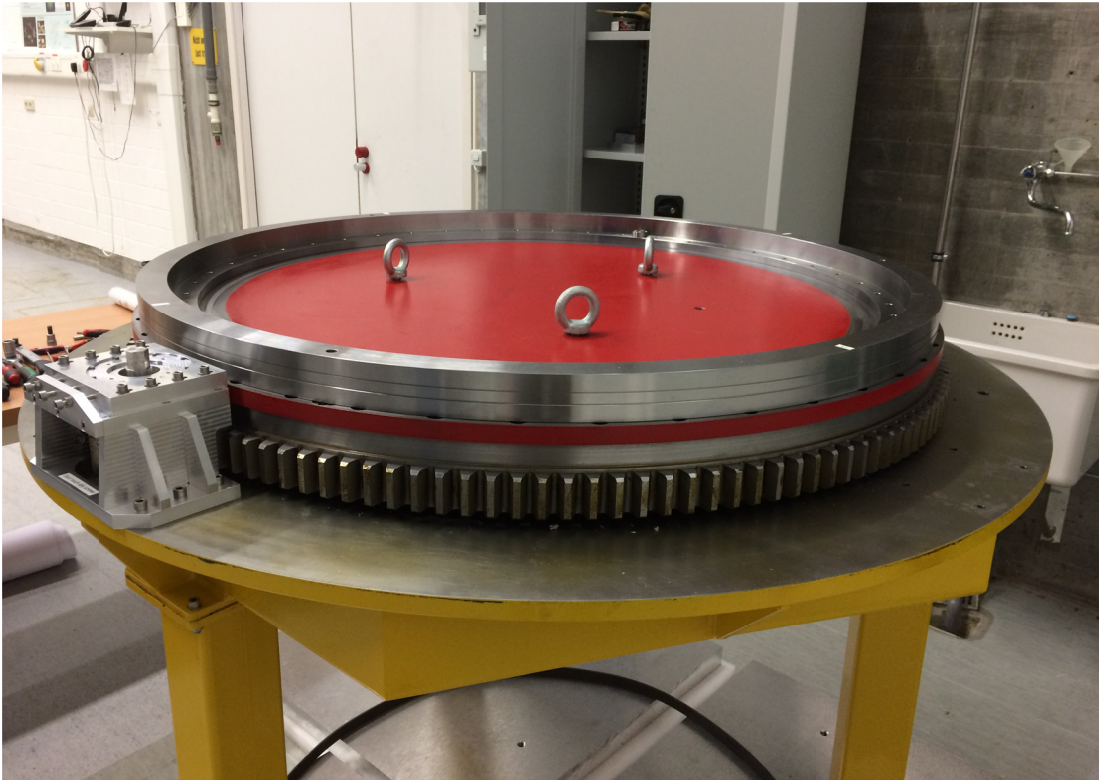


Figure 111: Encoder ring installed on top of the bearing interface flange.

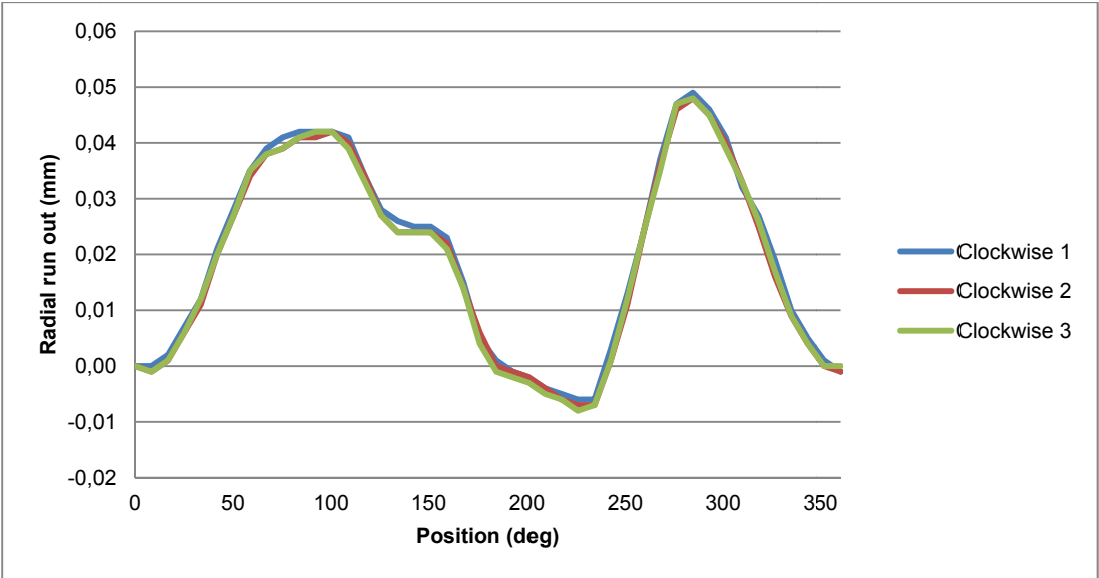
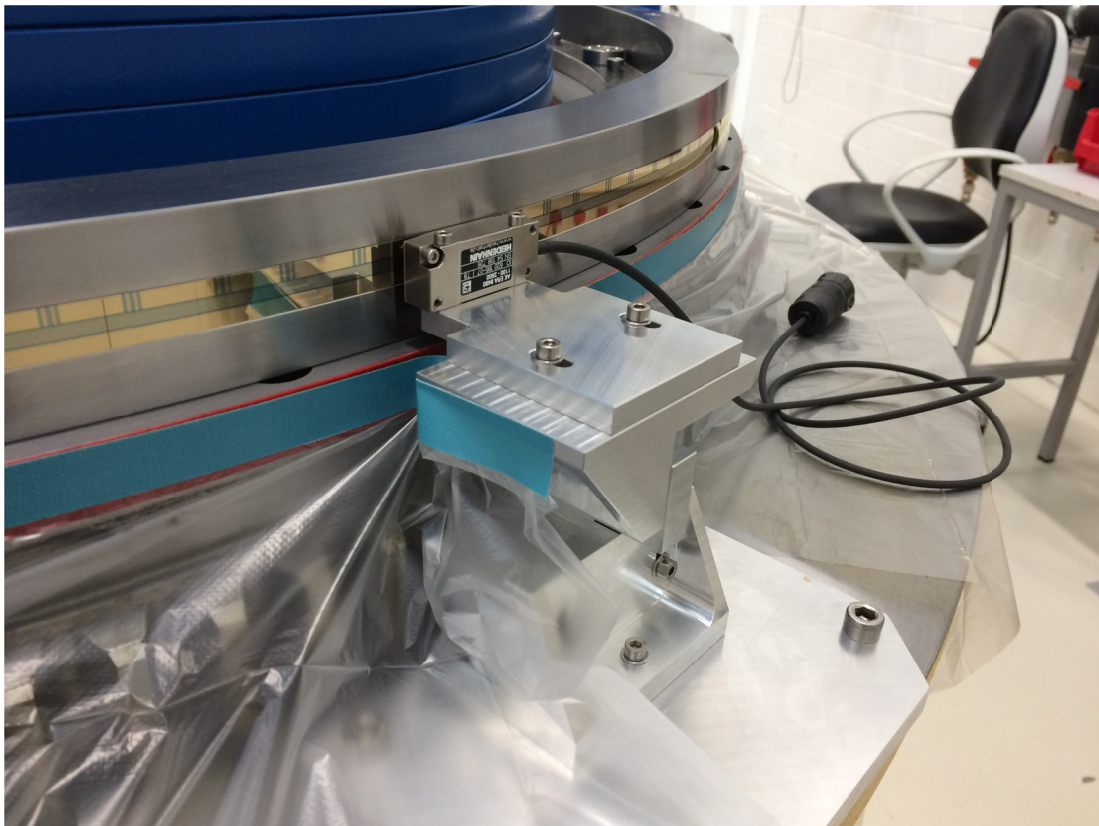
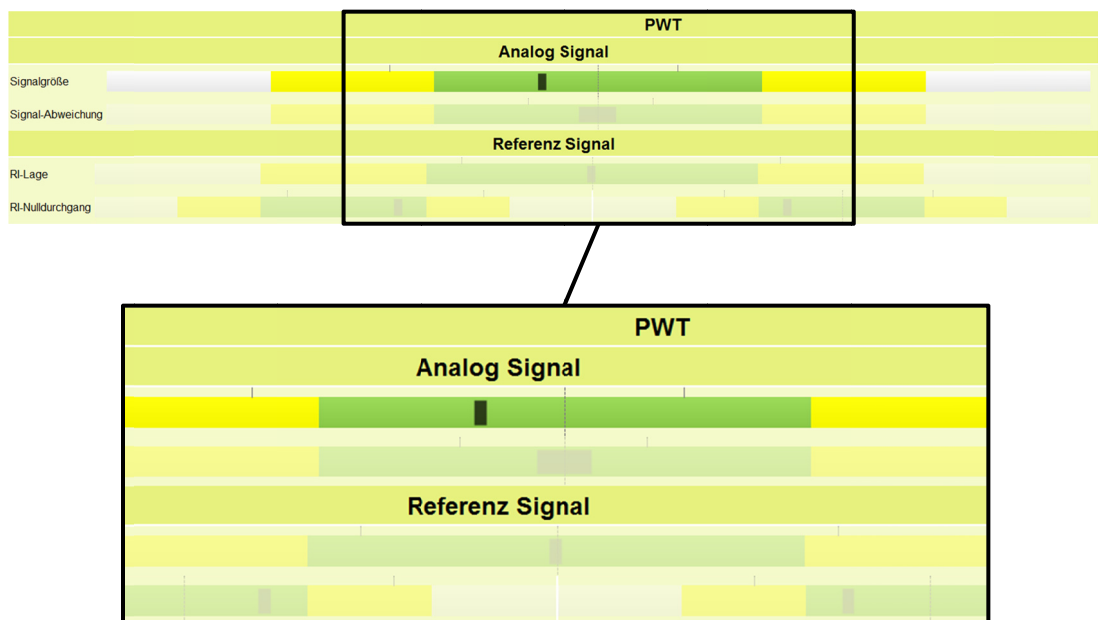


Figure 112: Measurement of the encoder ring radial runout after the application of the alignment process described in section 6.1.2.





**Figure 113:** Band encoder and scanning head installed in the derotator test stand.



**Figure 114:** Verification of the scanning head's signal quality. The small reference marks represent the maximum values for a full rotation of 360°. According to Heidenhain, having signal quality within the yellow range is considered good. The green area corresponds to perfect signal quality.

6.2 Assembly, integration and verification (AIV)

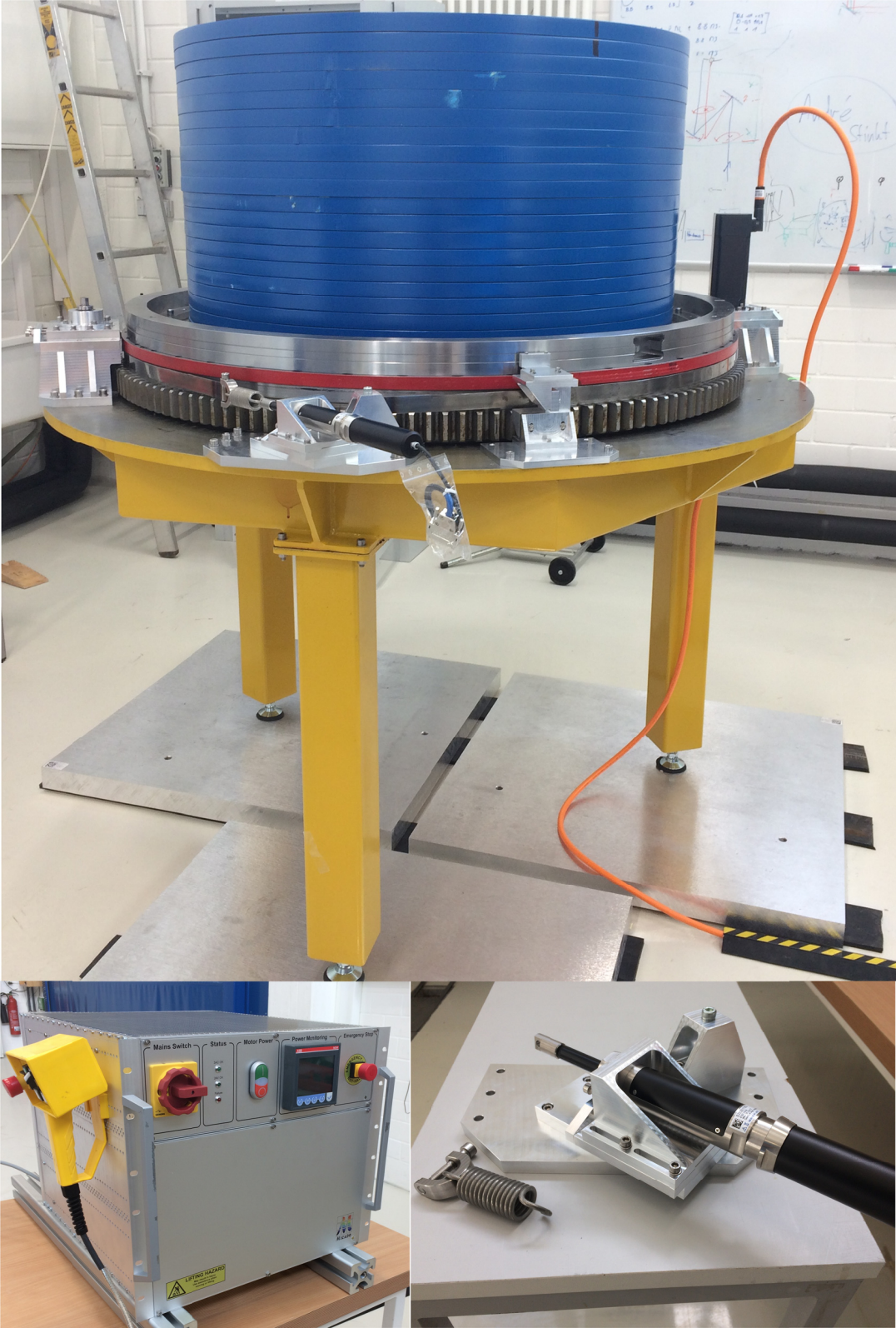


**Figure 115:** Derotator test stand completely integrated in the MPIA assembly hall, electronic cabinet (bottom left corner) and friction simulator (bottom right corner).



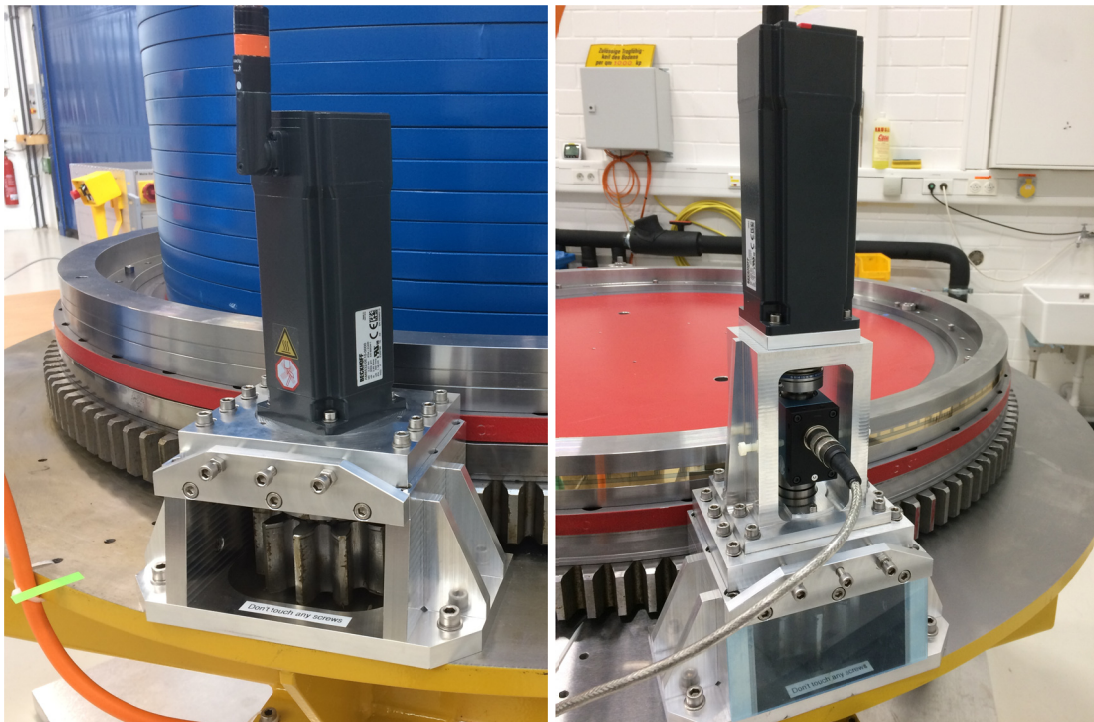


**Figure 116:** Standard Drive unit (left) and drive unit with the torque sensor on top.

### 6.3 Test campaign

The full test campaign proposal for the nominal derotator is described in detail in a dedicated PDR document (Barboza, 2017). In that case, all requirements driving the design of the derotator must be verified either by tests or analysis. The campaign is focused on the most relevant performance requirements. One of them is the relative angular positioning accuracy. Additionally, the parameter identification/verification of the mechanical system, as well as the parameter identification of the LuGre friction model has been performed with the derotator prototype within the framework of this dissertation. This section is dedicated to summarize the results of those three tasks. Other tests related to the derotator test stand are described by Häberle (2017) and Windgassen (2017).

Other key tests to be performed with the derotator test stand include the backlash suppression system and the verification of safety features. These will be conducted outside the frame work defined for this thesis. Furthermore, the optimization of the control system is described by Glück (2019).

### 6.3.1 Parameter Identification of the Friction Model

In order to identify the parameters  $F_c$ ,  $F_s$ ,  $F_v$  (see section 5.3), the system must be operated at steady state motion, which mean with constant velocity. When steady state is achieved, the term representing the rate of change of the bristle deflection is zero ( $dz/dt = 0$ ). Recalling equation (75) that defines the rate of change of the bristle deflection

$$\frac{dz}{dt} = v - \frac{|v|}{g(v)}z, \quad (77)$$

the steady state bristle deflection  $z_{ss}$  is defined through the following expression with  $dz/dt = 0$

$$z_{ss} = \frac{v}{|v|}g(v) = g(v) \operatorname{sgn}(v). \quad (77)$$

Using equation (74) the steady state friction force  $F_{ss}$  can then be written as follows

$$F_{ss} = \sigma_0 z_{ss} + F_v v. \quad (78)$$

Inserting equations (77) and (76) defining  $g(v)$  into equation (78), the steady state friction force can be finally written as

$$F_{ss} = F_c \operatorname{sgn}(v) + (F_s - F_c)e^{-(v/v_s)^{\delta_s}} \operatorname{sgn}(v) + F_v v. \quad (79)$$

If the steady state friction force (or torque in the case of the derotator) can be experimentally measured for the relevant range of velocities where the derotator will be operated, the so called Stribeck curve can be derived (Olsson, 1996) plotting the average friction force for each corresponding velocity. Then by curve fitting techniques, the parameters  $F_c$ ,  $F_s$ ,  $F_v$ ,  $v_s$ ,  $\delta_s$  of equation (79) can be determined. In this particular case of the MICADO derotator, the Least Squares Method has been used as curve fitting technique.

The results obtained with the derotator test stand are presented in Figure 117, while the identified parameters are given in Table 23. Despite Olsson (1996) provides some recommendations for the parameters  $v_s$  and  $\delta_s$ , the values provided in Table 23 give a better fit to the experimental data. Part of the experimental data corresponding

to the torque and velocity used for the identification of the Stribeck curve is presented in appendix C. The position of the bearing registered by the band encoder is provided as well. The Stribeck curve was measured for several angular positions of the bearing and a position dependency of the friction has been identified. This means that a single Stribeck curve cannot be used to characterize the whole  $360^\circ$  rotation range of the bearing. The parameter identification is described in more detail by Glück (2019).

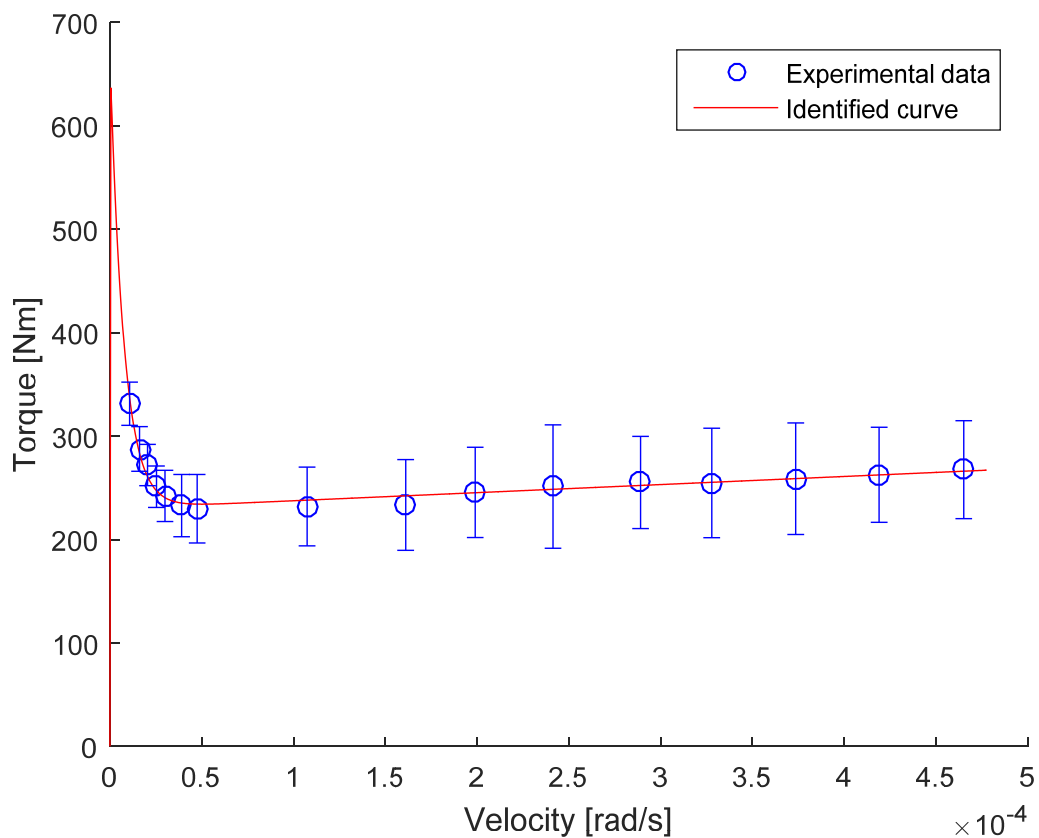


**Figure 117:** Identified Stribeck curve with the values referred to the bearing.

Friction parameters	Identified values
$F_c$	$0.023 \times 10^4 \text{ Nm}$
$F_s$	$0.066 \times 10^4 \text{ Nm}$
$F_v$	$7.7 \times 10^4 \text{ Nm}/(\text{rad/s})$
$v_s$	0.015
$\delta_s$	1

**Table 23:** Identified parameters of the Stribeck curve.

### 6.3.2 Parameters Identification of the Mechanical system

Some of the parameters used to represent the MICADO mechanical system can be obtained from catalogs i.e.  $j_M$ ,  $d_M$ ,  $j_{HD}$ ,  $k_{HD}$ . However, the rest of the parameters has to be estimated. The moment of inertia is calculated using the CAD software, while the stiffness and the damping coefficient are determined using equations (37) and (38). The complete list of parameters with the corresponding values used to simulate the dynamic behavior of the derotator test stand (a reduced version of the MICADO mechanical model) is presented in Table 24. The verification of the derotator test stand mechanical model is done using its harmonic response, where the simulated dynamic behavior is compared with the experimentally measured frequency response (see section 5.1.4). These results are presented in Figure 118 using the corresponding Bode plot of the derotator test stand.

Friction parameters	Identified values
$j_M$	$2.05 \times 10^{-4} \text{ kg m}^2$
$d_M$	$2.86 \times 10^{-5} \text{ Nm/(rad/s)}$
$j_{HD}$	$4.13 \times 10^{-5} \text{ kg m}^2$
$k_{HD}$	$5.7 \text{ c Nm/rad}$
$j_P$	$4.05 \times 10^{-3} \text{ kg m}^2$
$j_{GC}$	$325 \text{ kg m}^2$
$d_{GC} \approx F_v$	$7.7 \times 10^3 \text{ Nm/(rad/s)}$
$j_{BF}$	$81.75 \text{ kg m}^2$
$d_s$	$3.86 \times 10^3 \text{ Nm/(rad/s)}$
$k_s$	$1.6 \times 10^7 \text{ Nm/rad}$
$Z_M$	1
$Z_{HD}$	160
$Z_P$	12
$Z_G$	148

**Table 24:** Parameters of the test stand mechanical model used for the end-to-end simulation. For the implementation of the end-to-end simulation at this first stage, linear friction is assumed ( $d_{GC} \approx F_v$ ).



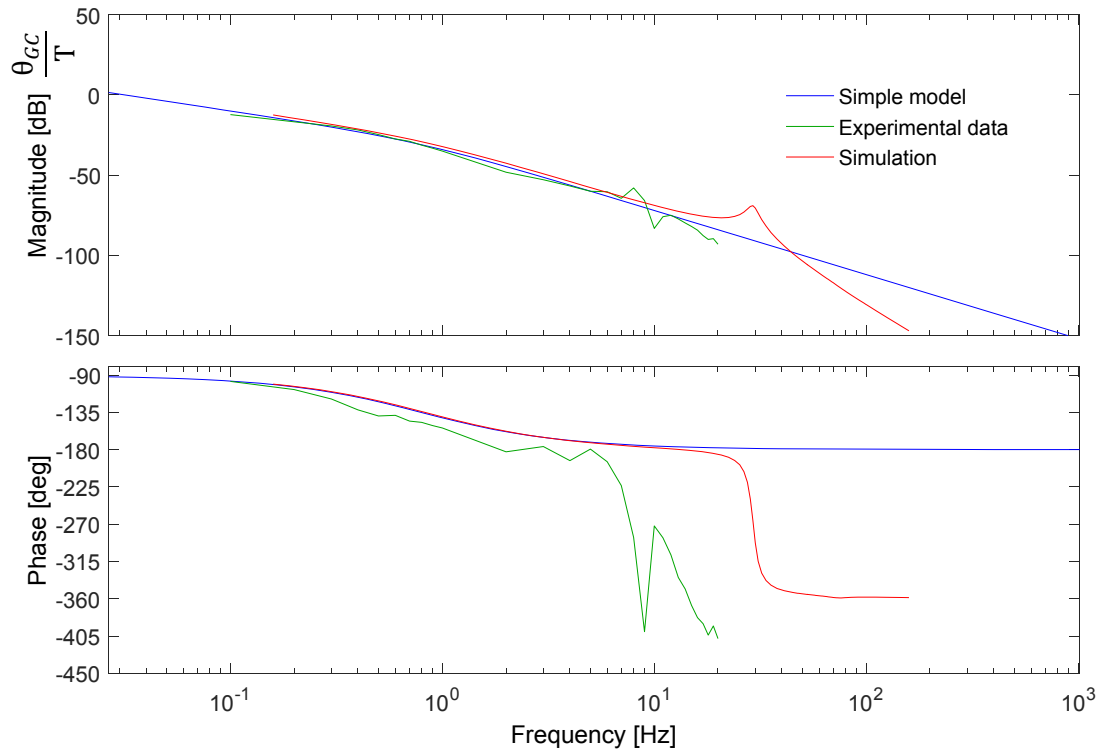


**Figure 118:** Frequency response of the derotator test stand.

The transfer function of the derotator test stand has been measured with the sine sweep method (green curve in Figure 118). A simplified mechanical model was fitted to the experimental data, which confirm a highly damped mechanical system due to the bearing friction. The highly damped system can be modeled as a single damper with an equivalent rotatory inertia, see Glück (2019)

$$H(s) = \frac{\theta_{GC}}{T} = \frac{1}{(j_E s^2 + d_E s)}, \quad (80)$$

where  $j_E$ ,  $d_E$  are the parameters fitted to the experimental data. In order to get a good match between the simulation and the frequency response measured experimentally, the parameter  $F_v$  (estimated for the identification of the Stribeck curve) had to be adjusted to the value given in Table 24. A possible reason for this discrepancy are the error bars in the friction torque measurements presented in Figure 117.

It has to be added that the harmonic response of the derotator test stand shows its rotational eigenfrequencies. The first (around 9 Hz) correspond to the rotation of the test stand support structure, the second one (around 30 Hz) corresponds to the degree

of freedom representing the Harmonic Drive gear. The eigenfrequencies corresponding to the lateral movement of the support structure are not registered. Due to restrictions in the electronic hardware it was not possible to perform the measurements at higher frequencies. The mathematical model of the test stand mechanical system only considers the rotational degree of freedom.

### 6.3.3 Relative Angular Positioning Accuracy

In order to test the relative angular positioning accuracy of the derotator test stand, a sine velocity profile covering the whole range of velocities expected for the field rotation trajectory at the ELT has been used. This is the same range of velocities previously presented in Figure 14. The test sine velocity profiles with its corresponding position trajectory are shown in Figure 119 and Figure 120. The angular positioning accuracy test has been performed with the controller architecture shown in Figure 57 and with the 3 tons of mass on top of the bearing.

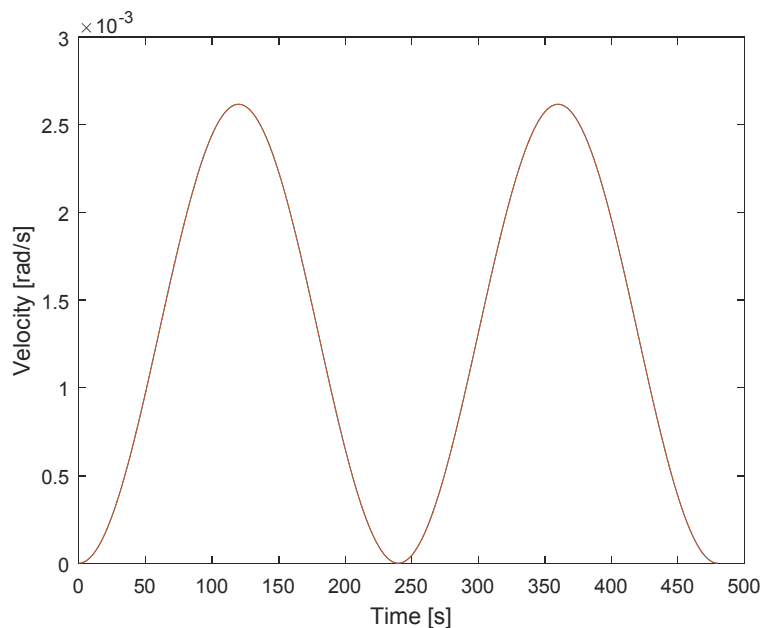


**Figure 119:** Sine velocity profile used for the relative angular positioning accuracy test.

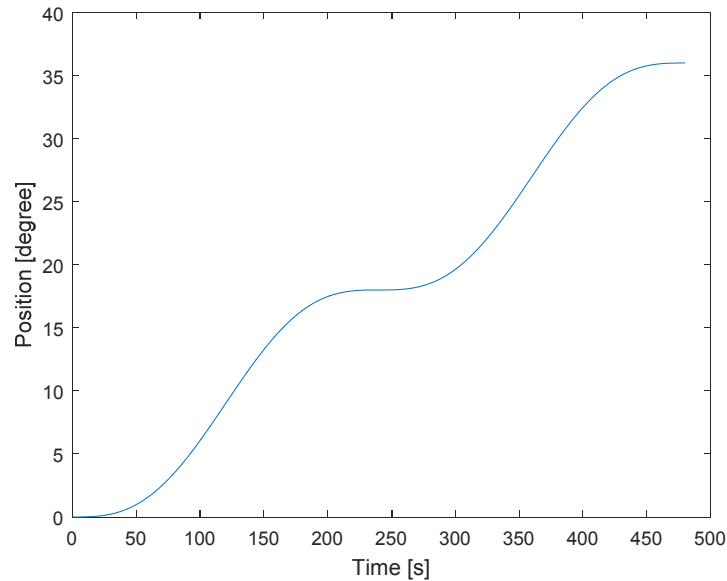


**Figure 120:** Position trajectory used for the relative angular positioning accuracy test.

The relative angular positioning accuracy is then calculated as the difference between the input trajectory (Figure 120) and the output trajectory registered by the band encoder installed on the test stand. The result of this test is presented in Figure 121. The peak error of about 20 arcsec while the trajectory is starting corresponds to the backlash between the gear wheel and the pinion. The rest of the curve shows a position error in the order of 1.4 arcsec (rms) being lower than the required positioning accuracy of 2 arcsec (rms). This is a very promising result for the overall derotator concept as the backlash suppression system is not yet installed.

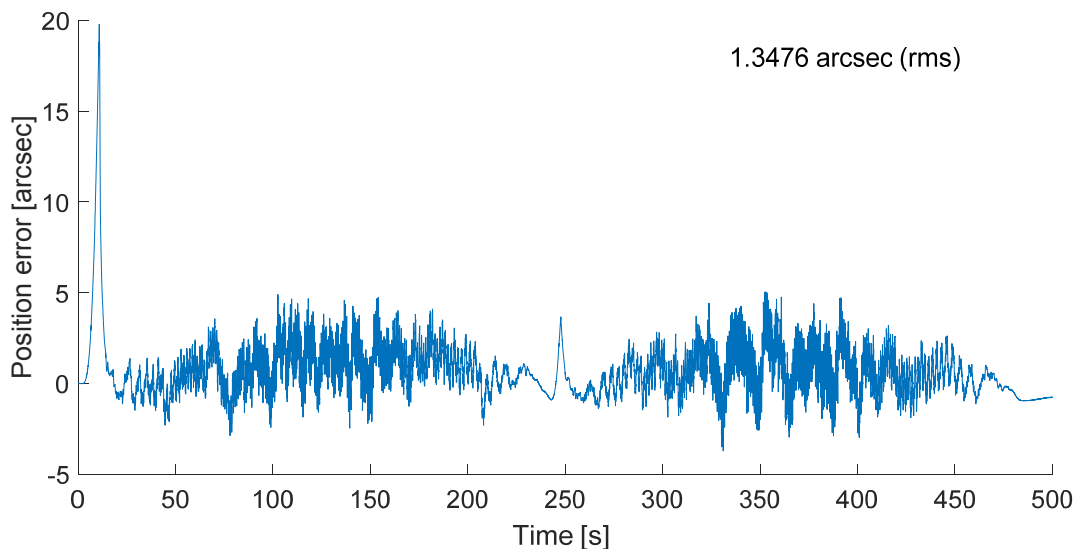


**Figure 121:** Position error of the test stand while following the test trajectory.

### 6.3.3.1 Relative Angular Positioning Accuracy with Simulated Friction Torque

The positioning accuracy test described in the previous section was repeated using the friction simulator installed on the derotator test stand. This test is used to simulate changes on the bearing friction torque. These changes could be generated by deformations coming into the bearing, for example, due to the movement of the attachments points on the ELT Nasmyth platform. The test demonstrates the robustness of the controller (Glück, 2019), especially as the backlash suppression system is still not installed, see Figure 122. The controller is able to react to the change of the friction torque (up to 4 times higher) keeping the position error.

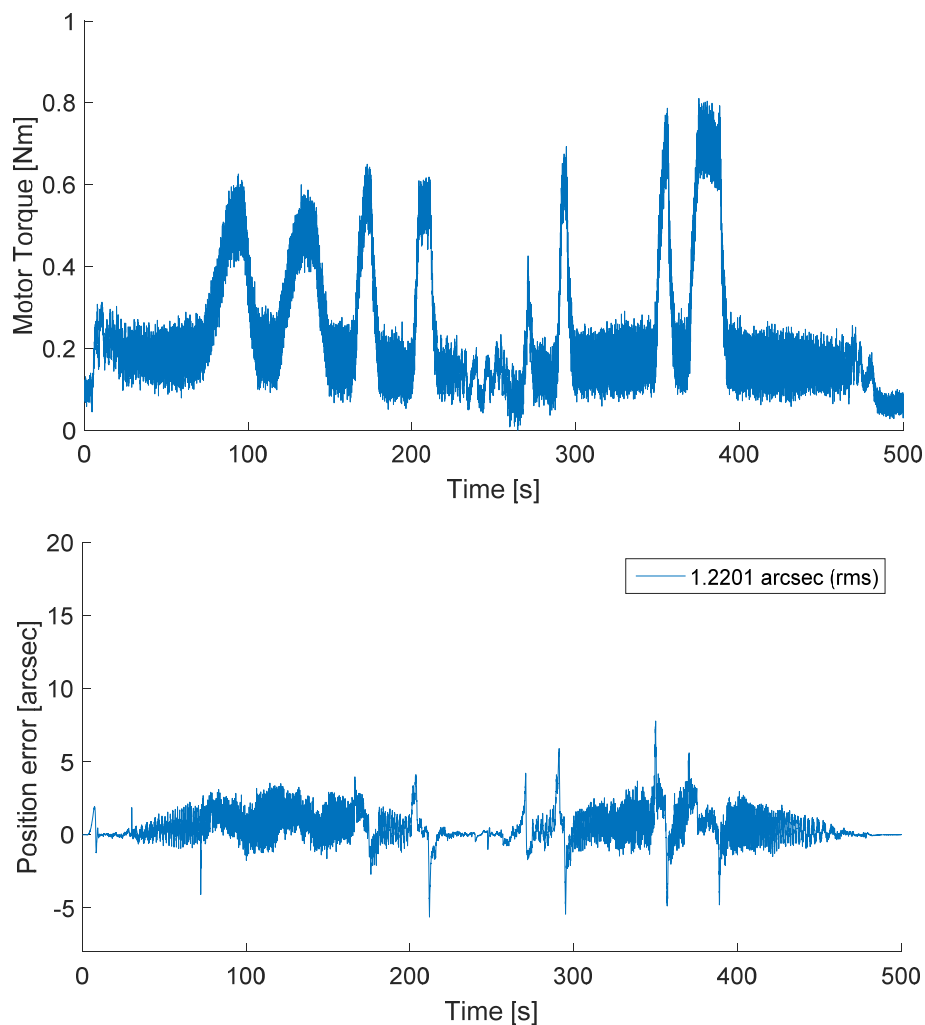


**Figure 122:** Position error of the test stand (bottom) with simulated friction torque changes(top).

## 6.4 Experimental results vs End-to-End Simulation

The correlation between the end-to-end simulation (only the mechanical model so far) and the behavior of the derotator test stand was already demonstrated in section 6.3.2 through the frequency response of the mechanical system, represented in the Bode plot. This section focuses on a more specific aspect, i.e., the verification of the friction model.

In order to probe the correct implementation of the LuGre friction model, the measured velocity (same data used for the identification of the Stribeck curve) is used as input for the Simulink model presented in Figure 98. Then the output of the model, the friction torque in this case, is plotted against the measured torque applied by the servomotor while the system is driven at constant velocity. The simulation is performed with the parameters given in Table 23 ( $F_v$  from Table 24) and  $\sigma_o = 2 \times 10^7$  and  $\sigma_1 = 2\sqrt{\sigma_o j_{GC}} 7.5$  as a rough estimation. Some of the results are presented in Figure 123 and Figure 124.

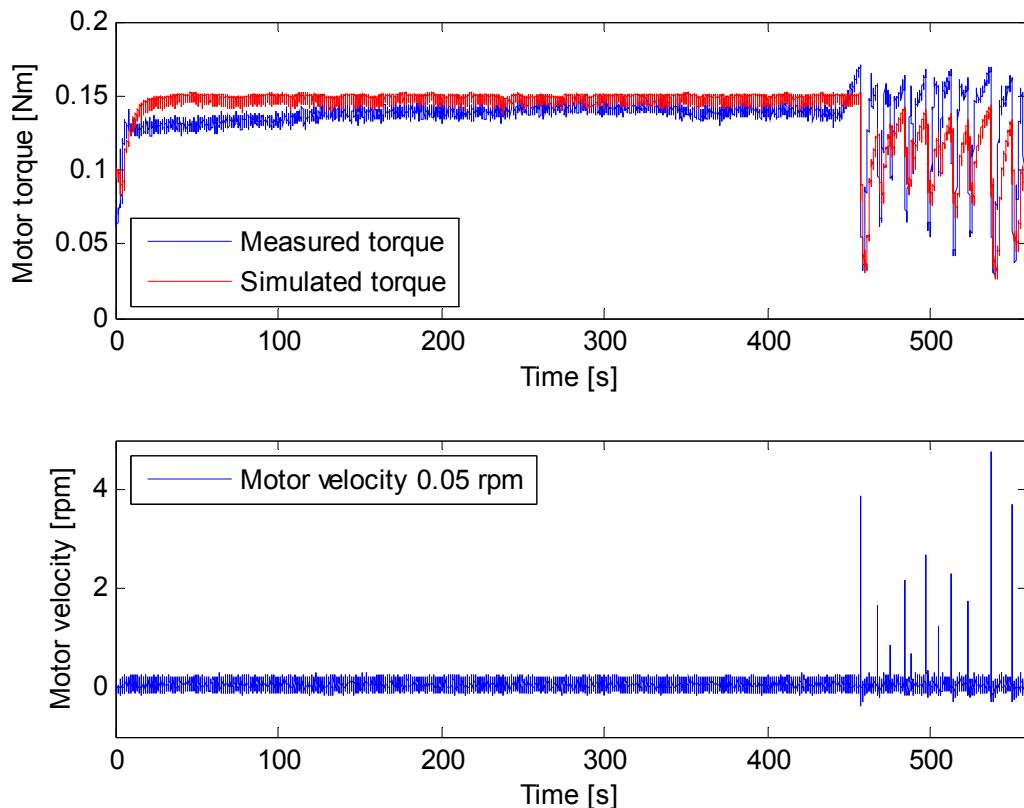


**Figure 123:** Simulated vs measured friction torque for a motor velocity of 0.05 rpm.

## 6.4 Experimental results vs End-to-End Simulation

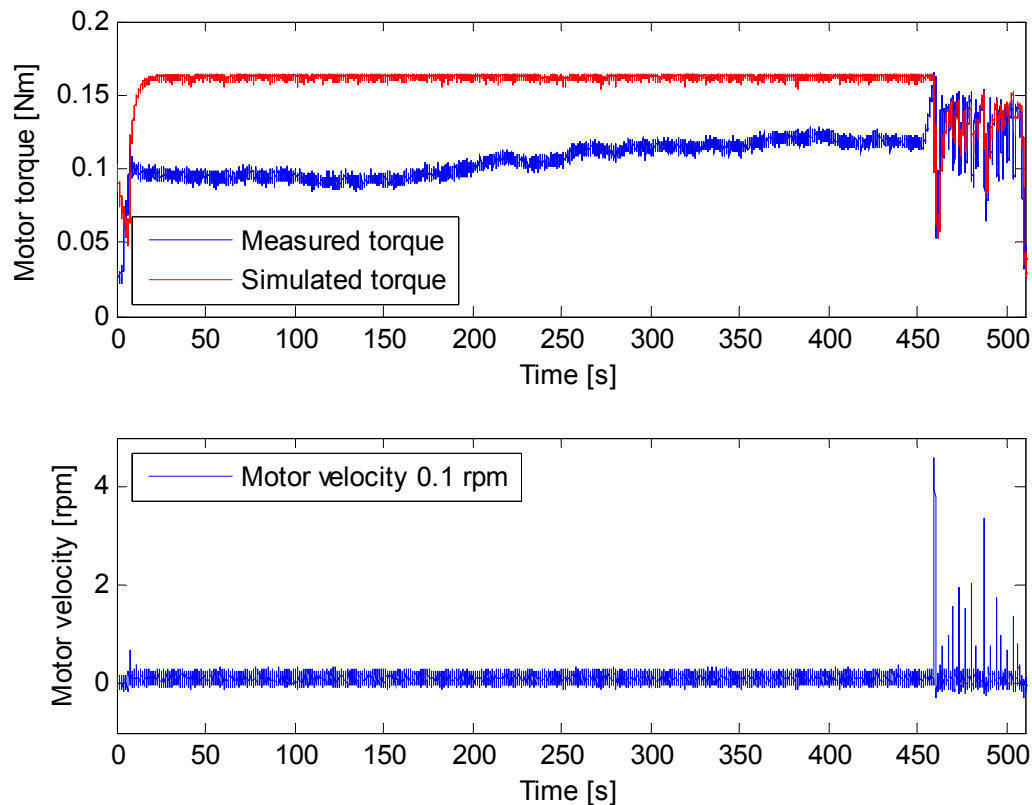


**Figure 124:** Simulated vs measured friction torque for a motor velocity of 0.1 rpm.

In both cases, the LuGre friction model is able to simulate the stick-slip effects starting around 450 s (this is in fact a coincidence, but the stick-slip effects are completely random and can appear any time as shown in appendix C). However, due to the friction position dependency previously commented, for the velocity of 0.1 rpm (Figure 124) the value of the average friction torque provided by the Stribeck curve does not corresponds to the measured torque. This confirms that the bearing friction cannot be characterized by one single Stribeck curve or only in a certain range of rotation. This position dependency friction behavior is expected to improve with the better quality nominal bearing in which additionally a cage instead of spacers is used to separate the balls inside the bearing. A good characterization of the bearing friction using several Stribeck curves will play a key role once the friction compensation is eventually implemented in the controller architecture (this has not been implemented yet). The correct modelling of the friction related stick-slip effects will contribute to improve the performance of the mechanical system to further improve its angular positioning accuracy.

Most of the key features of the design and simulation of the MICADO derotator could be experimentally verified, i.e. the bearing FEA, the dynamic behavior of the mechanical model implemented into the end-to-end simulation, the friction model, the relative angular positioning accuracy and the AIV process. However, some aspects like the performance of the mechanical model while following a trajectory (which means including the controller into the end-to-end simulation), the implementation of the friction compensation and the backlash suppression system will need an extended experimental approach.

The backlash suppression system could not be included into the frame work of the thesis due to the overall schedule of the MICADO project at MPIA. This feature is currently under development. On the other hand, the backlash suppression system has to be included into the simulation of the controller. For that reason the integration of the controller architecture into the end-to-end simulation can be performed only after wards.





## 7 Summary and Conclusions

This thesis has described the development of the image derotator for the MICADO instrument, one of the first light instruments for the ELT. The derotator is required to provide field rotation compensation with an angular positioning accuracy lower than 2 arcsec (rms). Three main aspects have been discussed in this dissertation.

**The design:** The task to be solved has been well understood and clearly defined by a set of requirements. As result, the design of the MICADO derotator is driven by those requirements; specifically the runout, the angular position accuracy of the derotator as a complete system and the mass limitation. The required runout at the level of 0.03 mm has been addressed with the selected bearing technology, i.e. slewing bearings. The custom designed four-point contact ball bearing proposed for the MICADO derotator was developed in collaboration with the bearing provider, where the integration of the band encoder into the bearing design is a key aspect contributing to simplify the mechanical interfaces of the derotator components. The static FEA of the derotator has been performed with a detailed FEM including frictional contact and bolt pretension between its main structural components. The bearing FEM implemented in this calculation, using spring element to model the ball inside the bearing, has been validated with dedicated test performed on the bearing used for the derotator test stand. According to the results of the static FEA of the derotator, the axial deformation of 0.021 mm coming into the bearing, is slightly higher than the maximal allowed deformation defined a requirement 0.015 mm. However, the bearing support ring can still be optimized to achieve the required stiffness with a 4- points interface with the instrument support structure, which is the current base line for the overall design of the MICADO instrument. The optimization

of this CFRP structure is part of the detailed design. However, given the proven robustness of the controller, it is expected that the slight friction changes due to this deformation can be handled without performance losses.

**The end-to-end simulation:** The basic tools to analyze the dynamic performance of the derotator design proposal through an end-to-end simulation have been provided here. Using the principle of structural dynamics and a lumped mass model (where rigid bodies are connected together with springs and dampers), the mathematical model representing the MICADO instrument mechanical system has been developed, implemented and verified with experimental data. In a first step, a general model with four degrees of freedom was established for the whole MICADO instrument, where the most relevant components that could affect the dynamic performance are represented, i.e. the instrument support structure, the derotator, the cryostat vessel, the internal cold structure and the drive unit. This model was then simplified to match the derotator test stand, where the degree of freedom corresponding to the internal cold structure of the cryostat was removed. The end-to-end simulation was implemented in a step wise approach using Matlab/Simulink. As the bearing friction is one of the most important effects to be considered for the dynamic performance of the derotator, it has been simulated using the LuGre friction model, where the corresponding parameters of the Stribeck curve were experimentally identified.

**The experiment:** The derotator test stand has been designed and built to represent as closely as possible the proposed concept to provide field rotation compensation for the MICADO instrument. It has been used as technology demonstrator for the selected bearing technology and for the verification of key elements of the end-to-end simulation, i.e. the mathematical model of the mechanical system and the LuGre friction model. A strong position dependency of the bearing friction has been identified on the test bearing with the experimental data. As result, it can be concluded that the whole range of rotation ( $360^\circ$ ) cannot be characterized by a single Stribeck curve, or a single Stribeck curve can only be used for a small section of the bearing. The control system has been optimized (Glück, 2019) with promising preliminary results, where the test stand loaded with 3 tons of mass is able to achieve

an angular positioning accuracy at the level of 1.4 arcsec while following a defined trajectory in which the velocity profile corresponds to the expected field rotation velocities at the ELT Nasmyth platform A. This results is already lower than the required 2 arcsec. To further improve these results and reach the accuracy limits of the bearing, a friction compensator based on the presented models will be investigated in Glück (2019).

### **Future work**

The tasks from now on of this contribution to the MICADO project will be focused mainly in two aspects: (i) upgrade the FEM to include other structural components as the cryostat and the instrument support structure in order to achieve a more realistic FEA and, (ii) the implementation of the friction compensation feature in the control system to investigate a further improvement of the current angular position accuracy. With the work presented in this thesis, it could be demonstrated that the proposed bearing technology is the adequate choice for solving the image derotation problem in MICADO. The detailed structural modeling of the bearing developed in this thesis is essential input in the overall structural design optimization process. Furthermore, It could be demonstrated with a self-designed fully functional laboratory testbed that the stringent rotation precision requirements are achievable with the proposed bearing technology while operating in close-loop with optimized controller architecture. The design proposal of the derotator described in this thesis will be used as baseline for the upcoming PDR of the MICADO project.

This research work has shown how mathematical tools as the FEA (static aspects of the analysis) and the modeling of mechanical systems (dynamic aspects of the analysis), can be used to optimize and improve the design and, the consequently analysis process of precision mechanisms. Once the problem to be solved is clearly defined with a set of requirements, these are powerful and versatile techniques that can be implemented to develop precision mechanisms for a wide range of applications. Even better results can be achieved when the design approaches here described are combined with advanced control techniques.



# Appendix A

## Drive Unit Calculations

### A.1 Motor Torque Estimation

$T_{TM}$  - Required motor torque  
 $K_S$  - Safety factor  
 $T_M$  - Motor torque  
 $T_{HD\ input}$  - Harmonic Drive input torque  
 $\eta_{HD}$  - Harmonic Drive efficiency  
 $T_{HD\ output}$  - Harmonic Drive output torque  
 $T_F$  - Frictional torque  
 $T_{FG}$  - Frictional torque bearing  
 $I_G$  - Gear ratio  
 $I_{HD}$  - Harmonic Drive gear ratio  
 $T_a$  - Acceleration torque  
 $J_T$  - Total inertia of the system  
 $\alpha$  - Angular acceleration  
 $\omega_{HD}$  - Harmonic Drive velocity  
 $t$  - Time for velocity change  
 $J_C$  - Cryostat inertia  
 $J_G$  - Gear inertia  
 $J_P$  - Pinion inertia  
 $J_M$  - Motor inertia  
 $D_C$  - Cryostat diameter  
 $m_C$  - Cryostat mass

$$T_{TM} = K_S T_M = \mathbf{2 Nm}$$

$$K_S = 2.5$$

$$T_M = \frac{T_{HD \text{ input}}}{\eta_{HD}} = 0.8 Nm$$

$$\eta_{HD} = 57 \%$$

$$T_{HD \text{ output}} = T_F + T_a = 0.45 Nm$$

$$T_F = \frac{T_{FG}}{I_G I_{HD}} = 0.38 Nm$$

$$T_{FG} = 1700 Nm \text{ (for the nominal bearing by RE)}$$

$$I_G = \frac{Z_P}{Z_G} = 27.71$$

$$Z_P = 17$$

$$Z_G = 471$$

$$I_{HD} = 160$$

$$T_a = J_T \alpha = 0.06 Nm$$

$$\alpha = \left( \frac{\omega_{HD} - \omega_0}{t} \right) = 92.84 \text{ rad/s}^2$$

$$\omega_{HD} = \omega_P I_G I_{HD} = 464.22 \text{ rad/s (4433 rpm)}$$

$$\omega_G = 0.1047 \text{ rad/s (1 rpm)}$$

$$\omega_0 = 0, t = 5 \text{ s}$$

$$J_T = J_C + J_G + 3 J_P = 7 \times 10^{-4} \text{ kg m}^2$$

$$J_C = \frac{1}{8} m_C D_C^2 \left( \frac{1}{I_G I_{HD}} \right)^2 = 2.5 \times 10^{-4} \text{ kg m}^2$$

$$J_G = \frac{1}{8} m_G (D_{G1}^2 + D_{G2}^2) \left( \frac{1}{I_G I_{HD}} \right)^2 = 3.8 \times 10^{-5} \text{ kg m}^2$$

$$J_P = \frac{1}{8} m_P D_P^2 \left( \frac{1}{I_{HD}} \right) = 1.6 \times 10^{-7} \text{ kg m}^2$$

## A.2 Harmonic Drive Gear Selection

The reduction gearing arrangement of the Harmonic Drive is shown in Figure 125 where CS is the circular spline, FS is the flex spline and WG is the wave generator. For the arrangement selected for the MICADO derotator drive units, CS is fixed, WG is the input and FS is the output of the Harmonic Drive gear.

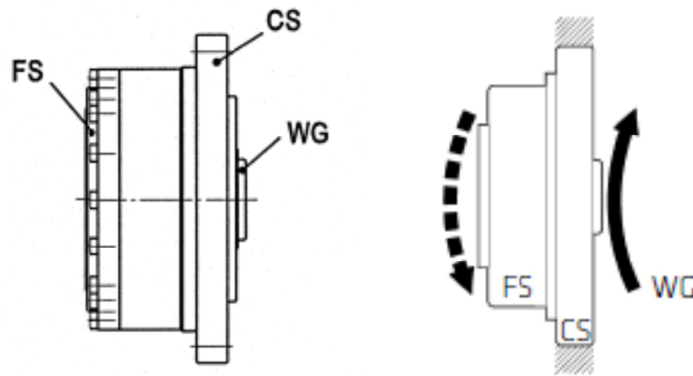


**Figure 125:** Simulated Harmonic Drive gearing arrangement (Image source: Harmonic Drive AG, 2014).

In this particular arrangement the gear ratio  $I_{HD}$  is defined as follow

$$I_{HD} = \frac{\text{output torque}}{\text{input torque}} = \frac{\text{input speed}}{\text{output speed}} \quad (81)$$

For the selection of the Harmonic Drive gear the output data presented in Table 25 is assumed.

Output torque	Operation time	Output speed
$T_1 = 70 \text{ Nm}$	$t_1 = 60 \text{ s}$	$n_1 = 27.1 \text{ rpm}$
$T_2 = 60 \text{ Nm}$	$t_2 = 120 \text{ s}$	$n_2 = 2.71 \text{ rpm}$
$T_3 = 65 \text{ Nm}$	$t_3 = 120 \text{ s}$	$n_3 = 2.71 \text{ rpm}$

**Table 25:** Output data assumed for the selection of the Harmonic Drive gear.

The selection of the Harmonic Drive gear is based in two parameters, the average output torque ( $T_{AV}$ ) and the average input speed ( $n_{out AV}$ ) which are defined by the following equations

$$T_{AV} = \sqrt[3]{\frac{|n_1 T_1^3| t_1 + |n_2 T_2^3| t_2 + |n_3 T_3^3| t_3}{|n_1| t_1 + |n_2| t_2 + |n_3| t_3}} \quad (82)$$

$$n_{out\ AV} = \frac{|n_1|t_1 + |n_2|t_2 + |n_3|t_3}{t_1 + t_2 + t_3}. \quad (83)$$

For the correct selection of the Harmonic drive gear,  $T_{AV}$  must be lower than the permissible average torque ( $T_A$ ) and the estimated average input speed must be lower than the permissible average input speed  $n_{in\ AV}$ . The input speed can be obtained according to equation (81). For the model HFUC-25-160-2UH used in the MICADO derotator drive unit the following values are valid

$$T_{AV} = 73\ Nm < T_A = 108\ Nm$$

$$n_{out\ AV} I_{HD} = 1241\ rpm < n_{in\ AV} = 3500\ rpm$$



## Appendix B

### Friction Simulator Calculations

The high precision bearing implemented in the MICADO derotator has a starting friction torque of 1700 Nm, while the standard bearing used in the test stand has a starting friction torque of 1000 Nm (information provided by Rothe Erde). Using the principle of the band brake shown in Figure 106, the linear actuator must apply a force of 212 N to generate a braking torque of 800 Nm - the difference between the starting friction torques of both bearings. The schematic representation of a band brake used as reference for the calculation is presented in Figure 126.

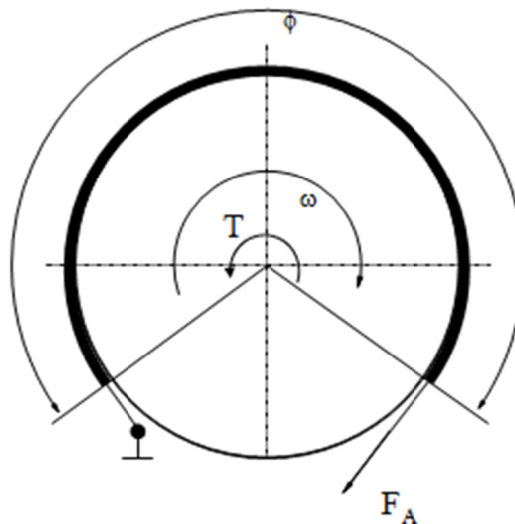


**Figure 126:** Schematic representation of the band brake (Source: MathWorks online documentation )

The equations used for the linear actuator axial force estimation are presented as follows (Mathworks, 2018):

$T$  - Braking torque

$F_A$  - Applied force

$r_D$  - Drum radius

$\mu$  - Friction coefficient

$\theta$  - Wrap angle

$$T = F_A(e^{\mu\theta} - 1)r_D = \mathbf{805 Nm}$$

$$F_A = 212 N$$

$$r_D = 0.578 m$$

$$\mu = 0.4 \text{ (provided by NB Parts)}$$

$$\theta = 5.1 \text{ rad (290 degree)}$$

Based on this calculation the linear actuator MA-35 DC-B-013 from the company PI was selected. The friction material used in the band brake was provided by the company NB parts.

# Appendix C

## Steady State Friction Torque

### Measurement

The stick-slip effects are clearly seen in the steady state friction torque measurements presented as follow.

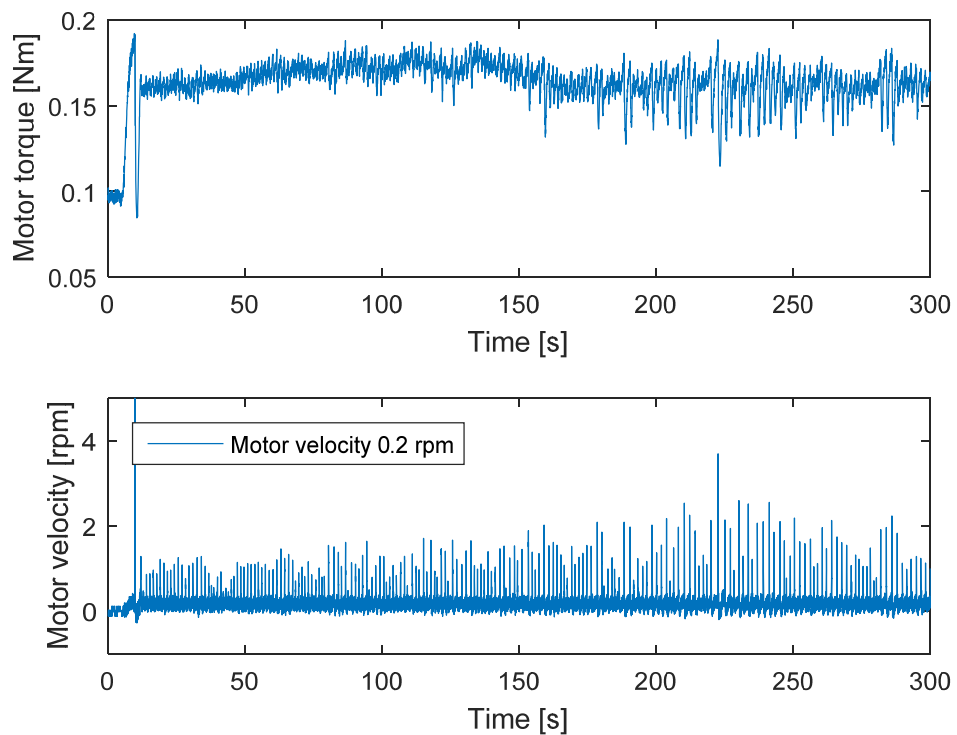


**Figure 127:** Steady state friction torque measurement for a motor velocity of 0.2 rpm.

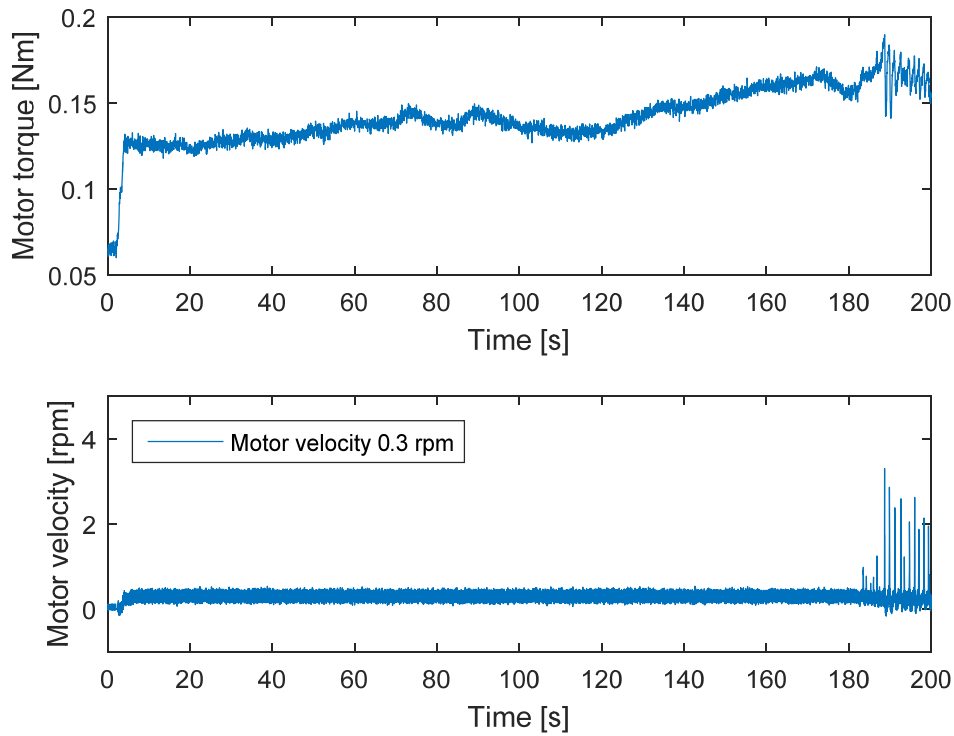


**Figure 128:** Steady state friction torque measurement for a motor velocity of 0.3 rpm.

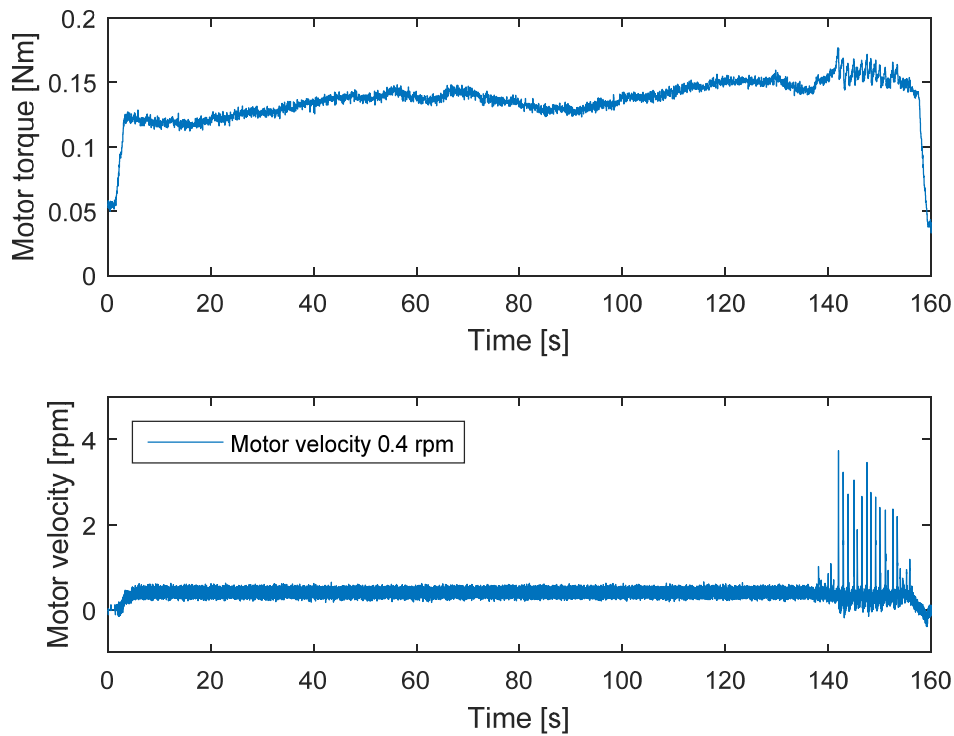


**Figure 129:** Steady state friction torque measurement for a motor velocity of 0.4 rpm.

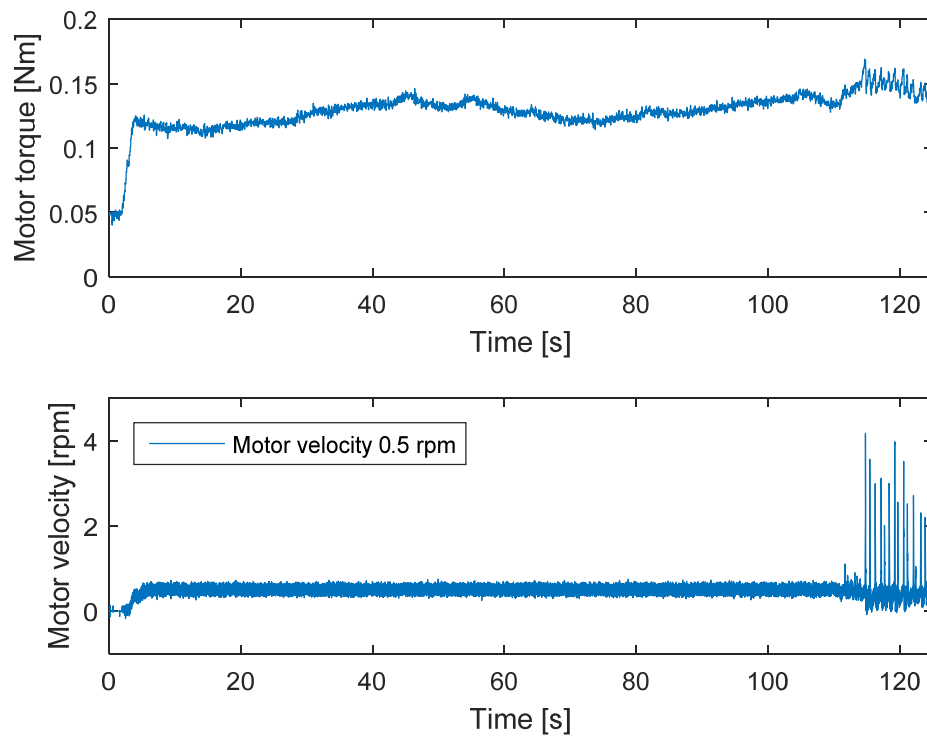


**Figure 130:** Steady state friction torque measurement for a motor velocity of 0.5 rpm.

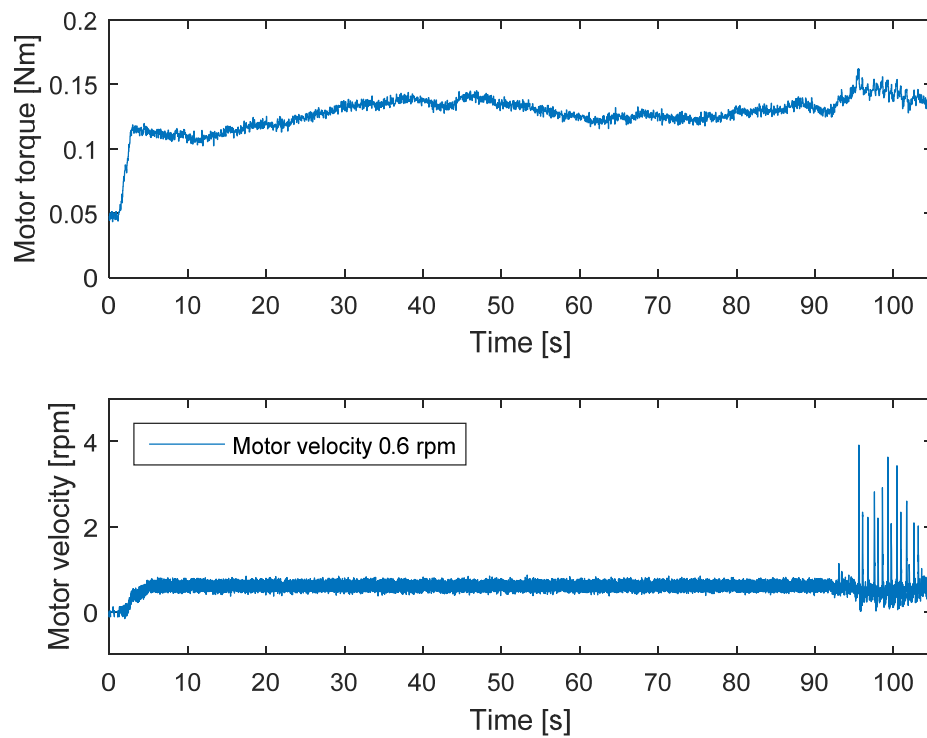


**Figure 131:** Steady state friction torque measurement for a motor velocity of 0.6 rpm.

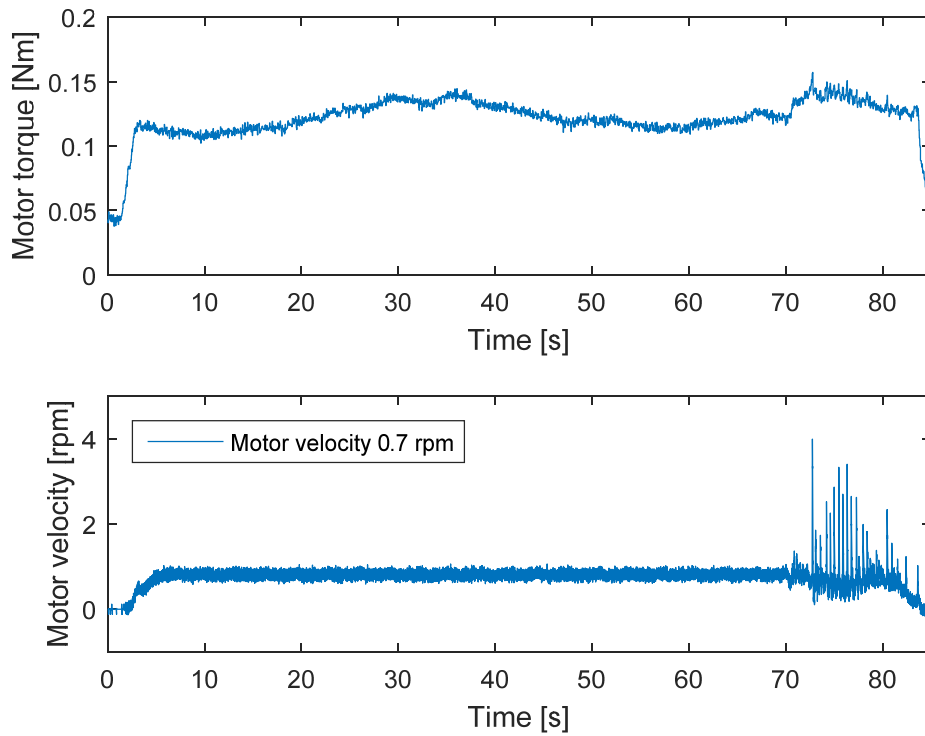


**Figure 132:** Steady state friction torque measurement for a motor velocity of 0.7 rpm.

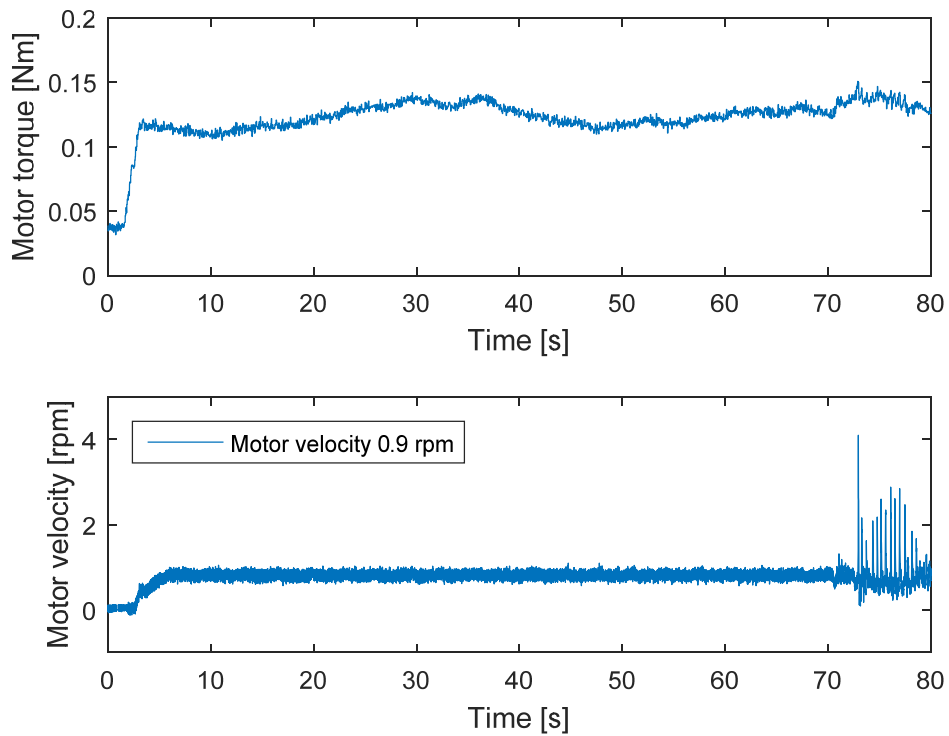


**Figure 133:** Steady state friction torque measurement for a motor velocity of 0.9 rpm.

# Bibliography

- Andersen, T., Ardeberg, A., Beckers, J., Flicker, R., Jessen, N. C., Gontcharov, A., . . . Riewaldt, H. (1999). The proposed 50 m Swedish Extremely Large Telescope. *Bäckaskog Workshop on Extremely Large Telescopes*.
- Andersen, T., Ardeberg, A. L., Beckers, J., Goncharov, A., Owner-Petersen, M., Riewaldt, H., . . . Walker, D. (2003). The Euro50 Extremely Large Telescope. *Proc. SPIE 4840, Future Giant Telescopes*.
- ANSYS. (2018). *ANSYS Documentation release 18.1*. ANSYS inc.
- Ardeberg, A., Andersen, T., Beckers, J., Browne, M., Enmark, A., Knutsson, P., & Owner-Petersen, M. (2006). From Euro50 toward a European ELT. *Proc. SPIE 6267, Ground-based and Airborne Telescopes*.
- Armstrong-Hélouvry, B., Dupont, P., & Canudas de Wit, C. (1994). A survey of Models, analysis Tools and Compensation Methods for the Control of Machines with Friction. *Automatica, Vol. 30, No. 7*.
- Ashby, D., & Meeks, R. (2007). *Instrument Rotator and Cable Chain Detailed Design Description (670s007c)*. LBT PROJECT.
- Åström, K. J., & Murray, R. M. (2009). *Feedback Systems: An Introduction for Scientists and Engineers*. Princeton University Press.
- Avila, G., & Wirenstrand, K. (1991). *Field and pupil rotations for the VLT 8 m unit telescopes*. ESO.
- Barboza, S. (2017). *Derotator Test Stand AIV Plan and Procedure. ELT-PLA-MCD-56301-0013. Issue 0.5*. MICADO Consortium.

## Bibliography

---

- Barboza, S. (2017). *MICADO De-Rotator MAIT Plan. ELT-PLA-MCD-56301-0011*. MICADO Consortium.
- Barboza, S., Pott, J.-U., Rohloff, R.-R., Müller, F., Wagner, J., & Kärcher, H. J. (2016). Design of a large image derotator for the E-ELT instrument MICADO. *Proc. SPIE 9908, Ground-based and Airborne Instrumentation for Astronomy*.
- Barboza, S., Rohloff, R.-R., Müller, F., Hofferbert, R., Pott, J.-U., Wagner, J. F., & Schlossmacher, W. (2017). Modelling a Large Four-Point Contact Slewing Bearing for Application in Astronomical Instrumentation. 35. *CADFEM ANSYS Simulation Conference*. Koblenz.
- Bathe, K.-J. (2014). *Finite Element Procedures*. Watertown, MA.: K.-J. Bathe.
- Beckers, J. (1999). Extremely large multiple mirror telescopes. Bäckaskog Workshop on Extremely Large Telescopes.
- BECKHOFF. (2015). *Synchronous Servomotors AM8000 & AM8500*.
- Beckwith, S. W. (2012). Quasi-Isotropic Composite Materials/Structures Design – Part I. *SAMPE Journal, Volume 48, No. 3*.
- Bely, P. Y. (2003). *The Design and Construction of Large Optical Telescopes*. New York: Springer.
- Bertram, T. (2015). *GWS Sensor Bearing Tests. LN-MPIA-TN-MECH-026*. LINC-NIRVANA Consortium.
- Bizenberger, P., Baumeister, H., Böhm, A., Herbst, T., Huber, A., Laun, W., . . . Trowitzsch, J. (2012). LINC-NIRVANA, integration of an interferometric and cryogenic camera: first verification results. *Ground-based and Airborne Instrumentation for Astronomy IV. SPIE Vol. 8446, 844647*.
- Brandl, B., Rainer, L., Eric, P., Alistair, G., Joris, B., Michael, M., . . . Frank, M. (2012). METIS: the thermal infrared instrument for the E-ELT. *Ground-based and Airborne Instrumentation for Astronomy IV*.
- Brickwood, H. (2016). *How much more effective is 3M™ Liquid Shim in comparison to traditional shims?* . Von [www.linkedin.com](http://www.linkedin.com/pulse/how-much-more-effective-3m-liquid-shim-comparison-shims-brickwood/): <https://www.linkedin.com/pulse/how-much-more-effective-3m-liquid-shim-comparison-shims-brickwood/> abgerufen



- Canudas de Wit, C., Olsson, H., Aström, K. J., & Lischinsky, P. (1995). A New Model for Control of Systems with Friction. *IEEE TRANSACTIONS ON AUTOMATIC CONTROL*, Vol 40, No 3.
- CarbonVision. (2014). *PFS SUMIRE Bench Technical Report (TR 140404)*.
- CarbonVision. (2017). *MICADO Bearing Support Ring Evaluation of Stiffness (TN171005)*.
- Cayrel, M. (2012). E-ELT Optomechanics: Overview. *Proc. of SPIE Vol. 8444, Ground-based and Airborne Telescopes IV*.
- Clénet, Y., Buey, T., Rousset, G., Gendron, E., Esposito, S., Hubert, Z., . . . Zins, G. (2016). Joint MICADO-MAORY SCAO mode: specifications, prototyping, simulations and preliminary design. *Proc. SPIE 9909, Adaptive Optics Systems V*.
- Crepy, B., Chaillot, S., Conan, J. M., Cousty, R., Delrez, C., Dimmler, M., . . . Petitgas, D. (2010). *Last progress concerning the design of the piezo stack M4 adaptive unit of the E-ELT*. *Proc. SPIE 7736, Adaptive Optics Systems II*.
- Daidié, A., Chaib, Z., & Ghosn, A. (2008). 3D Simplified Finite Elements Analysis of Load and Contact Angle in a Slewing Ball Bearing. *Journal of Mechanical Design*, Vol. 130 / 082601-1.
- Davies, R., Ageorges, N., Barl, L., Bedin, L. R., Bender, R., Bernardi, P., . . . al., e. (2010). MICADO: the E-ELT adaptive optics imaging camera. *Proc. SPIE 7735, Ground-based and Airborne Instrumentation for Astronomy III*.
- Davies, R., Pott, J.-U., & Tolstoy, E. (2017). *Operational Concept Description (ELT-PLA-MCD-56301-0004)*. MICADO Consortium.
- Davies, R., Schubert, J., Hartl, M., Alves, J., Clénet, Y., Lang-Bardl, F., . . . al., e. (2016). MICADO: first light imager for the E-ELT. *Proc. SPIE 9908, Ground-based and Airborne Instrumentation for Astronomy VI*.
- Dierickx, P., & Gilmozzi, R. (1999). OWL concept overview. *Bäckaskog Workshop on Extremely Large Telescopes*.
- Dierickx, P., & Gilmozzi, R. (2000). Progress of the OWL 100-m telescope conceptual design. *Proc. SPIE 4004, Telescope Structures, Enclosures, Controls, Assembly/Integration/Validation, and Commissioning*.

## Bibliography

---

- Diolaiti, E., Ciliegi, P., Abicca, R., Agapito, G., Arcidiacono, C., Baruffolo, A., . . . Cortecchia, F. (2016). MAORY: adaptive optics module for the E-ELT. *Proc. SPIE 9909, Adaptive Optics Systems V*.
- Dreyer, O., Ippa, A., Seubert, S., Kärcher, H. J., Jeffers, P., & Bonomi, G. (2014). Performance Verification of the DKIST Mount and Coudé Laboratory. *Ground-based and Airborne Telescopes V, Proc. of SPIE Vol. 9145, 91452A*.
- Dunn, J., Andersen, D., Chapin, E., Reshetov, V., Wierzbicki, R., Herriot, G., . . . Suzuki, R. (2016). The Infrared Imaging Spectrograph (IRIS) for TMT: Multi-tiered Wavefront Measurements and Novel Mechanical Design. *Proc. SPIE 9908, Ground-based and Airborne Instrumentation for Astronomy VI, 9908A9*.
- Dupont, P., Armstrong, B., & Hayward, V. (2000). Elasto-Plastic Friction Model: Contact Compliance and Stiction. *Proceedings of the American Control Conference, 0-7803-551 9-9*.
- Egner, S., & Bertram, T. (2009). *LINC-NIRVANA - Field Rotation*. LINC-NIRVANA Consortium.
- ESO. (2010). *E-ELT Site Chosen*. Von <https://www.eso.org/public/news/eso1018/> abgerufen
- ESO. (2011). *E-ELT Construction Proposal*. European Southern Observatory.
- ESO. (2016). *ESO Signs Largest Ever Ground-based Astronomy Contract for E-ELT Dome and Telescope Structure*. Von <https://www.eso.org/public/news/eso1617/> abgerufen
- ESO. (December 2016). [www.eso.org](http://www.eso.org). Von <https://www.eso.org/sci/facilities/eelt/site/> abgerufen
- Frank, C. (2015). MAORY & MICADO Design Volume. *CAD-118347*. ESO.
- Gao, X. H., Huang, X. D., Wang, H., & Chen, J. (2010). Modelling of ball-raceway contacts in a slewing bearing with non-linear springs. *Proc. IMechE Vol. 225 Part C: J. Mechanical Engineering Science*.
- Gebhardt, A., Damm, C., Kinast, J., Rohloff, R.-R., Lenzen, R., & Rochau, B. (2012). Ultraprecision Manufacture and Alignment of the GRAVITY K-

- Mirror for the Very Large Telescope Interferometer. *Proceedings of the 12th European International Conference*. Stockholm.
- Glück, M. (2019). PhD thesis. Institute for System Dynamics (ISYS), University of Stuttgart. Expected publication 2019.
- Green, R. M. (1985). *Spherical astronomy*. Cambridge: Cambridge Univ.
- Häberle, M. (2017). *Verifying the accuracy of the angle encoder for the MICADO derotator at the MPIA test stand*. Department of Physics and Astronomy, University of Heidelberg. Bachelor Thesis in Physics.
- Hake, E., & Meskouris, K. (2007). *Statik der Flächentragwerke*. Springer.
- Harmonic Drive AG. (2014). *Engineering Data HFUC-2UH Units*.
- HEIDENHAIN. (2011). *Adjustment unit for ERA 7xxx/8xxx (D737777-00-A-01)*.
- HEIDENHAIN. (2014). *Angle encoders Without Integral Bearing*.
- Herman, R. I. (2017). *SOLVING DIFFERENTIAL EQUATIONS USING SIMULINK*. R. I. Herman.
- Ingenieurbüro SCHLOSSMACHER. (2006). *GWS mount and bearing Tests and Measurements Report (2006-0511)*.
- Johnsa, M., Hulla, C., Mullera, G., Irrarazavala, B., Boucheza, A., Chyleka, T., . . . Buleri, C. (2014). Design of the Giant Magellan Telescope. *Proc. SPIE 9145, Ground-based and Airborne Telescopes V*.
- Kandpal, M. (1997). *Physics Discovering*. New Delhi: Hemkunt Press.
- Kärcher, H. J. (2008). Large telescopes and the art of bridge building. *Proc. SPIE 7012, Ground-based and Airborne Telescopes II*.
- Kärcher, H. J., Kühn, J., & Nicklas, H. (1988). An Alternative Concept to Current Alt-Azimuthal Mountings and an Estimate of the Related Tracking Accuracy. *ESO Conference on Very Large Telescopes and their Instrumentation*.
- Kärcher, H. J., Weis, U., Dreyer, O., Jeffers, P., & Bonomi, G. (2012). The azimuth axes mechanisms for the ATST telescope mount assembly. *Ground-based and Airbone Telescopes IV. Proc. of SPIE 8444, 84440A*.
- Krüsemann, B. (2015). *MICADO De-rotator Bearing Technical Proposal 16-36833*. ThyssenKrupp Rothe Erde GmbH.

## Bibliography

---

- Krynke, M., Selejdak, J., & Borkowski, S. (2013). Determination of static limiting load curves for slewing bearings with application of the finite element methods. *Materials Engineering Journal* 20.
- Laing, R. (2015). The Performance of the European ALMA Antennas. *36th ESA Workshop on Antennas*.
- Liske, J. (2015). *Top Level Requirements for ELT-CAM. ESO-193104 Version 2*. ESO.
- Lombini, M., Rosa, A. D., Ciliegi, P., Cortecchia, F., Diolaiti, E., Patti, M., . . . Stadler, E. (2016). Optical design of the post-focal relay of MAORY. *Proc. SPIE 9908, Ground-based and Airborne Instrumentation for Astronomy VI*.
- Mangum, J. G. (2015). The performance of the north american ALMA antennas. *36th ESA Workshop on Antennas*.
- Mathworks. (2018). *Band Brake*. Von Mathworks Documentation: <https://www.mathworks.com/help/physmod/sdl/ref/bandbrake.html> abgerufen
- MPE. (2015). Von Kick-off for a new era of precision astronomy: [http://www.mpe.mpg.de/6460131/News\\_20151006](http://www.mpe.mpg.de/6460131/News_20151006) abgerufen
- Mueller, F. (2017). *MICADO De-Rotator Subsystem Requirements Specification*. MICADO consortium.
- Nelson, J. E., Mast, T. S., & Faber, S. M. (1985). *The Design of the Keck Observatory and Telescope*. Caltech.
- Nelson, J., & Sanders, G. H. (2008). The status of the Thirty Meter Telescope project. *Proc. SPIE 7012, Ground-based and Airborne Telescopes II*.
- New Way Air Bearings. (2011). *SPECIFICATIONS AND TOLERANCING INFORMATION FOR CONCAVE AND CONVEX CONFIGURATIONS*.
- Nicklas, H. E., Anwand-Heerwart, H., Schubert, J., & Rhode, P. (2016). MICADO: the camera support structure at the E-ELT Nasmyth focus. *Proc. SPIE 9908, Ground-based and Airborne Instrumentation for Astronomy VI*.
- Olsson, H. (1996). *Control Systems with Friction*. Department of Automatic Control, Lund Institute of Technology, Sweden.
- Olsson, H., Aström, K., Caudas de Wit, C., Gäfvert, M., & Lischinsky, P. (1998). Friction Models and Friction Compensation. *European Journal of Control*.

- Paufique, J., Bruton, A., Glindemann, A., Jost, A., Kolb, J., & Jochum, L. (2010). GRAAL: a seeing enhancer for the NIR wide-field imager Hawk-I. *Adaptive Optics Systems II, Proc. of SPIE Vol. 7736, 77361P*.
- Pott, J.-U., & Barboza, S. (2017). *MPIA technical note - Derotator requirements*. MICADO consortium.
- Racine, R. (2004). The Historical Growth of Telescope Aperture. *Astronomical Society of the Pacific, Vol. 116, No. 815, 77-83*.
- Ramsay, S., Casali, M., Cirasuolo, M., Egner, S., Gray, P., Herrera, J. C., . . . Manescau, A. (2016). Progress along the E-ELT instrumentation roadmap. *Proc. SPIE 9908, Ground-based and Airborne Instrumentation for Astronomy VI*.
- Rohloff, R.-R., Münch, N., Böhm, A., Schlossmacher, W., Schöppinger, C., Neugeboren, H., . . . Wichmann, H. (2006). CFRP structure for the LBT instrument LINC-NIRVANA. *Proc. SPIE 6273, Optomechanical Technologies for Astronomy, 62730Z*.
- Sändig, K. (2016). *Error Budget: Derotator for Micado-Instrument (E-ELT)*. HEIDENHAIN.
- Schmid, C. (2015). *Common Requirements for E-ELT Instruments*. ESO.
- Schreiber, L., Lombini, M., Foppiani, I., Daniel, M., Fulvio, D. B., Peter, B., . . . Jacopo, F. (2008). Integration of the mid-high wavefront sensor to the LINC-NIRVANA postfocal relay. *Adaptive Optics Systems*.
- Sebring, T., Moretto, G., Bash, F., Ray, F., & Ramsey, L. (1999). The Extremely Large Telescope (ELT), a scientific opportunity; an engineering certainty. *Bäckaskog Workshop on Extremely Large Telescopes*.
- Shepherd, M. (2001). *Pointing the CBI*. Von <http://www.astro.caltech.edu/~mcs/CBI/pointing/> abgerufen
- Swift, D. W. (1972). Image rotation devices a comparative survey. *Optics and Laser Technology, 175-188*.
- Taghirad, H. (1995). *On the Modelling and Identification of Harmonic Drive Systems*. Center of Intelligent Machines, McGill University.

## Bibliography

---

- Tamai, R., Cirasuolo, M., González, J. C., Koehler, B., & Tuti, M. (2016). The E-ELT program status. *Proc. SPIE 9906, Ground-based and Airborne Telescopes VI*.
- ThyssenKrupp Rothe Erde. (2015). *Modelling of a large-diameter slewing bearing as part of a threedimensional finite element model*.
- Thyssenkrupp Rothe Erde. (2017). *Slewing Bearings Catalog*. Thyssenkrupp Rothe Erde GmbH.
- Todhunter, I., & Leathem, J. G. (2006). *Spherical Trigonometry*. Cambridge: C. J. CLAY, M.A. AND SON, AT THE UNIVERSITY PRESS.
- Turner, M. (2011). *Modelling and simulation of engineering systems*. Dept. of Engineering, University of Leicester.
- Tuttle, T. D. (1992). *Understanding and Modeling the Behavior of a Harmonic Drive Gear Transmission*. MIT Artificial Intelligence Laboratory.
- Vernet, E., Cayrel, M., Hubin, N., Biasi, R., Angerer, G., Andrighttoni, M., . . . Xompero, M. (2013). THE ADAPTIVE MIRROR FOR THE E-ELT. *Third AO4ELT Conference - Adaptive Optics for Extremely Large Telescopes*.
- Vernin, J., Muñoz-Tuñon, C., & Sarazin, M. (2008). E-ELT site characterization status. *Proc. SPIE 7012, Ground-based and Airborne Telescopes II*.
- Wagner, J., & Mlejnek, H.-P. (2012). *Dynamik I*. Institut für Statik und Dynamik der Luft- und Raumfahrtkonstruktionen, Universität Stuttgart.
- Wagner, J., & Mlejnek, H.-P. (2012). *Dynamik II*. Institut für Statik und Dynamik der Luft- und Raumfahrtkonstruktionen, Universität Stuttgart.
- Wagner, J., & Mlejnek, H.-P. (2015). *Tragwerksoptimierung*. Institut für Statik und Dynamik der Luft- und Raumfahrtkonstruktionen, Universität stuttgart.
- Windgassen. (2017). *MICADO prototype bearing test report (F&E-288\_00-17)*. Thyssenkrupp Rothe Erde.
- Zeeuw, T. d., Tamai, R., & Liske, J. (2014). Constructing the E-ELT. *ESO The Messenger* 158.

# Curriculum Vitae

## Personal Data

Name Santiago Barboza  
Born March 15, 1983 in Mérida Venezuela

## Education

2013 - 2014 Equivalence of Master's degree to be officially accepted as PhD student, University of Stuttgart, Germany.  
2011 Magister Scientiae (M.Sc) in Mechanical Engineering, Universidad de los Andes, Mérida, Venezuela.  
2008 Third period (Student Interchange). Master on Mechanical Engineering, National Autonomous University of Mexico, Mexico city, Mexico.  
2007 - 2008 First and second period. Master on Mechanical Engineering, Universidad de los Andes, Mérida, Venezuela.  
2001 - 2007 Mechanical Engineer, Universidad de los Andes, Mérida, Venezuela.

## Work Experience

2014 - present Mechanical Design Engineer, Engineering Design Department, Max-Planck Institute for Astronomy, Heidelberg, Germany.  
2013 - 2014 Master Thesis (equivalence), Engineering Design Department, Max-Planck Institute for Astronomy, Heidelberg, Germany.  
2007 - 2013 Mechanical Design Engineer, Technical Department, CIDA, Mérida, Venezuela.  
2006 - 2007 Internship. Review, reparation and improvements of the dome and gate of the Double Astrograph Telescope, Centro de Investigaciones de Astronomía (CIDA), Mérida, Venezuela.